Statistical Models of Nominally Flat Rough Surface Contact

by

Yang Xu

A dissertation submitted to the Graduate Faculty of
Auburn University
in partial fulfillment of the
requirements for the Degree of
Doctor of Philosophy

Auburn, Alabama
Dec 16, 2017

Keywords: Rough surface, Contact mechanics, Fracture mechanics, Adhesion, Boundary Element Method

Approved by

Robert Jackson, Chair, Professor of Mechanical Engineering
Hareesh Tippur, Professor of Mechanical Engineering
Jeffrey Suhling, Professor of Mechanical Engineering
Narendra Govil, Professor of Mathematics and Statistics

Abstract

In this dissertation, the linear elastic contact between a nominally-flat rough surface and a rigid flat is studied analytically and numerically. When the roughness is excluded from the surface, the corresponding contact area is referred to as the nominal contact area and it is larger than the real area of contact when the roughness is included. At the stage of early contact, where the real area of contact is nearly vanishing, the historical development of the corresponding statistical models is studied systematically based on the various combinations of the different forms of the asperity contact model and the probability density function. At the stage of nearly complete contact, where the real area of contact almost reaches the nominal contact area, various statistical models are proposed under the framework of the statistical model at the stage of early contact. At this stage, the non-contact area (the complimentary of the real area of contact) consists of multiple non-contact regions which can be considered by pressurized "cracks". Through the study of the area and the trapped volume of each pressurized "crack", the (non-)contact ratio and the average interfacial gap can be formulated following the statistical approach.

For the purpose of validation, the boundary element method (Polonsky and Keer model) is adapted for the periodic nominally-flat rough surface contact problem. A new surface generation algorithm is developed to generate a rough surface which is isotropic, Gaussian and fractal. Multiple surface groups are generated numerically associated with different parameters (i.e., the lower/upper cut-off wavenumber and Hurst dimension) and each group contains 50 generated surfaces. The statistical models at the stage of early contact and the nearly complete contact are validated by the solutions solved by the boundary element method. Finally, an empirical model is found through a curve-fit based on the statistical model of nearly complete contact and the boundary element method results.

Acknowledgments

I would like to express the deepest appreciation to my advisor, Dr. Robert Jackson, for his excellent guidance, inspired discussions and trusts. Dr. Jackson lead me to the study of the rough surface contact in his class, Friction, Wear and Lubrication, in fall semester of 2010. The knowledge of Greenwood-Williamson model I learned from his class eventually becomes main focus in this dissertation. During my entire Ph.D. program, Dr. Jackson constantly provided me with multiple research opportunities and those research projects are excellent chance to apply the knowledge of tribology to the real engineering practices. I would like to thank my committee member, Dr. Hareesh Tippur, for his guidance and inspired discussions in the area of fracture mechanics. The analogy between the contact mechanics and the fracture mechanics is inspired by his graduate level course, Fracture Mechanics. Later one, this idea was emphasized by Dr. Tippur constantly in our discussions. I would like to thank my committee member, Dr. Jeffrey Suhling, for his inspired suggestions for my dissertation. I would like to thank my committee member, Dr. Narendra Govil, for the complex analysis I learned from his excellent courses. Complex analysis is an universal tool for two dimensional elasticity and it eventually helps me to finish one paper on the periodic waviness contact which is not documented in this dissertation. I would also like to thank Prof. Michele Ciavarella from Politecnico di Bari, Italy. Without his constant inputs and inspired discussions, I would never finish the statistical model including the adhesion in Chapter 6. I would like to thank Dr. Bart Prorok from materials engineering at Auburn University for his excellent teaching in the failure of engineering meaterials and his guidance in our research project.

I would never finish my Ph.D program without the help of my colleagues and friends in Auburn University. I am indebted to Xianzhang Wang, Bowen An, Xiaohan Zhang, Kamran Kardel, Ali Khoshkhoo, Nianju Fu, Sudan Ahmed, MariAnne Sullivan, Yan Chen, Anqi Zhang, Hamid Ghaednia, Ozdes Cermik, Swarna Saha, Alex Locker, Nolan Chu, Dr. Andres

Carrano and Dr. Dan Marghitu for their assistance and inspiring discussions on multiple research projects. I would like to thank Xianzhang for his permission to use his figure in Fig. 1.10. I would like to thank my friends in Auburn, Jason Smith, David Smith, Xinyu Zhu, Xin Wang, Zhuonan Wang, for being nice hosts in the weekend.

I am grateful for the support of the Auburn University Hopper Cluster for the assistance of this dissertation. I would like to thank Allegheny Plastic and Molex for their financial support through graduate research assistantships. I would like to thank Taiho Kogyo Tribology Research Foundation (TTRF) for granting a funding to support a one-year (2017-2018) tribological study on the measurement of the real area of contact. I would like to thank American Society of Mechanical Engineers (ASME) tribology division and the Auburn University Graduate School for their travel awards in years 2013-2016.

I would like to dedicate this dissertation to the giant in the contact mechanics, Prof. Kenneth Johnson, who passed away Sep 21, 2015. His classic work, The contact of Elastic Regular Wavy Surfaces, published in 1985 inspired me in a various way.

Finally, I would like to thank my wife Dan Zhang, for her patience and understanding. I would also like to thank my parents and Dan's parents for their faith in me.

Table of Contents

List of Figures

List of Tables

Chapter 1

Introduction

Rough surface contact is an important branch of the contact mechanics field where the interaction between rough surfaces is studied. When the analytical analysis and computer aided engineering (CAE) is applied to the various engineering practices where the contact interfaces are involved, nearly all the interfaces are assumed to be smooth and deterministic. In the study of tribology, however, rough surfaces are an important concern. Traditionally, rough surface contact is never explicitly mentioned in the definition of tribology which is defined as the study and application of the principles of friction, lubrication and wear of interacting surfaces. This is also reflected in the world-wide tribology conferences where few sessions are dedicated to rough surface contact (or broadly contact mechanics). The logic behind this is unclear since the study of the rough surface contact is the key to all major three topics in tribology. Friction between the interacting surfaces stems from the interaction between the asperities. The rough surface contact plays a major role in the mixed and boundary lubrication. One of the major types of wear, abrasive wear, is due to the ploughing of harder asperities over the softer counter surfaces. In order to give more vivid example of how rough surface contact affects machine components, two examples are given below:

Electrical connector Rough surface contact originally stems from the study of the electrical contact between the connectors. Researchers, nearly one hundred years ago, found a strange phenomenon that the summation of the bulk resistances is lower than the measured resistance of the connector pair [1]. This leads to an important suggestion that the mating surfaces are not in contact everywhere within the nominal contact area. This hypothesis has been revisited by experiments [2]. The increasing part of the resistance is called the *contact resistance* (constriction resistance), which is attributed to the constriction of the current flow within the discretized contact spots, see Fig. 1.1. Those contact spots are known as the *a-spots* in the study of the electrical contact literature. Joule heating is a direct consequence of the constriction of the current lines and it eventually results in failure at the vicinity of the a-spots in the form of oxidation.

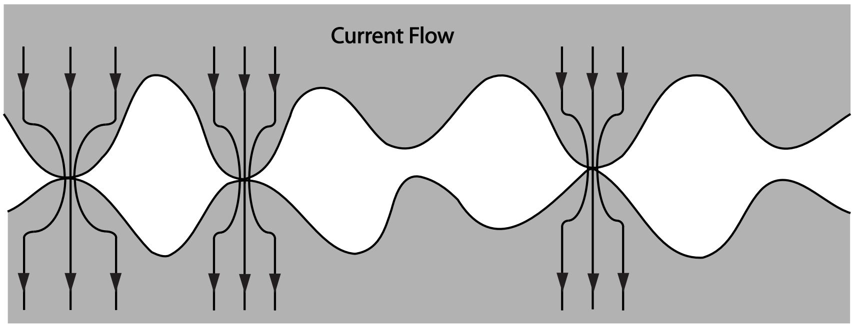

Figure 1.1: Schematic representation of the current lines constricted by the A-spots between the two rough surfaces.

Seal Industrial sealing devices can be divided into two categories, namely, the static and dynamic seals. Gaskets are one of the static seals which “are clamped between two separable members of a mechanical joints” [3]. To prevent the leakage of the pressurized fluids/gas, the roughness of the surfaces of the sealing interfaces are commonly lapped down to a fine level so that the bearing area (real area of contact) is as large as possible. Regardless of advanced polishing technique, the roughness is inevitable on the machined surface. Therefore, zero-leakage can never be achieved [4]. The researchers found that the leakage correlates with the contact area distribution [5–7]. The mechanical face seal is a dynamic seal which is widely used in the pump industry. The leakage of the fluids and gas are prevented by the flat face interaction between two primary seal rings, as well as the secondary O-rings. The failure of the mechanical seal is mainly due to the wear of the two primary seal rings. The lubricant is applied to separate two interfaces in order to reduce the frictional torque [8]. However, the asperity interaction still exists which eventually causes wear.

The reviews of the experimental, analytical and numerical work conducted in the past are presented in the rest of this chapter.

1.1 Review of Experimental Work

In the area of rough surface contact, the main topic is how to measure the interfacial properties, e.g., the real area of contact, interfacial gap distribution, contact pressure distribution, etc. Among all the interfacial properties, the real area of contact is the most heated topic. Therefore, this review is biased towards the work associated with the measurement of real area of contact.

The methods developed for the measurement of the real area of contact and interfacial properties can be generally divided into two categories, namely, the indirect and direct methods. Depending on whether the measurements and the physical contact are taken in the same time and location, some methods are in-situ and the rest are ex-situ. In the following sections, attempts in the past to tackle these two challenges are divided into five main categories, namely, (i) the contact resistance method, (ii) acoustic method, (iii) pressure sensitive paper, (iv) CT/micro-CT/MRI, (v) coating method and (vi) optical method. A brief survey of different experimental techniques applied to the rough surface contact, along with the corresponding technical specifications, are summarized in Table 1.1 at the end of Section 1.1. More details on the historical development of the experimental techniques can be found in the following literature reviews: [9–14]. Indeed the experimental work shall never be succeed without the development of the rough surface measurement technique (e.g., stylus profilometer, optical profilometer, atomic force microscope (AFM) and etc). However, this will not be touched in this review and the interested reader should refer to [15–17] for more details.

1.1.1 Contact Resistance Method

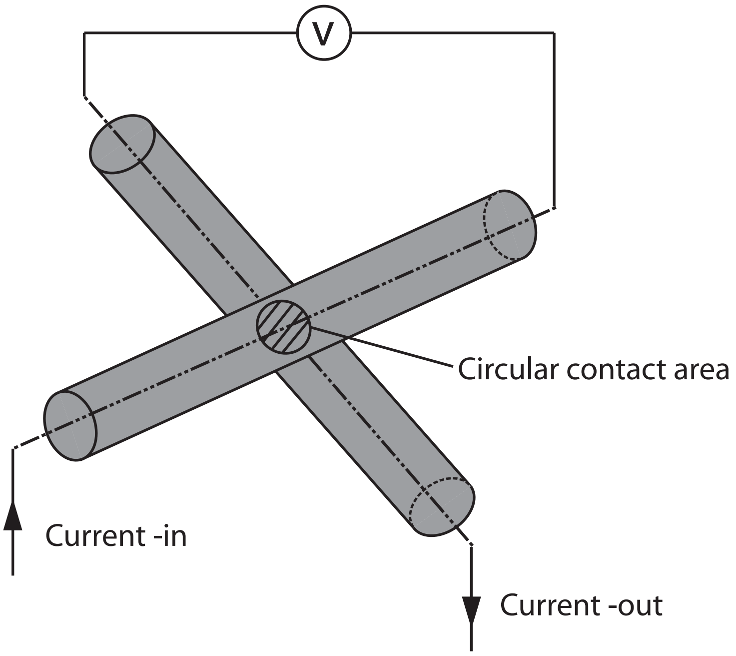

Figure 1.2: Schematic representation of the contact resistance measurement between two cylindrical pins using four-wire method.

The contact resistance method is an in-situ and indirect measurement of the contact area. This method plays an important role in the early stage of the development of the rough surface contact theory. Before 1912, electrical conductance between contacting bodies had been widely studied. Binder [1] in 1912 found that the measured conductance across two contacting bodies is smaller than the summation of the conductance of each contact body. Based on this experimental result, Binder made an important assumption that only a small portion of the area is in solid contact. In the later years, this assumption had been approved by other advanced experimental work, which will be discussed later, and is treated as a basic principle in the study of the rough surface contact. From the author's perspective, the rough surface contact stems from the work of Binder.

Contact resistance method can be applied to measure the apparent contact area of the axisymmetric indenter. When two similar cylindrical pins are in contact within a nominal circular/elliptical region, the current is flowing from one metal to another and it is constricted within this region, see Fig. 1.1. If we neglect the contaminants over the contact interfaces (e.g., oxide layer), the constriction of the current line results in the contact resistance. The contact resistance is in a function of the electric conductivities of the mating metals and the radius of the contact [2]. Based on this closed-form solution, the apparent circular contact region can be quantified indirectly by measuring the contact resistance first [1, 18]. This method is restricted to the case where two surfaces are smooth and the apparent contact region is circular, see Fig. 1.2. For the non-circular contact region, the corresponding closed-form relation between the contact resistance and the real area of contact may not be available. Assuming the each asperity contact area is the same, Tabor [18] was able to estimate the number of contacting asperity and the mean asperity contact area of a nominally flat rough surface contact. Another restriction of this method is that both contact bodies has to be conductive, i.e., the contact pairs involving the ceramic and polymer are not suitable for this method.

1.1.2 Acoustic Method

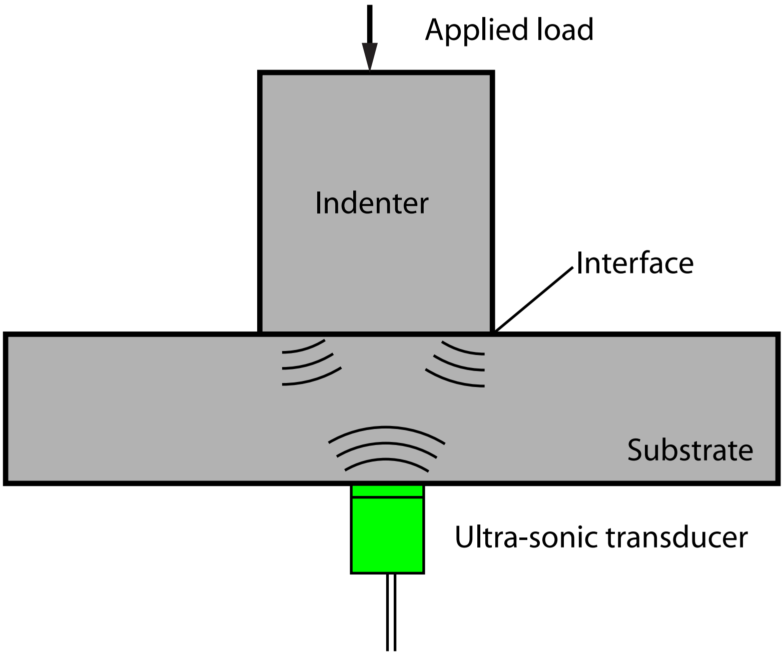

Figure 1.3: Schematic representation of the acoustic method.

The acoustic method is an in-situ and indirect measurement of the contact area. A schematic representation of the acoustic method is shown in Fig. 1.3. The acoustic method has many successful applications to the contact problems (e.g., spherical contact [19, 20], universal joint contact [19], wheel-rail contact [21], dovetail milling cutter-steel plate contact [24], etc.) where the dimensions of the contact area are commonly in the macro-scale. Except for the mapping of real area of contact, the acoustic method can also predict the contact stiffness [22, 23].

In the acoustic method, the mapping of the real area of contact relies on the distribution of the reflection coefficient R. At the solid-solid contact interface, R approaches 0. When the interfaces are out-of-contact with infinite gap (i.e., out-of-contact), R approaches 1. For the location where the air of finite gap is trapped between rough interfaces, R should between 0 and 1. However, the acoustic transducer has a focused spot with the radius of several hundred μm, which is larger than 1 μm (an common lateral resolution in characterizing the rough surfaces). This causes blurred boundaries between the distribution of the reflection coefficient at contact and out-of-contact area. Therefore, the acoustic method cannot distinguish the contact area from the out-of-contact area down to the micron/nano-scale. Its application is mainly restricted to the large-scale contact problem where the size of the contact area is significantly larger than the that of the focused spot of the acoustic transducer. Another limitation of the acoustic method is that the acoustic transducer needs to be emerged in the water bath for a good focusing of the incident wave over the interface.

1.1.3 Pressure Sensitive Paper

Pressure sensitive paper/film is used in the study of faults friction [25–27], tire-road interaction [28] and wheel-rail interaction [29]. This method can indirectly measure the contact pressure distribution and the real area of contact. This method is simple and does not require complicated equipment. This method is normally for the purely normal contact. During the contact, a thin pressure sensitive paper manufactured by Fujifilm® (Japan, Tokyo) is inserted between the indenter and the sample, see Fig. 1.4(a). After detaching of the contact pair, the contact spots on the pressure sensitive paper turn to different colors which are correlated with the corresponding contact pressure. After scanning of the paper, the contact pressure distribution and the contact spot distribution can be identified through image processing, see Fig. 1.4(b). The resolution is limited by the size of the ink capsular in the paper. Additionally, the insertion of a third body (pressure sensitive paper) between the contacting rough surfaces may change the contact status, especially when the thickness of the paper is larger than the roughness. Therefore, this

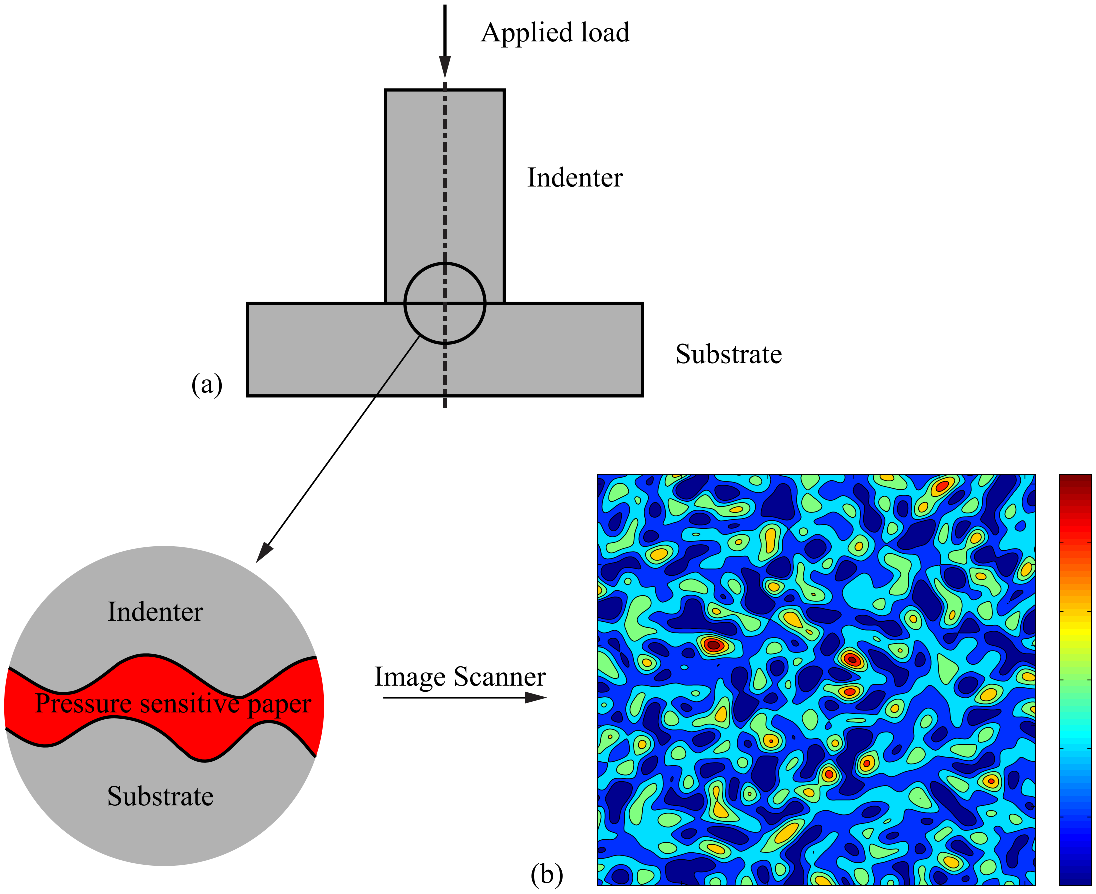

Figure 1.4: Schematic representation of the (a) indentation scheme and (b) the color distribution on the pressure sensitive paper after the indentation. Blue and red colors are associated with the low and high contact pressure.

method can only be applied to the large scale contact problem where the roughness/waviness is significantly larger than the thickness of the paper. Under the larger load, some sharp asperities may cause the penetration of the paper. The contact pressure may also create surface tension outside the contact area where the color is changed and that spot may be mistakenly treated as contact spot. Therefore, this method tends to exaggerate the real area of contact and cannot be applied to case where local contact pressure is extremely high.

1.1.4 CT/micor-CT/MRI

Computed Tomograph (CT)/ micro-Computed Tomograph (micro-CT)/Magnetic resonance image (MRI) is a non-destructive method to create cross-sections of a physical object. The cross-sections are combined to form 3D image. These advanced techniques are wildly used in the

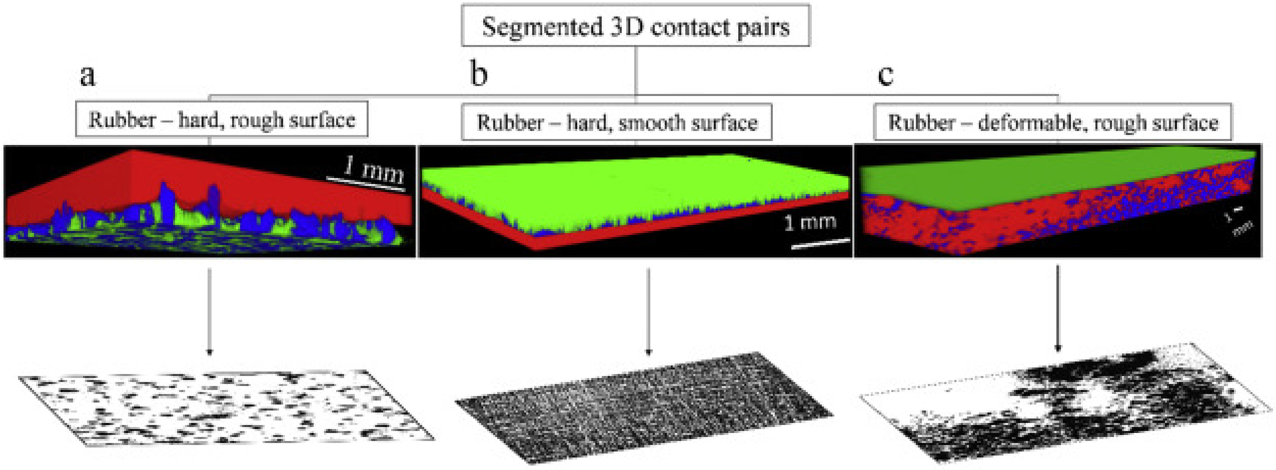

Figure 1.5: 3D plots of the contact interfaces and the corresponding contact area distribution [34] associated with three different contact pair. Reprinted from Polymer Testing, **53**, Kriston, A., Fülöp, T., Isitman, N.A., Kotecký, O. and Tuononen, A.J., A novel method for contact analysis of rubber and various surfaces using micro-computerized-tomography, pp. 136, 2016, with permission from Elsevier.

radiology and many engineering practices (e.g., defect detect in the engineering materials). CT/micro-CT/MRI scan is an ideal method for the measurement of the contact area and the interfacial gap. However, it is until recently that CT/micro-CT/MRI is applied to the study of the real area of contact. The contact area and the interfacial gap can later be identified through image processing of the recorded 3D images, see Fig. 1.5. Unless material is magnetic, CT/micro-CT is capable of measuring most engineering materials. The clinical MRI scanner is also suitable for bio-materials. The clinical MRI scanner was used in the study of joint contact [30]. The CT scanner was frequently used to study the electrical contact interface by the group of Swingler [31–33]. Recently, Kriston et al. [34] used the micro-CT to study the contact between rubber and various rough surfaces.

Since the contact pair must be loaded inside the chamber of the CT/micro-CT, the sample size is restricted. Due to the relatively long scanning time, the CT/micro-CT/MRI scanner is currently suitable for the quasi-static loading only. The resolution of the micro-CT scanner is also limited to $2\ \mu m$ [34]. A better resolution can be achieved using the nano-CT, but the working space for the specimen is further reduced.

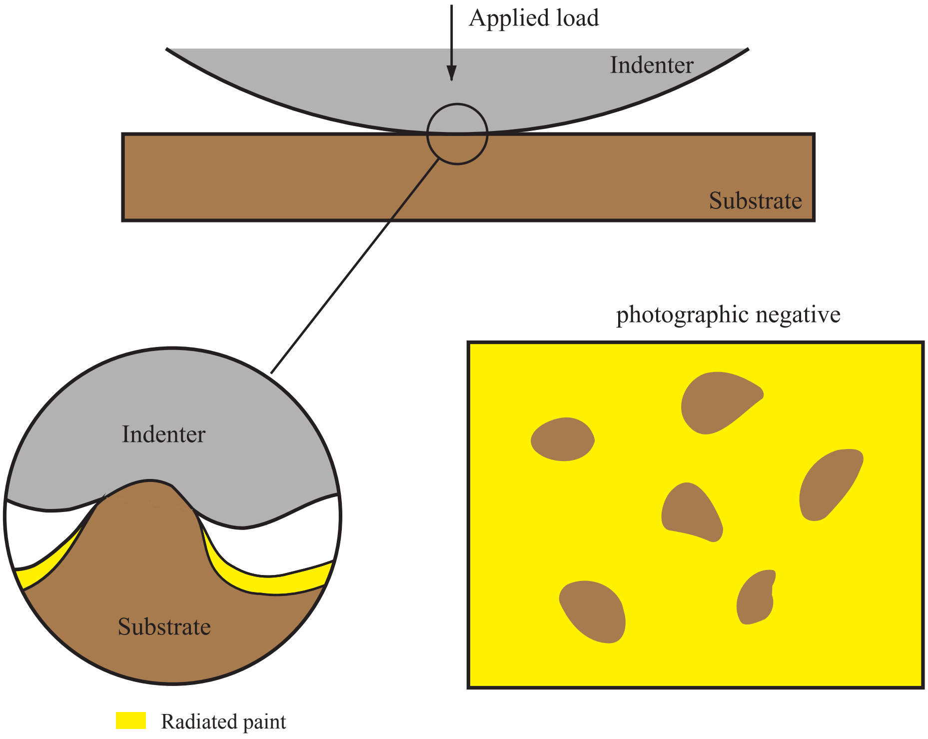

Figure 1.6: Schematic representation of the coating method proposed by Tarasenko et al. [35].

1.1.5 Thin Coating Method

The thin coating method is an indirect and ex-situ method. A thin film of coating can be used to identify the location of contact between two rough surfaces in various ways. The literatures related to this topic are relatively rare compared with the other methods. Tarasenko et al. [35] applied a thin, radiated paint onto one surface. The paint was suspended in the solvent and was deposited on the surface once the solvent evaporated. After detachment of the contact pair, the radiated paint is assumed to be transferred from one surface to another only within the contact area. The original rough surfaces are irradiated. On the photographic negative of the rough surface (originally without paint), the area with transferred paint (contact area) has a great contrast with the area without paint (out-of-contact area). Schematic representation of Tarasenko's method is illustrated in Fig. 1.6. A similar idea has been used by D'yachenko et al. [36]. Before mating of two rough surfaces, one of them is radio-activated. After detachment of the contact pair, the metallic particles from the activated surface are assumed to be transferred to the counter surface, which is not activated. The real area of contact can be mapped using the radiographic methods. Nitta [38] inserted a thin film of poly(ethyleneterephthalate, PET) between two rough surfaces. After contact, the PET film is severely deformed within the contact area. Then, the contact area distribution can be indirectly obtained through the optical measurement of the indents on the PET film. Bettscheider et al. [37] deposited a thin film of gold (Au80Pb20) on the surface of a substrate which is indented by a bearing ball. When the deposited surface is scanned by the scanning electron microscope (SEM), the second electron image can create a strong contrast inside and outside the contact area due to the the difference of the topographical gradient. The coating method can only applied to the quasi-static contact where no sliding occurs. The methods rely on the local behavior of the coating. In refs. [35,36], it is nearly impossible to prove that the transfer of coating occurs throughout the entire contact area. In refs. [37, 38], the methods rely on the permanent deformation of the coating and its substrate may overestimate the real area of contact since the coating outside the contact area (closing to the contact edges) may also have severe deflection. The deflected part of coating also may not always be part of the contact area.

1.1.6 Optical Method

The optical method is an in-situ and direct method and a schematic representation is shown in Fig. 1.7. It is the most popular technique applied to the rough surface contact problem in the various aspects of tribology. It can measure the contact area spots between contacting bodies at either purely normal dry contact [10, 39–43, 45, 47, 52, 56, 57], the pre-sliding dry contact [44, 48, 50, 51], the sliding dry contact [47, 53–55, 58], torsional contact [46, 49] and the wet/lubricated contact [54, 58–60]. The major restriction of the optical method is that one or both contacting bodies are transparent materials. The early studies of contact area using the optical method has been extensively discussed in the review papers [6, 7, 25]. The commonly used transparent bodies are glass (e.g., sapphire [44, 45] and elastomers (e.g., PMMA [51], PDMS [48, 50, 52] and rubber [43, 49, 54]). This significantly limits its application to the contact problem associated with the soft materials. Different types of optical devices are used in different applications. For the sliding contact occurring over a very short time (e.g., the pre-sliding [50,51] and fingertip sliding [53]), high-speed cameras with high frame per second (fps)

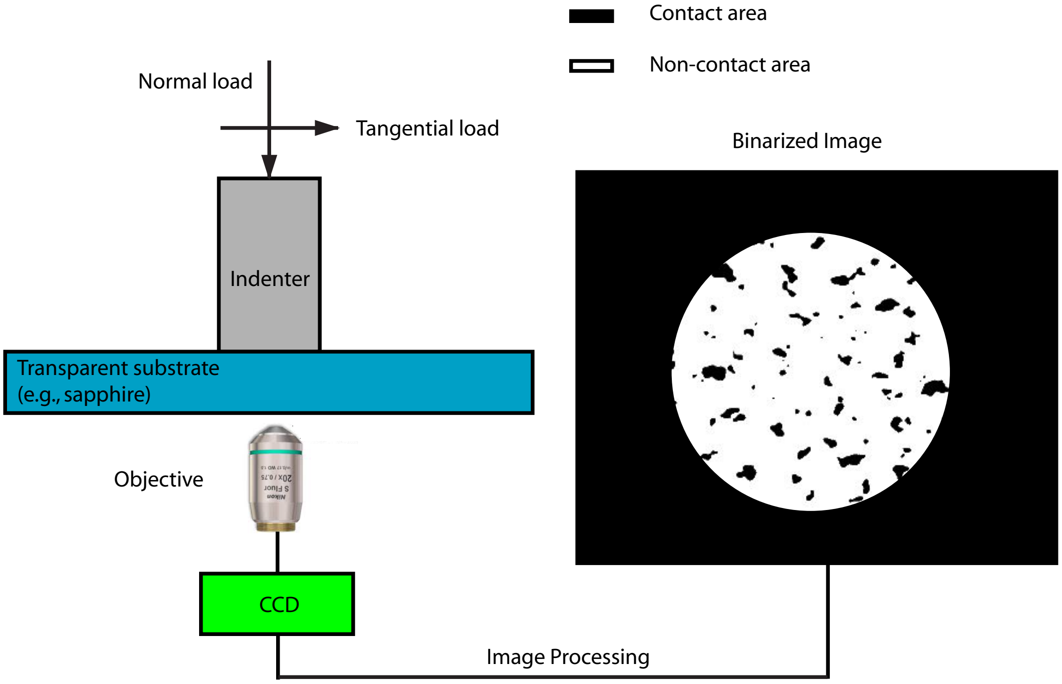

Figure 1.7: Schematic representation of the optical method.

are used. For other contact problems under quasi-static loading, digital cameras [43,59], optical profilometry [37, 42, 56, 57] or digital microscope cameras [44, 47] are used. Additionally, the lateral resolution of the optical method is restricted by the theoretical limit of the optical device, i.e., $0.2\mu m$. The reported (in-plane) resolutions of the measurements (interval between pixels) taken by the optical method vary from $0.2\ \mu m$ [40] to $8\ \mu m$ [42]. The resolution is usually deteriorated significantly to $156\ \mu m$ if a high-speed camera [51] is used.

1.1.7 Remarks

Table 1.1 summarizes the main features of the experimental technique discussed above. It is clear there no univerisal approach to measure the real area of contact. An appropriate approach should be picked based on the practical problems.

1.2 Review of Analytical Work

Ever since the experimentalists [1, 2, 18] confirmed that only a fraction of the apparent contact area is in contact based on the electrical contact, many theoretical attempts have been made

Table 1.1: Summarization of various experimental techniques

Method	Lateral resolution[a]	Contact scheme	In-situ/Ex-situ	Specimen restriction
Contact resistance method	> 1 mm	Normal/sliding contact	In-situ	Specimen must be conductive
Acoustic method	> 1 mm	Normal/sliding contact	In-situ	No
Pressure sensitive paper	> 1 mm	Normal contact	Ex-situ	No
CT/micro-CT/MRI	$> 1\ \mu$m	Normal/sliding contact	In-situ	Specimen should not be magnetic
Thin coating method	> 1 nm	Normal contact	Ex-situ	No fluid
Optical method	$> 0.2\ \mu$m	Normal/sliding contact	IN-situ	One of bodies is transparent

Method	Test rig restriction
Contact resistance method	Contact area may be overestimated due to the inclusion of the bulk resistance method
Acoustic method	Acoustic sensor need to be emerged in the water
Pressure sensitive paper	Low to medium contact pressure (< 300 MPa)
CT/micro-CT/MRI	Loading device must be small enough to fit in the chamber
Thin coating method	No
Optical method	No

---

[a] Only the rough lower limits are given based on the results published in the past literatures.

to accurately calculate the real area of contact. Analytical work developed in the past can be divided into two main categories: *random process model* and the *multi-scale model*. The random process model is also known as the *statistical model* or the *multi-asperity contact model*. In the former category, the roughness is considered as a random process, i.e., the geometry of the roughness is indeterministic. The rough surface contact problem in this category is solved in a statistical manner. In the later category, the rough surface is assumed to have a multi-scale nature where more geometrical features are shown as the length scale is decreased. This multi-scale nature of rough surface indeed changes the real area of contact, the contact pressure, etc, as more and more finer scales are included. The development of the models in these two categories are briefly discussed and the inter-connections between them are also touched upon. Before we move to the introduction of these two major models, some fundamental works performed by Barber [61, 62] need to be introduced. Barber [61] rigorously proved that, for a purely normal contact between a rigid punch with a smooth surface and an elastic half-space, the indentation depth and the real area of contact increased monotonically with the normal load. This monotonic trend is obvious in many statistical and multi-scale models under certain loading condition and assumptions. However, it is Barber who firstly gave the rigorous proof based on the fundamental equations. It is obvious that Barber's theorem is suitable for the rough surface contact. Barber [62] later showed the analogy between the electrostatic problem and purely normal contact problem. Additionally, he rigorously proved that the purely normal elastic contact between two half-spaces with rough surfaces is equivalent to an elastic half-space indented by a rigid rough surface.

1.2.1 Random Process Model

It is commonly known that the first[1] random process model is developed by Greenwood and Williamson [63] in 1966 and it is referred to as the GW model. In their classic paper, Greenwood and Williamson studied the purely normal contact between a nominally flat rough surface

---

[1] The very first statistical model is developed long before the Greenwood-Williamson model by the Soviet Union scholar Zhuravlev in 1940. The English version of this historical paper is translated by Borodich [67].

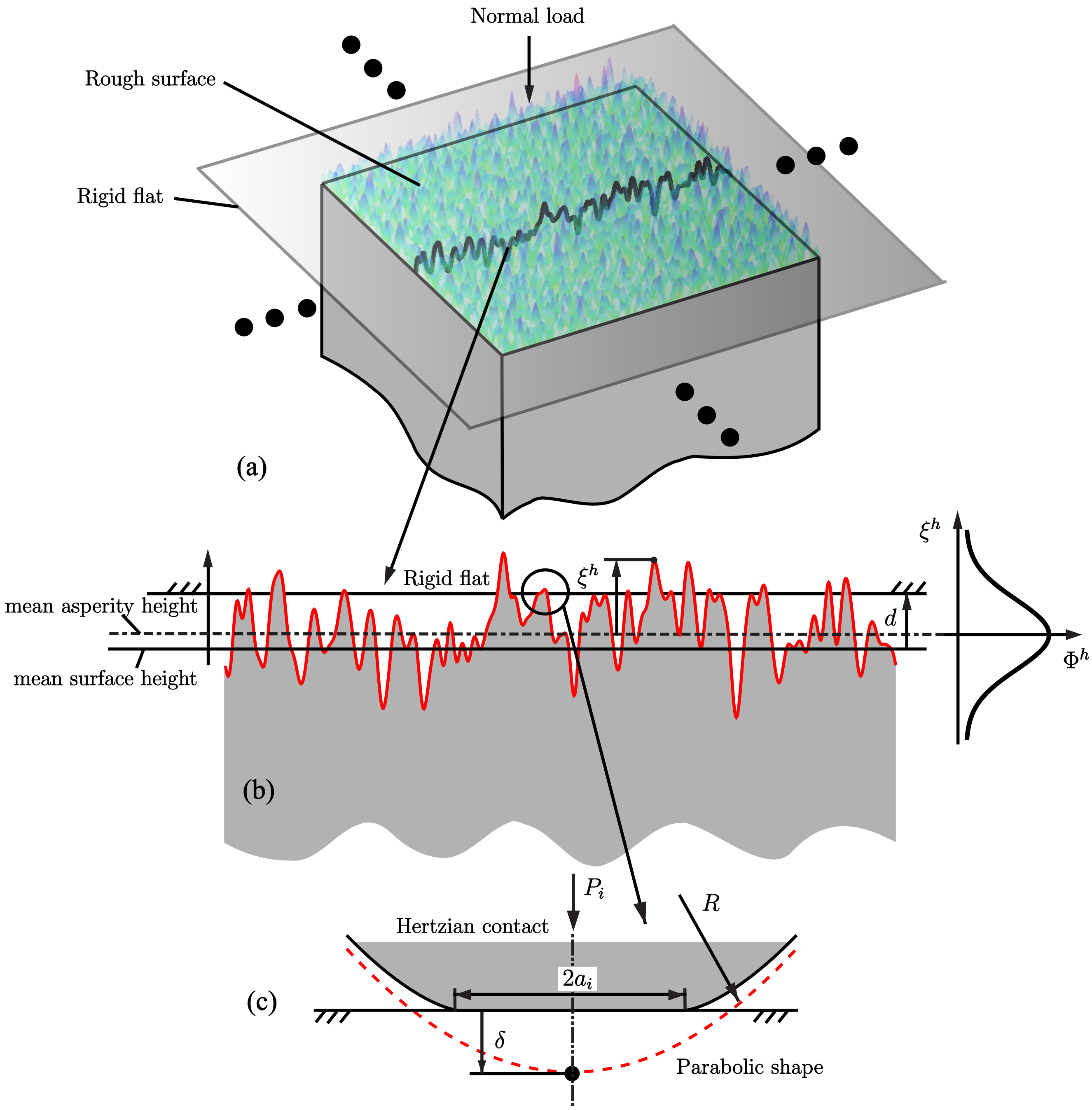

Figure 1.8: A schematic representation of the GW model at (a) a global view. The detailed interaction between the rough surface and the rigid flat is illustrated in (b). The contact at the asperity level is shown in (c).

and a rigid flat, see Fig. 1.8(a). The contact load is supported by individual contacting asperities and a cross-sectional view of the contact interface is shown in Fig. 1.8(b). Each asperity is assumed to have an axisymmetric parabolic shape. The contact load, P_i, and the corresponding contact radius, a_i, of each contacting asperities are in the function of the indentation depth, δ, see Fig. (1.8)(c). The classic Hertzian theory is used [65, 75] to calculate $P_i(\delta)$ and $a_i(\delta)$. The indentation depth is the subtraction of the surface separation, d, from the asperity height, ξ, i.e., $\delta = \xi - d$. Taking the asperity height as the only random variable and assuming it follows the Gaussian distribution, $\Phi^h(\xi)$, then the *statistical expectation* (*ensemble average*) of the contact load and the contact area of all asperities is

$$\langle A_i \rangle = \int_d^\infty \pi a_i^2(\xi - d)\Phi^h(\xi)d\xi, \quad \langle P_i \rangle = \int_d^\infty P_i(\xi - d)\Phi^h(\xi)d\xi. \tag{1.1}$$

Therefore, the real area of contact, A_r, and the total applied load, P, associated with the surface separation, h, is

$$A_r = n\langle A_i \rangle, \quad P = n\langle P_i \rangle, \tag{1.2}$$

where n is the total number of asperities. Asperity density η, a ratio of n to the nominal contact area, A_n, is often used to replace n, thus the above relation is rewritten as

$$A^* = \eta\langle A_i \rangle, \quad \bar{p} = \eta\langle P_i \rangle, \tag{1.3}$$

where $A^* = A_r/A_n$ is the contact ratio and $\bar{p} = P/A_n$ is the average contact pressure.

Some important assumptions adopted in the GW model are summarized below:

- **Assumption 1.** The asperities have the same radius of curvature, R;
- **Assumption 2.** Neighboring contacting asperities do not interact[2];
- **Assumption 3.** The asperity deformation is linear elastic;
- **Assumption 4.** The asperity height follows the Gaussian distribution.

---

[2] This assumption is commonly referred to as the *asperity interaction*, even though it may confuse readers who are not in this area. An appropriate description may be stated as: “Neighboring contacting asperities are not coupled due to the elastic deformation of the substrate”.

In the rest of this section, the improvements of the GW model relating to the above four assumptions in the past literatures are briefly reviewed.

Assumption 1 is due to the fact that the radius of curvature of the asperity is not a random variable. Some attempts have been made from the tribologists and mathematicians to include the radius of curvature as a random variable. Based on the measured rough surfaces, Whitehouse and Archard [68] found a correlation that the higher asperities have sharper tips (smaller radius of curvature). By assuming an exponential-like auto-correlation function and the tips of the asperities are all axisymmetric, Whitehouse and Archard derived a joint probability density function (PDF) $\Phi^h(\xi, C)$ where C is the radius of curvature of the asperity tip. This joint PDF is used by Onions and Archard [69] under the framework of the GW model. In fact, a more rigorous and systematic study of the statistics of the isotropic random stationary surface [70], as well as the random moving surface [71], has been conducted by the mathematician Longuet-Higgins in the late 1950s. It was Nayak [72] in 1971 who applied the Longuet-Higgins' random theory to the characterization of the engineering surfaces and it is commonly known as the *Nayak's random theory*. In his classic paper, the statistics of the isotropic random surface (3D) and random profile (2D) are distinguished for the first time and studied individually. Various forms of PDF have been derived analytically and some are essential to the later development of the statistical models. Starting from Nayka's paper [72], moments(m_0^h, m_2^h and m_4^h), describing the variance of the surface height, surface slope and the surface curvature, and the bandwidth parameter, $\alpha^h = m_0^h m_4^h/(m_2^h)^2$, became popular in the statistical characterization of the isotropic rough surfaces. A more detailed compilation of the statistics of the isotropic Gaussian random surface (profile) can be found in Thomas's excellent textbook [73]. Bush, Gibson and Thomas [74] in 1975 proposed the most complete random process model (known as the BGT model) for the linear elastic Gaussian surface contact. The asperity is assumed to have a parabolic shape associated with major and minor principle curvatures. Hertzian theory [75] for the single asperity contact is naturally applied to calculate the normal load and the elliptical contact area on the single asperities in a function of penetration. The joint PDF of the asperity is in a function of the asperity height, major and minor principle curvatures of the asperity summit. When the normal load is vanishing, the contact ratio (real area of contact normalized by the nominal contact area) is asymptotically proportional to the average pressure (normal load normalized by the nominal contact area) with the constant of proportionality depending on the root mean square (rms) slope and the reduced modulus, E^*, only. The complete BGT model involves triple integrals for the calculation of the real area of contact and the applied load. Some efforts have been made to simplify the BGT model through reducing the number of the random variables [73, 77, 79]. In the original GW model, several inputs (e.g., asperity density) need to be obtained from the measured rough surface data. For a strictly Gaussian surface, those inputs should be in a function of the moments, m_0^h, m_2^h and m_4^h [72, 74, 76] which makes the GW model much easier to be applied as long as the moments are known in advance. This simplification of the inputs of the GW model was first proposed by McCool [76].

Assumption 2 is due to the fact that the substrate beneath the rough surface is rigid, which is not explicitly claimed by Greenwood and Williamson in the GW model [63]. Therefore, the GW model can also be treated as a Winkler elastic foundation [65] with nonlinear springs. When the real area of contact is a negligibly small fraction of the nominal contact area, each contacting asperity is distantly away from each other. Therefore, each contacting asperity can be studied individually and assumption 2 is approximately satisfied. As the applied load increases, the distance between the neighbouring contacting asperities is reduced and the state of stress at one asperity may eventually affect its neighboring contacting asperities (by lower their height) and it is known as the *asperity interaction*. As the applied load further increases, the isolated circular/elliptical asperity contact areas may coalesce into irregular shaped contact patches. Therefore, *most of the random process models can only be applied to the light load case*. Since the roughness in the random process model is indeterministic, it is nearly impossible to include the deflection of the substrate accurately. Alternatively, the deflection has been included in an average sense [81, 82, 89]. Few attempts have been made to include the asperity coalescence [83, 84].

Assumption 3 restricts the application of the GW model to linear elastic materials. Nowadays, the GW model has been adapted to cover various material types. Among those, the elastoplastic rough surface contact is the most active area. The key to the adaption of the GW model to cover different material types is to develop the corresponding asperity contact model. In the elastoplastic asperity contact model, the deformation of the single asperity has usually been divided into three stages based on the extent of the indentation depth [85]: (i) linear elastic stage; (ii) elastoplastic stage and (iii) fully plastic stage. The linear elastic stage is governed by the Hertzian theory [65, 75]. The fully plastic stage is commonly described by a truncation model known as the Abbott-Firestone (AF) model. However, in the original paper of Abbott and Firestone [86], no truncation model of fully plastic stage is mentioned. Instead, they invented a way to study the properties of the bearing surfaces known as the Abbott-Firestone curve. Up till now, the first paper on the fully plastic model is still unknown. In the fully plastic stage, the contact pressure distribution is assumed to be the same as the hardness which is considered as a "common sense" ever since the classic text book of Tabor [18]. This "common sense" has been revisited by Jackson and Green [85] using finite element method (FEM) and Jackson et al. [87] by the slip line theory. They found that the hardness is not constant at three times and the yield strength and the ratio of hardness to yield strength is reduced with the increase of the contact area. In the elastoplastic stage, the contact region and the substrate beneath it are in a mixture of elastic and plastic deformation. An approximated solution was proposed by Chang et al. [88] for the elastoplastic stage based on the volume conservation and it is commonly known as the CEB model. Zhao et al. [89] fixed the discontinuity in the CEB model using a polynomial fit. For a more accurate approximation, the curve-fit results of $P_i(\delta)$ and $a_i(\delta)$ are obtained based on the FEM results [85,90,96]. If the asperity contact is no longer in the (quasi-)stage stage, the impact model should be used instead [92–97]. More information on the development of the elastoplastic asperity contact can be found in a recent review by Ghaednia et al. [98]. Using the above mentioned single asperity models, different elastoplastic rough surface contact models are proposed [99–101].

The application of GW model is restricted to the Gaussian surfaces by Assumption 4. However, the Gaussianity of some engineering surfaces have been questioned by Borri and Paggi [102] and Borodich et al. [103]. Except for the Gaussian distribution, the Weibull distribution [104, 105], Pearson distribution [106, 107] and other asymmetric distributions in a function of the skewness and kurtosis [108] are used in the random process model.

1.2.2 Multi-scale Model

It is commonly accepted that the first multi-scale model for the rough surfaces contact is developed by Archard [109] in 1957. In the Archard model [109], a rough sphere of radius R_0 is in contact with a rigid flat. Archard [109] claimed that the rough surface on the sphere should have the following structure: spherical protuberances of radius $R_1 \ll R_0$ are evenly distributed over the smooth sphere. This "protuberances on protuberances" structure is repeated self-similarly as the the length scale decreases, see Fig. 1.9. At the finer scales, the protuberances of radius R_n, which are subjected to the contact pressure, evenly distributed over the larger protuberances of radius R_{n-1}. The Hertzian theory [65, 75] is applied to calculate the contact area on each single protuberance. Starting from initial two scale structure (only includes the base sphere of radius R_0 and protuberances of radius R_1), the contact load, P, vs. the real area of contact, A_r, can be derived hierarchically. As the number of scales, n, increases, Archard [109] found that the P vs. A_r relation gradually approaches a linear relation. Note that the Hertzian theory (single asperity contact model) predicts a non-linear relation, so Archard model implies that the roughness induces a linearizing effect. Compared with the other popular analytical models, the Archard model is seldom used these days due to the following drawbacks:

- The rough spherical surface depicted in the Archard model is unrealistic.
- The load P vs. A_r relation associated with n scales structure should be manually derived. As n increases, the derivation becomes tedious.

As the first multi-scale model, some of the breakthroughs achieved in the Archard model are listed below and all of them more or less inspired the rest of the multi-scale models and

- The "protuberances on protuberances" structure is equivalent to the concept of (self-similar) fractals found by Mandelbrot [112] and applied firstly by Majumdar [110, 111] in 1991. It is surprised that Archard has already applied this concept successfully to the rough surface contact 34 years ago.
- The Archard model is the first model to predict that the linear relation between the contact load P and the real area of contact A_r could possibly occur in the rough surface contact.

This linearity has been observed in the numerical model of nominally flat rough surface contact [113, 114].

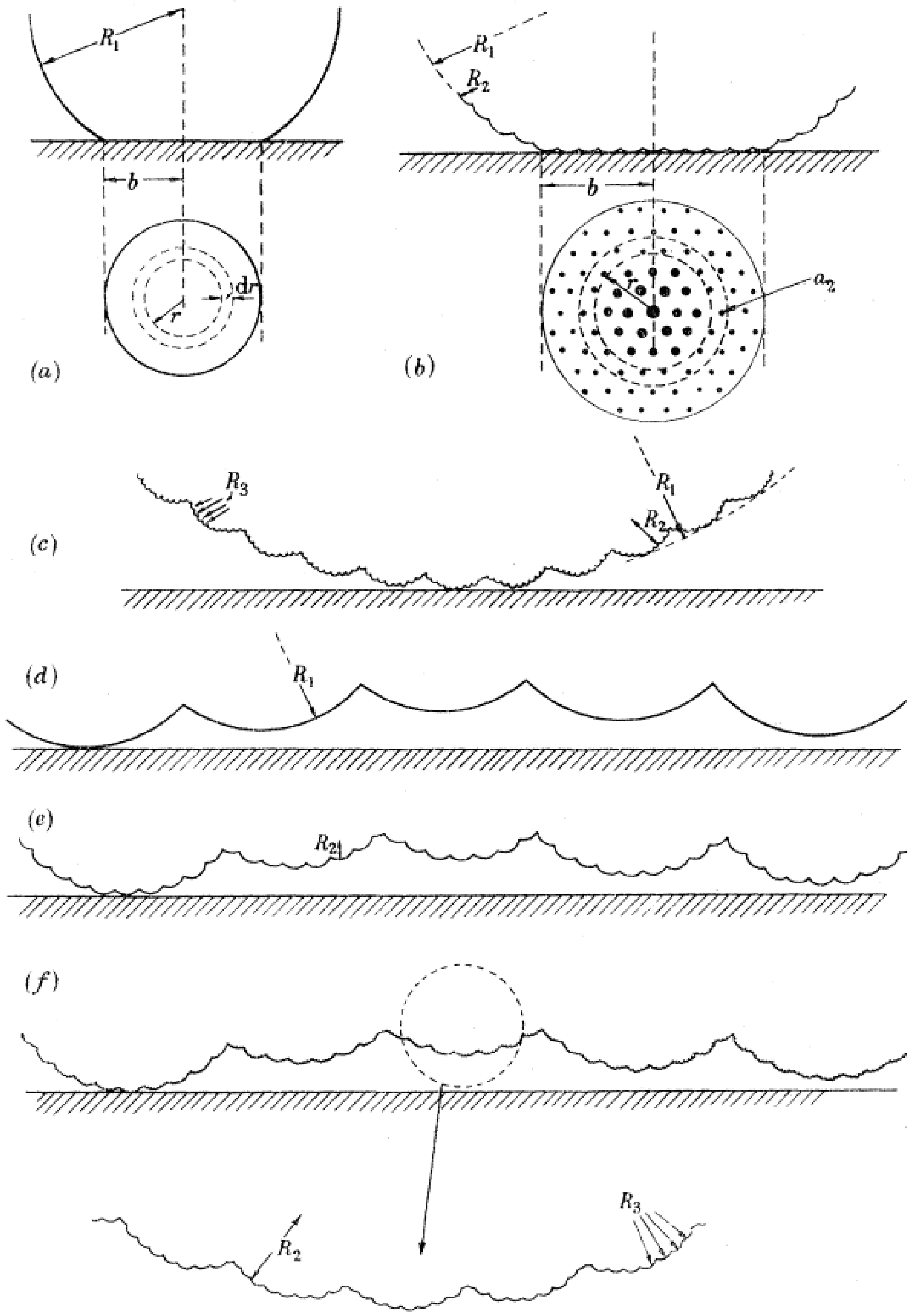

Figure 1.9: Multi-scale structure of (b) the real area of contact and (b) the roughness (c-f) proposed by Archard [109]. Archard, J.F., Elastic deformation and the laws of friction., Proceedings of the Royal Society of London A: Mathematical, Physical and Engineering Sciences, 1957, **243**(1233), pp. 193, by permission of the Royal Society.

The fractal geometry, invented by Mandelbrot [112], is one way to characterize multi-scale nature of rough surfaces. The rough profile (2D) can be represented by the Weierstrass-Mandelbrot (WM) function [111, 115]. The WM function for the rough surface (3D) is proposed by Ausloos and Berman [116] (see also a similar form proposed by Yan and Komvoupolous [117]). Two parameters in the WM function are essential to the fractal characterization: D and G. D is the fractal dimension where $D \in [1, 2]$ for rough profile and $D \in [2, 3]$ for rough surface. G is the characteristic length scale of the surface. Recently, Zhang et al. [118] questioned the validity of the fractal characterization since the different methods of evaluating D and G do not give a consistent prediction for the rough surfaces.

Majumdar and Bhushan [111] proposed the first fractal (MB) model where the multi-scale nature of the rough surface is introduced to the rough surface contact model. The rough surface height was assumed to follow the Gaussian distribution. The contact area at a given surface separation was calculated based on Abbott-Firestone curve [86]. The contact load at a given contact spot of size a was calculated by the Hertzian theory [75]. Due to the known probability density function of the contact spot size found by Mandelbrot [112], the total contact load was obtained based on the statistical expectation of the contact load at each asperity. The MB model has been criticized for its anti-physical phenomenon when it is applied to the elastoplastic contact. For instances, the MB model predicts a transition from plastic to elastic contact as the load is increased [134]. A 3D rough surface contact model has been proposed by Yan and Komvoupolous [117].

Ciavarella et al. [119] adapted the Archard model to the case where a nominally flat rough profile (2D) is in contact with a rigid flat. The rough profile is represented by the WM function which is the summation of the sinusoidal waviness components of increasing frequency. The "protuberance on protuberance" structure in the Archard model is replaced by the "waviness on waviness" model. The classic sinusoidal waviness (2D) model solved by Westergaard [66] is used to determine the real area of contact as the number of higher frequency components are increased (i.e., the length scale is decreased). Ciavarella et al. [119] gives a striking prediction that the real area of contact may monotonically decrease to zero if an infinite number of frequency components are included (i.e., the sampling points interval in the rough profile approaches zero). Additionally, Ciavarella et al. [119] firstly considers the probability of the contact pressure distribution in the rough surface contact. This important concept will be used by Persson [120] and eventually lead to the well-known Persson's model.

Except for the WM function, the fractal geometry is often characterized by its power spectrum density(PSD) vs. frequency relation. More and more measurements [121–124] point to the fact that there is a wide group of engineering surfaces whose (angular average) PSD vs. frequency relation follows a linear relation in a wide span of frequencies. This linear relation has been tested within a large span of wavelengths, $[1\text{nm}, 1000\text{m}]$, associated with different measurement technique (e.g., optical profilometer, atomic force microscope (AFM) and scanning tunneling microscope (STM)). Two fractal parameters, G and D, can be obtained from the linear fit of the PSD vs. frequency relation. However, Zhang et al. [118] questioned if those fractal surfaces associated with linear PSD vs. frequency relation are real fractal.

Persson [120] analytically derived an ingenious model for the frictional contact between a rigid fractal surface and a viscoelastic half-space. The PSD vs. frequency relation of the roughness is linear. The real area of contact in a function of average contact pressure is derived, in the Appendix B of [120], based on the probability density function of the contact pressure distribution which evolves with the number of the included frequency components. An alternative explanation of the Persson's model on the real area of contact is given by Manners and Greenwood [126] where a simpler form of the probability density function of the contact pressure is given. The real area of contact is found to be represented by an error function of the average contact pressure [126, 127]. This simple relation has been tested extensively by different numerical methods [113, 114, 128] and it is proved to be a good approximation to the numerical solution. The Persson model has been extended to calculate different interfacial properties and contact schemes, namely, the adhesive rough contact, average interfacial contact [127], leakage rate of seals [129], interfacial stiffness [130] and etc. The Persson model has been criticized that it is solely based on the geometry arguments and lack of information on the elasticity [131]. Recently, Ciavarella [132] obtained a similar error function for the real area of contact based on a random process model developed by Xu et al. [133]. This indeed shows a close relation between the Persson model and the random process model built under the framework of the GW model. This will be discussed in detail in Chapter 5.

In fact, not all the rough surface can be characterized either by the WM function or the linear PSD vs. frequency relation. An universal way of representing the rough surface is the Fourier series. Jackson and Streator [134] adopt Archard's idea of "protuberance on protuberance" [109]. The fast Fourier transform (FFT) is applied to obtain the amplitude of each sinusoidal component. The number of scales depends on the number of the sampling points. The tip of the sinusoidal waviness is considered as a protuberance with a parabolic shape. In this way, the Archard model which needs manual derivation has been adapted to an automated algorithm. The real area of contact shows a convergent trend as n reaches the maximum value. A simplified version of the Jackson and Streator model is proposed by Jackson [135]. The Jackson and Streator model has been applied to many aspects of tribology, e.g., the electrical contact resistance [136–138], thermal contact resistance [139], liquid-mediated collapse [140], adhesive contact [141], elastoplastic contact [134, 142], viscoplastic contact [138] and liquid-mediated adhesion [143, 144].

1.3 Review of Numerical Work

In the current tribological study, tribologists are facing important challenges when modeling the contact interfaces:

1. The contact body is far more complicated than a bulk of continuum media. The substrate may be covered by multiple layers of different medias, e.g., thin film coating, oxide layer, contaminants, organic film, etc.

2. The rough surface has a multi-scale structure which needs higher resolution of profilometry down to the nano-scale. This may result in an unrealistic number of sampling points and the increases of the memory and computational time.

3. The mechanism between the interaction of the mating surfaces may beyond the scope of the classical mechanics where different disciplines, e.g., the chemical reaction and quantum mechanics, may be involved, especially when the considered length scales include the nano-scale.

4. Fluid-structure interaction, wear, third bodies and thermal effects may also play a key role in the interface.

It is clear that the analytical models can never satisfy the accuracy needed to the modeling of such complicated interfacial contact. This can only be achieved by the deterministic numerical models. The deterministic numerical models in the past literatures can be divided into two main categories: finite element method (FEM) and boundary element method (BEM).

1.3.1 FEM

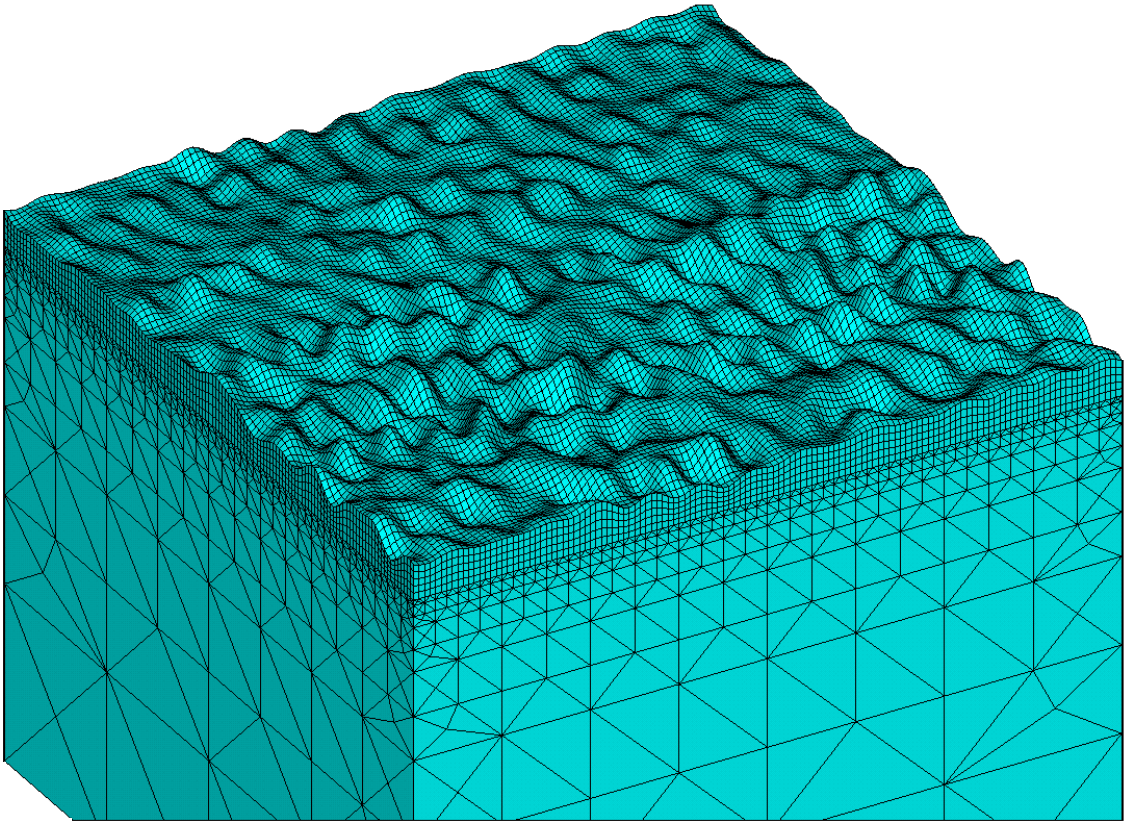

Figure 1.10: A schematic representation of a meshed rough surface, as well as the substrate, created in ANSYS®. Figure courtesy of Xianzhang Wang.

The general theory of the computational contact mechanics using FEM is well documents in [145–148]. However, the rough surface contact is barely touched in those monographs. As far as the author knows, the first rough surface contact finite element (FE) model is proposed by Komvopoulos and Choi [149] in 1992. The (rigid) rough surface in their FE model consists of multiple parabolic asperities and the contact problem is in plane-strain condition. The first 3D rough surface contact model is proposed by Hyun et al. [113] in 2004. Most of the FE models developed later are mainly dedicated to the fundamental study of the rough elastoplastic contact [150–152]. Due to the popularity of the FEM in the applied mechanics community and the mature commercial products (e.g., ANSYS® and ABAQUS®), tribologists prefer to use the FEM software package to simulate the rough contact problem in many engineering practice, e.g., the lip seal [153] and electrical connectors [154, 155]. Fig. 1.10 schematically illustrates a meshed rough surface, as well as the substrate.

In the fundamental study of the rough surface contact, FEM is less popular than BEM due to the following reason:

1. The discretization is performed on the boundary, as well as the volume. Commonly, the FE model contains more nodes than that of the BEM (at least for the linear elastic analysis), especially when the interface is discretized according to the measured rough surface data with fine resolution.

2. Few algorithms are applied to accelerate the FE model.

The above drawbacks prevent the FE models from being widely utilized for the rough surface contact in the tribological model.

1.3.2 BEM

Broadly speaking, the Boundary Element Method (BEM) is referring to any numerical tools which solve the approximated solutions on the boundary of a specific problem. In the computational mechanics, the BEM is referring to a general-purpose numerical tool established in the late 1970s. A brief historical development of BEM can be found in [156]. For the linear elastic problem, the general-purpose BEM utilizes the Betti's reciprocal theorem to connect the boundary values (tractions and the surface displacement) of the current problem and that of a special problem [156]. This special problem should have the closed-form solution. Since few linear elasticity problems have closed-form solutions, the infinite domain subjected by a point load is commonly chosen as the special problem. The corresponding solution is known as Kelvin's solution [156]. Then, the relation between the traction and the surface displacement components are obtained in an integral form known as the boundary integral equation (BIE). Combining with the boundary conditions (e.g., Karush-Kuhn-Tucker condition), the boundary values can be solved iteratively. The enforcement of contact in the general-purpose BEM is more or less similar to that in the FEM, e.g., the penalty method. The very first the general-purpose BEM model of contact problem is published in 1982 by Andersson et al [157]. The application of BEM to the contact problem has been discussed in many the general-purpose BEM-related monographs [158–160]. The general-purposeBEM has also been applied to some tribological problems, see adhesive Hertzian contact [161] and thermal mechanical wear under dry sliding contact [162].

Unfortunately, few general-purpose BEM models are created for the rough surface contact. Two drawbacks in the BEM models bring inefficiency to the rough surface contact modeling as the number of nodes (sampling points) increases:

1. The discretized form of the BIE involves the matrix-scalar production which consumes most of the time before the solving process.
2. The stiffness matrix is nearly fully populated which makes the solving process computationally expensive.

These are the main reasons why the general-purpose BEM models in the examples of many BEM papers are restricted to node counted in the thousands or less. The above two drawbacks may be overcome by fast algorithms, e.g., the fast multipole BEM [163], but the application of the fast multipole BEM to the contact problem is rare to find [164], not to mention the rough surface contact.

In the same time as the birth of the BEM, a special form of BEM is developed by the tribologists. In order to distinguish both, the general-purpose BEM is referred to as the conventional BEM and the one developed in tribology is the special BEM. From the perspective of the conventional BEM, the special problem in the special BEM is a half-space subjected to a point load on the boundary solved by Boussinesq [64]. In some rare cases, the quarter space subjected to a point load on the boundary [165] is used as the special problem. In Chapter 3, it will be proved that the special BEM with the Boussinesq solution can be derived from the conventional BEM using the Kelvin's solution. The restriction brought by the Boussinesq solution is that the special BEM can only be applied to the contact problem where any flexible contact bodies are half-spaces. In many contact problem, e.g., the Hertzian contact, the dimensions of the contact area are usually several orders of magnitude less than the dimensions of the contact bodies. Therefore, the approximation of the contact body by a half-space is reasonable.

The special BEM is extremely popular in the numerical analysis of rough surface contact. Based on the periodicity of the boundary conditions, the special BEM can be divided into non-periodic [166, 167] and periodic BEM [168, 169]. The fundamental solutions in the non-periodic and periodic BEM are the Boussinesq solution [64] and the Westergaard solution [66]. The special BEM can be divided into two parts: the BIE and contact modeling.

For a purely normal contact, a closed-form solution of the normal surface displacement in an integral form of the contact pressure is given by the BIE. Commonly, the computational boundary (either the same size as the nominal contact area or the size of one period) is a flat rectangle. To match with the sampling points measured by the profilometry, the computational boundary is discretized rectilinearly into rectangular elements with constant lengths, Δ_x and Δ_y. Some numerical models use the triangular elements [65, 161, 171]. Nearly all the models utilizes constant element[3] on the boundary, i.e., the tractions are uniform within the neighborhood, $[x_i-\Delta_x/2, x_i+\Delta_x/2]\times[y_j-\Delta_y/2, y_j+\Delta_y/2]$, of the sampling point at (x_i, y_j). The corresponding influence coefficient has the closed-form solution developed by Love [170]. Higher order elements, e.g., the bi-linear triangular element [65,161,171,172] and the bi-quadratic element [173,174], are rarely used since (i) the forms of the influence coefficients are complicated and (ii) the assembly of the stiffness matrix from the influence function is not straight-forward. After the discretization, the surface displacement at all nodes can be represented by a matrix-vector production where the matrix and the vector consist of the Love's influence coefficients and the tractions, respectively. This discretized form has been widely used not only in the rough surface contact, but also in the lubrication problem to account for the surface deflection due to the lubricant pressure [166]. As the number of the sampling points (nodes) are increased to a large number (for example: 512×512), the time consumed in performing the matrix-vector production significantly increases. Two acceleration schemes, namely, the Multi-Level-Multi-Integration (MLMI) [175] and Fast Fourier Transform (FFT) [176], are developed. The MLMI is mainly used under the framework of the multi-grid method [166, 177]. In the frequency domain, the spectrum of the normal surface displacement and the contact pressure has a closed form solution [66]. Note that the fast algorithm for the periodic [169] and non-periodic contact [176] should be handled differently due to the alias brought by the fourier transform. For the elastoplastic contact, an extra term is added to the BIE to account for the effect due to the residual stress (strain) inside the substrate [178, 179].

The contact modeling is mainly associated with the boundary conditions. For a purely normal contact excluding the adhesion, it is the Karush-Kuhn-Tucker (KKT) condition where the interfacial gap and the contact pressure are zero within the contact and non-contact area, respectively. Inspired by the numerical method used in solving the Reynolds equation, the relaxation method (e.g., the Newton-Raphson method) has been applied to iteratively correct the contact

---

[3] In the traditional computational mechanics, the geometry of the boundary is assumed to the smooth or piecewisely smooth. Therefore, the BEM model with the higher order elements approximates the true solutions better than that with the lower order elements. This golden rule, however, does not apply to the boundary represented by the rough surface. The multi-scale and random natures of the roughness makes its geometry unpredictable within the two neighboring sampling points. Rigorously speaking, the interpolation of the traction between the sampling points (nodes) with any orders are not appropriate.

pressure [166]. To ensure the zero pressure at the non-contact area, the negative pressure is set to zero. Another method is to treat the contact problem as an optimization problem. Since the product of the interfacial gap and the contact pressure is zero everywhere, then the contact problem is equivalent to a Linear Complementarity Problem (LCP) [180–182]. Since the influence matrix used for the calculation of the surface displacement is positive definite, then the LCP problem is equivalent to a quadratic programming problem [180]. From the mechanics perspective, the physical meaning of the quadratic problem is that the true solution results in the minimization of the total complementary energy [171]. This concept should be very familiar since the entire theory of FEM is built upon the variational formulation. Many numerical solvers designated for the quadratic programming problem (e.g., the simplex method [171, 183]) and LCP (e.g., conjugate gradient method (CGM) [182, 184, 185] and pivoting method [186, 187]) are applied to the rough surface contact model. Among all the solvers, the CGM solver proposed by the Polonsky and Keer [185] is the most popular one.

Rough surfaces usually require the measurement of the rough surface geometry with a fine resolution down to the nano-scale. At this small scale, the conventional treatment of the material as a continuous media may not be sufficient to accurately capture the interfacial interaction [188]. Instead, the interaction at the molecular and atomic levels, as well as the quantum effect, may become dominant. An all-atoms simulation for a reasonably large domain may be too computationally expensive. A common structure of such a multi-scale computational model [189] is (i) to simulate the deformation of the substrate using the BEM or FEM, (ii) the creating of several layers of atoms over the bulk interface to account for the interaction at the atomic level using the molecular dynamics (MD) simulation and (iii) to create a bridge domain between the bulk and the interface composed of atoms to guarantee the continuity. One of such multi-scale computational models used wildly in the rough surface contact is the Green's Function Molecular Dynamics (GFMD) proposed by Campañá and Müser [190]. A similar multi-scale model can also be found in [191]. In GFMD, the substrate is discretized into lattices (e.g., face-centered cubic) and the corresponding lattice Green function is used to account for the elastic substrate deformation. The lattice Green function can be treated as the counterpart of the Kelvin's or Mindlin's solution of the lattice space.

1.4 Problem Statement

A common statement of contact problem of elastic rough surfaces interaction is as follows: *Consider two linear elastic, isotropic, homogeneous half-spaces with the rough interfaces,* $h_1(x, y)$ *and* $h_2(x, y)$*, under the purely normal compressive load pair,* P*, acting at the far end of both half-spaces. The Young's modulus and the Poisson's ratio are* E_i *and* ν_i *(*$i = 1, 2$*). Determine the stress,* σ_{ij}*, strain,* ϵ_{ij} *and displacement,* u_i*, components (*$i = x, y, z$*) on the interface and in the substrate of each half-space.*

Based on the above fundamental solutions, we can extract the useful results that have important applications:

- Contact pressure $p(x, y) = -\sigma_{zz}(x, y)$

  For the non-adhesive contact, i.e., no tensile normal traction is allowed, the contact pressure is everywhere non-negative. If the adhesion is included, $p(x, y)$ is a mixture of tensile and compressive stress. In the non-adhesive contact, $p(x, y)$ is used to distinguish the contact boundary, Γ_c, and non-contact boundary, Γ_{nc}. Γ_c is a set of in-plane points (x, y) where the corresponding pressures are positive. Similarly, Γ_{nc} is a set including all the non-contact points where $p(x, y) = 0$.

- Contact ratio A^*

  The real area of contact, A_r, can be measured based on the distribution of the points in the contact boundary Γ_c. Since the nominal contact area A_n (which is the size of the entire $z = 0$ plane) is infinite, it is reasonable to use the ratio which is defined as follows:

  $$A^* = \lim_{A_n \to \infty} A_r / A_n. \tag{1.4}$$

- Average interfacial gap $\bar{g}$

  The interfacial gap $g(x, y)$ within Γ_c is zero and is positive within Γ_{nc}. The average interfacial gap over the entire nominal contact area is defined as follows:

  $$\bar{g} = \lim_{A_n \to \infty} \frac{1}{A_n} \iint_{\Omega_{nc}} g(x, y) dx dy. \tag{1.5}$$

The assumptions are tabulated below:

1. *The spectrum to wavelength ratios of the rough surfaces should be small;*

   This enables the validity of the half-space assumption and small deformations in the linear elasticity,

2. *No interfacial friction;*

   The interfacial friction introduces coupling between the normal (shear) stress and tangential (normal) displacement component and inevitably increases the complexity of the model. Additionally, the inclusion of interfacial friction (e.g., the Coulomb law) will only reduce the contact area by a small portion [65].

3. *Rough surface is characterized by a Gaussian, isotropic and random process.*

According to Barber [62], the contact problem stated above can be further simplified to a rough half-space with a composite rough surfaces, $h(x, y) = h_1(x, y) + h_2(x, y)$, in purely normal contact with a rigid flat. The Young's modulus and the Poisson's ratio of the only half-space satisfy:

$$\frac{1}{E^*} = \frac{1-\nu^2}{E} = \frac{1-\nu_1^2}{E_1} + \frac{1-\nu_2^2}{E_2}. \tag{1.6}$$

Finally, the contact problem which is studied throughout the entire dissertation should be stated as follows:

Consider a linear elastic, isotropic, homogeneous half-space with the rough interface, $h(x, y)$, in the purely normal contact with a fixed rigid flat under the compressive load, P, acting at the far end of the half-space. The Young's modulus and the Poisson's ratio satisfy Eq. (1.6). *Determine the corresponding contact pressure, $p(x, y)$, the contact ratio, A^*, and the average interfacial gap, $\bar{g}$.*

1.5 Outline of this dissertation

In Chapter 2, the statistical characterization of a nominally flat, isotropic, Gaussian rough surface is briefly introduced. The different forms of the PDFs of the asperities of a rough surface and the corresponding “pressure surface”[4] in the functions of different combinations of the random variables (e.g., asperity height). The closed-form of the moments of a fractal, Gaussian and isotropic rough surface and the corresponding “pressure surface” are given where the PSD of the rough surface shows a linear relation against the frequency. In Chapter 3, statistical models of the early contact proposed in the past literature are studied systematically for the first time. Important statistical models proposed in the past literature are reviewed according to the different forms of the PDFs and the Hertzian contact models. In Chapter 4, a general formulation of the new statistical models of the nearly complete contact is given. Multiple statistical models are proposed due to their different PDFs and the Hertzian contact models. In Chapter 5, the adhesion in the form of the Dugdale model is introduced to the statistical model of nearly complete contact. In Chapter 6, the special BEM formulation wildly used in the rough surface contact is derived from the conventional BEM. The BEM model is validated by some analytical solutions. In Chapter 7, the statistical model of early and nearly complete contact is validated by the BEM. In Chapter 8, an empirical model is developed for the prediction of the real area of contact (contact ratio) when the load is increased from null to infinity. The empirical model is a curve-fit function based on the statistical model at nearly complete contact and the BEM.

---

[4] The geometry of the contact pressure when the roughness is completely flattened

References

[1] Bowden, F.P. and Tabor, D., 1939. The area of contact between stationary and between moving surfaces. Proceedings of the Royal Society of London. Series A, Mathematical and Physical Sciences, **169**(938), pp.391-413.

[2] Holm, R., 2000, *Electric contacts*, 4th edition, Springer-Verlag, Berlin.

[3] Brink, R.V., Czernik, D.E. and Horve, L.A., 1993. *Handbook of fluid sealing*. McGraw-Hill Companies.

[4] Buchter, H.H., 1979. *Industrial sealing technology*. Wiley.

[5] Bottiglione, F., Carbone, G., Mangialardi, L. and Mantriota, G., 2009. Leakage mechanism in flat seals. Journal of Applied Physics, **106**(10), p.104902.

[6] Green, C.K., Streator, J.L., Haynes, C. and Lara-Curzio, E., 2011. A Computational Leakage Model for Solid Oxide Fuel Cell Compressive Seals. Journal of Fuel Cell Science and Technology, **8**(4), p.041003.

[7] Dapp, W.B., Lücke, A., Persson, B.N. and Müser, M.H., 2012. Self-affine elastic contacts: percolation and leakage. Physical Review Letters, **108**(24), p.244301.

[8] Green, I., 2002. A transient dynamic analysis of mechanical seals including asperity contact and face deformation. Tribology Transactions, **45**(3), pp.284-293.

[9] Woo, K.L. and Thomas, T.R., 1980. Contact of rough surfaces: a review of experimental work. Wear, **58**(2), pp.331-340.

[10] Bhushan, B., 1985. The real area of contact in polymeric magnetic media I: Critical assessment of experimental techniques. ASLE Transactions, **28**(1), pp.75-86.

[11] Bhushan, B., 1985. The real area of contact in polymeric magnetic media II: Experimental data and analysis. ASLE Transactions, **28**(2), pp.181-197.

[12] O'Callaghan, P.W. and Probert, S.D., 1987. Prediction and measurement of true areas of contact between solids. Wear, **120**(1), pp.29-49.

[13] Sawyer, W.G. and Wahl, K.J., 2008. Accessing inaccessible interfaces: in situ approaches to materials tribology. MRS bulletin, **33**(12), pp.1145-1150.

[14] Wahl, K.J. and Sawyer, W.G., 2008. Observing interfacial sliding processes in solid-solid contacts. MRS bulletin, **33**(12), pp.1159-1167.

[15] Bowden, F.P. and Tabor, D., 2001. *The friction and lubrication of solids (Vol. 1)*. Oxford university press.

[16] Thomas, T.R., 1999. *Rough surfaces*, 2nd Edition. Imperial College Press, London.

[17] Whitehouse, D.J., 2010. *Handbook of surface and nanometrology*. CRC press.

[18] Tabor, D., 1951, *The hardness of metals*, Clarendon Press, Oxford.

[19] Dwyer-Joyce, R.S. and Drinkwater, B.W., 2003. In situ measurement of contact area and pressure distribution in machine elements. Tribology letters, **14**(1), pp.41-52.

[20] Aymerich, F. and Pau, M., 2004. Assessment of nominal contact area parameters by means of ultrasonic waves. ASME Journal of Tribology, **126**, pp.639-645.

[21] Dwyer-Joyce, R.S., Yao, C., Zhang, J., Lewis, R. and Drinkwater, B.W., 2009. Feasibility study for real time measurement of wheel-rail contact using an ultrasonic array. ASME Journal of Tribology, **131**(4), pp. 041401.

[22] Dwyer-Joyce, R.S., Drinkwater, B.W. and Quinn, A.M., 2001. The use of ultrasound in the investigation of rough surface interfaces. ASME Journal of Tribology, **123**(1), pp.8-16.

[23] Robinson, A.M., Drinkwater, B.W., Dwyer-Joyce, R.S. and Payne, J.F.B., 2001. Measurement of the stiffness of joints in a graphite brick assembly. Proceedings of the Institution of Mechanical Engineers, Part C: Journal of Mechanical Engineering Science, **215**(2), pp.167-177.

[24] Yao, C.W., Zhou, L.Z. and Chien, Y.X., 2013. Measurement of the contact area of a dovetail milling cutter using an ultrasonic method. Measurement, **46**(9), pp.3211-3219.

[25] Selvadurai, P.A. and Glaser, S.D., 2012. Direct measurement of contact area and seismic stress along a sliding interface. In 46th US Rock Mechanics/Geomechanics Symposium. American Rock Mechanics Association.

[26] Selvadurai, P.A. and Glaser, S.D., 2015. Laboratory-developed contact models controlling instability on frictional faults. Journal of Geophysical Research: Solid Earth, **120**(6), pp.4208-4236.

[27] Saltiel, S., Selvadurai, P.A., Bonner, B.P., Glaser, S.D. and Ajo-Franklin, J.B., 2017. Experimental development of low-frequency shear modulus and attenuation measurements in mated rock fractures: Shear mechanics due to asperity contact area changes with normal stress. Geophysics, **82**(2), pp. M19-M36.

[28] Wang, D., Ueckermann, A., Schacht, A., Oeser, M., Steinauer, B. and Persson, B.N.J., 2014. Tireroad contact stiffness. Tribology Letters, **56**(2), pp.397-402.

[29] Lekue, J., Dörner, F., and Schindler, C., 2017, On the Source of the Systematic Error of the Pressure Measurement Film Applied to Wheel-Rail Normal Contact Measurements, ASME Journal of Tribology, doi:10.1115/1.4037358.

[30] Johnson, J.E., McIff, T.E., Lee, P., Toby, E.B. and Fischer, K.J., 2014. Validation of radiocarpal joint contact models based on images from a clinical MRI scanner. Computer methods in biomechanics and biomedical engineering, **17**(4), pp.378-387.

[31] Swingler, J., 2010. The resolution dependence of measured fractal characteristics for a real un-dismantled electrical contact interface. Wear, **268**(9), pp. 1178-1183.

[32] Roussos, C. and Swingler, J., 2015. The 3D nature of a real un-dismantled electrical contact interface. Wear, **328**, pp.115-122.

[33] Roussos, C.C. and Swingler, J., 2017. A 3D contact analysis approach for the visualization of the electrical contact asperities. AIP Advances, **7**(1), p.015023.

[34] Kriston, A., Fülöp, T., Isitman, N.A., Kotecký, O. and Tuononen, A.J., 2016. A novel method for contact analysis of rubber and various surfaces using micro-computerized-tomography. Polymer Testing, **53**, pp.132-142.

[35] Tarasenko, V.S., 1959. The experimental determination of actual areas of contact between touching surfaces. Scientific Notes, Odessa Polytechnic Institute, 16.

[36] D'yachenko, P.E., Tolkacheva, N.N., Andreev, G.A. and Karpova, T.M., 1964. The actual contact area between touching surfaces, translated by Consultant Bureau. New York, NY.

[37] Bettscheider, S., Gachot, C. and Rosenkranz, A., 2016. How to measure the real contact area? A simple marker and relocation foot-printing approach. Tribology International, **103**, pp.167-175.

[38] Nitta, I., 1995. Measurements of real contact areas using PET films (thickness, 0.9 μm). Wear, **181**, pp.844-849.

[39] Dyson, J. and Hirst, W., 1954. The true contact area between solids. Proceedings of the Physical Society. Section B, **67**(4), pp.309-312.

[40] Bhushan, B. and Dugger, M.T., 1990. Real contact area measurements on magnetic rigid disks. Wear, **137**(1), pp.41-50.

[41] Dieterich, J.H. and Kilgore, B.D., 1994. Direct observation of frictional contacts: New insights for state-dependent properties. Pure and Applied Geophysics, **143**(1), pp.283-302.

[42] Hendriks, C.P., and Visscher, M., 1995. Accurate real area of contact measurements on polyurethane. ASME Journal of Tribology, **117**, pp.607-611.

[43] Castillo, J., Blanca, A.P.D.L., Cabrera, J.A. and Simn, A., 2006. An optical tire contact pressure test bench. Vehicle System Dynamics, **44**(3), pp.207-221.

[44] Ovcharenko, A., Halperin, G., Etsion, I. and Varenberg, M., 2006. A novel test rig for in situ and real time optical measurement of the contact area evolution during pre-sliding of a spherical contact. Tribology Letters, **23**(1), pp.55-63.

[45] $\breve{Z}$ugelj, B.B., and Kalin, M., 2017, In-situ observations of a multi-asperity real contact area on a submicron scale. Journal of Mechanical Engineering, **63**(6), pp.351-362.

[46] Chateauminois, A., Fretigny, C. and Olanier, L., 2010. Friction and shear fracture of an adhesive contact under torsion. Physical Review E, **81**(2), p.026106.

[47] Krick, B.A., Vail, J.R., Persson, B.N. and Sawyer, W.G., 2012. Optical in situ micro tribometer for analysis of real contact area for contact mechanics, adhesion, and sliding experiments. Tribology letters, **45**(1), pp.185-194.

[48] Prevost, A., Scheibert, J. and Debr$\acute{e}$geas, G., 2013. Probing the micromechanics of a multi-contact interface at the onset of frictional sliding. The European Physical Journal E, **36**(2), pp.1-12.

[49] Trejo, M., Fretigny, C. and Chateauminois, A., 2013. Friction of viscoelastic elastomers with rough surfaces under torsional contact conditions. Physical Review E, **88**(5), p.052401.

[50] Romero, V., Wandersman, E., Debregeas, G. and Prevost, A., 2014. Probing locally the onset of slippage at a model multicontact interface. Physical Review Letters, **112**(9), p.094301.

[51] Svetlizky, I. and Fineberg, J., 2014. Classical shear cracks drive the onset of dry frictional motion. Nature, **509**(7499), pp.205-208.

[52] Song, B.J., Yan, S.Z. and Xiang, W.W.K., 2015. A measurement method for distinguishing the real contact area of rough surfaces of transparent solids using improved Otsu technique. Chinese Physics B, **24**(1), p.014601.

[53] Wiertlewski, M., Friesen, R.F. and Colgate, J.E., 2016. Partial squeeze film levitation modulates fingertip friction. Proceedings of the National Academy of Sciences, **113**(33), pp.9210-9215.

[54] Matsuda, K., Hashimoto, D. and Nakamura, K., 2016. Real contact area and friction property of rubber with two-dimensional regular wavy surface. Tribology International, **93**, pp.523-529.

[55] Maegawa, S., Itoigawa, F. and Nakamura, T., 2015. Optical measurements of real contact area and tangential contact stiffness in rough contact interface between an adhesive soft elastomer and a glass plate. Journal of Advanced Mechanical Design, Systems, and Manufacturing, **9**(5), pp.JAMDSM0069-JAMDSM0069.

[56] McBride, J.W., 2006, The loaded surface profile: a new technique for the investigation of contact surfaces At 23rd International Conference on Electrical Contacts, together with International Session on Electro-Mechanical Devices, pp.150-156.

[57] McBride, J.W. and Cross, K.C., 2008, An experimental investigation of the contact area between a glass plane and both metallic and carbon-nano-tube electrical contacts. Proceedings of the 54th IEEE Holm Conference, pp.325-331.

[58] Lo, S.W., and Tsai, S.D., 2000, Real-time observation of the evolution of contact area under boundary lubrication in sliding contact, Journal of Tribology, **124**, pp. 229-238

[59] Putignano, C., Reddyhoff, T., Carbone, G. and Dini, D., 2013. Experimental investigation of viscoelastic rolling contacts: a comparison with theory. Tribology Letters, **51**(1), pp.105-113.

[60] Persson, B.N., Prodanov, N., Krick, B.A., Rodriguez, N., Mulakaluri, N., Sawyer, W.G. and Mangiagalli, P., 2012. Elastic contact mechanics: Percolation of the contact area and fluid squeeze-out. The European Physical Journal E: Soft Matter and Biological Physics, **35**(1), pp.1-17.

[61] Barber, J.R., 1974. Determining the contact area in elastic-indentation problems. Journal of Strain Analysis, **9**(4), pp.230-232.

[62] Barber, J.R., 2003, Bounds on the electrical resistance between contacting elastic rough bodies. Proceedings of the Royal Society of London A: Mathematical, Physical and Engineering Sciences, **459**(2029), pp.53-66.

[63] Greenwood, J.A. and Williamson, J.B.P., 1966. Contact of nominally flat surfaces. Proceedings of the Royal Society of London A: Mathematical, Physical and Engineering Sciences, **295**(1442), pp. 300-319.

[64] Boussinesq, J., 1885. Application des potentiels l'tude de l'quilibre et du mouvement des solides lastiques: principalement au calcul des dformations et des pressions que produisent, dans ces solides, des efforts quelconques exercs sur une petite partie de leur surface ou de leur intrieur: mmoire suivi de notes tendues sur divers points de physique, mathematique et d'analyse (Vol. 4). Gauthier-Villars.

[65] Johnson, K.L., 1987. *Contact Mechanics*. Cambridge University Press.

[66] Westergaard, H.M., 1939, Bearing Pressure and Cracks," ASME Journal of Applied Mechanics, **6**, pp.49-53.

[67] Zhuravlev, V.A., 2007. On the question of theoretical justification of the Amontons-Coulomb law for friction of unlubricated surfaces. Proceedings of the Institution of Mechanical Engineers, Part J: Journal of Engineering Tribology, **221**(8), pp.893-898.

[68] Whitehouse, D.J. and Archard, J.F., 1970, The properties of random surfaces of significance in their contact. In Proceedings of the Royal Society of London A: Mathematical, Physical and Engineering Sciences **316**(1524), pp.97-121.

[69] Onions, R.A. and Archard, J.F., 1973. The contact of surfaces having a random structure. Journal of Physics D: Applied Physics, **6**(3), pp.289-304.

[70] Longuet-Higgins, M.S., 1957. Statistical properties of an isotropic random surface. Philosophical Transactions of the Royal Society of London A: Mathematical, Physical and Engineering Sciences, **250**(975), pp.157-174.

[71] Longuet-Higgins, M.S., 1957. The statistical analysis of a random, moving surface. Philosophical Transactions of the Royal Society of London A: Mathematical, Physical and Engineering Sciences, **249**(966), pp.321-387.

[72] Nayak, P.R., 1971. Random Process Model of Rough Surfaces. ASME Journal of Lubrication Technology, **93**, pp.398-407.

[73] Thomas, T.R.(Ed), *Rough Surfaces*, First ed. Longman, London.

[74] Bush, A.W., Gibson, R.D. and Thomas, T.R., 1975. The elastic contact of a rough surface. Wear, **35**(1), pp.87-111.

[75] Hertz, H., 1896. *Miscellaneous papers*. Macmillan.

[76] McCool, J.I., 1986. Comparison of models for the contact of rough surfaces. Wear, **107**(1), pp.37-60.

[77] Greenwood, J.A., 2006. A simplified elliptic model of rough surface contact. Wear, **261**(2), pp.191-200.

[78] Carbone, G. and Bottiglione, F., 2008. Asperity contact theories: Do they predict linearity between contact area and load?. Journal of the Mechanics and Physics of Solids, **56**(8), pp.2555-2572.

[79] Carbone, G., 2009. A slightly corrected Greenwood and Williamson model predicts asymptotic linearity between contact area and load. Journal of the Mechanics and Physics of Solids, **57**(7), pp.1093-1102.

[80] Zhao, Y., Chang, L., 2001. A Model of Asperity Interactions in Elastic-Plastic contact of Rough Surfaces. ASEM Journal of Tribology, **123**, pp.857-864.

[81] Ciavarella, M., Greenwood, J.A., Paggi, M., 2008. Inclusion of "Interaction" in the Greenwood and Williamson Contact Theory. Wear. **265**, pp.729-734.

[82] Yashima, S., Romero, V., Wandersman, E., Fretigny, C., Chaudhury, M.K., Chateauminois, A., Prevost, A.M., 2015. Normal Contact and Friction of Rubber with Model Randomly Rough Surfaces. Soft Matter. **11**, pp.871-881.

[83] Eid, H. and Adams, G.G., 2007. An elasticplastic finite element analysis of interacting asperities in contact with a rigid flat. Journal of Physics D: Applied Physics, **40**(23), pp.7432-7439.

[84] Afferrante, L., Carbone, G., Demelio, G., 2012. Interacting and Coalescing Hertzian Asperities: A New Multiasperity Contact Model. Wear. **278-279**, pp.28-33.

[85] Jackson, R.L. and Green, I., 2005. A finite element study of elasto-plastic hemispherical contact against a rigid flat. ASME Journal of Tribology, **127**(2), pp.343-354.

[86] Abbott, E.J., and Firestone, F.A., 1933. Specifying surface quality: a method based on accurate measurement and comparison. Mechanical Engineering. **55**, pp.569572.

[87] Jackson, R.L., Ghaednia, H. and Pope, S., 2015. A solution of rigidperfectly plastic deep spherical indentation based on slip-line theory. Tribology Letters, **58**(3), pp.47.

[88] Chang, W. R., Etsion, I., and Bogy, D. B., 1987. An elastic-plastic model for the contact of rough surfaces. ASME Journal of Tribology, **109**, pp.257263.

[89] Zhao, Y., Maletta, D. M., and Chang, L., 2000. An asperity microcontact model incorporating the transition from elastic deformation to fully plastic flow, ASME Journal of Tribology, **122**, pp.8693.

[90] Kogut, L., and Etsion, I., 2002. Elastic-plastic contact analysis of a sphere and a rigid flat. ASME Journal of Applied Mechanics., **69**(5), pp.657662.

[91] Ghaednia, H., Pope, S.A., Jackson, R.L. and Marghitu, D.B., 2016. A comprehensive study of the elasto-plastic contact of a sphere and a flat. Tribology International, **93**, pp.78-90.

[92] Ghaednia, H., Marghitu, D.B. and Jackson, R.L., 2015. Predicting the permanent deformation after the impact of a rod with a flat surface. ASME Journal of Tribology, **137**(1), p.011403.

[93] Gheadnia, H., Cermik, O. and Marghitu, D.B., 2015. Experimental and theoretical analysis of the elasto-plastic oblique impact of a rod with a flat. International Journal of Impact Engineering, **86**, pp.307-317.

[94] Kardel, K., Ghaednia, H., Carrano, A.L. and Marghitu, D.B., 2017. Experimental and theoretical modeling of behavior of 3D-printed polymers under collision with a rigid rod. Additive Manufacturing, **14**, pp.87-94.

[95] Ghaednia, H., Cermik, O. and Marghitu, D.B., 2015. Experimental and theoretical study of the oblique impact of a tennis ball with a racket. Proceedings of the Institution of Mechanical Engineers, Part P: Journal of Sports Engineering and Technology, **229**(3), pp.149-158.

[96] Ghaednia, H. and Marghitu, D.B., 2016. Permanent deformation during the oblique impact with friction. Archive of Applied Mechanics, **86**(1-2), pp.121-134.

[97] Ghaednia, H., Cermik, O., Marghitu, D.B. and Kardel, K., 2017. Collision measurements using digital image correlation techniques. International Journal of Mechanical Sciences, **131**, pp.836-846.

[98] Ghaednia, H., Wang, X., Saha, S., Xu, Y., Sharma, A. and Jackson, R.L., 2017. A Review of ElasticPlastic Contact Mechanics. ASME Applied Mechanics Reviews, **69**(6), p.060804.

[99] Chang W.R., Etsion I., Bogy D.B., 1987. An elasticplastic model for the contact of rough surfaces. ASME Journal of Tribology, **109**, pp.25763.

[100] Kogut L., and Etsion I., 2003. A finite element based elasticplastic model for the contact of rough surfaces. Tribology Transaction, **46**, pp.38390.

[101] Jackson, R.L. and Green, I., 2006. A statistical model of elasto-plastic asperity contact between rough surfaces. Tribology International, **39**(9), pp. 906-914.

[102] Borri, C. and Paggi, M., 2015. Topological characterization of antireflective and hydrophobic rough surfaces: are random process theory and fractal modeling applicable?. Journal of Physics D: Applied Physics, **48**(4), p.045301.

[103] Borodich, F.M., Pepelyshev, A. and Savencu, O., 2016. Statistical approaches to description of rough engineering surfaces at nano and microscales. Tribology International, **103**, pp.197-207.

[104] McCool, J. I., 1992. Non-Gaussian Effects in Microcontact. International Journal of Machine Tools and Manufacture, **321**(1), pp.115123.

[105] Yu, N., and Polycarpou, A. A., 2002, Contact of rough surfaces with asymmetric distribution of asperity heights, ASME Journal of Tribology, **124**, pp.367376.

[106] Kotwal, C. A., and Bhushan, B., 1996. Contact analysis of non-Gaussian surfaces for minimum static and kinetic friction and wear. Tribology Transaction, **39**, pp.890898.

[107] Lee, C.H., Eriten, M. and Polycarpou, A.A., 2010. Application of elastic-plastic static friction models to rough surfaces with asymmetric asperity distribution. ASME Journal of Tribology, **132**(3), p.031602.

[108] Jeng, Y., and Peng, S., 2006, Elastic-plastic contact behavior considering asperity interactions for surfaces with various height distributions. ASME Journal of Tribology, **128**, pp.245251.

[109] Archard, J.F., 1957, Elastic deformation and the laws of friction. Proceedings of the Royal Society of London A: Mathematical, Physical and Engineering Sciences, **243**(1233), pp.190-205.

[110] Majumdar, A., 1989, Fractal Surfaces and Their Applications to Surface Phenomena, PhD dissertation, Department of Mechanical Engineering, University of California, Berkeley.

[111] Majumdar, A. and Bhushan, B., 1990. Role of fractal geometry in roughness characterization and contact mechanics of surfaces. ASME Journal of Tribology, **112**(2), pp.205-216.

[112] Mandelbrot, B.B., 1983. *The fractal geometry of nature*. W.H. Freeman and Company, New York.

[113] Hyun, S., Pei, L., Molinari, J.F. and Robbins, M.O., 2004. Finite-element analysis of contact between elastic self-affine surfaces. Physical Review E, **70**(2), p.026117.

[114] Yastrebov, V.A., Anciaux, G. and Molinari, J.F., 2015. From infinitesimal to full contact between rough surfaces: evolution of the contact area. International Journal of Solids and Structures, **52**, pp.83-102.

[115] Berry, M.V. and Lewis, Z.V., 1980. On the Weierstrass-Mandelbrot fractal function. Proceedings of the Royal Society of London A: Mathematical, Physical and Engineering Sciences, **370**(1743), pp. 459-484.

[116] Ausloos, M. and Berman, D.H., 1985. A multivariate Weierstrass-Mandelbrot function. Proceedings of the Royal Society of London A: Mathematical, Physical and Engineering Sciences, **400**(1819), pp. 331-350.

[117] Yan, W. and Komvopoulos, K., 1998. Contact analysis of elastic-plastic fractal surfaces. Journal of Applied Physics, **84**(7), pp.3617-3624.

[118] Zhang, X., Xu, Y. and Jackson, R.L., 2017. An analysis of generated fractal and measured rough surfaces in regards to their multi-scale structure and fractal dimension. Tribology International, **105**, pp.94-101.

[119] Ciavarella, M., Demelio, G., Barber, J.R. and Jang, Y.H., 2000, Linear elastic contact of the Weierstrass profile. Proceedings of the Royal Society of London A: Mathematical, Physical and Engineering Sciences, **456**(1994), pp. 387-405

[120] Persson, B.N., 2001. Theory of rubber friction and contact mechanics. Journal of Chemical Physics, **115**(8), pp.3840-3861.

[121] Sayles, R.S. and Thomas, T.R., 1978. Surface topography as a nonstationary random process. Nature, **271**(5644), pp. 431-434.

[122] Persson, B.N.J., Albohr, O., Tartaglino, U., Volokitin, A.I. and Tosatti, E., 2005. On the nature of surface roughness with application to contact mechanics, sealing, rubber friction and adhesion. Journal of Physics: Condensed Matter, 17(1), p.R1.

[123] Carbone, G. and Putignano, C., 2014. Rough viscoelastic sliding contact: theory and experiments. Physical Review E, **89**(3), p.032408.

[124] Persson, B.N.J., 2014. On the fractal dimension of rough surfaces. Tribology Letters, **54**(1), pp.99-106.

[125] Jacobs, T.D., Junge, T. and Pastewka, L., 2017. Quantitative characterization of surface topography using spectral analysis. Surface Topography: Metrology and Properties, **5**(1), p.013001.

[126] Manners, W. and Greenwood, J.A., 2006. Some observations on Persson's diffusion theory of elastic contact. Wear, **261**(5), pp.600-610.

[127] Persson, B.N.J., 2002. Adhesion between an elastic body and a randomly rough hard surface. The European Physical Journal E: Soft Matter and Biological Physics, **8**(4), pp.385-401.

[128] Campañà, C., M$\ddot{u}$ser, M.H. and Robbins, M.O., 2008. Elastic contact between self-affine surfaces: comparison of numerical stress and contact correlation functions with analytic predictions. Journal of Physics: Condensed Matter, **20**(35), p.354013.

[129] Persson, B.N.J. and Yang, C., 2008. Theory of the leak-rate of seals. Journal of Physics: Condensed Matter, **20**(31), p.315011.

[130] Persson, B.N.J., 2007. Relation between interfacial separation and load: a general theory of contact mechanics. Physical Review Letters, **99**(12), p.125502.

[131] Borodich, F.M., 2002. Comment on Elastoplastic contact between randomly rough surfaces. Physical Review Letters, **88**(6), p.069601.

[132] Ciavarella, M., 2016. Rough contacts near full contact with a very simple asperity model. Tribology International, **93**, pp.464-469.

[133] Xu, Y., Jackson, R.L. and Marghitu, D.B., 2014. Statistical model of nearly complete elastic rough surface contact. International Journal of Solids and Structures, **51**(5), pp.1075-1088.

[134] Jackson, R.L. and Streator, J.L., 2006. A multi-scale model for contact between rough surfaces. Wear, **261**(11), pp.1337-1347.

[135] Jackson, R.L., 2010. An analytical solution to an Archard-type fractal rough surface contact model. Tribology Transactions, **53**(4), pp.543-553.

[136] Wilson, W. E., Angadi, S., and Jackson, R. L., 2008. Electrical Contact Resistance Considering Multi-Scale Roughness. The 54th IEEE Holm Conference on Electrical Contacts, Orlando, FL, October 27-29.

[137] Wilson, W.E., Angadi, S.V. and Jackson, R.L., 2010. Surface separation and contact resistance considering sinusoidal elasticplastic multi-scale rough surface contact. Wear, **268**(1), pp.190-201.

[138] Goedecke, A., Jackson, R. L., Bachmaier, G., 2014. Time-dependent Contact Resistance in a Multi-scale Surface Model, 27th International Conference on Electrical Contacts, Dresden, Germany, June 22 - 26, 2014, pp.1-6.

[139] Jackson, R.L., Bhavnani, S.H. and Ferguson, T.P., 2008. A multiscale model of thermal contact resistance between rough surfaces. ASME Journal of Heat Transfer, **130**(8), p.081301.

[140] Streator, J.L. and Jackson, R.L., 2009. A model for the liquid-mediated collapse of 2-D rough surfaces. Wear, **267**(9), pp.1436-1445.

[141] Jackson, R. L., 2011. A Model for the Adhesion of Multiscale Rough Surfaces in MEMS, 2011 Joint IEEE International Conference on Industrial Electronics (ICIT), Auburn, AL, USA, March 14-17, 2011.

[142] Goedecke, A., Jackson, R.L. and Mock, R., 2013. A fractal expansion of a three dimensional elasticplastic multi-scale rough surface contact model. Tribology International, **59**, pp.230-239.

[143] Rostami, A. and Streator, J.L., 2015. Study of liquid-mediated adhesion between 3D rough surfaces: A spectral approach. Tribology International, **84**, pp.36-47.

[144] Rostami, A. and Streator, J.L., 2015. A deterministic approach to studying liquid-mediated adhesion between rough surfaces. Tribology Letters, **58**(1), p.2.

[145] Wriggers, P., 2006. *Computational contact mechanics*. Springer Science & Business Media.

[146] Kikuchi, N. and Oden, J.T., 1988. *Contact problems in elasticity: a study of variational inequalities and finite element methods*. Society for Industrial and Applied Mathematics.

[147] Yastrebov, V.A., 2013. *Numerical methods in contact mechanics*. John Wiley & Sons.

[148] Laursen, T.A., 2013. *Computational contact and impact mechanics: fundamentals of modeling interfacial phenomena in nonlinear finite element analysis*. Springer Science & Business Media.

[149] Komvopoulos, K. and Choi, D.H., 1992. Elastic finite element analysis of multi-asperity contacts. ASME Journal of Tribology, **114**, pp.823-823.

[150] Pei, L., Hyun, S., Molinari, J.F. and Robbins, M.O., 2005. Finite element modeling of elasto-plastic contact between rough surfaces. Journal of the Mechanics and Physics of Solids, **53**(11), pp.2385-2409.

[151] Yastrebov, V.A., Durand, J., Proudhon, H. and Cailletaud, G., 2011. Rough surface contact analysis by means of the finite element method and of a new reduced model. Comptes Rendus M*é*canique, **339**(7-8), pp.473-490.

[152] Song, H., Van der Giessen, E. and Liu, X., 2016. Strain gradient plasticity analysis of elasto-plastic contact between rough surfaces. Journal of the Mechanics and Physics of Solids, **96**, pp.18-28.

[153] Wenk, J.F., Stephens, L.S., Lattime, S.B. and Weatherly, D., 2016. A multi-scale finite element contact model using measured surface roughness for a radial lip seal. Tribology International, **97**, pp.288-301.

[154] Angadi, S.V., Wilson, W.E., Jackson, R.L., Flowers, G.T. and Rickett, B.I., 2008, A multi-physics finite element model of an electrical connector considering rough surface contact. Proceedings of the 54th IEEE Holm Conference, pp. 168-177.

[155] Liu, H. and McBride, J.W., 2016, A finite element based electrical resistance study for rough surfaces: Applied to a bi-layered Au/MWCNT composite for micro-switching applications. Proceedings of the 62th IEEE Holm Conference, pp. 65-71.

[156] Brebbia, C.A., Telles, J.C.F. and Wrobel, L., 2012. *Boundary element techniques: theory and applications in engineering*. Springer Science & Business Media.

[157] Andersson, T., 1981. The boundary element method applied to two-dimensional contact problems with friction. In Boundary element methods, Springer, Berlin, Heidelberg.

[158] Karami, G., 1989. *Lecture Notes in Engineering: A Boundary Element Method for Two-Dimensional Contact Problems (Vol. 51)*. Springer-Verlag, Berlin.

[159] Takahashi, S., 1991. *Elastic contact analysis by boundary elements (Vol. 67)*. Springer-Verlag, Berlin.

[160] Becker, A.A., 1992. *The boundary element method in engineering: a complete course*. McGraw-Hill.

[161] Wu, J.J. and Lin, Y.J., 2017. Boundary element analyses on the adhesive contact between an elastic sphere and a rigid half-space. Engineering Analysis with Boundary Elements, **74**, pp.61-69.

[162] Dargush, G.F. and Soom, A., 2016. Contact modeling in boundary element analysis including the simulation of thermomechanical wear. Tribology International, **100**, pp.360-370.

[163] Liu, Y., 2009. *Fast multipole boundary element method: theory and applications in engineering*. Cambridge university press.

[164] Liu, D. and Shen, G., 2005. Multipole BEM for 3-D elasto-plastic contact with friction. Tsinghua Science & Technology, **10**(1), pp.57-60.

[165] Hetenyi, M., 1970. A general solution for the elastic quarter space. ASME, Journal of Applied Mechanics. **37**(1), pp. 7076.

[166] Venner, C.H. and Lubrecht, A.A., 2000. *Multi-level methods in lubrication (Vol. 37)*, Chap. 5, Elsevier, Amsterdam.

[167] Borri-Brunetto, M., Carpinteri, A. and Chiaia, B., 1998. Lacunarity of the contact domain between elastic bodies with rough boundaries. In Probamat-21st century: probabilities and materials (pp. 45-64). Springer, Netherlands.

[168] Johnson, K.L., Greenwood, J.A. and Higginson, J.G., 1985. The contact of elastic regular wavy surfaces. International Journal of Mechanical Sciences, **27**(6), pp.383-396.

[169] Stanley, H.M. and Kato, T., 1997. An FFT-based method for rough surface contact. ASME Journal of Tribology, **119**, pp.481-485.

[170] Love, A.E.H., 1929. The stress produced in a semi-infinite solid by pressure on part of the boundary. Philosophical Transactions of the Royal Society of London. Series A, Containing Papers of a Mathematical or Physical Character, **228**, pp.377-420.

[171] Kalker, J.J. and Van Randen, Y., 1972. A minimum principle for frictionless elastic contact with application to non-Hertzian half-space contact problems. Journal of engineering mathematics, **6**(2), pp.193-206.

[172] Li, J. and Berger, E.J., 2001. A BoussinesqCerruti solution set for constant and linear distribution of normal and tangential load over a triangular area. J ournal of elasticity, **63**(2), pp.137-151.

[173] Hou, K., Zhu, D. and Wen, S., 1985. A new numerical technique for computing surface elastic deformation caused by a given normal pressure distribution. Journal of Tribology, **107**(1), pp.128-131.

[174] Liu, S.B., Ju, M.J. and Yang, C.X., 1993. Elliptic-paraboloid method for calculating surface elastic deformation in EHL. Tribology International, **26**(6), pp.443-448.

[175] Brandt, A. and Lubrecht, A.A., 1990. Multilevel matrix multiplication and fast solution of integral equations. Journal of Computational Physics, **90**(2), pp.348-370.

[176] Liu, S., Wang, Q. and Liu, G., 2000. A versatile method of discrete convolution and FFT (DC-FFT) for contact analyses. Wear, **243**(1), pp.101-111.

[177] Lubrecht, A.A. and Ioannides, E., 1991. A fast solution of the dry contact problem and the associated sub-surface stress field, using multilevel techniques. ASME Journal of Tribology, **113**(1), pp. 128-133.

[178] Mayeur, C., Sainsot, P. and Flamand, L., 1995. A numerical elastoplastic model for rough contact. ASME Journal of Tribology, **117**(3), pp.422-429.

[179] Jacq, C., Nelias, D., Lormand, G. and Girodin, D., 2002. Development of a three-dimensional semi-analytical elastic-plastic contact code. ASME Journal of Tribology, **124**(4), pp.653-667.

[180] Cottle, R.W., Pang, J.S., and Stone, R.E., 1992 *The linear complementarity problem*. SIAM.

[181] Hu, Y.Z., Barber, G.C. and Zhu, D., 1999. Numerical analysis for the elastic contact of real rough surfaces. Tribology transactions, **42**(3), pp.443-452.

[182] Bemporad, A. and Paggi, M., 2015. Optimization algorithms for the solution of the frictionless normal contact between rough surfaces. International Journal of Solids and Structures, **69**, pp.94-105.

[183] Conry, T.F. and Seireg, A., 1971. A mathematical programming method for design of elastic bodies in contact. ASME Journal of Applied Mechanics, **38**(2), pp.387-392.

[184] Nogi, T., and Kato, T., 1997, Influence of hard surface layer on the limit of elastic contact Part I. Analysis using a real surface model, ASME Journal of Tribology, **119**, pp.493-500.

[185] Polonsky, I.A. and Keer, L.M., 1999. A numerical method for solving rough contact problems based on the multi-level multi-summation and conjugate gradient techniques. Wear, **231**(2), pp. 206-219.

[186] Xi, Y., Almqvist, A., Shi, Y., Mao, J. and Larsson, R., 2016. A Complementarity ProblemBased Solution Procedure for 2D Steady-State Rolling Contacts with Dry Friction. Tribology Transactions, **59**(6), pp.1031-1038.

[187] Xi, Y., Almqvist, A., Shi, Y., Mao, J. and Larsson, R., 2016. Linear complementarity framework for 3D steady-state rolling contact problems including creepages with isotropic and anisotropic friction for circular Hertzian contact. Tribology Transactions, pp.1-13.

[188] Luan, B. and Robbins, M.O., 2005. The breakdown of continuum models for mechanical contacts. Nature, **435**(7044), p.929.

[189] Liu, W.K., Karpov, E.G. and Park, H.S., 2006. *Nano mechanics and materials: theory, multiscale methods and applications*. John Wiley & Sons.

[190] Campañá, C. and Müser, M.H., 2006. Practical Greens function approach to the simulation of elastic semi-infinite solids. Physical Review B, **74**(7), p.075420.

[191] Yang, C., Tartaglino, U. and Persson, B.N.J., 2006. A multiscale molecular dynamics approach to contact mechanics. The European Physical Journal E: Soft Matter and Biological Physics, **19**(1), pp.47-58.

Chapter 2

Statistical Characterization of A Nominally Flat, Isotropic, Gaussian Rough Surface

2.1 Introduction

Engineering surfaces are always *rough* and always deviate from the designed (mean) surface. This uneveness can be easily visualized when the surface height is measured over a finite area using the profilometry, see Fig. 2.1. Applying the Fast Fourier transform (FFT), the spectrums of the rough surfaces can be obtained. Then, the rough engineering surface is considered to be the superposition of the waviness and the roughness. The waviness is related to the lower frequency (larger wavelength) components of the spectrum and can be extracted using a low-pass filter. The roughness is related to the higher frequency (lower wavelength) components of the spectrum and can be extracted using a high-pass filter. Many factors can cause the waviness over the engineering surfaces, e.g., the vibration of the machine tools [1]. Additionally, waviness is sometimes created artificially on the mating surfaces to improve the tribological performances (e.g., reducing friction, achieving higher load capacity and lower wear rate) between the machine components, e.g., the laser texure [2]. The roughness of the engineering surfaces is mainly due to the fracture of the material at the micro-scale or even lower scales during the machining. The material at the smaller scales can no longer be considered as continua due to the existence of the micro-structures, e.g., the voids, second phase particles, inclusions and grain boundaries. Due to the action of the cutting tool, the crack propagation (fracture of the material) should follow the designed profile macroscopically. Depending on the different micro-structures in front of the crack, the crack propagation cannot maintain a straight path and therefore it is kinked [3]. For example, some cracks prefer to propagate along the grain boundaries which have random directions. Thus, the randomness and the small scales of the micro-structures cause the crack propagation being kinked about the design path at a high frequency rate and the roughness is created. It is shown numerically that the statistics of the roughness is largely dependent of the spatial distribution of the micro-structure [3].

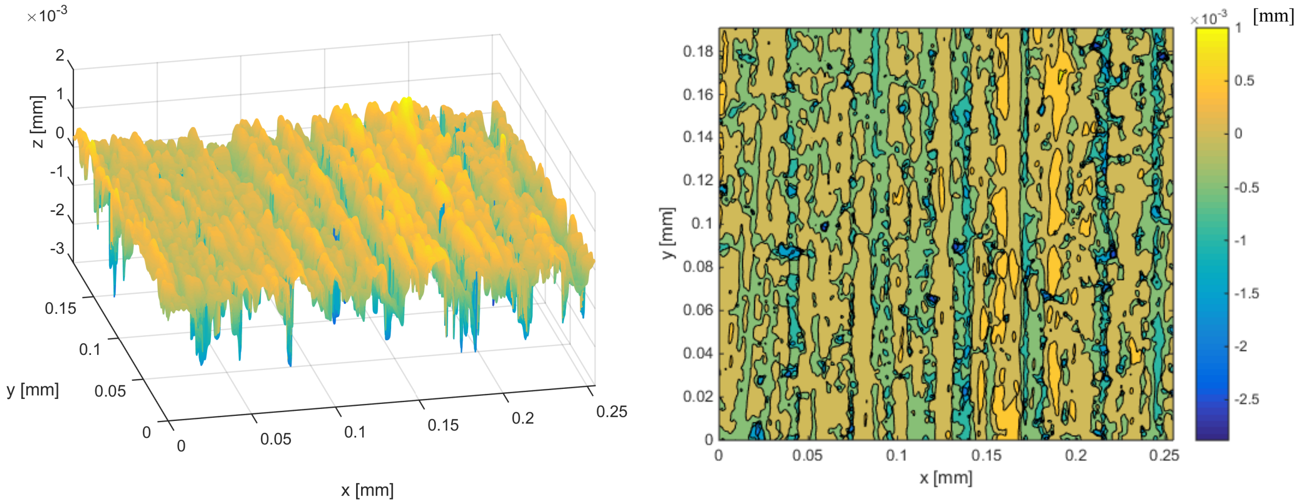

(a) (b)

Figure 2.1: (a) 3D surface height and (b) the corresponding contour measured from the electrical connector by the optical profilometer.

Generally, the contacts between the machine components are either *conforming* or *non-conforming*. A contact is conforming if "two mating surfaces can fit exactly or closely together without deformation" [4]. This type of contact can be found in the journal bearing between the shaft and the bearing bore (or bushing). The radius of the shaft and bearing bore are slightly different in order to include the lubricant between the mating surfaces. Non-conforming contact can be found in the contact pair where the mating surfaces have dissimilar profile. Non-conforming contact can be easily found in the ball/roller bearing where the rolling elements/rollers are in non-conforming contact with the inner/outer race.

Regardless of the global geometries of the contact interfaces, the contact between rough surfaces at the smaller scales are quite the same. Consider a non-conforming contact between a rolling element and the inner race in the ball bearing for example, see Fig. 2.2(a). The nominal contact area in the macro-scale should be an ellipse according to the Hertzian contact theory, see Fig. 2.2(c). Due to the roughness, solid contact does not occur everywhere inside the elliptic region but is only concentrated on the higher asperities, see Fig. 2.2(b). Therefore, the elliptic nominal contact area has been broken into finite smaller asperity contact regions, see Fig. 2.2(c). To further simplify the contact problem, usually the curvatures of the mating surfaces are assumed to be so large compared with the nominal contact area that each body can be considered by a half-space. Thus, the rough surface, $h(x, y)$, over the contact interface (boundary of the half-space) can be considered as a nominal flat which oscillates about $z = 0$ plane, see Fig. 2.2(d) for the interface height of the inner race. The surface height is measured about its mean level[1], i.e., $\langle h \rangle = 0$.

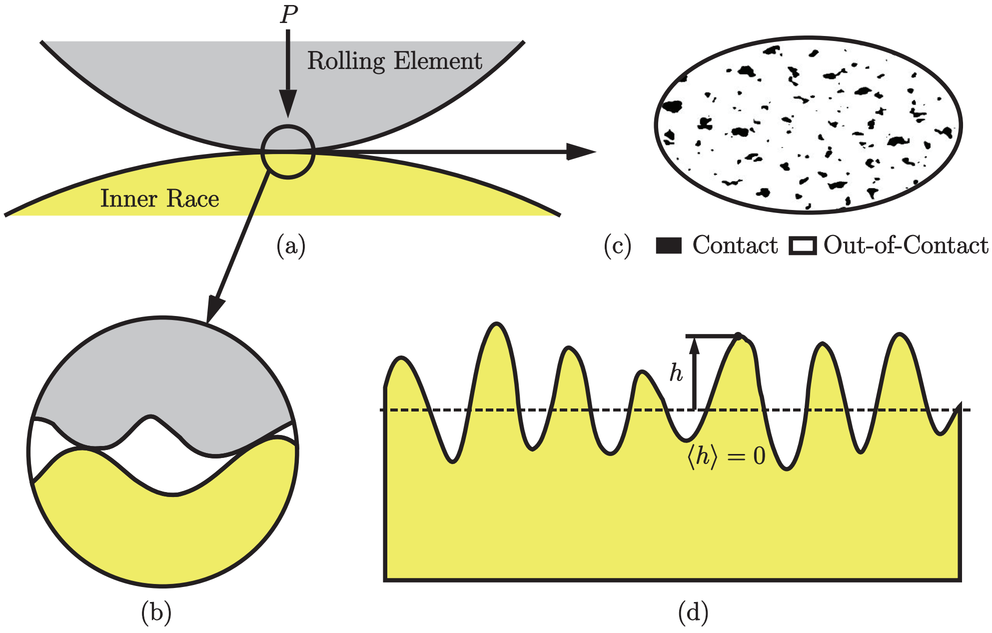

Figure 2.2: (a) Schematic representation of a rolling element in contact with a inner race; (b) Detailed interfacial contact between the asperities; (c) Schematic representation of the nominal contact area (bounded by the solid line) and the real area of contact (black region); (d) Nominal flat rough interface of the inner race leveled about $\langle h \rangle = 0$.

Before the start of the next section, I would like to introduce an important naming convention which will be used throughout the rest of this dissertation. In Chapter 4 of statistical models at early contact, the asperities and the probability density functions are related to the rough surfaces. In Chapter 5, similar type of statistical models are built at another extreme, i.e., *nearly complete contact*. The "asperities" and the probability density functions (PDF) are

---

[1] $\langle h \rangle$ represents the ensemble average of the rough surface height since the rough surface is a random process which has infinite statistically similar realizations.

related to the "pressure surface" which is the geometry of the contact pressure at complete contact. *The superscripts h and p are used to represent the statistical and geometrical parameters of the rough surfaces and the corresponding "pressure surface".* For example: ξ^h means the summit height of a rough surface and κ_1^p is the principle curvature of the asperity of the "pressure surface".

2.2 Spectral Moments and its Statistical Meaning

The Fourier transform pair is widely used in the entire dissertation. Due to its various forms, the following ones are adapted in the rest of the dissertation:

$$\mathcal{F}[f](k_x, k_y) = \int_{-\infty}^{\infty}\int_{-\infty}^{\infty} f(x, y)\text{exp}\left[-i2\pi(k_x x + k_y y)\right] dxdy, \tag{2.1}$$

$$f(x, y) = \mathcal{F}^{-1}[\mathcal{F}[f]](x, y) = \int_{-\infty}^{\infty}\int_{-\infty}^{\infty} \mathcal{F}[f](k_x, k_y)\text{exp}\left[i2\pi(k_x x + k_y y)\right] dk_x dk_y. \tag{2.2}$$

where k_x and k_y are the wave number in the x and y directions.

Recalling the problem statement in Section 1.4, the rough surface, $h(x, y)$, covers the entire $z = 0$ plane. Since the Fourier transform requires $\iint_{-\infty}^{\infty} |f(x, y)|dxdy < \infty$ and $h(x, y)$ is not bounded at $r = \sqrt{x^2 + y^2} \to \infty$, Eq. (2.1) cannot be applied to $h(x, y)$ to obtain the spectrum, $\mathcal{F}[h](k_x, k_y)$. An alternative is to obtain the power spectrum density (PSD), $S^h(k_x, k_y)$, through the Fourier transform of the auto-correlation function (ACF), $R^h(x, y)$. The definition of $R^h(x, y)$ is [5]

$$R^h(x, y) = \langle h(\xi, \eta)h(\xi + x, \eta + y)\rangle. \tag{2.3}$$

For a *stationary* and *non-periodic* random process, $h(x, y)$, with $\langle h\rangle = 0$, $R^h(x, y)$ is bounded at the infinity [13], i.e., $R^h(r \to \infty) \to 0$ and $\iint_{-\infty}^{\infty} |R^h(x, y)|dxdy < \infty$. Therefore, the Fourier transform is valid to be applied to $R^h(x, y)$. The Fourier transform of the ACF[2] is PSD[3] [5]:

$$S^h(k_x, k_y) = \int_{-\infty}^{\infty} \int_{-\infty}^{\infty} R^h(x, y) \text{exp}\left[-i2\pi(k_x x + k_y y)\right] dxdy, \tag{2.7}$$

and the inverse Fourier transform of PSD is ACF:

$$R^h(x, y) = \int_{-\infty}^{\infty} \int_{-\infty}^{\infty} S^h(k_x, k_y) \text{exp}\left[i2\pi(k_x x + k_y y)\right] dk_x dk_y. \tag{2.8}$$

Substituting Eq. (2.3) into Eq. (2.7) and changing the integral order in Eq. (2.7), we can get the relation between PSD and the spectrum:

$$S^h(k_x, k_y) = \lim_{A_0 \to \infty} \frac{1}{A_0} |\mathcal{F}[h](k_x, k_y)|^2. \tag{2.9}$$

In the practice, A_0 is the sampling area and is finite.

Alternatively, the random rough surface can be "regarded as being the sum of an infinite number of infinitesimally small, uncorrelated, sinusoidal waviness" [5, 8, 10]:

$$h(x, y) = \sum_{n}^{\infty} B(k_{xn}, k_{yn}) \cos(x k_{xn} + y k_{yn} + \epsilon_n), \tag{2.10}$$

---

[2] Due to various forms of Fourier transform pairs, the expression and unit of PSD may also be varied [6]. The following Fourier transform pair is wildly used by Persson [7–9] and many other researchers:

$$\mathcal{F}[f](k_x, k_y) = \frac{1}{(2\pi)^2} \int_{-\infty}^{\infty} \int_{-\infty}^{\infty} f(x, y) \text{exp}\left[-i(w_x x + w_y y)\right] dxdy, \tag{2.4}$$

$$f(x, y) = \mathcal{F}^{-1}[\mathcal{F}[f]](x, y) = \int_{-\infty}^{\infty} \int_{-\infty}^{\infty} \mathcal{F}[f](w_x, w_y) \text{exp}\left[i2\pi(w_x x + w_y y)\right] dw_x dw_y. \tag{2.5}$$

where $w_{x(y)} = 2\pi k_{x(y)}$ is the angular frequency . Thus, the corresponding PSD is $1/(2\pi)^2$ times the one defined in Eq. (2.7) [6]. Therefore, the corresponding relation between $B(w_x, w_y)$ and $S^h(w_x, w_y)$ in Eq. (2.11) should be rewritten as [7, 8]

$$B(w_x, w_y) = \lim_{A_0 \to \infty} \frac{2\pi}{\sqrt{A_0}} \sqrt{S^h(w_x, w_y)}. \tag{2.6}$$

where $A_0 = L_x L_y$. In the practice, A_0 is the sampling area and is finite.

[3] Some authors refer to $S^h(k_x, k_y)$ as "power spectrum" [7–9] or "height spectrum" [11, 12]

where there are infinite number of wave vector, (k_{xn}, k_{yn}) and ϵ_n is the random phase between $[0, 2\pi]$. The amplitude, $B(k_x, k_y)$, can be related with the PSD, $S^h(k_x, k_y)$, through [7]

$$B(k_x, k_y) = \frac{1}{\sqrt{L_x L_y}} \sqrt{S^h(k_x, k_y)}, \tag{2.11}$$

Since, the amplitude, $B(k_x, k_y)$, of a rough surface, $h(x, y)$, can be calculated through FFT, Eq. (2.11) is one of the approaches to calculate PSD.

Following the Nayak's random theory [5], the spectral moments, m^h_{pq}, are defined as:

$$m^h_{pq} = \iint_{-\infty}^{\infty} w_x^p w_y^q S^h(k_x, k_y) dk_x dk_y, \tag{2.12}$$

where w_x and w_y are angular wave number: $w_{x(y)} = 2\pi k_{x(y)}$.

The above spectral moments, m^h_{pq}, are related to the variances of the partial derivatives of h with respect to (w.r.t) x and y coordinates:

$$m^h_{pq} = \begin{cases} 0, & p \text{ or } q \text{ is odd} \\ \left\langle \left(\dfrac{\partial^{(p/2+q/2)} h}{\partial x^{(p/2)} \partial y^{(q/2)}} \right)^2 \right\rangle. & p \text{ and } q \text{ are even} \end{cases} \tag{2.13}$$

Since $S^h(k_x, k_y)$ is an even function of k_x and k_y, $m^h_{pq} = 0$ is easily deduced when at least one of p and q is odd [5]. The proof of Eq. (2.13) when p and q are even is given below:

Proof. Let $R^h \left[\dfrac{\partial^{(p/2+q/2)} h}{\partial x^{(p/2)} \partial y^{(q/2)}} \right] (x, y)$ and $S^h \left[\dfrac{\partial^{(p/2+q/2)} h}{\partial x^{(p/2)} \partial y^{(q/2)}} \right] (k_x, k_y)$ be the ACF and PSD of the partial derivatives of h w.r.t x and y. Resorting to the identity in Eq. (2.8), we have

$$R^h \left[\frac{\partial^{(p/2+q/2)} h}{\partial x^{(p/2)} \partial y^{(q/2)}} \right] (0, 0) = \iint_{-\infty}^{\infty} S^h \left[\frac{\partial^{(p/2+q/2)} h}{\partial x^{(p/2)} \partial y^{(q/2)}} \right] (k_x, k_y) dk_x dk_y. \tag{2.14}$$

Using the following identity [13]:

$$S^h \left[\frac{\partial^{(m+n)} h}{\partial x^m \partial y^n} \right] (k_x, k_y) = w_x^{2m} w_y^{2n} S^h(k_x, k_y),$$

and the definition of $R(x, y)$ in Eq. (2.3), Eq. (2.14) is rewritten as:

$$\left\langle \left(\frac{\partial^{(p/2+q/2)} h}{\partial x^{(p/2)} \partial y^{(q/2)}} \right)^2 \right\rangle = \iint_{-\infty}^{\infty} w_x^p w_y^q S^h(k_x, k_y) dk_x dk_y = m_{pq}.$$

$\square$

In most published analytical work, the rough surface is commonly simplified by the assumption of isotropy. A rough surface is isotropic if the spectral moments of the rough profiles in any arbitrary directions are the same [5]. This assumption implies that the PSD has an axisymmetric form, i.e., $S^h(k_x, k_y) = S^h(k)$ where $k = \sqrt{k_x^2 + k_y^2}$. For the sake of simplicity, only the moments related to the variance of $\partial^{(p/2)} h / \partial x^{(p/2)}$ and $\partial^{(p/2)} h / \partial y^{(p/2)}$, i.e., m_{p0}^h and m_{0p}^h are used. Since $m_{p0}^h = m_{0p}^h$, an abbreviated notation, m_n^h, is used to represent m_{p0}^h and m_{0p}^h.

Under the assumption of isotropy, Eq. (2.12) is simplified to (let $k_x = k\cos\theta$ and $k_y = k\sin\theta$):

$$m_n^h = \begin{cases} 2\pi \dfrac{1 \cdot 3 \cdot \cdots \cdot (n-1)}{2 \cdot 4 \cdot \cdots \cdot n} \int_0^\infty S^h(k) \, (2\pi k)^n k dk & n = 0, 2, 4, ..., \\ 0, \quad n = 1, 3, 5, ... \, . \end{cases} \tag{2.15}$$

The bandwidth parameter, α^h, defined by Nayak [5] is essential to the statistical models and is based on the first three non-zero moments:

$$\alpha^h = \frac{m_0^h m_4^h}{(m_2^h)^2}. \tag{2.16}$$

The root mean square (rms) surface slope, $\sqrt{\langle |\nabla h|^2 \rangle}$, is widely used in many rough surface contact models. For an isotropic rough surface, we have the following identity [10, 16]:

$$\sqrt{\langle |\nabla h|^2 \rangle} = \sqrt{m_2^h / 2}. \tag{2.17}$$

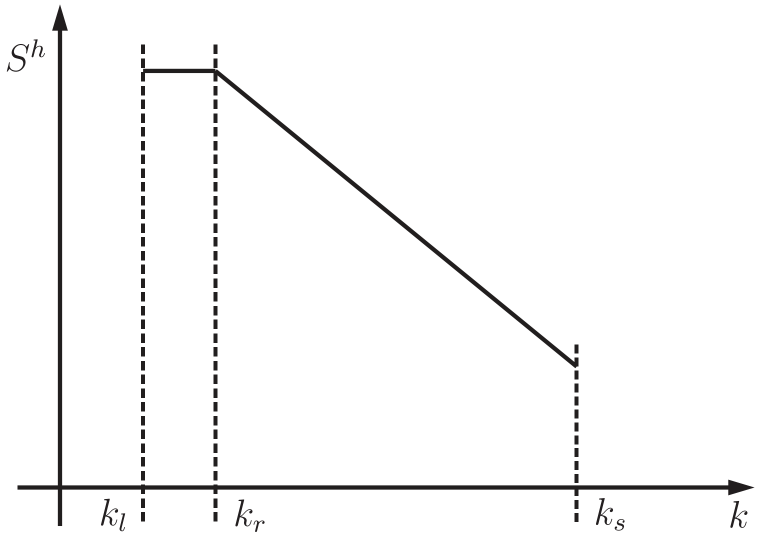

Figure 2.3: Schematic representation of the power spectrum density (PSD) of a self-affine fractal surface.

2.3 Example: Spectral Moments of a Self-Affine Fractal Surface

The fractal surface is widely used in the rough surfaces contact as the surface inputs of the numerical models [14–16] and other multi-scale models [19, 20] even though it receives criticisms [21, 22]. One PSD frequently used in the rough surface contact has the form illustrated in Fig. 2.3. The closed-form is given piece-wisely below:

$$S^h(k) = \begin{cases} Ck^{-2(1+H)} & k \in [k_r, k_s], \\ Ck_r^{-2(1+H)} & k \in [k_l, k_r), \\ 0 \quad \text{otherwise}, \end{cases} \tag{2.18}$$

where k_s and k_l are the cut-off wavenumbers associated with the shortest (λ_s) and the longest (λ_l) wavelengths, respectively. k_r is the roll-off wavenumber. The fractal surface associated with the above PSD is called *self-affine* since the surface geometry is not scaled uniformly in the x, y and z directions when the length scale decreases.

Applying Eq. (2.15) to the fractal surface, the non-zero (even order) moments are

$$m_n^h = (2\pi)^{n+1} \frac{\prod_{k=1}^{n/2}(2k-1)C}{\prod_{k=1}^{n/2}(2k)} \left[\frac{k_r^{-2(1+H)}}{n+2}(k_r^{n+2} - k_l^{n+2}) + \frac{1}{n-2H}\left(k_s^{n-2H} - k_r^{n-2H}\right) \right], \tag{2.19}$$

where $\prod_{k=1}^{0}(\cdot) = 1$.

According to the PSD of many measured rough surfaces, the frequencies, k_r and k_l, are almost identical. Thus, $k_r \approx k_l$ and the above closed-form can be further reduced to [16]:

$$m_n^h = \frac{\prod_{k=1}^{n/2}(2k-1)}{\prod_{k=1}^{n/2}(2k)} \frac{(2\pi)^{n+1}C}{n-2H}(k_s^{n-2H} - k_l^{n-2H}). \tag{2.20}$$

The first four non-zero moments can be written as [16]:

$$m_0^h = \frac{\pi C}{H}\left(k_l^{-2H} - k_s^{-2H}\right), \tag{2.21}$$

$$m_2^h = \frac{1}{4}\frac{(2\pi)^3 C}{1-H}\left(k_s^{2-2H} - k_l^{2-2H}\right), \tag{2.22}$$

$$m_4^h = \frac{3}{16}\frac{(2\pi)^5 C}{2-H}\left(k_s^{4-2H} - k_l^{4-2H}\right), \tag{2.23}$$

$$m_6^h = \frac{5}{32}\frac{(2\pi)^7 C}{3-H}\left(k_s^{6-2H} - k_l^{6-2H}\right). \tag{2.24}$$

The bandwidth parameter has the closed form as follows [16]

$$\alpha^h = \frac{3}{2}\frac{(1-H)^2}{H(2-H)}\frac{(1-\xi^{-2H})(\xi^{4-2H}-1)}{(\xi^{2-2H}-1)^2}, \tag{2.25}$$

where the magnification ratio is $\xi = k_s/k_l$. It is obvious that, except for m_0^h, the other three moments shown above are unbounded as the magnification ratio ξ reaches infinity (i.e., the entire frequency range is included) [17]. Generally, all the non-zero order moments are unbounded as $\xi \to \infty$.

2.4 Asperities of the Rough Surface

The terminology "*asperity*", a fundamental concept in the tribology, especially in the rough surface contact, is frequently used in the previous sections without a proper definition. An asperity is visualized as a protuberance with a higher altitude then all its surroundings. Commonly, the highest point on the asperity of the rough surface is called the *summit* [5]. In the measured rough surfaces, the asperities can be pinpointed by "four nearest neighbor" or "eight nearest neighbor" [18].

When the rough surface contact is in the early stage where the contact ratio is negligibly small, nearly all the solid contacts occur on the higher asperities. Thus, the geometry of the single asperity is essential to the modelling of the rough surfaces contact at the early stage.

Consider a local coordinates, $x'y'$, parallel to xy plane. The projection of the origin, o', of $x'y'$ coordinates on $z = 0$ coincides with that of the summit. The geometrical form of the asperity might be described by[4]

$$h(x', y') = \xi^h - \frac{1}{2}\kappa_1^h (x')^2 - \frac{1}{2}\kappa_2^h (y')^2, \tag{2.26}$$

where ξ^h is the *summit height.* $\kappa_1^h = 1/R_1^h$ and $\kappa_1^h = 1/R_2^h$ are the (positive) *principle curvatures* ($\kappa_2^h \geq \kappa_1^h \geq 0$) of the summit along the principles axes x' and y'.

Back to the base coordinate, xy, the geometry of the asperity is defined as $h(x, y)$ where $[x, y]^T = R_{2\times2}[x', y']^T + [x_0, y_0]^T$. $R_{2\times2}$ is the rotation matrix. The corresponding *Hessian* matrix is

$$H_h(x, y) = \begin{bmatrix} \dfrac{\partial^2 h}{\partial x^2} & \dfrac{\partial^2 h}{\partial x \partial y} \\ \dfrac{\partial^2 h}{\partial y \partial x} & \dfrac{\partial^2 h}{\partial y^2} \end{bmatrix}. \tag{2.27}$$

Since $H_h(x, y)$ is invariant of the translation, $[x_0, y_0]^T$, and the rotation, $R_{2\times2}$, the absolute values of two eigenvalues of $H_h(x, y)$ are the principal curvatures: κ_1^h and κ_2^h. The following curvatures will be used in the later sections:

- *Absolute mean curvature* of the summit:

$$\kappa_m^h = (\kappa_1^h + \kappa_2^h)/2. \tag{2.28}$$

---

[4] Parabolic form of asperity is dominant in the rough surface contact models proposed in the past literatures. This is mainly due to to the Hertzian theory where the interfaces are also parabolic form.

- *Geometrical curvature* of the summit:

$$\kappa_g^h = \sqrt{\kappa_1^h \kappa_2^h}. \tag{2.29}$$

- *Absolute semi-difference curvature* of the summit:

$$\kappa_d^h = |\kappa_1^h - \kappa_2^h|/2 = \sqrt{(\kappa_m^h)^2 - (\kappa_g^h)^2}. \tag{2.30}$$

Absolute mean curvature and the geometric curvature of the summit play a central role in simplifying the Hertzian elliptical contact model into two different circular contact models. We will back to this topic in Section 4.2.

Since κ_1^h and κ_2^h are eigen values of $H_f(x, y)$, κ_m^h, κ_g^h and κ_d^h can also be defined in the base coordinates as[5] [5, 23]:

$$\kappa_m^h = -\left(\frac{\partial^2 h}{\partial x^2} + \frac{\partial^2 h}{\partial y^2}\right)/2, \tag{2.31}$$

$$\kappa_g^h = \left[\frac{\partial^2 h}{\partial x^2}\frac{\partial^2 h}{\partial y^2} - \left(\frac{\partial^2 h}{\partial x \partial y}\right)^2\right]^{1/2}, \tag{2.32}$$

$$\kappa_d^h = \left[\frac{1}{4}\left(\frac{\partial^2 h}{\partial x^2} - \frac{\partial^2 h}{\partial y^2}\right)^2 + \left(\frac{\partial^2 h}{\partial x \partial y}\right)^2\right]^{1/2}. \tag{2.33}$$

The above equations have practical usage when the measured rough surface data is available.

2.5 The Joint Probability Density Functions of Asperity

At the early contact, the load is distributed over the higher asperities. In order to calculate the real area of contact and the total load for a fixed surface separation, all the contacting asperities should be identified and the corresponding contact area and contact load should be calculated. This methodology works for the deterministic (measured) surfaces in which the number of asperities are finite. However, the corresponding results are not representative of the other statistically similar realizations.

---

[5] Product of the eigen values is the determinant of the matrix. Sum of the eigen values is the trace of the matrix.

In Section2.4, a parabolic asperity is shown to be uniquely represented by (ξ^h, κ_1^h, κ_2^h), see Eq. (2.26). Since the rough surfaces are random processes, an equivalent statistical approach is to find the probability density of the contacting asperities with the summit height, $\xi^h > d$, and the principle curvatures, $0 \leq \kappa_1^h \leq \kappa_2^h$. In the rest of this section, Nayak's random theory [5] is introduced which is mainly used to find the probability density functions (PDF) of the asperities of the random, isotropic, Gaussian rough surface. The alternative forms of the PDF with different random variables derived by Greenwood [23] are also discussed. A total of four different PDFs with different random variables combination are given. Different forms of the PDF together with different types of asperity contact models in Section 4.1 are used to form different statistical models in Chapter 4.

The random theory was firstly developed by the mathematician Longuet-Higgins [24, 25] to study the statistics of the surface of the ocean. It is Nayak [5] who introduced the Longuet-Higgins' random theory to the tribology community. Nayak [5] defined the following notations:

$$\begin{aligned} &\xi_1^h = h, \quad \xi_2^h = \frac{\partial h}{\partial x}, \xi_3^h = \frac{\partial h}{\partial y}, \\ &\xi_4^h = \frac{\partial^2 h}{\partial x^2}, \quad \xi_5^h = \frac{\partial^2 h}{\partial x \partial y}, \quad \xi_6^h = \frac{\partial^2 h}{\partial y^2}. \end{aligned}$$

In this classic paper [72], Nayak gave the joint probability[6] of a point on the random, isotropic, Gaussian surface is a function of random variables ($\xi_1^h, ..., \xi_6^h$), see Eq. (35) in [5].

Defining the following dimensionless groups [23]:

$$\begin{aligned} \xi^{h*} &= \xi^h / \sqrt{m_0^h}, \\ (\xi_4^{h*}, \xi_5^{h*}, \xi_6^{h*}) &= (\xi_4^h, \xi_5^h, \xi_6^h) / \sqrt{m_4^h}, \\ (u_1, u_2, u_3) &= \left(\frac{\xi_4^{h*} + \xi_6^{h*}}{2}, \xi_5^{h*}, \frac{\xi_4^{h*} - \xi_6^{h*}}{2} \right), \end{aligned} \tag{2.34}$$

---

[6] The random variables are up to the second order derivatives of the height because the height of the parabolic asperity is a second-order polynomial.

then the PDF of the asperity[7] in a function of the summit hight, ξ^{h*}, and other curvatures of the summit, (u_1, u_2, u_3), is [23]:

$$\begin{aligned}\Phi(\xi^{h*}, u_1, u_2, u_3) =& \frac{m_4^h}{m_2^h} \frac{\sqrt{C_1}}{(2\pi)^2} 3\sqrt{3} \exp\left[-C_1 \left(\xi^{h*}\right)^2\right] |u_1^2 - u_2^2 - u_3^2| \times \\ & \exp\left\{-\frac{3}{2}\left[C_1 u_1^2 + u_2^2 + u_3^2 + C_1 \sqrt{\frac{2}{\alpha^h}} u_1 \xi^{h*}\right]\right\},\end{aligned} \tag{2.35}$$

where $C_1 = \alpha^h/(2\alpha^h - 3)$.

Eq. (2.35), however, does not have a practical usage in the rough surface contact, since none of the curvatures in (u_1, u_2, u_3) are directly used in any of the Hertzian asperity contact models (this will be discussed in detail in Section. 4.2). In the rest of this section, an alternative form of Eq. (2.35) developed by Greenwood [23] is introduced. Based on Greenwood's new PDF, three more PDFs are derived.

Substituting the dimensionless groups in Eq. (2.34) into Eqs. (2.31) and (2.33), we have the following identity [23]:

$$\kappa_m^{h*} = \kappa_m^h / \sqrt{m_4^h} = -u_1, \tag{2.36}$$

$$\kappa_d^{h*} = \kappa_d^h / \sqrt{m_4^h} = \sqrt{u_2^2 + u_3^2}. \tag{2.37}$$

Then, the PDF of the asperity in Eq. (2.35) can be transformed into an equivalent PDF[8] with the random variables $(\xi^{h*}, \kappa_m^{h*}, \kappa_d^{h*})$ [23]:

$$\begin{aligned}\Phi(\xi^{h*}, \kappa_m^{h*}, \kappa_d^{h*}) =& \frac{27}{2\pi} \sqrt{C_1} \exp\left[-C_1 \left(\xi^{h*} - \frac{3\kappa_m^{h*}}{2\sqrt{\alpha^h}}\right)^2\right] \left[(\kappa_m^{h*})^2 - (\kappa_d^{h*})^2\right] \kappa_d^{h*} \times \\ & \exp\left[-\frac{3}{4}(\kappa_m^{h*})^2 - \frac{3}{2}(\kappa_d^{h*})^2\right].\end{aligned} \tag{2.38}$$

---

[7] Asperity is identified by $\xi_2^h = \xi_2^h = 0$, $\xi_4^h < 0$, $\xi_6^h < 0$ and $\xi_4^h \xi_6^h - (\xi_5^h)^2 > 0$. The detailed derivation of the PDF of the asperity can be found in [5].

[8] Rewriting $u_2 = \kappa_d^{h*}\cos(\theta)$, $u_3 = \kappa_d^{h*}\sin(\theta)$ and $du_2 du_3 = \kappa_d^{h*} d\kappa_d^{h*} d\theta$ and integrating over $0 \leq \theta \leq 2\pi$ results in Eq. (2.38)

The PDF in a function of the random variables: ξ^{h*}, κ_1^{h*} and κ_2^{h*} Using the relation between (κ_1^h, κ_2^h) and (κ_m^h, κ_d^h) shown in Eqs. (2.28) and (2.30), the PDF[9] of the asperity with $(\xi^{h*}, \kappa_1^{h*}, \kappa_2^{h*})$ can be obtained from Eq. (2.38) is [27]:

$$\begin{aligned}\Phi(\xi^{h*}, \kappa_1^{h*}, \kappa_2^{h*}) =& \frac{27}{8\pi}\sqrt{C_1}\exp\left[-C_1\left(\xi^{h*} - \frac{3(\kappa_1^{h*}+\kappa_2^{h*})}{4\sqrt{\alpha^h}}\right)^2\right]\kappa_1^{h*}\kappa_2^{h*}(\kappa_2^{h*}-\kappa_1^{h*})\times \\ & \exp\left\{-\frac{9}{16}\left[(\kappa_1^{h*})^2 + (\kappa_2^{h*})^2 - \frac{2}{3}\kappa_1^{h*}\kappa_2^{h*}\right]\right\}. \qquad (2.39)\end{aligned}$$

The PDF in a function of the random variables: ξ^{h*} and κ_m^{h*} This PDF can be obtained by integrating Eq. (2.38) over $\kappa_d^{h*} \in [0, \kappa_m^{h*}]$ [5]:

$$\begin{aligned}\Phi(\xi^{h*}, \kappa_m^{h*}) =& \frac{3\sqrt{C_1}}{2\pi}\exp\left[-C_1\left(\xi^{h*}\right)^2\right]\left\{3(\kappa_m^{h*})^2 - 2 + 2\exp\left[-\frac{3}{2}(\kappa_m^{h*})^2\right]\right\}\times \\ & \exp\left\{-\frac{1}{2}\left[3C_1(\kappa_m^{h*})^2 - \sqrt{3}C_2\kappa_m^{h*}\xi^{h*}\right]\right\}, \qquad (2.40)\end{aligned}$$

where $C_2 = C_1\sqrt{12/\alpha^h}$.

The PDF in a function of the random variables: ξ^{h*} and κ_g^{h*} This PDF can be obtained by substituting Eq. (2.30) into Eq. (2.38) and integrating Eq. (2.38) over $\kappa_m^{h*} \in [\kappa_g^{h*}, \infty)$ [23]:

$$\begin{aligned}\Phi(\xi^{h*}, \kappa_g^{h*}) =& \frac{9}{2\sqrt{2\pi}}\sqrt{\frac{\alpha^h}{\alpha^h - 1}}(\kappa_g^{h*})^3\text{erfc}\left[\mu\left(3\kappa_g^{h*} - \frac{\xi^{h*}\sqrt{\alpha^h}}{\alpha^h - 1}\right)\right]\times \\ & \exp\left[\frac{-\alpha^h\left(\xi^{h*}\right)^2}{2(\alpha^h - 1)} + \frac{3(\kappa_g^{h*})^2}{2}\right], \qquad (2.41)\end{aligned}$$

where $\mu = \sqrt{\frac{1}{2}\frac{\alpha^h - 1}{2\alpha^h - 3}}$.

The PDF in a function of single random variable: ξ^{h*} Further integrating Eq. (2.41) over the $\kappa_g^{h*} \geq 0$, the PDF of the asperity in a function of the asperity height ξ^{h*} only is

---

[9] The following identity is used:

$$d\kappa_m^{h*}d\kappa_d^{h*} = \det\begin{pmatrix} \partial\kappa_m^{h*}/\partial\kappa_1^{h*} & \partial\kappa_m^{h*}/\partial\kappa_2^{h*} \\ \partial\kappa_d^{h*}/\partial\kappa_1^{h*} & \partial\kappa_d^{h*}/\partial\kappa_2^{h*}\end{pmatrix} d\kappa_1^{h*}d\kappa_2^{h*} = \frac{1}{2}d\kappa_1^{h*}\kappa_2^{h*}.$$

obtained[10] [5,23]:

$$\begin{aligned}\Phi(\xi^{h*}) =& \frac{3}{2\pi}\frac{\sqrt{2\alpha^h-3}}{\alpha^h}\xi^{h*}\text{exp}\left[-C_1(\xi^{h*})^2\right] + \frac{3\sqrt{3}}{2\sqrt{2\pi}}\frac{1}{\alpha^h}\left[(\xi^{h*})^2-1\right]\times \\ & \text{exp}\left[-\frac{1}{2}(\xi^{h*})^2\right]\left[1+\text{erf}\,(\beta)\right] + \sqrt{\frac{\alpha^h}{2\pi(\alpha^h-1)}}\times \\ & \text{exp}\left[\frac{-\alpha^h(\xi^{h*})^2}{2(\alpha^h-1)}\right]\left[1+\text{erf}(\gamma)\right], \end{aligned} \tag{2.42}$$

where $\beta = \xi^{h*}\sqrt{\frac{3}{2(2\alpha^h-3)}}$ and $\gamma = \xi^{h*}\sqrt{\frac{\alpha^h}{2(\alpha^h-1)(2\alpha^h-3)}}$. The error function reads as:

$$\text{erf}(x) = \frac{2}{\sqrt{\pi}}\int_0^x e^{-t^2}dt.$$

McCool's Relations In order to analytically express the inputs of the original GW model [32]: (η^h, m^h, R^h, σ_s^h), McCool [33] summarized the corresponding results derived by Nayak [5] and Bush et al. [31]:

$$\eta^h = \frac{1}{6\sqrt{3}\pi}\left(\frac{m_4^h}{m_2^h}\right), \tag{2.43}$$

$$m^h = 4\left(\frac{m_0^h}{\pi\alpha^h}\right)^{1/2}, \tag{2.44}$$

$$R^h = \frac{3}{8}\left(\frac{\pi}{m_4^h}\right)^{1/2}, \tag{2.45}$$

$$\sigma_s^h = \left(1-\frac{0.8968}{\alpha^h}\right)^{1/2}(m_0^h)^{1/2}, \tag{2.46}$$

where η^h is the asperity density; m^h is the distance between the mean asperity level and mean surface level. R^h is the average radius of asperity; σ_s^h is the root mean square (rms) of the asperity height. *Note that McCool's relations are only valid for the Gaussian surfaces.*

---

[10] The original solution (Eq. (50) in [5]) is misprinted. The correct one can be found in Appendix A in [23].

2.6 Statistical Characterization of the "Pressure Surface"

When a nominally flat rough surface, $h(x, y)$, is completely flattened by a rigid flat under the purely normal contact, the corresponding contact pressure can be determined analytically through the Fourier transform [4, 30]:

$$p_c(x, y) = \mathcal{F}^{-1}\left[\pi E^* k\, \mathcal{F}[h](k_x, k_y)\right]. \tag{2.47}$$

where $k = \sqrt{k_x^2 + k_y^2}$. It is obvious that $\langle p_c \rangle = 0$ since $\langle h \rangle = 0$. The geometry of the pressure distribution, $-p_c(x, y)$, is referred to as the "pressure surface" and it plays a key role in modeling the nearly complete contact where the real area of contact is almost the same as the nominal contact area. More details can be found in Chapter 6.

In the beginning of this section, the statistical nature the "pressure surface" can be described as *being isotropic and Gaussian as long as the corresponding rough surface is isotropic and Gaussian process.* A proof is given below:

- **Isotropy**

  According to Eq. (2.9), the PSDs of $h(x, y)$ and $-p_c(x, y)$ have the following relation

  $$S[p_c](k_x, k_y) = \frac{1}{4}(E^*)^2(2\pi k)^2 S[h](k_x, k_y). \tag{2.48}$$

  Since the rough surface is isotropic, i.e., $S[h](k_x, k_y) = S[h](k)$, the "pressure surface" must be isotropic.

- **Gaussianity**

  Firstly, a general theorem states that if p_1 and p_2 are two Gaussian random variables, then $p = p_1 + p_2$ is still a Gaussian random variable [13]. Secondly, Eq. (2.47) can be rewritten in a convolution form:

  $$p_c(\xi, \zeta) = \iint_\Omega K(\xi - x, \zeta - y) h(x, y) dx dy. \tag{2.49}$$

Representing the above integral using the Riemann sum, then $p_c(x_k, y_l)$ is the summation, $\sum_{i=1}^{\infty}\sum_{j=1}^{\infty} A_{ijkl}h_{ij}$, of an infinite set of Gaussian random variables multiplied by a constant forth order tensor A_{ijkl}. As a matter of fact, the "pressure surface", $-p_c(x, y)$, is a Gaussian random process.

According to the above statement, the "pressure surface" and the rough surface equivalently the same in a statistical sense. Following the definition of the asperity given in Section. 2.4, the geometry of the asperity of the pressure surface can also be represented by

$$p(x', y') = \xi^p - \frac{\kappa_1^p}{2}(x')^2 - \frac{\kappa_2^p}{2}(y')^2, \tag{2.50}$$

where axes x' and y' are the principal axes along which the principal curvatures are defined. The summit height of the asperity is ξ^p and the unit is [**Pressure**]. The absolute minimum and maximum principal curvatures of the summit of the asperity are κ_1^p and κ_2^p, respectively. The unit of the curvatures is [**Pressure/Length**^{2}].

The joint PDF $\Phi^p(\xi_1^h, \kappa_1^h, \kappa_2^h)$, as well as its other simplified forms, of the asperity of the rough surface tabulated in Section. 2.5 can be directly applied to that of the "pressure surface". The only difference is that the moments m_n^p should be calculated based on the "pressure surface".

2.6.1 Moments m_n^p

Since the "pressure surface" is isotropic, the definition of the moments of the isotropic rough surface in Eq. (2.15) can be directly applied to m_n^p while the superscript "h" is replaced by "p". Similar to the moments of the rough surface in Eq. (2.15), the moments of the "pressure surface" can also be defined in an integral form of its own PSD. Replacing the superscript "h" by "p" and substituting Eq. (2.48) into Eq. (2.15), the non-zero moments m_n^p can be written in an integral form of $S[h](k)$:

$$m_n^p = (E^*)^2 \frac{\pi}{2} \frac{1 \cdot 3 \cdots (n-1)}{2 \cdot 4 \cdots n} \int_0^{\infty} S^h(k)(2\pi k)^{n+2} k dk \quad n = 0, 2, 4, \cdots . \tag{2.51}$$

Comparing with the form of m_n^h in Eq. (2.15), the following relation between m_n^h and m_n^p are obtained [17,34]:

$$m_n^p = \frac{n+2}{4(n+1)}(E^*)^2 m_{n+2}^h \quad n = 0, 2, \cdots , \tag{2.52}$$

and the identities of the first three non-zero moments are:

$$m_0^p = \frac{1}{2}(E^*)^2 m_2^h, \quad m_2^p = \frac{1}{3}(E^*)^2 m_4^h, \quad m_4^p = \frac{3}{10}(E^*)^2 m_6^h. \tag{2.53}$$

Following the definition of α^h in Eq. (2.16), the bandwidth parameter of the "pressure surface", α^p, is

$$\alpha^p = \frac{m_0^p m_4^p}{(m_2^p)^2} = \frac{27}{20}\frac{m_2^h m_6^h}{(m_4^h)^2}. \tag{2.54}$$

For the fractal surface with the PSD in Eq. (2.18), the corresponding non-zero moments, m_n^p, are

$$m_n^p = (E^*)^2 \frac{\prod_{k=1}^{n/2}(2k-1)}{\prod_{k=1}^{n/2}(2k)} \frac{(2\pi)^{n+3}C}{4(n+2-2H)}(k_s^{n+2-2H} - k_l^{n+2-2H}). \tag{2.55}$$

The first three non-zero moments m_n^p are

$$m_0^p = (E^*)^2 \frac{1}{8}\frac{(2\pi)^3 C}{1-H}\left(k_s^{2-2H} - k_l^{2-2H}\right), \tag{2.56}$$

$$m_2^p = (E^*)^2 \frac{1}{16}\frac{(2\pi)^5 C}{2-H}\left(k_s^{4-2H} - k_l^{4-2H}\right), \tag{2.57}$$

$$m_4^p = (E^*)^2 \frac{3}{64}\frac{(2\pi)^7 C}{3-H}\left(k_s^{6-2H} - k_l^{6-2H}\right). \tag{2.58}$$

and the bandwidth parameter α^p is

$$\alpha^p = \frac{3}{2}\frac{(2-H)^2}{(1-H)(3-H)}\frac{(\xi^{2-2H}-1)(\xi^{6-2H}-1)}{(\xi^{4-2H}-1)^2}. \tag{2.59}$$

For the fractal rough surface, only zero order moment is bounded. Different from the moments of the fractal rough surface, all not moments of the "pressure surface" are bounded regardless of its order.

2.7 Conclusions

In this chapters, the statistical characterization of the random, isotropic, Gaussian rough surfaces, mainely the moments, m_n^h, and the various forms of the PDF of the asperities, Φ^h, are discussed in detail. It is proved rigorously that

- the moments of the rough surface are equivalent to the variance of the derivatives of the surface height with respect (w.r.t) the in-plane coordinates (i.e., x and y), see Eq. (2.13);
- the moments of the rough surface can be determined based on the PSD, see Eq. (2.15).

The moments of a fractal surface with a fixed PSD shown in Eq. (2.18) are explicitly given. Four different PDFs of asperities, Eqs. (2.39-2.42), are tabulated based on the findings of Nayak [5], Greenwood [23] and Carbone [27] and will be used to build various statistical models of early contact with different types of Hertzian contact models in Chapter 4. The similar statistical characterization is also applied to the "pressure surface" when a random, isotropic, Gaussian rough surface is completely flattened. A rigorous proof is given to show that the "pressure surface" is also a random, Gaussian, isotropic surface. Closed-form relations between the moments of the "pressure surface", m_n^p, and m_n^h are given, see Eq. (2.52). The PDFs of the asperities of the rough surface can be directly applied to describe the PDF of the asperities of the "pressure surface" where the superscript "h" is replaced by "p".

References

[1] Li, P., Zhai, Y., Huang, S., Wang, Q., Fu, W. and Yang, H., 2017. Investigation of the contact performance of machined surface morphology. Tribology International, **107**, pp.125-134.

[2] Etsion, I., 2005. State of the art in laser surface texturing. ASME Journal of Tribology, **127**(1), pp.248-253.

[3] Needleman, A., Tvergaard, V. and Bouchaud, E., 2012. Prediction of ductile fracture surface roughness scaling. ASME Journal of Applied Mechanics, **79**(3), p.031015.

[4] Johnson, K.L., 1987. *Contact Mechanics*. Cambridge University Press.

[5] Nayak, P.R., 1971. Random process model of rough surfaces. ASME Journal of Lubrication Technology, **93**, pp.398-407.

[6] Jacobs, T.D., Junge, T. and Pastewka, L., 2017. Quantitative characterization of surface topography using spectral analysis. Surface Topography: Metrology and Properties, **5**(1), p.013001.

[7] Persson, B.N.J., Albohr, O., Tartaglino, U., Volokitin, A.I. and Tosatti, E., 2005. On the nature of surface roughness with application to contact mechanics, sealing, rubber friction and adhesion. Journal of Physics: Condensed Matter, 17(1), p.R1.

[8] Persson, B.N., 2006. Contact mechanics for randomly rough surfaces. Surface Science Reports, **61**(4), pp.201-227.

[9] Persson, B.N.J., 2014. On the fractal dimension of rough surfaces. Tribology Letters, **54**(1), pp.99-106.

[10] Manners, W. and Greenwood, J.A., 2006. Some observations on Persson's diffusion theory of elastic contact. Wear, **261**(5), pp.600-610.

[11] Müser, M.H. and Dapp, W.B., 2015. The contact mechanics challenge: Problem definition. arXiv preprint arXiv:1512.02403.

[12] Müeser, M.H., 2016. A dimensionless measure for adhesion and effects of the range of adhesion in contacts of nominally flat surfaces. Tribology International, **100**, pp.41-47.

[13] Newland, D.E., 1993. *An Introduction to Random Vibration, Spectral & Wavelet Analysis*. 3rd Edition, Dover, New York.

[14] Putignano, C., Afferrante, L., Carbone, G., and Demelio, G., 2012. A Multiscale Analysis of Elastic Contacts and Percolation Threshold for Numerically Generated and Real Rough Surfaces. Triobology International, **64**, pp.148154.

[15] Prodanov, N., Dapp, W.B., and Müser, M.H., 2014. On the Contact Area and Mean Gap of Rough, Elastic Contact: Dimensional Analysis, Numerical Corrections, and Reference Data. Tribology Letter, **53**, pp.433-448.

[16] Yastrebov, V.A., Anciaux, G., Molinari, J.-F., 2015. From Infinitesimal to Full Contact between Rough Surfaces: Evolution of the Contact Area. International Journal of Solids and Structures. **52**, pp.83-102.

[17] Ciavarella, M., 2015. Adhesive rough contacts near complete contact. International Journal of Mechanical Sciences, **104**, pp.104-111.

[18] Sayles, R.S. and Thomas, T.R., 1978. Surface topography as a nonstationary random process. Nature, **271**(5644), pp.431-434.

[19] Ciavarella, M., Demelio, G., Barber, J.R., Jang, Y.H., 2000. Linear elastic contact of the weierstrass profile. Proceedings of the Royal Society of London A: Mathematical, Physical and Engineering Sciences, **456**, pp.387-405.

[20] Jackson, R.L., Streator, J.L., 2006. A multiscale model for contact between rough surfaces. Wear. **261**, pp.1337-1347.

[21] Borri, C., Paggi, M., 2015. Topological characterization of antireflective and hydrophobic rough surfaces: Are random process theory and fractal modeling applicable? Journal of Physics D: Applied Physics, **48**, p.045301.

[22] Zhang, X., Xu, Y. and Jackson, R.L., 2017. An analysis of generated fractal and measured rough surfaces in regards to their multi-scale structure and fractal dimension. Tribology International, **105**, pp.94-101.

[23] Greenwood, J.A., 2006. A simplified elliptic model of rough surface contact. Wear, **261**(2), pp.191-200.

[24] Longuet-Higgins, M.S., 1957. The statistical analysis of a random, moving surface. Philosophical Transactions of the Royal Society of London A: Mathematical, Physical and Engineering Sciences, **249**(966), pp. 321-387.

[25] Longuet-Higgins, M.S., 1957. Statistical properties of an isotropic random surface. Philosophical Transactions of the Royal Society of London A: Mathematical, Physical and Engineering Sciences, **250**(975), pp.157-174.

[26] Thomas, T.R. (Ed), 1982. *Rough surfaces*. Longman, London.

[27] Carbone, G., 2009. A slightly corrected Greenwood and Williamson model predicts asymptotic linearity between contact area and load. Journal of Mechanics and Physics of Solids, **57**(7), pp.1093-1102.

[28] Xu, Y., Jackson, R.L., Marghitu, D.B., 2014. Statistical model of nearly complete elastic rough surface contact. International Journal of Solids and Structures. **51**, pp.1075-1088.

[29] Johnson, K.L., Greenwood, J.A. and Higginson, J.G., 1985. The contact of elastic regular wavy surfaces. International Journal of Mechanical Sciences, **27**(6), pp.383-396.

[30] Stanley, H.M. and Kato, T., 1997. An FFT-based method for rough surface contact. ASME Journal of Tribology, **119**(3), pp.481-485.

[31] Bush, A.W., Gibson, R.D. and Keogh, G.P., 1976. The limit of elastic deformation in the contact of rough surfaces. Mechanics Research Communications, **3**(3), pp.169-174.

[32] Greenwood, J.A. and Williamson, J.B.P., 1966. Contact of nominally flat surfaces. Proceedings of the Royal Society of London A: Mathematical, Physical and Engineering Sciences, **295**(1442), pp.300-319.

[33] McCool, J.I., 1986. Comparison of models for the contact of rough surfaces. Wear, **107**(1), pp.37-60.

[34] Xu, Y., and Jackson, R.L., 2017, Statistical models of nearly complete elastic rough surface contact-comparison with numerical solutions, Tribiology International, **105**, pp.274-291.

Chapter 3

Boundary Element Method for Rough Surface Contact Problem

3.1 Introduction

In this chapter, Boundary Element Method (BEM) applied to the rough surface linear elastic contact problem is discussed in detail. The main reason why BEM models are discussed before the statistical models at early (Chapter 4) and nearly complete contact (Chapter 5) is that BEM models are served as a tool to validate the statistical models. The statistical models discussed in Chapter 4 and 5 are proposed for the extreme cases where the load is extremely small and large. Due to the lack of experimental data (not to mention the rough surface is nearly yielded everywhere at nearly complete contact), the results of BEM models can be served as the reference to be compared with. Additionally, from the education perspective, BEM models are also observation tools to offer the straight evidences for the reasonings upon which the statistical models are built.

Commonly, the numerical models fall into three categories, namely, the Finite Element Method (FEM) [1–12], the Boundary Element Method (BEM) [**?**, 13–24, 26–32] and other multi-scale models [33–35]. Since the multi-scale nature of the interfacial geometry is crucial to the accuracy of the numerical model, BEM is extremely popular in modeling the rough surfaces contact. However, the numerical models commonly referred to as BEM in the rough surface contact literatures are slightly different from the general-purpose BEM in many BEM textbooks [36–39]. Those general-purpose BEM models are mostly associated with the Kelvin (fundamental) solution for the elastostatics problems. Many classic BEM models have been applied to plane (2D), axisymmetric, and spatial (3D) contact problem (e.g., [40–42]) with finite domain. However, the BEM frequently applied to the rough surfaces contact problem is using the Boussinesq solution as the fundamental solution, i.e., the boundary is perfectly flat.

A common point of all the BEM models applied to the rough surface contact problem is that the displacement of the rough interface can be expressed as the convolution of the traction and the closed-form kernel, see [45]. It is surprising to see that different names have been assigned to this type of method in the past literatures of the rough surface contact, e.g., the FFT method [22,46] and the minimum principle/mathematical programming method [13,14]. Since the Boussinesq solution is applied in nearly all the BE models mentioned above, then the corresponding BEM is only valid theoretically for the contact problem where a rigid rough surface is in contact with a linear elastic half-space where the boundary is perfectly flat. Since the rough surface height and slope over the interface is negligibly small, those BEM models are still a good approximation to the problems where a rigid flat is in contact with an elastic rough half-space or two rough surfaces are in contact. Recently, the general-purpose BEM with the Kelvin solution is applied by Li and Kahraman in a series of articles [47–51] to some tribological problems. The BEM formulation of the interfacial displacement and the sub-surface state of stress considering the effect of the rough interface was initially proposed [47] in the mixed lubricated point contact problem. A similar BEM formulation [48] in the plane stress/strain condition was also developed for the mixed lubricated line contact. The infinite boundary outside the contact area is meshed with the infinite line/quadralateral elements [47,48]. Li also showed the difference of the sub-surface stress distribution with and without the effect of the rough interface [49]. The BEM of the half-space/half-plane was applied to study the micro-pitting in the mixed lubricated line/point contact [50,51].

In the following sections, the dry contact problem between an elastic half-space and a rigid flat is formulated using the general-purpose BEM with the Kelvin solution. In Section 3.2 and Section 3.3, the Boundary Integral Equations (BIEs) for the displacement components of the rough boundary subjected to the prescribed traction is formulated firstly. If we neglect the roughness on the boundary, BIEs derived in Section is exactly the Boussinesq solution and this is shown in Section 3.4. The numerical integral of the kernel is introduced in Section 3.5 for both the periodic and non-periodic problems. The boundary conditions and different approaches of solving the dry rough contact problem are briefly introduced in Section 3.6 and Section 3.7, respectively. The validity of the BEM model is approved in Section 3.8 using two classic problems.

3.2 The Kelvin Solution

A closed-form, fundamental solution is essential to the classic BEM. In the three-dimensional (3D) elastostatic problem, the Kelvin solution is dominantly used in all the general-purpose BEM. The other fundamental solutions (e.g., the Mindlin solution and Boussinesq solution) can be derived directly from the Kelvin solution. .

The Kelvin solution quantifies the response of the displacement and the traction at the *field* point $\boldsymbol{x} = (x, y, z)$ due to a unit point load $\boldsymbol{e}_i$ ($i = 1, 2, 3$) acting at the *source* point $\boldsymbol{\xi} = (\xi, \zeta, \eta)$ of an infinite, linear elastic body. The unit vector $\boldsymbol{e}_i$ is parallel to the axis of the based coordinate (x, y, z). The displacement, body force, stress and the traction components are written in the tensorial forms: u_i, f_i, σ_{ij} and p_i where

$$p_i = \sigma_{ij} n_j. \tag{3.1}$$

The normal direction of the boundary Γ is n_i and is pointing to the opposite direction of domain, Ω. The distance between the source and field points is:

$$\rho = \sqrt{(\xi - x)^2 + (\zeta - y)^2 + (\eta - z)^2}. \tag{3.2}$$

The resultant displacement components, $u_i(\boldsymbol{x})$ where $i = 1,\ 2,\ 3$, due to a unit point load $\boldsymbol{e}_j$ at $\boldsymbol{\xi}$ is denoted by u_{ij}^* and has the following closed-form [36]:

$$u_{ij}^*(\boldsymbol{\xi}, \boldsymbol{x}) = \frac{1}{16\pi(1-\nu)Gr}\left[(3-4\nu)\delta_{ij} + \rho_{,i}\rho_{,j}\right], \tag{3.3}$$

where G and ν are the shear modulus and Poisson's ratio of the domain, Ω, respectively. Noticing that $G = E/\left[2(1+\nu)\right]$ where E is Young's modulus. Similarly, the traction components, $p_i(\boldsymbol{x})$ where $i = 1,\ 2,\ 3$, on the boundary with the normal direction, $\boldsymbol{n} = [n_1, n_2, n_3]$, due to a unit point load $\boldsymbol{e}_j$ at $\boldsymbol{\xi}$ is denoted by p^*_{ij} and has the closed-form [36]:

$$p^*_{ij}(\boldsymbol{\xi},\boldsymbol{x}) = \frac{-1}{8\pi(1-\nu)\rho^2}\left\{[(1-2\nu)\delta_{ij}+3\rho_{,i}\rho_{,j}]\frac{\partial\rho}{\partial n}-(1-2\nu)(\rho_{,i}n_j-\rho_{,j}n_i)\right\}, \tag{3.4}$$

where $\rho_{,i}$ is the partial derivative of ρ with respect to $\boldsymbol{x}$:

$$\rho_{,1}=(x-\xi)/\rho, \quad \rho_{,2}=(y-\zeta)/\rho, \quad \rho_{,3}=(z-\eta)/\rho, \tag{3.5}$$

and $\dfrac{\partial\rho}{\partial n}$ is the normal derivative:

$$\frac{\partial\rho}{\partial n}=\nabla\rho\cdot\boldsymbol{n}=\sum_{i=1}^{3}\rho_{,i}n_i. \tag{3.6}$$

3.3 Boundary Integral Equations of a Half-Space Problem with an Arbitrary Rough Boundary $\Gamma=\{(x,y,z)|(x,y)\in\mathbb{R}^2, z=-h(x,y)\}$

Consider a finite domain Ω enclosed by the boundary $\Gamma=\{(x,y,z)|(x,y)\in\mathbb{R}^2, z=-h(x,y)\}$, see Fig. 3.1.

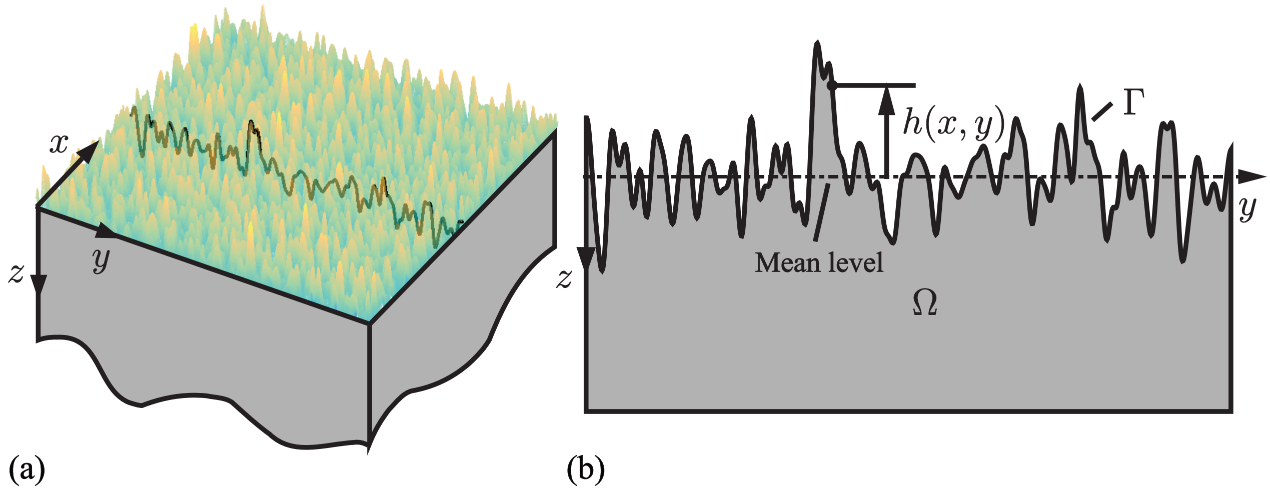

Figure 3.1: Schematic representation of the (a) the rough surface on the half-space and (b) one rough profile (highlighted in (a)) along y-axis. The colored figure is available online.

The internal displacement components, $u_i=[u,v,w]$ where $i=1,\ 2,\ 3$, inside Ω under the action of the applied tractions p_i, $i=1,\ 2,\ 3$, and surface displacements $\bar{u}_i=[\bar{u},\bar{v},\bar{w}]$ over

Γ can be expressed by the *Somigliana's identity* [36]:

$$u_i(\boldsymbol{\xi}) = \iint_\Gamma u^*_{ij}(\boldsymbol{\xi},\boldsymbol{x})p_j(\boldsymbol{x})d\Gamma(\boldsymbol{x}) - \iint_\Gamma p^*_{ij}(\boldsymbol{\xi},\boldsymbol{x})\bar{u}_j(\boldsymbol{x})d\Gamma(\boldsymbol{x}) + \iint_\Omega u^*_{ij}(\boldsymbol{\xi},\boldsymbol{x})f_j(\boldsymbol{x})d\Omega(\boldsymbol{x}), \tag{3.7}$$

where f_j is the body force component.

The Somigliana's identity is a direct consequence of the Betti's reciprocal theorem and the stress static equilibrium equation. In the Betti's reciprocal theorem, one of the solution set is replaced by Kelvin's fundamental solution discussed in Section. 3.2. Based on Eq. (3.7), the strain components, ϵ_{ij}, inside Ω can be directly determined using the definition:

$$\epsilon_{ij} = \frac{1}{2}(u_{i,j} + u_{j,i}), \tag{3.8}$$

and the state of stress, σ_{ij}, inside Ω is determined using the Hook's law:

$$\sigma_{ij} = 2G\epsilon_{ij} + \frac{2G\nu}{1-\nu}\epsilon_{kk}\delta_{ij}, \tag{3.9}$$

where $\epsilon_{kk} = \epsilon_{xx} + \epsilon_{yy} + \epsilon_{zz}$. A tensorial form of σ_{ij} inside Ω can be found in [36].

For a 3D elastostatic problem, the advantage of using BEM is to reduce the dimension of the problem from three to two. This reduction of dimensionality is achieved by moving $\boldsymbol{\xi}$ onto the boundary Γ, then the final BIE for the 3D elastostatic problem is [36]:

$$C_{ij}(\boldsymbol{\xi})\bar{u}_j(\boldsymbol{\xi}) + \iint_\Gamma p^*_{ij}(\boldsymbol{\xi},\boldsymbol{x})\bar{u}_j(\boldsymbol{x})d\Gamma(\boldsymbol{x}) = \iint_\Gamma u^*_{ij}(\boldsymbol{\xi},\boldsymbol{x})p_j(\boldsymbol{x})d\Gamma(\boldsymbol{x}) + \iint_\Omega u^*_{ij}(\boldsymbol{\xi},\boldsymbol{x})f_j(\boldsymbol{x})d\Omega(\boldsymbol{x}). \tag{3.10}$$

Some remarks of Eq. (3.10) are drawn as follows:

- p^*_{ij} and u^*_{ij} are singular kernels where the singularity occurs when $\boldsymbol{\xi} \to \boldsymbol{x}$ over the boundary Γ. The kernel p^*_{ij} has a strong singularity $O(\frac{1}{\epsilon^2})$ and u^*_{ij} has a weak singularity $O(\frac{1}{\epsilon})$ where $\epsilon = |\boldsymbol{\xi} - \boldsymbol{x}|$. Thus, the boundary integrals related to p^*_{ij} and u^*_{ij} are in the sense of the *Cauchy principal value*, i.e., [36]

$$\iint_\Gamma p^*_{ij}(\boldsymbol{\xi},\boldsymbol{x})\bar{u}_j(\boldsymbol{x})d\Gamma(\boldsymbol{x}) = \iint_{\Gamma-\Gamma_\epsilon} p^*_{ij}(\boldsymbol{\xi},\boldsymbol{x})\bar{u}_j(\boldsymbol{x})d\Gamma(\boldsymbol{x}),$$

where Γ_ϵ is an infinitesimally small surface of radius ϵ centered about $\boldsymbol{\xi}$. The remaining integral in Eq. (3.10) is in the normal (Riemann) sense.

- The Betti's reciprocal theorem generally requires the domain Ω to be bounded by Γ. Consequently, Eq. (3.10) cannot be applied to the half-space problem. Betti's reciprocal theorem may still be applied to the half-space problem if $\sigma_{ij}\rho^2 \to 0$ as $\rho \to \infty$ [53]. In the purely normal rough contact problem, this asymptotic behavior implies that the mean normal traction over the entire interface Γ is vanishing, i.e., $\bar{p} = 0$. Otherwise, the half-space subjected to the non-uniform the traction distribution $p(x,y) - \bar{p}$ (with zero mean) and the uniform traction $\bar{p}$ should be studied separately.
- If the boundary, $\Gamma = \{(x,y,z)|(x,y) \in \mathbb{R}^2, z = -h(x,y)\}$, is differentiable of class C^1, i.e., the first order derivatives of $h(x,y)$, namely, $h_{,x}$ and $h_{,y}$, exist and continuous over the entire Γ [36], then, $C_{ij}(\boldsymbol{\xi}) = \frac{1}{2}\delta_{ij}$. If the boundary is differentiable of class C^1 piecewisely, $C_{ij}(\boldsymbol{\xi})$ can be determined based on the fact that the rigid body motion is excluded [36, 37].

If the body force components are ignored, the domain integral in Eq. (3.10) is avoided. For a purely normal contact between a rigid flat and half-space with the rough boundary Γ, i.e., $p_1(\boldsymbol{x}) = p_2(\boldsymbol{x}) = 0$ and $p(\boldsymbol{x}) = p_3(\boldsymbol{x})$. Therefore, the simplified BIEs of a half-space problem with an arbitrary, differentiable up to class C^1 boundary $\Gamma = \{(x,y,z)|(x,y) \in \mathbb{R}^2, z = -h(x,y)\}$ is

$$\frac{1}{2}\bar{u}_i(\boldsymbol{\xi}) + \iint_\Gamma p^*_{ij}(\boldsymbol{\xi},\boldsymbol{x})\bar{u}_j(\boldsymbol{x})d\Gamma(\boldsymbol{x}) = \iint_\Gamma u^*_{i3}(\boldsymbol{\xi},\boldsymbol{x})p(\boldsymbol{x})d\Gamma(\boldsymbol{x}). \tag{3.11}$$

Eq. (3.11) is a composition of three Fredholm integral equations of the second kind. For an arbitrary Γ, Eq. (3.11) is nearly impossible to be solved analytically to get the interfacial displacement, $\bar{u}_j$, as the integral transform of the normal traction p. Numerical techniques in the BEM, e.g., the Gaussian quadrature, can be applied to perform the numerical integral of the kernels [36, 37]. A resulting system of linear equations can be formed based on the applied constraints over the entire interface. Unlike FEM, the stiffness matrix in the BEM is full rank.

The problems with a small number of degree of freedom (D.O.F), the Gaussian elimination can be used. For the rough surface contact (easily associated with more than hundred thousands of D.O.Fs), more advanced solvers should be used (e.g., the element-by-element technique [38], parallel programming [38], fast multipole BEM [39], etc).

In the following section, the complexity of the above BIEs are relaxed by assuming that the boundary Γ is nominally flat with negligibly small roughness heights and slopes. As a matter of fact, the rough boundary Γ can be approximated by $z = 0$ and the classic Boussinesq solution can be retrieved from Eq. (3.11).

3.4 Boundary Integral Equations of a Half-Space Problem with the Boundary $\Gamma = \{(x, y, z)|(x, y) \in \mathbb{R}^2, z = 0\}$

As the boundary Γ is simplified to $z = 0$, the corresponding Kelvin's solution, Eqs. (3.3) and (3.4), can be simplified and are tabulated in Eq. (A.2) in Appendix A. Let $\eta = 0$ in Eq. (A.2), we can get the fundamental solutions over $z = 0$:

$$\begin{aligned}
&u^*_{13}(\xi', \zeta', 0) = u^*_{23}(\xi', \zeta', 0) = 0,\\
&u^*_{33}(\xi', \zeta', 0) = \frac{3 - 4\nu}{16\pi(1 - \nu)G}\frac{1}{r},\\
&p^*_{11}(\xi', \zeta', 0) = p^*_{12}(\xi', \zeta', 0) = p^*_{21}(\xi', \zeta', 0) = p^*_{22}(\xi', \zeta', 0) = 0,\\
&p^*_{13}(\xi', \zeta', 0) = -p^*_{31}(\xi', \zeta', 0) = \frac{1 - 2\nu}{8\pi(1 - \nu)}\frac{\xi'}{r^3},\\
&p^*_{23}(\xi', \zeta', 0) = -p^*_{32}(\xi', \zeta', 0) = \frac{1 - 2\nu}{8\pi(1 - \nu)}\frac{\zeta'}{r^3},\\
&p^*_{33}(\xi', \zeta', 0) = \delta(\xi - x, \zeta - y).
\end{aligned} \tag{3.12}$$

where $r = \sqrt{(\xi - x)^2 + (\zeta - y)^2} = \sqrt{\xi'^2 + \zeta'^2}$ and $\delta(x, y)$ is two-dimensional Dirac's function.

Substituting the simplified Kelvin solutions in Eq. (3.12) into Eq. (3.11), we have following three integral equations[1]:

$$\frac{1}{2}\bar{u}(\xi,\zeta)+\iint_{\Gamma} p^*_{13}(\xi-x,\zeta-y,0)\bar{w}(x,y)d\Gamma(x,y)=0, \tag{3.13}$$

$$\frac{1}{2}\bar{v}(\xi,\zeta)+\iint_{\Gamma} p^*_{23}(\xi-x,\zeta-y,0)\bar{w}(x,y)d\Gamma(x,y)=0, \tag{3.14}$$

$$\frac{1}{2}\bar{w}(\xi,\zeta)+\iint_{\Gamma}\left[p^*_{31}(\xi-x,\zeta-y,0)\bar{u}(x,y)+p^*_{32}(\xi-x,\zeta-y,0)\bar{v}(x,y)\right]d\Gamma(x,y)= \iint_{\Gamma} u^*_{33}(\xi-x,\zeta-y,0)p(x,y)d\Gamma(x,y). \tag{3.15}$$

Applying the convolution theorem to Eqs. (3.13)-(3.15), the resulting surface displacement components, $\bar{u}_i$, after the rearrangement, are[2]

$$\mathcal{F}\left[\bar{u}\right](k_x,k_y)=\frac{i(1-2\nu)}{4\pi G}\frac{k_x}{k^2}\mathcal{F}\left[p\right](k_x,k_y), \tag{3.16}$$

$$\mathcal{F}\left[\bar{v}\right](k_x,k_y)=\frac{i(1-2\nu)}{4\pi G}\frac{k_y}{k^2}\mathcal{F}\left[p\right](k_x,k_y), \tag{3.17}$$

$$\mathcal{F}\left[\bar{w}\right](k_x,k_y)=\frac{1-\nu}{2\pi G}\frac{1}{k}\mathcal{F}\left[p\right](k_x,k_y). \tag{3.18}$$

After the inverse Fourier transform, BIEs in Eq. 3.11 are reduced to the following three decoupled BIEs of surface displacement components:

$$\bar{u}(\xi,\zeta)=-\frac{1-2\nu}{4\pi G}\iint_{\Gamma}\frac{\xi-x}{r^2}p(x,y)dxdy, \tag{3.19}$$

$$\bar{v}(\xi,\zeta)=-\frac{1-2\nu}{4\pi G}\iint_{\Gamma}\frac{\zeta-y}{r^2}p(x,y)dxdy, \tag{3.20}$$

$$\bar{w}(\xi,\zeta)=\frac{1}{4\pi G}\iint_{\Gamma}\frac{1}{r}p(x,y)dxdy. \tag{3.21}$$

Eqs. (3.19) - (3.21) are exactly the same as that derived by the Boussinesq potentials [45] and it will be the foundation of the special BEM applied to the rough surface contact.

---

[1] $\iint_{\Gamma} p^*_{33}(\xi-x,\zeta-y,0)\bar{w}(x,y)=0$ since this integral is in the sense of Cauchy principal value

[2] Eq. (3.12) in the frequency domain can be found by setting $\eta=0$ in Eq. (A.3) in Appendix A.

3.4.1 Displacement, Strain and Stress Components

Setting $f_j = 0$ and substituting the surface displacement components, $\bar{u}_i$, in Eqs. (3.19)-(3.21) into Eq. (3.7) , the displacement components inside Ω in the frequency domain are

$$\mathcal{F}\left[u\right](k_x, k_y, \eta) = \frac{i}{2G}e^{-2\pi k\eta}\left(-\eta\frac{k_x}{k} + \frac{1-2\nu}{2\pi}\frac{k_x}{k^2}\right)\mathcal{F}\left[p\right](k_x, k_y), \tag{3.22}$$

$$\mathcal{F}\left[v\right](k_x, k_y, \eta) = \frac{i}{2G}e^{-2\pi k\eta}\left(-\eta\frac{k_y}{k} + \frac{1-2\nu}{2\pi}\frac{k_y}{k^2}\right)\mathcal{F}\left[p\right](k_x, k_y), \tag{3.23}$$

$$\mathcal{F}\left[w\right](k_x, k_y, \eta) = \frac{1}{2G}e^{-2\pi k\eta}\left(\frac{1-\nu}{\pi}\frac{1}{k} + \eta\right)\mathcal{F}\left[p\right](k_x, k_y). \tag{3.24}$$

The inverse Fourier transform of the transfer function of above displacement components can be found in [45].

The internal strain components, ϵ_{ij}, in the frequency domain are

$$\begin{aligned}
\mathcal{F}[\epsilon_{xx}](k_x, k_y, \eta) &= -\frac{\pi}{G}e^{-2\pi k\eta}\left[-\eta\frac{k_x^2}{k} + \frac{1-2\nu}{2\pi}\frac{k_x^2}{k^2}\right]\mathcal{F}\left[p\right](k_x, k_y), \\
\mathcal{F}[\epsilon_{yy}](k_x, k_y, \eta) &= -\frac{\pi}{G}e^{-2\pi k\eta}\left[-\eta\frac{k_y^2}{k} + \frac{1-2\nu}{2\pi}\frac{k_y^2}{k^2}\right]\mathcal{F}\left[p\right](k_x, k_y), \\
\mathcal{F}[\epsilon_{zz}](k_x, k_y, \eta) &= -\frac{1}{2G}e^{-2\pi k\eta}\left(1 - 2\nu + 2\pi k\eta\right)\mathcal{F}\left[p\right](k_x, k_y), \\
\mathcal{F}[\epsilon_{xy}](k_x, k_y, \eta) = \mathcal{F}[\epsilon_{yx}](k_x, k_y, \eta) &= -\frac{\pi}{G}e^{-2\pi k\eta}\left(-\eta\frac{k_x k_y}{k} + \frac{1-2\nu}{2\pi}\frac{k_x k_y}{k^2}\right)\mathcal{F}\left[p\right](k_x, k_y), \\
\mathcal{F}[\epsilon_{yz}](k_x, k_y, \eta) = \mathcal{F}[\epsilon_{zy}](k_x, k_y, \eta) &= \frac{i\pi}{G}e^{-2\pi k\eta}\eta k_y\mathcal{F}\left[p\right](k_x, k_y), \\
\mathcal{F}[\epsilon_{xz}](k_x, k_y, \eta) = \mathcal{F}[\epsilon_{zx}](k_x, k_y, \eta) &= \frac{i\pi}{G}e^{-2\pi k\eta}\eta k_x\mathcal{F}\left[p\right](k_x, k_y), \\
\mathcal{F}[\epsilon_{kk}](k_x, k_y, \eta) &= -\frac{1-2\nu}{G}e^{-2\pi k\eta}\mathcal{F}\left[p\right](k_x, k_y).
\end{aligned} \tag{3.25}$$

The internal stress components, σ_{ij}, in the frequency domain are

$$\begin{aligned}
\mathcal{F}[\sigma_{xx}](k_x,k_y,\eta) &= -\left(\frac{k_x^2}{k^2} - 2\pi\eta\frac{k_x^2}{k} + 2\nu\frac{k_y^2}{k^2}\right) e^{-2\pi k\eta}\mathcal{F}\left[p\right](k_x,k_y),\\
\mathcal{F}[\sigma_{yy}](k_x,k_y,\eta) &= -\left(\frac{k_y^2}{k^2} - 2\pi\eta\frac{k_y^2}{k} + 2\nu\frac{k_x^2}{k^2}\right) e^{-2\pi k\eta}\mathcal{F}\left[p\right](k_x,k_y),\\
\mathcal{F}[\sigma_{zz}](k_x,k_y,\eta) &= -\left(1 + 2\pi k\eta\right) e^{-2\pi k\eta}\mathcal{F}\left[p\right](k_x,k_y),\\
\mathcal{F}[\sigma_{xy}](k_x,k_y,\eta) = \mathcal{F}[\sigma_{yx}](k_x,k_y,\eta) &= -\frac{k_xk_y}{k^2}\left[(1 - 2\nu - 2\pi k\eta\right] e^{-2\pi k\eta}\mathcal{F}\left[p\right](k_x,k_y),\\
\mathcal{F}[\sigma_{yz}](k_x,k_y,\eta) = \mathcal{F}[\sigma_{zy}](k_x,k_y,\eta) &= i2\pi k_y\eta e^{-2\pi k\eta}\mathcal{F}\left[p\right](k_x,k_y),\\
\mathcal{F}[\sigma_{xz}](k_x,k_y,\eta) = \mathcal{F}[\sigma_{zx}](k_x,k_y,\eta) &= i2\pi k_x\eta e^{-2\pi k\eta}\mathcal{F}\left[p\right](k_x,k_y). \qquad (3.26)
\end{aligned}$$

The inverse Fourier transform of the transfer functions of the above state of stresses can be found in [45]. Note that Tripp [54] gave the similar transfer functions associated with the boundary normal stress: $\sigma_{zz}|_{z=0} = p_0\cos(\alpha x)\cos(\alpha y)$ which is only a subset of the solutions developed above. Tripp's solution can be recovered from Eqs. (3.26) if k_x, k_y and p are replaced by the angular frequencies and the normal stress, $\sigma_{zz}|_{z=0}$.

3.4.2 Remarks

In Section 3.4, it is shown that, under the assumption that the boundary Γ is perfectly flat, the coupled system of BIEs in Eq. (3.11) for the arbitrary rough boundary is deduced to three decoupled BIEs in Eqs. (3.19) - (3.21). This can be considered as an alternative to derive the Boussinesq solution. The same problem is also visited by Boussinesq [43] using Boussinesq potentials and by Sneddon [55] using Papkovitch-Neuber potentials and the integral transform method. The Fourier transform used in the BEM formulation is inspired by the integral transform method developed by Sneddon [55].

Now it is clear that numerical methods using Boussinesq solutions applied to the rough surface contact are essentially BEM. In the mean time, several restrictions arise which are listed below:

1. *The height of the rough boundary, $z = -h(x,y)$, should be continuous and piece-wise differentiable of class C^1.*

2. *The local slope of the rough boundary should be several order of magnitude smaller than the unity.*

3. *The mean traction over the entire* Γ *should be zero. This ensures the validity of the extension of the Betti's reciprocal theorem to the half-space.*

The first assumption is against the measurement data and the some analytical models (e.g., Weierstrass-Mandelbrot (WM) function [56, 57]) that the rough surfaces are continuous but non-differentiable everywhere. Depending on the shape function used in the elements[3], the rough boundary is smoothed to some extent and it is the main reason why the rough surface in BEM is (piece-wisely) smooth. The second assumption implies that the rough surface height is negligibly small compared with the lateral dimension as long as the rough boundary is nominally flat. The third assumption implies that when Eqs. (3.19) - (3.21) (or (3.16)-(3.18)) are used to calculate the normal displacement due to the applied normal traction, the mean value of the applied normal traction should not be included in the calculation. The mean value of the applied normal traction only adds a rigid body motion to the displacement components which is indeterministic and a uniform internal state of stresses which can be determined through the Hook's law.

The validity of Eqs. (3.19)-(3.21) used in the rough surface contact can be quantified by the root mean square (rms) slope: $\sqrt{m_2^h}$. As long as $\sqrt{m_2^h} \ll 1$, then Eqs. (3.19)-(3.21) are good approximations to the true relation between $u_i(\boldsymbol{x})$ and $p_i(\boldsymbol{x})$. Otherwise, the strongly coupled system in Eqs. (3.11) needs to be solved and the computational complexity is increased significantly.

3.5 Numerical Integral of Kernel

3.5.1 Non-Periodic Point Load Kernel

Since the rough surface is under purely normal contact and the interface is frictionless, only the normal surface displacement (i.e.,. Eq. (3.19)) matters. The kernel, $\frac{1}{r}$, in the corresponding

---

[3] The shape function used in the rough surface contact model is discussed in the next section.

convolution is denoted by

$$K(\xi - x, \zeta - y) = \frac{1}{\sqrt{(\xi - x)^2 + (\zeta - y)^2}}, \tag{3.27}$$

and its physical meaning is the normal displacement at $(\xi, \zeta, 0)$ of a half-space due to the action of a unit, normal, point load acting on $(x, y, 0)$. This kernel is commonly referred to as the influence function in the contact mechanics. If the unit, normal, point load is periodically distributed with the periods: λ_x and λ_y, the corresponding influence function is available in Eq. (B.11), see Appendix B.

3.5.2 Discretized Form of Normal Displacement

Let us denote a finite, rectangular region on $z = 0$ boundary by Γ_p. If a non-periodic normal traction distribution, $p(x, y)$, is acting upon Γ_p, then the resultant normal displacement of $z = 0$ can be determined by:

$$\bar{w}(\xi, \zeta) = \frac{1}{\pi E^*} \iint_{\Gamma_p} K(\xi - x, \zeta - y) p(x, y) dx dy, \tag{3.28}$$

where the influence function, $K(x, y)$, has the form in Eq. (3.27). If the normal traction, $p(x, y)$, is λ_x- and λ_y- periodic and one of the period is Γ_p:

$$\Gamma_p = \{(x, y, z) | x \in [0, \lambda_x), y \in [0, \lambda_y), z = -h(x, y)\}$$

then the normal displacement can still be formulated by the same form of the convolution shown above where $K(x, y)$ has the closed-form in Eq. (B.11) in Appendix B.

Discretizing Γ_p uniformly with the uniform intervals: Δ_x and Δ_y, we have

$$\Gamma_p = \left\{(x_i, y_j, 0) | x_i = \Delta_x (i - 1), y_j = \Delta_y (j - 1), i(j) = 0, \cdots, N_{x(y)}\right\}. \tag{3.29}$$

where $N_{x(y)} = L_{x(y)} / \Delta_{x(y)} + 1$.

Non-Periodic Discretized Boundary

Assuming $p(x, y)$ is approximated by a piecewise function with constant value, $p_{ij} = p(\xi_i, \zeta_j)$, within the neighborhood: $[\xi_i - \Delta_x/2, \xi_i + \Delta_x/2] \times [\zeta_j - \Delta_y/2, \zeta_j + \Delta_y/2]$, then the discretized $\bar{w}_{ij}$ can be approximated by a double summation:

$$\bar{w}_{ij} = \frac{1}{\pi E^*} \sum_{k=1}^{N_x} \sum_{l=1}^{N_y} K_{ijkl}\, p_{kl}, \tag{3.30}$$

where K_{ijkl} is a fourth order tensor and can be further reduced to K_{rs} where $r = |i - k| + 1$ and $s = |j - l| + 1$ because of the symmetry:

$$\begin{aligned} K_{ijkl} = K_{rs} =& (R + \Delta_x/2) \ln \left\{ \frac{(S + \Delta_y/2) + [(S + \Delta_y/2)^2 + (R + \Delta_x/2)^2]^{1/2}}{(S - \Delta_y/2) + [(S - \Delta_y/2)^2 + (R + \Delta_x/2)^2]^{1/2}} \right\} \\ &+ (S + \Delta_y/2) \ln \left\{ \frac{(R + \Delta_x/2) + [(S + \Delta_y/2)^2 + (R + \Delta_x/2)^2]^{1/2}}{(R - \Delta_x/2) + [(S + \Delta_y/2)^2 + (R - \Delta_x/2)^2]^{1/2}} \right\} \\ &+ (R - \Delta_x/2) \ln \left\{ \frac{(S - \Delta_y/2) + [(S - \Delta_y/2)^2 + (R - \Delta_x/2)^2]^{1/2}}{(S + \Delta_y/2) + [(S + \Delta_y/2)^2 + (R - \Delta_x/2)^2]^{1/2}} \right\} \\ &+ (S - \Delta_y/2) \ln \left\{ \frac{(R - \Delta_x/2) + [(S - \Delta_y/2)^2 + (R - \Delta_x/2)^2]^{1/2}}{(R + \Delta_x/2) + [(S - \Delta_y/2)^2 + (R + \Delta_x/2)^2]^{1/2}} \right\}, \end{aligned} \tag{3.31}$$

where $R = |x_i - \xi_k|$ and $S = |y_j - \zeta_l|$.

In the BEM, the element used with the zero order approximation scheme is referred to as the *constant element* [36–39]. The higher order approximation schemes (e.g., quadratic shape function) were also applied by Hou et al. [58] and Liu et al. [59].

Periodic Discretized Boundary

Applying the zero order approximation scheme to the traction $p(x, y)$, $\bar{w}_{x,y}$ can also be approximated by Eq. (3.30) where the discretized influence function is:

$$\begin{aligned} K_{ijkl} = K_{rs} = & \sum_{m=1}^{\infty} \sum_{n=1}^{\infty} \frac{1}{\pi^2 mn \sqrt{m^2/\lambda_x^2 + n^2/\lambda_y^2}} \times \\ & \left\{ \sin\left[\frac{2\pi m}{\lambda_x}(R + \Delta_x/2)\right] - \sin\left[\frac{2\pi m}{\lambda_x}(R - \Delta_x/2)\right] \right\} \times \\ & \left\{ \sin\left[\frac{2\pi n}{\lambda_y}(S + \Delta_y/2)\right] - \sin\left[\frac{2\pi n}{\lambda_y}(S - \Delta_y/2)\right] \right\}. \end{aligned} \tag{3.32}$$

Alternatively, $\bar{w}(x, y)$ can also be determined using the Fourier transform pairs:

$$\bar{w}(x, y) = \mathcal{F}^{-1}\left[\frac{1}{\pi E^* \sqrt{k_x^2 + k_y^2}} \mathcal{F}[p]\right], \tag{3.33}$$

based on the correspondence shown in Eqs. (B.9) and (B.10).

3.6 Governing Equations and Boundary Conditions

The region, Γ_p, can be further divided into the contact region, Γ_c, and the non-contact region, Γ_{nc}. The boundary conditions at Γ_c and Γ_{nc} are:

$$p(x, y) > 0, \quad g(x, y) = 0 \quad \text{where} \quad (x, y) \in \Gamma_c, \tag{3.34}$$

$$p(x, y) = 0, \quad g(x, y) > 0 \quad \text{where} \quad (x, y) \in \Gamma_{nc}. \tag{3.35}$$

One of the governing equations is based on the geometrical relation on the *deformed* contact interface, see Fig. 3.2:

$$g(x, y) = \langle h(x, y) - \bar{w}(x, y)\rangle|_{\Gamma_c} - [h(x, y) - \bar{w}(x, y)] \quad (x, y) \in \Gamma_p, \tag{3.36}$$

where $\bar{w}(x, y)$, is determined either by Eq. (3.30) with the discretized influence function in Eq. (3.32) or Eq. (3.33) using the fast Fourier transform (FFT).

The force balance equation is written as

$$\frac{1}{\lambda_x \lambda_y} \iint_{\Gamma_p} p(x,y)dxdy = \bar{p}. \tag{3.37}$$

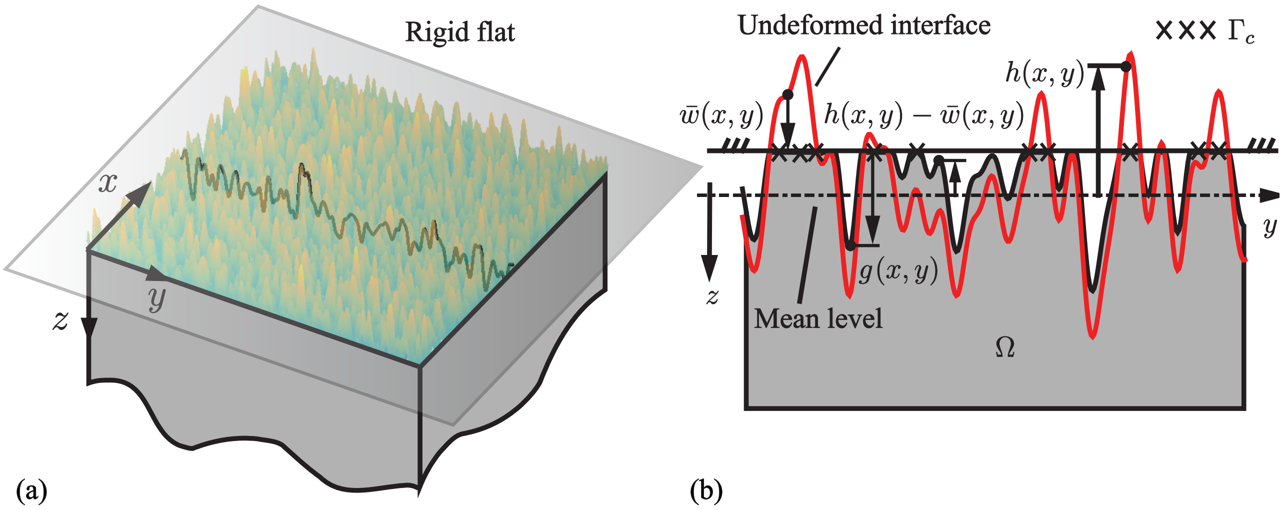

Figure 3.2: Schematic representation of the (a) rough surface contact problem and (b) the deformed shape of the rough profile (highlighted in (a)) along y-axis. The colored figure is available online.

3.7 Numerical Implementations

The solving of purely normal rough surface contact is equivalent to finding the contact pressure distribution, $p(x,y)$, which satisfies (i) the boundary conditions in Eqs. (3.34) and (3.35) and (ii) the load balance equation (Eq. (3.37)). Commonly, the solver used in the rough surface contact can be divided into two categories: the relaxation method and the optimization method.

3.7.1 The Relaxation Method

The relaxation method is introduced by Venner and Lubrecht [60] and it is inspired by the similar method applied to solving the Reynolds equation in the hydrodynamic and elastohydrodynamic lubrication [60].

An alternative form of Eq. (3.36) is

$$g(x,y) = d - h(x,y) + \bar{w}(x,y). \tag{3.38}$$

Since $\langle \bar{w} \rangle = 0$, the deformed and undeformed rough interface share the same mean level. Therefore, d is the mean interfacial gap.

Expanding Eq. (3.38) in Taylor series within the discretized contact region Γ_c and keeping the terms only up to the first order:

$$g_{ij} + \sum_{k=1}^{N_x} \sum_{l=1}^{N_y} \frac{\partial g_{ij}}{\partial p_{kl}} \delta p_{kl} = 0, \tag{3.39}$$

where

$$\frac{\partial g_{ij}}{\partial p_{kl}} = \frac{1}{\pi E^*} K_{rs}.$$

The above identity is clear based on Eq. (3.30). As $|i - k|$ and $|j - l|$ are increased, K_{rs} is decreased significantly. Consequently, only the residual pressure, δp_{kl}, within the closest neighborhood of (x_i, y_j) have the obvious impact on the equilibrium of Eq. (3.39). If the four nearest neighbors of (x_i, y_j) is utilized, Eq. (3.39) is rewritten as:

$$K_{11} \delta p_{ij} + K_{21}(\delta p_{i+1\ j} + \delta p_{i-1\ j}) + K_{12}(\delta p_{i\ j+1} + \delta p_{i\ j-1}) = -\pi E^* g_{ij}. \tag{3.40}$$

and it is referred to as the five-point-relaxation scheme [60]. Eq. (3.40) can solved differently depending on the relaxation method (e.g., the point/line Gauss-Seidel relaxation). The boundary conditions in Eqs. (3.34) and (3.35) are achieved by setting all the negative pressure to zero.

It is commonly accepted that the relaxation method is superior for reducing the out-of-balance error associated with the higher frequency, but can hardly reduce the low frequency components [60]. This can be overcome by the Multi-Grid Method (MGM). For more detail of this advanced technique, readers should refer to [60].

3.7.2 The Optimization Method

The optimization method is firstly applied to the frictionless, purely normal, elastic contact problem by Conry and Seireg [13] and Kalker and van Randen [14].

In a discretized boundary Γ, Eq. (3.38) can be written in a tensorial form:

$$\mathbf{g} = \mathbf{u}_1 + \mathbf{K}\,\mathbf{p}, \tag{3.41}$$

where $\mathbf{g}$, $\mathbf{p}$ and $\mathbf{u}_1$ are the first order tensor of g_{ij}, p_{ij} and $d - h_{ij}$. $\mathbf{K}$ in Eq. (3.32) is the second order tensor and positive definite.

The boundary conditions in Eqs. (3.34) and (3.35) are transformed as follows:

$$\mathbf{p} \geq 0 \quad \mathbf{g} \geq 0 \quad \text{and} \quad \mathbf{p}^T\mathbf{g} = 0 \quad \text{at} \quad \Gamma. \tag{3.42}$$

The above conditions are *Karush-Kuhn-Tucker* (KKT) conditions. Eqs. (3.41) and (3.42) form the *Linear Complementary Problem* (LCP) [23, 61]. A brief introduction on the application of the LCP formulation in the various contact mechanics problems is given by Xi et al. [62, 63]. Since $\mathbf{K}$ is positive definite, the uniqueness of the solutions of the above LCP is guaranteed if either $\bar{p}$ or d is given. The *Conjugate Gradient*(CG) algorithm is one of the efficient solvers of the LCP [21, 24, 32]. The CG solver is firstly applied by Nogi and Kato [21] and later by Polonsky and Keer [24] to the *non-periodic* rough surface contact model in which $\mathbf{K}$ has the form of Eq. (3.31). The boundary conditions in Eq. (3.42) can be strictly imposed in each iteration [24]. The Polonsky and Keer model [24] can be easily adapted to cover the periodic cases as long as $\mathbf{K}$ takes the form of Eq. (3.32). Without further noticing, the Polonsky and Keer model is used as the only numerical model throughout the rest of the dissertation.

Finding the solution of the LCP is equivalent to minimizing the following quadratic problem (QP):

$$\min f = \mathbf{p}^T\,\mathbf{u}_1 + \frac{1}{2}\mathbf{p}^T\,\mathbf{K}\,\mathbf{p}, \tag{3.43}$$

where

$$\mathbf{p} \geq 0 \quad \text{and} \quad \mathbf{g} \geq 0 \quad \text{at} \quad \Gamma. \tag{3.44}$$

Eqs. (3.43) and (3.44) are the variational formulation proposed by Kalker and van Randen [14]

In the rest of this section, the variational method and the relaxation method discussed in the previous section are linked based on the theory of optimization and the downsides of using the relaxation method are explicitly explained. By setting the gradient $\nabla f = 0$, Eq. (3.43) is equivalent to Eq. (3.39) and can be solved in the way discussed in the previous section. Thus, the relaxation method basically solves the unconstrained linear system $\mathbf{u}_1 + \mathbf{K}\ \mathbf{p} = 0$ using the *steepest descent method*. However, KKT conditions in Eq. (3.42) are only achieved approximately by setting the negative pressure to zero in each iteration. This is referred to as the greedy method [32] and this is dominantly applied in the numerical models. Bemporad and Paggi [32] claimed that no rigorous proof can be found to show that this method can impose the KKT conditions rigorously. Moreover, Bemporad and Paggi used a counterexample, see Fig. 2 in [32], to illustrate that the greedy method fails to rigorously fulfill the KKT conditions at some nodes. Yastrebov et al. [30] also reported that the real area of contact between the bi-sinusoidal waviness and the rigid flat determined by Stanley and Kato model [22] (which uses the relaxation method) deviates from the closed-from solution at the nearly complete contact, see Fig. 4 in [30] for more details. Additionally, obvious deviations can also be found in the similar plots shown by Xu et al. [64], see Figs. 7 and 8 in [64].

3.7.3 Convergent Criterion

The outputs of the BEM model are, namely, p_{ij} and g_{ij}. The contact ratio, A^*, can be extracted from $p(x, y)$ based on the number of contacting nodes[4]

$$A^* = N/(N_x N_y). \tag{3.45}$$

where N is the number of the sampling points associated with $p_{ij} > 0$.

---

[4] However, this method is questioned by Yastrebov et al. [31, 65] since A^* is a upper limit of the true contact ratio. The lower limit of the true contact ratio can be estimated by:

$$S = \frac{\pi}{4} S^d,$$

where S^d is the perimeter of the discretized contact area. Thus, the true contact area is the mean value of the lower and upper limits. Comparing with the contact ratio predicted in the nearly complete contact, the error introduced by using Eq. (3.45) may be significant at the early contact [31, 65]. The gap between upper limit and the true contact ratio should be decreased by the finer mesh.

The average interfacial gap $\bar{g}$ is extracted from g_{ij} by

$$\bar{g} = \frac{1}{N_x N_y} \sum_{(x_i, y_j) \in \Gamma_c} g_{ij}. \tag{3.46}$$

In order to make sure all the interfacial results are truly converged, a specified convergence criterion should be addressed. At the beginning of k^{th} iteration, the initial contact pressure, contact ratio and average interfacial gap are labeled as: $\tilde{p}_{ij}^{(k)}$, $\tilde{A}^{*(k)}$ and $\tilde{\bar{g}}^{*(k)}$. The results came after the iteration are without the tilde. The commonly used criterion is that the difference of the relaxed and unrelaxed $p_{ij}^{(k)}$ and $\tilde{p}_{ij}^{(k)}$ should be lower than a critical value:

$$\|p_{ij}^{(k)} - \tilde{p}_{ij}^{(k)}\|_2 / \|p_{ij}^{(k)}\|_2 < 5 \times 10^{-5}, \tag{3.47}$$

where $\|\cdot\|_2$ is the L_2 norm.

However, the above criterion may not guarantee that the contact ratio is also converged, thus the following criterion is added:

$$|A^{*(k)} - \tilde{A}^{*(k)}| / A^{*(k)} < \frac{2}{N_x N_y}. \tag{3.48}$$

This criterion only allows the number of contacting nodes to be changed between neighboring iterations, at most, by one node.

Assuming the average contact pressure, $\bar{p}$, is monotonically increased, based on the Barber's theorem [66], A^* should also monotonically increase. Similarly, we can expect that $\bar{g}$ is monotonically decreased and a rigorous proof is given in Appendix C. Therefore, the following restrictions should also be satisfied:

$$A^*(\bar{p}) > A^*(\bar{p}_0), \quad \bar{g}(\bar{p}) < \bar{g}_0(\bar{p}_0) \quad \text{where} \quad \bar{p} > \bar{p}_0. \tag{3.49}$$

Theoretically, the gap within the contact region should be zero. In the BEM, however, the interpenetration/out-of-contact still exists within Γ_c at each iteration. In the calculation of $\bar{g}$, $g(x, y)$ is assumed to be zero within Γ_c. To quantify the interpenetration/out-of-contact within

Γ_c, let us define the root mean square (rms) of the gap within Γ_c as:

$$\sigma_h = \sqrt{\frac{1}{N} \sum_{(x_i, y_j) \in \Omega_c} g_{ij}^2}. \tag{3.50}$$

At early contact, σ_h should be negligible compared with $\sqrt{m_0^h}$. At the nearly completely contact, σ_h should be negligible compared with $\bar{g}$. Thus, the following criterion is proposed:

$$\sigma_h < \min(0.0001\sqrt{m_0^h}, 0.01\bar{g}). \tag{3.51}$$

Consequently, the convergence of the solutions should satisfy a composite criterion consisting of Eqs. (3.47), (3.48), (3.49) and (3.51). If this composite criterion is not satisfied within 200 iterations and the process shows a slow convergent trend, then the solution is assumed to be converged.

3.8 Examples

In this section, the boundary element method developed above is used to solve the following two problems:

1. an elastic contact between a half-space with periodic, sinusoidal wavy boundary and a rigid flat.
2. an elastic contact between a half-space with periodic, nominally flat roughness and a rigid flat.

3.8.1 Sinusoidal Waviness Contact

Consider a contact pair between a sinusoidal waviness and a rigid flat under a uniform contact pressure $\bar{p}$. The similar study has been done by many researchers [30,44,64,67]. The waviness height has the sinusoidal form leveled about $z = 0$ plane of the half-space:

$$h(x, y) = \Delta \cos(2\pi x/\lambda_x) \cos(2\pi y/\lambda_y), \tag{3.52}$$

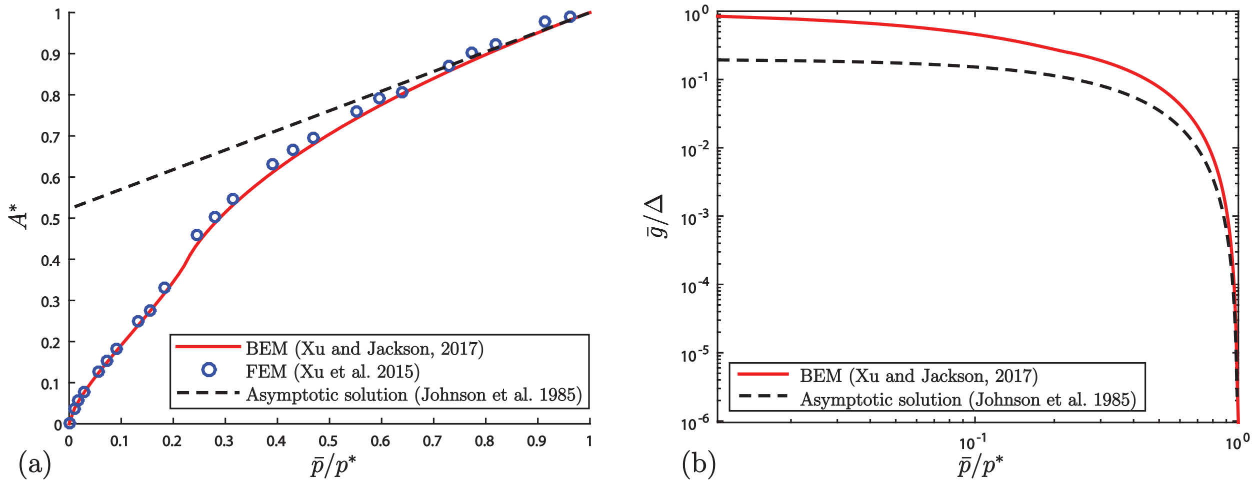

Figure 3.3: (a) The contact ratio, A^*, and (b) the average interfacial gap, $\bar{g}/\Delta$, through the entire range of $\bar{p}/p^*$ predicted by various methods.

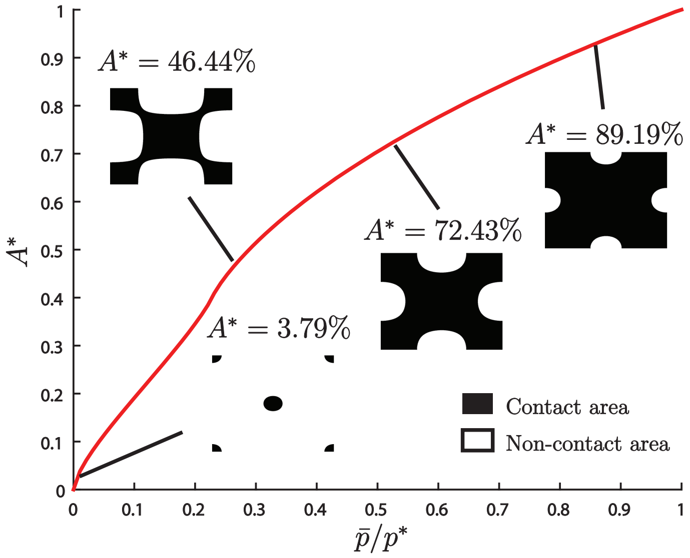

Figure 3.4: The evolution of the contact area distribution

where $x \in [0, \lambda_x)$ and $y \in [0, \lambda_y)$. When the waviness is achieved complete contact for the first time when $\bar{p}^*$ monotonically increases from zero, the corresponding average contact pressure is denoted by p^* [44]:

$$p^* = \frac{1}{2} E^* \sqrt{\alpha^2 + \beta^2} \Delta, \tag{3.53}$$

where $\alpha = 2\pi/\lambda_x$ and $\beta = 2\pi/\lambda_y$.

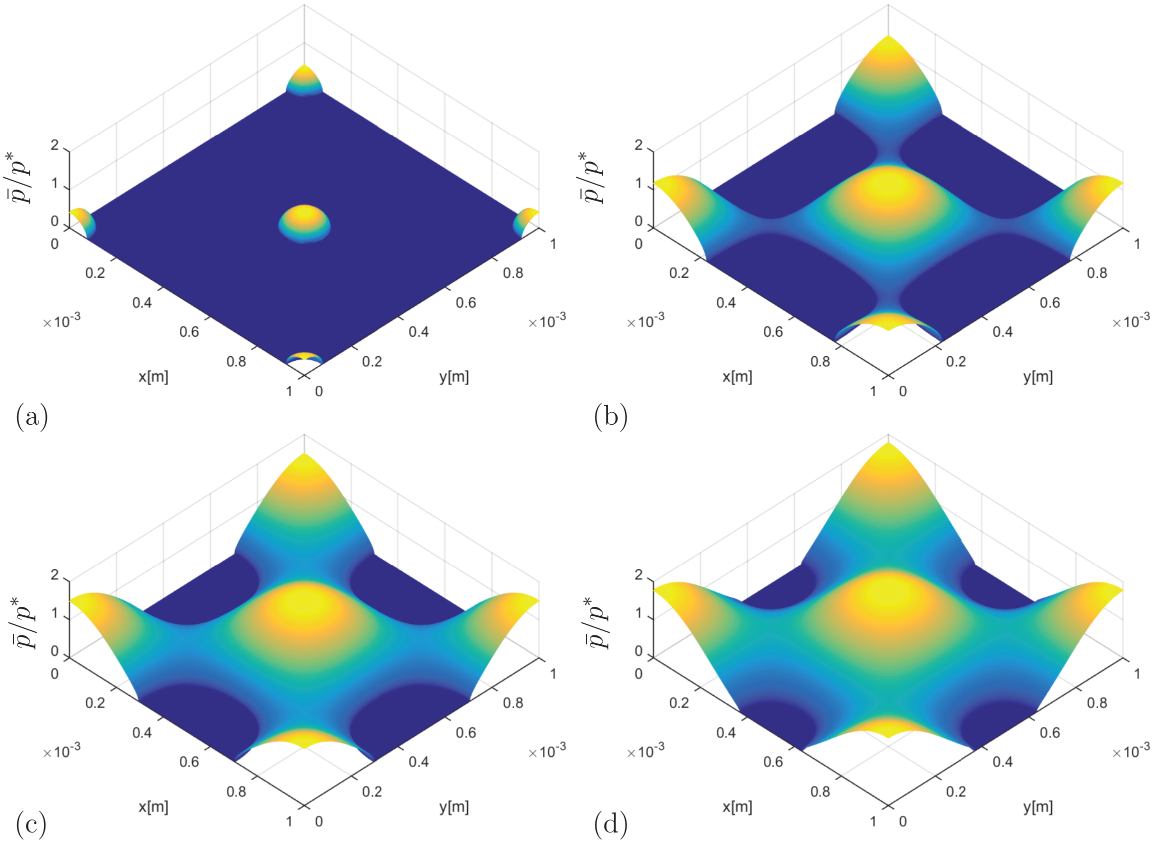

(a) (b) (c) (d)

Figure 3.5: The dimensionless contact pressure distribution, p/p^*, associated with (a) $A^* = 3.79\%$, (b) $A^* = 46.44\%$, (c) $A^* = 72.43\%$ and (d) $A^* = 89.19\%$.

The closed-form solution is only available asymptotically when $\bar{p} \to 0$ and $\bar{p} \to p^*$. At extremely light load, the contact only occurs over the asperities and it can be approximated by the Hertzian contact theory [44, 64], see Section 4.2 for more detail. When $\bar{p} \to p^*$, the non-contact area can be divided into multiple penny-shaped cracks, see Section 5.2 for more detail. The final closed-forms of the asymptotic solutions are given by Johnson et al. [44]:

$$A^*(\bar{p}) = 1 - \frac{3}{2\pi}(1 - \bar{p}/p^*), \tag{3.54}$$

$$\bar{g}(\bar{p}) = \frac{16\Delta}{15\pi^2}\left(\frac{3}{2}\right)^{3/2}(1 - \bar{p}/p^*)^{5/2}. \tag{3.55}$$

This waviness problem is also solved by the finite element method using ANSYS® and results were reported in [64]. The constants used in the numerical simulations are tabulated Table 3.1.

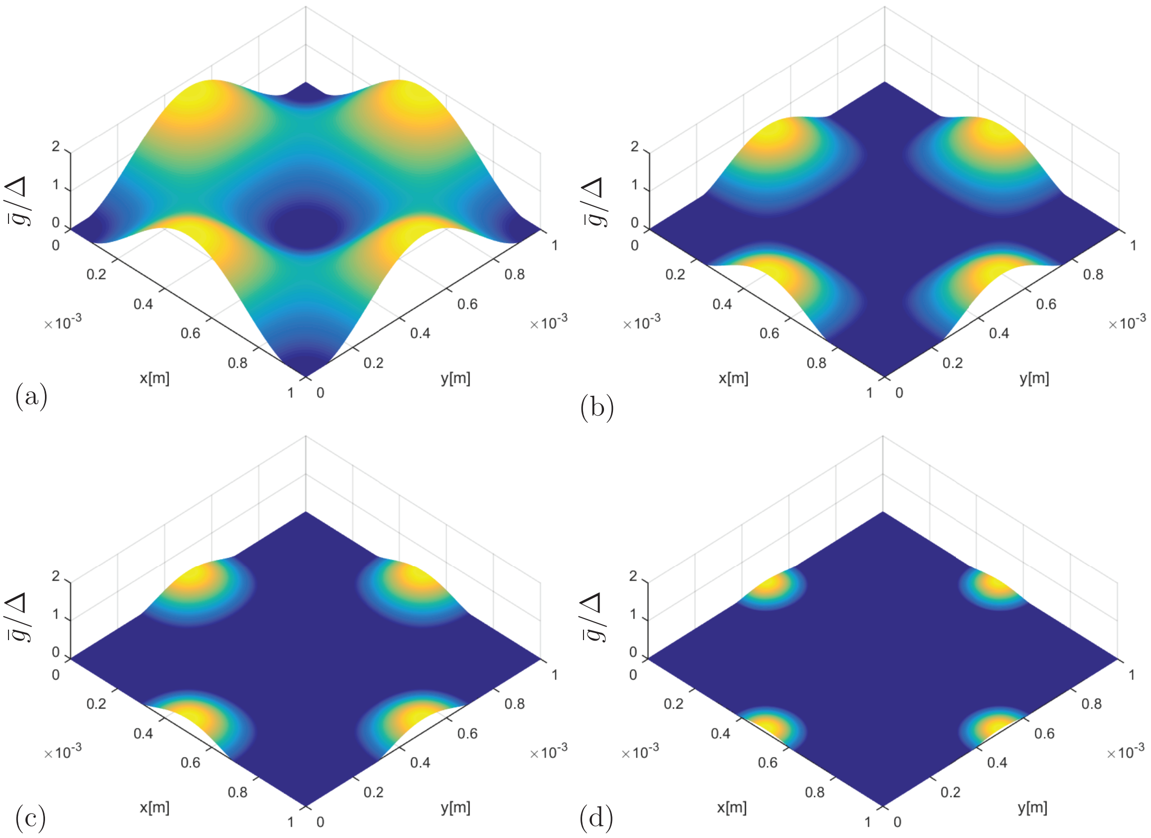

Figure 3.6: The dimensionless interfacial gap distribution, g/Δ, associated with (a) $A^* = 3.79\%$, (b) $A^* = 46.44\%$, (c) 72.43% and (d) $A^* = 89.19\%$.

Table 3.1: Constants

E^* [GPa]	λ_x [m]	$k' = \lambda_y/\lambda_x$	Δ/λ_x
220	0.001	1	0.02

The BEM results have a good agreement with the finite element results throughout the entire loading range (from first touch till the initial complete contact), see Fig. 3.3. As shown in Fig. 3.4(a), the contact area concentrated at the peak of the sinusoidal waviness at the initial loading stage where $A^* = 3.79\%$. The corresponding pressure, Fig. 3.5(a), is similar to the Hertzian contact pressure and the interfacial gap distribution, Fig. 3.6(a), is similar to the shape of the sinusoidal waviness. As the load is increased, the isolated contact area over peaks are gradually increased and are coalesced into an irregular contact patch at a transition point. At the vicinity of this transition point, the change of A^* is accelerated against $\bar{p}$, see Fig. 3.4. As the load is further increased, the deformed shape of the interface at the non-contact area are close to penny-shaped cracks, see Fig. 3.6(c). At the high load range, the non-contact regions are almost the same as penny-shaped cracks and are distantly located, see Fig. 3.6(d). The contact pressure gradually transformed from the Hertzian contact pressure distribution, Fig. 3.5(a), to the one in, Fig. 3.5(d), similar to the sinusoidal pressure distribution at complete contact.

3.8.2 Rough Surface Contact

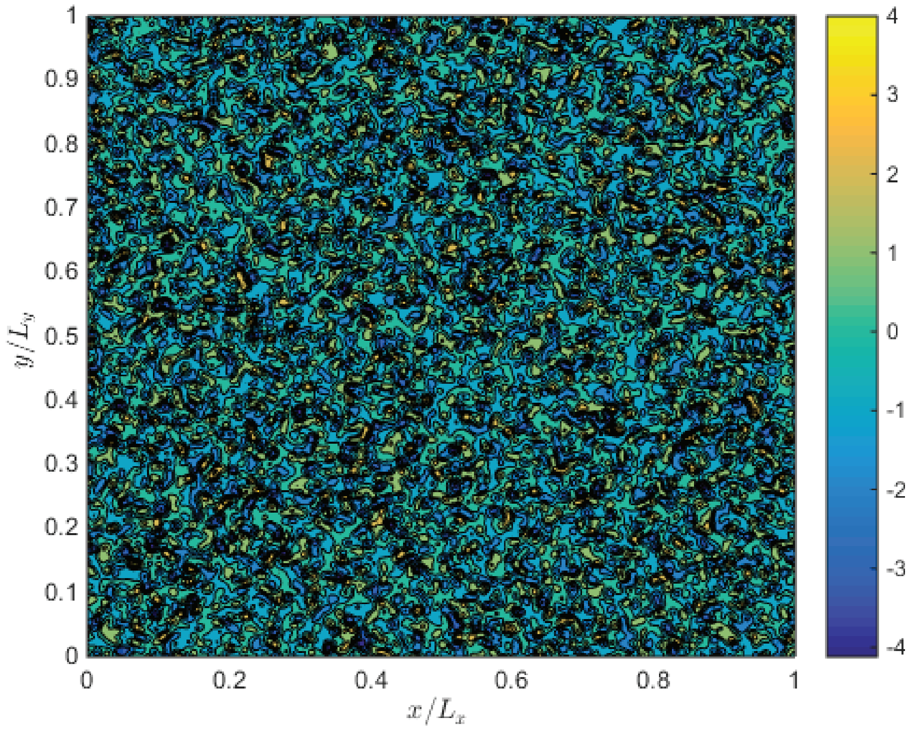

Figure 3.7: Contour of the dimensionless height of the generated rough surface $h/\sqrt{m_0^h}$.

A nominally flat rough surface, shown in Fig. 3.7, is generated numerically based on the algorithm developed by Xu and Jackson [52] and it will be discussed in details in Chapter 7. Since the generated roughness is not strictly Gaussian, the corresponding closed-form solution is not available. As shown in Fig. 3.8, the contact ratio, A^*, and the average interfacial gap, $\bar{g}^* = \bar{g}/\sqrt{m_0^h}$, monotonically increases and decrease, respectively, with the increase of $\bar{p}$. At the initial loading stage, the contacting asperities create numerous isolated asperity contact areas with approximately elliptical/circular shapes, see Fig. 3.9(a). As load increases, the asperity coalescence occurs where multiple isolated asperity contact areas are combined into

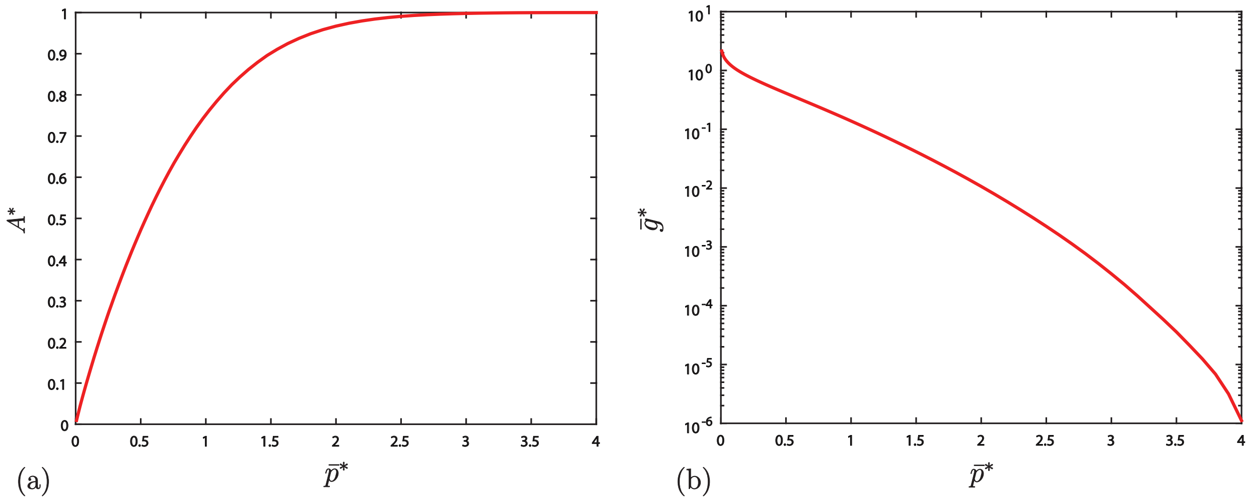

Figure 3.8: (a) The contact ratio, A^*, and (b) the average interfacial gap, $\bar{g}^* = \bar{g}/\sqrt{m_0^h}$, through the entire range of $\bar{p}^* = \bar{p}/\sqrt{m_0^p}$ predicted by the BEM. The colored figure is available online.

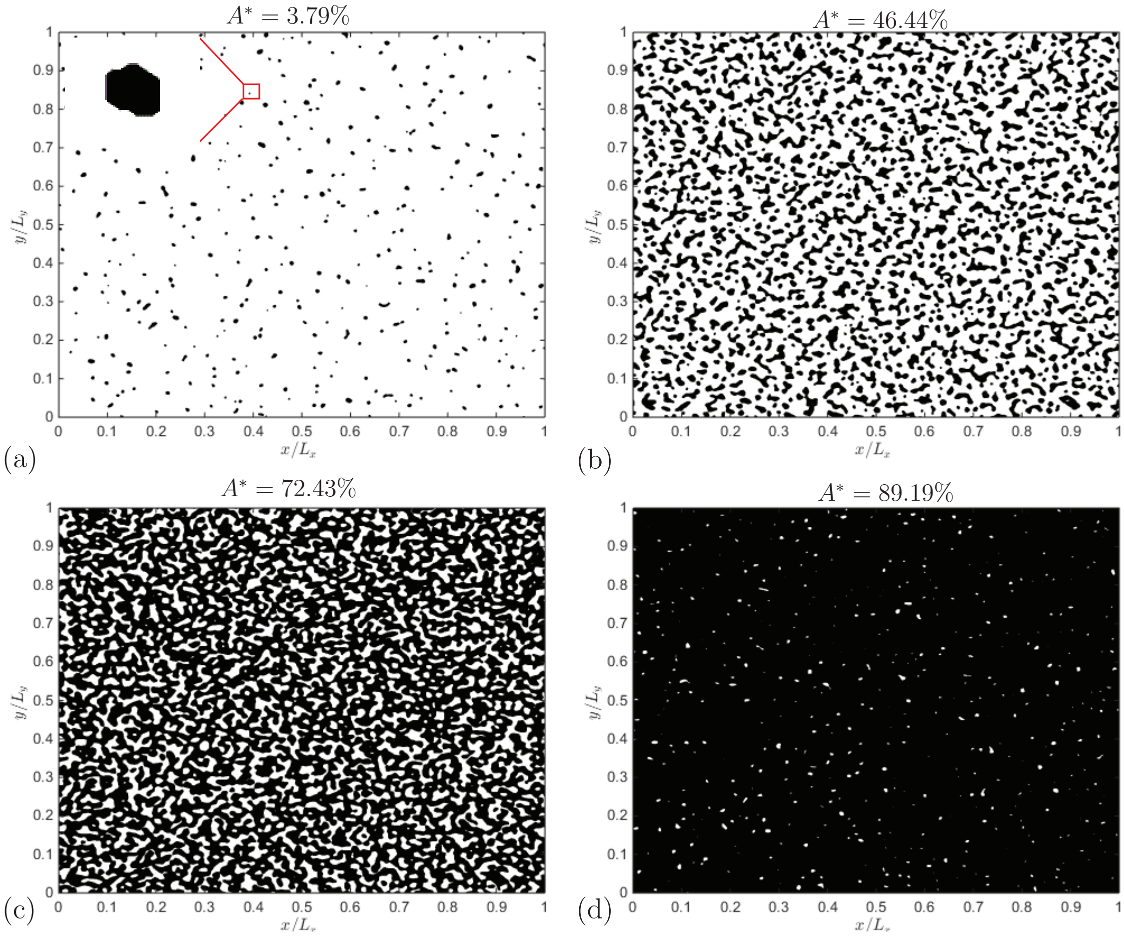

Figure 3.9: The contact area distribution associated with (a) $A^* = 3.79\%$, (b) $A^* = 46.44\%$, (c) 72.43% and (d) $A^* = 89.19\%$.

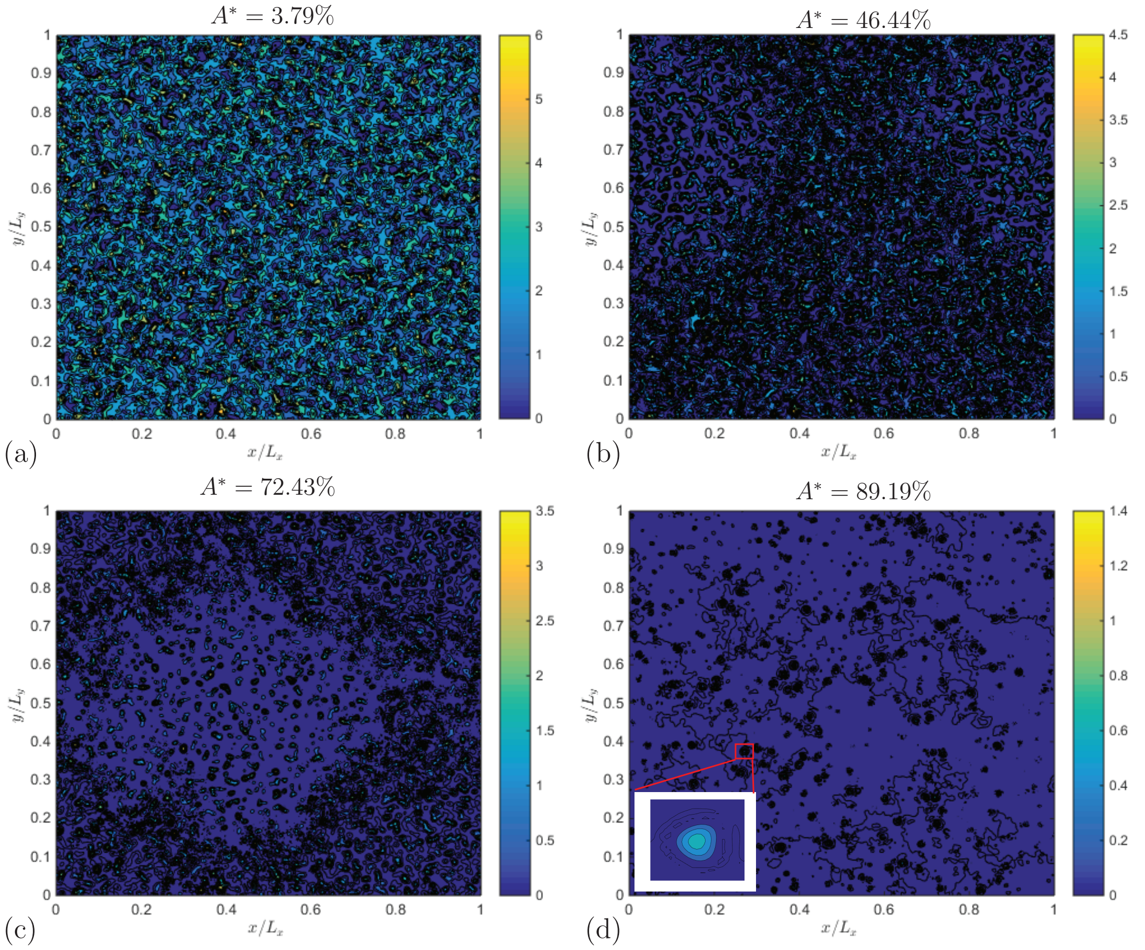

Figure 3.10: The interfacial gap distribution associated with (a) $A^* = 3.79\%$, (b) $A^* = 46.44\%$, (c) 72.43% and (d) $A^* = 89.19\%$. The colored figure is available online.

one irregular contact patch, see Fig. 3.9(b). Figs. 3.9(a,b) are the direct evidence why the statistical models discussed in Chapter 4 is only valid for the early contact where $\bar{p}$ and A^* are nearly vanishing. As the load further increases, the contact area becomes larger than non-contact area and the non-contact patches are surrounded by the contact area, see Fig. 3.9(c). At high load range, the contact area is nearly the same as the nominal contact area and each isolated non-contact regions are can be approximated by elliptical/circular shapes, see Fig. 3.9(d). The evolution of the interfacial gap follows the same trend observed in the waviness contact, see Fig. 3.10. Figs. 3.9(d) and 3.10(d) clearly shows that, at the nearly complete contact, the contact problem can be decomposed into numerous individual elliptical/circular (half) "cracks" with certain trapped volumes. .

3.9 Discussions

In the above sections, a special BEM is applied to the rough contact problem where the domain is a half-space with the boundary $z = 0$. In the study of contact mechanics, this special BEM is dominantly applied mainly in the form of the Boussinesq influence function (continuous boundary: Eq. (3.27)) or Love's influence coefficient (discontinuous boundary: Eq. (3.31)). Two important reasons are contributed to the popularity of this special BEM. One reason is that many contact problem is localized to a negligibly small region. Compared with the contact area, the contact bodies (domains) are approximately half-spaces as long as the curvature of the mating interface is small. From author's personal opinion, the second reason is related to the classic book, *Contact Mechanics*, written by Johnson [45]. Unlike the other contact mechanics monographs [68–70] in the past using the complex variable method, the derivation of the plane and spatial contact problem in Johnson's book relies heavily on the superposition of the point load (Flamant (2D) and Boussinesq (3D)) solution. The following sentence from his monograph accurately states his idea of solving contact mechanics problem from an engineering perspective: *"to start from the stresses and displacements produced by concentrated normal and tangential forces. The stress distribution and deformation resulting from any distributed loading can then be formed by superposition"*.

However, in many contact/tribological problems, the spherical domain can not be approximated by the half-space with the boundary $z = 0$. In the seal industry, the deformation of the rubber ring seals due to the normal and shear stresses from the lubricant and the counter surface may be inaccurate if the Boussinesq solution is used. The other problems includes (1) plastic thrust bearing, (2) gear tooth contact, (3) the wheel-rail interaction, (4) tire-road interaction, etc. Unfortunately, the conventional BEM may not be suitable for the rough surface contact problem where the number of sampling points (nodes) nowadays easily exceeds one million. If we restrict out discussion within the scope of linear elastostatic problem, the conventional BEM, usually introduced in the BEM textbook, suffers the following shortages:

1. The stiffness matrix is full-rank and asymmetric. The size of the memory needed for the storage of this stiffness matrix is $\mathcal{O}(N^2)$ where N is number of nodes.

2. Solving the system of N-equations by the traditional Gauss elimination requires $\mathcal{O}(N^3)$.

Among all the fast BEM, the fast multipole BEM [39] may be a solution to improve the efficiency of the conventional BEM in the large-scale simulation. The fast multipole BEM uses the fast multipole method [71] together with the tree-code [71] to reduce the storage of the stiffness matrix and the computational complexity in solving the system equations. The fast multipole BEM can reduce the computational complexity down to $\mathcal{O}(N\log(N))$. This is the same complexity many fast methods are claimed when applied to the rough surface contact, e.g., the fast FFT [72] and the Multi-Level-Multi-Integration (MLMI) [73]. However, those methods requires a rectilinear grid with constant intervals and these restriction can be abandoned in the fast multipole BEM. In the past literatures, the fast multipole BEM has a superior behavior when applied to the 3D elasticity [39, 74]. Discussion of application of multipole BEM to the elastostatic problem is out of scope of this dissertation, readers should refer to Liu's book [39] for more detail.

3.10 Conclusions

In this chapter, the periodic and non-periodic rough surface contact between an elastic half-space and a rigid flat is formulated using the BEM with the Kelvin solution. The BIE is obtained for the half-space with the boundaries $z = 0$ and $z = -h(x, y)$, respectively. For the case of $z = 0$, the Boussinesq solutions are rederived. The surface displacement, strain and stress components in the substrate and on the boundary are derived in the frequency domain. The normal interfacial displacement is the convolution of the contact pressure. The corresponding influence function is derived in the closed-form for both periodic and non-periodic problem. The governing equations and the boundary conditions are explicitly given and solved by the optimization. Finally, the convergent criterion is proposed for the numerical solutions, namely, the contact ratio, the contact pressure and the interfacial gap. The validity of the numerical model is examined by solving the sinusoidal waviness contact problem. A good agreement of A^* and $\bar{g}$ predicted by the BEM, FEM and the asymptotic solution is found. The BEM is also applied to solve the rough surface contact problem. The contact area distribution and the average interfacial gap distribution are explored in details. As an observation tool, BEM shows that (i) the rough surface only in contact with the rigid flat at numerous elliptical/circular regions when the applied load/nearly complete contact is vanishing and (ii) when the real area of contact is close to the nominal contact area, the non-contact area consists of numerous elliptical/circular (half) “cracks” with certain trapped volumes. The above observation can be served as the foundations upon which the statistical model at early contact (Chapter 4) and at nearly complete contact (Chapter 5) are built.

References

[1] Komvopoulos, K. and Choi, D.H., 1992. Elastic finite element analysis of multi-asperity contacts. ASME Journal of Tribology, **114**(4), 823-831.

[2] Hyun, S., Pei, L., Molinari, J.F. and Robbins, M.O., 2004. Finite-element analysis of contact between elastic self-affine surfaces. Physical Review E, **70**(2), 026117.

[3] Hyun, S. and Robbins, M.O., 2007. Elastic contact between rough surfaces: Effect of roughness at large and small wavelengths. Tribology International, **40**(10), 1413-1422.

[4] Sahoo, P. and Ghosh, N., 2007. Finite element contact analysis of fractal surfaces. Journal of Physics D: Applied Physics, **40**(14), 4245

[5] Thompson, M.K., 2007. A Multi Scale Iterative Approach for Finite Element Modeling of Thermal Contact Resistance, Ph.D. Thesis, Massachusetts Institute of Technology.

[6] Walter, C. and Mitterer, C., 2009. 3D versus 2D finite element simulation of the effect of surface roughness on nanoindentation of hard coatings. Surface and Coatings Technology, **203**(20), 3286-3290

[7] Yastrebov, V.A., Durand, J., Proudhon, H. and Cailletaud, G., 2011. Rough surface contact analysis by means of the finite element method and of a new reduced model. Comptes Rendus Mécanique, **339**(7-8), pp.473-490.

[8] Megalingam, A. and Mayuram, M.M., 2012. Comparative contact analysis study of finite element method based deterministic, simplified multi-asperity and modified statistical contact models. ASME Journal of Tribology, **134**(1), 014503.

[9] Xu, Y., 2012, An Analysis of Elastic Rough Contact Models, Master Thesis, Auburn University, Auburn, USA.

[10] Olshevskiy, A., Yang, H.I. and Kim, C.W., 2012. Finite element simulation of inelastic contact for arbitrarily shaped rough bodies. Proceedings of the Institution of Mechanical Engineers, Part C: Journal of Mechanical Engineering Science, **226**(3), 595-606.

[11] Poulios, K. and Klit, P., 2013. Implementation and applications of a finite-element model for the contact between rough surfaces. Wear, **303**(1), 1-8.

[12] Wenk, J.F., Stephens, L.S., Lattime, S.B. and Weatherly, D., 2016. A multi-scale finite element contact model using measured surface roughness for a radial lip seal. Tribology International, **97**, 288-301.

[13] Conry, T.F. and Seireg, A., 1971. A mathematical programming method for design of elastic bodies in contact. ASME Journal of Applied Mechanics, **38**(2), pp.387-392.

[14] Kalker, J.J. and Van Randen, Y., 1972. A minimum principle for frictionless elastic contact with application to non-Hertzian half-space contact problems. Journal of Engineering Mathematics, **6**(2), pp.193-206.

[15] Webster, M.N. and Sayles, R.S., 1986. A numerical model for the elastic frictionless contact of real rough surfaces. ASME Journal of Tribology, **108**(3), pp.314-320.

[16] Xian, L. and Zheng, L., 1991. A numerical model for the elastic contact of three-dimensional real rough surfaces. Wear, **148**(1), pp.91-100.

[17] Lubrecht, A.A. and Ioannides, E., 1991. A fast solution of the dry contact problem and the associated sub-surface stress field, using multilevel techniques. ASME Journal of Tribology, **113**(1), pp.128-133.

[18] Ren, N. and Lee, S.C., 1993. Contact simulation of three-dimensional rough surfaces using moving grid method. ASME Journal of Tribology, **115**, pp.597-597.

[19] Poon, C.Y. and Sayles, R.S., 1994. Numerical contact model of a smooth ball on an anisotropic rough surface. ASME Journal of Tribology, **116**, pp.194-194.

[20] Bhushan, B. and Tian, X., 1996. A numerical three-dimensional model for the contact of rough surfaces by variational principle. ASME Journal of Tribology, **118**, pp.33-42.

[21] Nogi, T. and Kato, T., 1997. Influence of a hard surface layer on the limit of elastic contact – Part 1: Analysis using a real surface model. ASME Journal of Tribology, **119**(2), pp.493-500.

[22] Stanley, H.M. and Kato, T., 1997. An FFT-based method for rough surface contact. ASME Journal of Tribology, **119**(3), pp.481-485.

[23] Hu, Y.Z., Barber, G.C. and Zhu, D., 1999. Numerical analysis for the elastic contact of real rough surfaces. Tribology Transactions, **42**(3), pp.443-452.

[24] Polonsky, I.A. and Keer, L.M., 1999. A numerical method for solving rough contact problems based on the multi-level multi-summation and conjugate gradient techniques. Wear, **231**(2), pp. 206-219.

[25] Borri-Brunetto, M., Carpinteri, A. and Chiaia, B., 1998. Lacunarity of the contact domain between elastic bodies with rough boundaries. In Probamat-21st century: probabilities and materials (pp. 45-64). Springer Netherlands.

[26] Bhushan, B. and Peng, W., 2002. Contact mechanics of multilayered rough surfaces. Applied Mechanics Reviews, **55**(5), pp.435-480.

[27] Sainsot, P. and Lubrecht, A.A., 2011. Efficient solution of the dry contact of rough surfaces: a comparison of fast Fourier transform and multigrid methods. Proceedings of the Institute of Mechanical Engineerings, Part J: J. Engineering Tribology, **225**(6), pp.441-448.

[28] Putignano, C., Afferrante, L., Carbone, G. and Demelio, G., 2012. A new efficient numerical method for contact mechanics of rough surfaces. International Journal of Solids and Structures, **49**(2), pp.338-343.

[29] Pohrt, R., Popov, V.L. and Filippov, A.E., 2012. Normal contact stiffness of elastic solids with fractal rough surfaces for one-and three-dimensional systems. Physical Review E, **86**(2), pp.026710.

[30] Yastrebov, V.A., Anciaux, G. and Molinari, J.F., 2014. The contact of elastic regular wavy surfaces revisited. Tribology Letters, **56**(1), pp.171-183.

[31] Yastrebov, V.A., Anciaux, G. and Molinari, J.F., 2015. From infinitesimal to full contact between rough surfaces: evolution of the contact area. International Journal of Solids and Structures, **52**, pp.83-102.

[32] Bemporad, A. and Paggi, M., 2015. Optimization algorithms for the solution of the frictionless normal contact between rough surfaces. International Journal of Solids and Structures, **69**, pp.94-105.

[33] Campañá, C. and Müser, M.H., 2006. Practical Greens function approach to the simulation of elastic semi-infinite solids. Physical Review B, **74**(7), pp.075420.

[34] Yang, C., Tartaglino, U. and Persson, B.N.J., 2006. A multiscale molecular dynamics approach to contact mechanics. The European Physical Journal E, **19**(1), pp.47-58.

[35] Müser, M.H., 2015. A dimensionless measure for adhesion and effects of the range of adhesion in contacts of nominally flat surfaces. Tribology International. **100**, 41-47.

[36] Brebbia, C.A., Telles, J.C.F. and Wrobel, L., 1984. *Boundary element techniques: theory and applications in engineering*. Springer-Verlag.

[37] Becker, A.A., 1992. *The boundary element method in engineering: a complete course*. McGraw-Hill Companies.

[38] Beer, G., Smith, I. and Duenser, C., 2008. *The boundary element method with programming: for engineers and scientists*. Springer Science & Business Media.

[39] Liu, Y., 2009. *Fast multipole boundary element method: theory and applications in engineering*. Cambridge university press.

[40] Karami, G., 1989. *Lecture Notes in Engineering: A Boundary Element Method for Two-Dimensional Contact Problems (Vol. 51)*. Springer Verlag, Heidelberg.

[41] Takahashi, S., 1991. *Lecture Notes in Engineering: Elastic contact analysis by boundary elements (Vol. 67)*. Springer Verlag, Heidelberg.

[42] Cavalcante, B.M., Shaterzadeh-Yazdi, M.H., Sollero, P., Albuquerque, E.L. and Doca, T., 2017. Analysis of a Cattaneo-Mindlin problem using the boundary element method. Tribology International, **108**, pp.194-201.

[43] Boussinesq, J., 1885. Application des potentiels à Íètude de Íéquilibre et du mouvement des solides élastiques: principalement au calcul des dformations et des pressions que produisent, dans ces solides, des efforts quelconques exercés sur une petite partie de leur surface ou de leur intrieur: mémoire suivi de notes tendues sur divers points de physique, mathematique et d́analyse (Vol. 4). Gauthier-Villars.

[44] Johnson, K.L., Greenwood, J.A. and Higginson, J.G., 1985. The contact of elastic regular wavy surfaces. International Journal of Mechanical Sciences, **27**(6), pp.383-396.

[45] Johnson, K.L., 1987. *Contact Mechanics*. Cambridge University Press.

[46] Jackson, R.L. and Green, I., 2011. On the modeling of elastic contact between rough surfaces. Tribology Transactions, **54**(2), pp.300-314.

[47] Li, S. and Kahraman, A., 2013. A physics-based model to predict micro-pitting lives of lubricated point contacts. International Journal of Fatigue, **47**, pp.205-215.

[48] Li, S. and Kahraman, A., 2014. A micro-pitting model for spur gear contacts. International Journal of Fatigue, **59**, pp.224-233.

[49] Li, S., 2014. A boundary element model for near surface contact stresses of rough surfaces. Computational Mechanics, **54**(3), pp.833-846.

[50] Li, S., 2015. A computational study on the influence of surface roughness lay directionality on micropitting of lubricated point contacts. ASME Journal of Tribology, **137**(2), pp.021401.

[51] Li, S., 2015. An investigation on the influence of misalignment on micro-pitting of a spur gear pair. Tribology Letters, **60**(3), pp.1-12.

[52] Xu, Y., and Jackson, R.L., 2017, Statistical Models of Nearly Complete Elastic Rough Surface Contact-Comparison with Numerical Solutions, Tribiology International, **105**, 274291

[53] Sternberg, E., 1954. On Saint-Venant's principle. Quarterly of Applied Mathematics, **11**(4), pp.393-402.

[54] Tripp, J.H., Van Kuilenburg, J., Morales-Espejel, G.E. and Lugt, P.M., 2003. Frequency response functions and rough surface stress analysis. Tribology transactions, **46**(3), pp.376-382.

[55] Sneddon, I.N., 1964. The use of transform methods in elasticity. Air Force Office of Scientific Research, United States Air Force.

[56] Berry, M.V. and Lewis, Z.V., 1980, On the Weierstrass-Mandelbrot fractal function. Proceedings of the Royal Society of London A: Mathematical, Physical and Engineering Sciences, **370**(1743), pp. 459-484.

[57] Ausloos, M., and D. H. Berman, 1985, A multivariate Weierstrass-Mandelbrot function. Proceedings of the Royal Society of London A: Mathematical, Physical and Engineering Sciences, **400**(1819), pp. 331-350.

[58] Hou, K., Zhu, D. and Wen, S., 1985. A new numerical technique for computing surface elastic deformation caused by a given normal pressure distribution. ASME Journal of Tribology, **107**(1), pp.128-131.

[59] Liu, S.B., Ju, M.J. and Yang, C.X., 1993. Elliptic-paraboloid method for calculating surface elastic deformation in EHL. Tribology international, **26**(6), pp.443-448.

[60] Venner, C.H. and Lubrecht, A.A. eds., 2000. Multi-level methods in lubrication. Elsevier.

[61] Cottle, R.W., Pang, J.S. and Stone, R.E., 2009. *The linear complementarity problem*. Society for Industrial and Applied Mathematics.

[62] Xi, Y., Almqvist, A., Shi, Y., Mao, J. and Larsson, R., 2016. A complementarity problem-based solution procedure for 2D steady-state rolling Contacts with dry friction. Tribology Transactions, **59**(6), pp.1031-1038.

[63] Xi, Y., Almqvist, A., Shi, Y., Mao, J. and Larsson, R., 2016. Linear complementarity framework for 3D steady-state rolling contact problems including creepages with isotropic and anisotropic friction for circular Hertzian contact. Tribology Transactions, pp.1-13.

[64] Xu, Y., Rostami, A. and Jackson, R.L., 2015. Elastic contact between a geometrically anisotropic bisinusoidal surface and a rigid base. ASME Journal of Tribology, **137**(2), pp. 021402.

[65] Yastrebov, V.A., Anciaux, G. and Molinari, J.F., 2017. On the accurate computation of the true contact-area in mechanical contact of random rough surfaces. Tribology International, **114**, pp.161-171.

[66] Barber, J.R., 1974. Determining the contact area in elastic-indentation problems. The Journal of Strain Analysis for Engineering Design, **9**(4), pp.230-232.

[67] Krithivasan, V. and Jackson, R.L., 2007. An analysis of three-dimensional elasto-plastic sinusoidal contact. Tribology Letters, **27**(1), pp.31-43.

[68] Muskhelishvili, N.I., 1949, *Some basic problems of hte mathematical theory of elasticity*, 3rd Edn., Moscow (English transltion by J.R.M. Radok, Noordhoff, 1953).

[69] Galin, L.A., 1953. *Contact problems in the theory of elasticity*, Moscow. (English translation by H.Moss, North Carolina State College, Department of Mathematics, 1961)

[70] Gladwell, G.M., 1980. *Contact problems in the classical theory of elasticity*. Sijthoff & Noordhoff, The Netherlands.

[71] Greengard, L., 1988. *The rapid evaluation of potential fields in particle systems*. MIT press.

[72] Liu, S., Wang, Q. and Liu, G., 2000. A versatile method of discrete convolution and FFT (DC-FFT) for contact analyses. Wear, **243**(1), pp.101-111.

[73] Brandt, A. and Lubrecht, A.A., 1990. Multilevel matrix multiplication and fast solution of integral equations. Journal of Computational Physics, **90**(2), pp.348-370.

[74] Popov, V. and Power, H., 2001. An $\mathcal{O}(N)$ Taylor series multipole boundary element method for three-dimensional elasticity problems. Engineering Analysis with Boundary Elements, **25**(1), pp.7-18.

Chapter 4

Statistical Models of Early Contact

At early contact where the applied load/real area of contact is vanishing, the contact between a nominally flat rough surface and a rigid flat only occurs at individual regions with nearly elliptical/circular shape on the higher asperities. A direct observation of the contact area distribution by BEM at the early contact is shown in Fig. 3.9(a). In this chapter, statistical models of early contact, proposed in the past literatures, are systematically studied.

4.1 Introduction

It is commonly accepted that the first statistical model was developed by Greenwood and Williamson [1] to describe the purely normal contact between a rigid flat and a linear elastic half-space with the nominally flat rough surface of *small amplitude* on the boundary, see Fig. 4.1(a). This type of rough surface is also referred to as a *nominally flat* rough surface and its height is measured about its mean level. The Young's modulus and Poisson's ratio are E and ν. It is assumed that a uniform normal pressure, $\bar{p}$, is applied at the far end of the half-space, respectively. The rigid flat is fixed.

Due to the uneveness of the boundary, the contact between the half-space and rigid flat does not occur everywhere over $z = 0$ plane. The nominal contact area is indicated by A_n and it is obvious that $A_n \to \infty$. The contact boundary, Γ_c, consists of multiple contact regions with different sizes and shapes. The real area of contact is indicated by A_r which is only a small fraction of A_n and the fraction is quantified by the contact ratio, A^*, which is defined in Eq. (1.4).

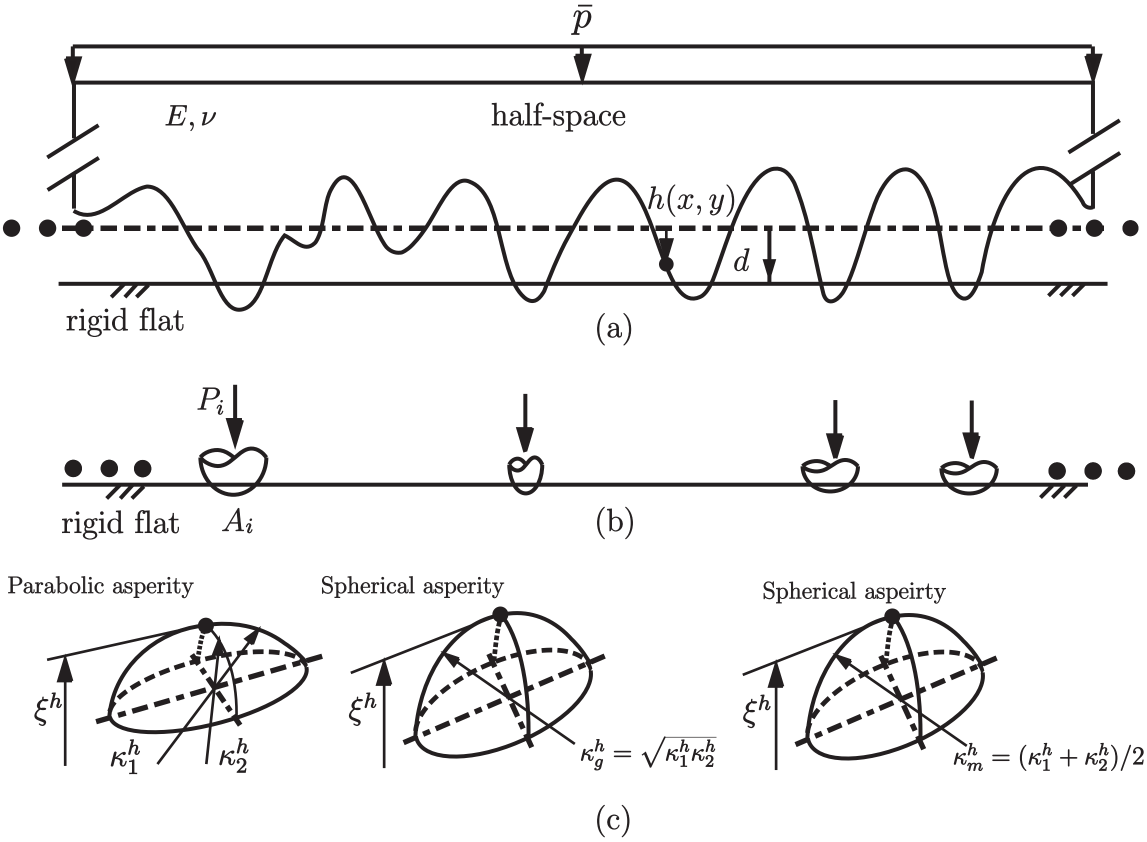

Figure 4.1: Schematic representation of the nominally flat rough surface contact problem

One assumption commonly accepted in the statistical model is that A_r is *negligibly small* compared with A_n (i.e., $A^* < 1 \sim 2\%$). This assumption stems from two reasons. The first reason is related to the *plastic deformation* at the asperity level. The statistical model is originally developed for the electrical contact and is, later on, widely applied to the other engineering practices where the application of the metallic materials are dominant. When $\bar{p}$ is gradually increased from zero, the higher summits of the rough surfaces are easily deformed plastically. Thus, the elasticity can only be maintained under the small contact pressure which results in a negligibly small A^*. This stage is referred to as the *early contact*.

Another reason is that the assumption of small A^* enables the decomposition of the rough surface contact into multiple asperity contact problems, see Fig. 4.1(b). The computational resource in the 60s to early 90s were not adequate to completely solve the rough surface contact problem with enough fine details of the roughness on the interface. This approximation is very essential to the early study of the rough surfaces contact. In the stage of the early contact, the interaction between the rigid flat and the rough surface only occurs on the higher asperities. Due to the small $\bar{p}$ and small isolated contacts, the couplings between the contacting asperities are negligible. Consequently, the original problem is equivalent to the superposition of multiple normal asperity contact pairs.

Under the action of small $\bar{p}$, the vertical distance between the rigid flat and the mean level of the undeformed rough surface is d. The asperity contact pairs can be identified by $\xi^h > d$ where ξ^h is the summit height of the asperity, see Fig. 4.1(c). Commonly, the asperities upon the roughness are approximated in the parabolic forms, see Section 2.4 for more detail. A parabolic asperity is uniquely represented by a vector of geometrical parameters: $(\xi^h, \kappa_1^h, \kappa_2^h)$. The corresponding contact area, $A_i(\xi^h, \kappa_1^h, \kappa_2^h)$, and the contact load, $P_i(\xi^h, \kappa_1^h, \kappa_2^h)$, on a certain asperity can be determined by the Hertzian contact theory [2, 3] which will be discussed in detail in next section. It is commonly known that the rough surfaces are random processes, thus $(\xi^h, \kappa_1^h, \kappa_2^h)$ is a vector of random variables. Since the geometry of a random process is indeterministic, the distribution of a certain asperity in a function of $(\xi^h, \kappa_1^h, \kappa_2^h)$ can be quantified by the joint probability density function (PDF), $\Phi(\xi^h, \kappa_1^h, \kappa_2^h)$. Then, the ensemble average of the contact area, A_i, of a single asperity is obtained

$$\langle A_i \rangle = \int_d^\infty \int_0^{\kappa_2^h} \int_0^\infty A_i(\xi^h, \kappa_1^h, \kappa_2^h)\Phi(\xi^h, \kappa_1^h, \kappa_2^h) d\kappa_2^h d\kappa_1^h d\xi^h. \tag{4.1}$$

Provided that the number of asperities, N, of the rough surface within the nominal contact area is known, the resultant real area of contact is: $A_r(d) = N\langle A_i \rangle$ where N is infinite since $A_n \to \infty$. A more rigorous way is to use the asperity density: $\eta = \lim_{A_n \to \infty} N/A_n$. Then, the contact ratio, A^*, can be formulated as [13, 16]:

$$A^*(d) = \eta^h \int_d^\infty \int_0^{\kappa_2^h} \int_0^\infty A_i(\xi^h, \kappa_1^h, \kappa_2^h)\Phi(\xi^h, \kappa_1^h, \kappa_2^h) d\kappa_2^h d\kappa_1^h d\xi^h. \tag{4.2}$$

Similarly, the external load, $\bar{p}$, is balanced by the superposition of the asperity contact loads [13, 16]:

$$\bar{p}(d) = \eta^h \int_d^\infty \int_0^{\kappa_2^h} \int_0^\infty P_i(\xi^h, \kappa_1^h, \kappa_2^h)\Phi(\xi^h, \kappa_1^h, \kappa_2^h) d\kappa_2^h d\kappa_1^h d\xi^h. \tag{4.3}$$

If the rough surface is Gaussian process, then the above formulations are equivalent to the BGT model [14].

In Section 4.2, a brief discussion on the single asperity contact models is given. Different statistical models are introduced in Section 4.3 by using the different combinations of the single asperity contact models and the PDFs explored in Section 2.5. The numerical results are shown in Section 4.4.

4.2 Single Asperity Contact Models

The statistical models at early contact, as well as some other analytical rough surface contact model, rely on the Hertzian theory to model the elastic contact between the single asperity and the rigid flat. In this section, the general form of the Hertzian theory, as well as its simplified forms, are briefly introduced.

4.2.1 Hertzian Elliptical Contact Model

Consider a linear elastic parabolic asperity of which the geometry is defined by Eq. (2.26), see also the parabolic asperity in Fig. 4.1(c). When it is in purely normal contact with a rigid flat at a small penetration depth of δ, the applied normal surface displacement, $\bar{w}(x, y)$, within the contact area is conformed with the shape of the asperity defined in Eq. (2.26):

$$\bar{w}(x, y) = \delta - \frac{1}{2}\kappa_1^h x^2 - \frac{1}{2}\kappa_2^h y^2, \tag{4.4}$$

and the corresponding pressure distribution has the following parabolic form [2, 3]:

$$p(x, y) = p_0 \left[1 - (x/a)^2 - (y/b)^2\right]^{1/2}, \tag{4.5}$$

where p_0 is the maximum pressure. a and b (noting $b < a$) are the *semi-major* radius and *semi-minor* radius of the contact area. The normal load and the depth of penetration are P_i and δ, respectively. The inter-relations between the unknowns p_0, P_i, a and b are summarized in [3]. For a given penetration, δ, the corresponding contact area, $A_i = \pi ab$, and the contact load, P_i, are [2, 3]:

$$A_i(\delta, \kappa_1^h, \kappa_2^h) = \pi(\kappa_g^h)^{-1}\delta F_1^2(e)/F_2(e), \tag{4.6}$$
$$P_i(\delta, \kappa_1^h, \kappa_2^h) = \frac{4}{3}E^*(\kappa_g^h)^{-1/2}\delta^{3/2}F_2(e)^{-3/2}, \tag{4.7}$$

where $E^* = E/(1-\nu^2)$ is the reduced modulus, and $\kappa_g^h = \sqrt{\kappa_1^h\kappa_2^h}$ is the *geometrical curvature*. $F_1(e)$ and $F_2(e)$ are in a function of the eccentricity $e = \sqrt{1 - b^2/a^2}$ and have the following forms [2, 3]:

$$F_1^3(e) = \frac{4}{\pi}e^{-2}(1-e^2)^{3/4}\left\{\left[\mathbf{E}(e)/(1-e^2) - \mathbf{K}(e)\right]\left[\mathbf{K}(e) - \mathbf{E}(e)\right]\right\}^{1/2}, \tag{4.8}$$
$$F_2(e) = \frac{2}{\pi}(1-e^2)^{1/4}\left[F_1(e)\right]^{-1}\mathbf{K}(e), \tag{4.9}$$

where $\mathbf{K}(\cdot)$ and $\mathbf{E}(\cdot)$ are complete elliptic integrals of the first and second kind, respectively:

$$\mathbf{K}(e) = \int_0^{\pi/2}\frac{d\theta}{\sqrt{1-e^2\sin(\theta)}},$$
$$\mathbf{E}(e) = \int_0^{\pi/2}\sqrt{1-e^2\sin(\theta)}d\theta.$$

The only unknown e can be solved from the following nonlinear relation [3]:

$$\frac{\kappa_1^h}{\kappa_2^h} = \frac{\mathbf{K}(e) - \mathbf{E}(e)}{\mathbf{E}(e)/(1-e^2) - \mathbf{K}(e)}. \tag{4.10}$$

A fit solution of e is adapted from the one given by Xu et al [4]:

$$\sqrt{1-e^2} = \exp\left[0.006709 \times \log^2(\kappa_1^h/\kappa_2^h) + 0.6692 \times \log(\kappa_1^h/\kappa_2^h)\right]. \tag{4.11}$$

The accuracy of the above empirical solution is confirmed in Fig. 4.2. The above problem is originally solved by Hertz [2] and it is referred to as the *Hertzian elliptical contact model*.

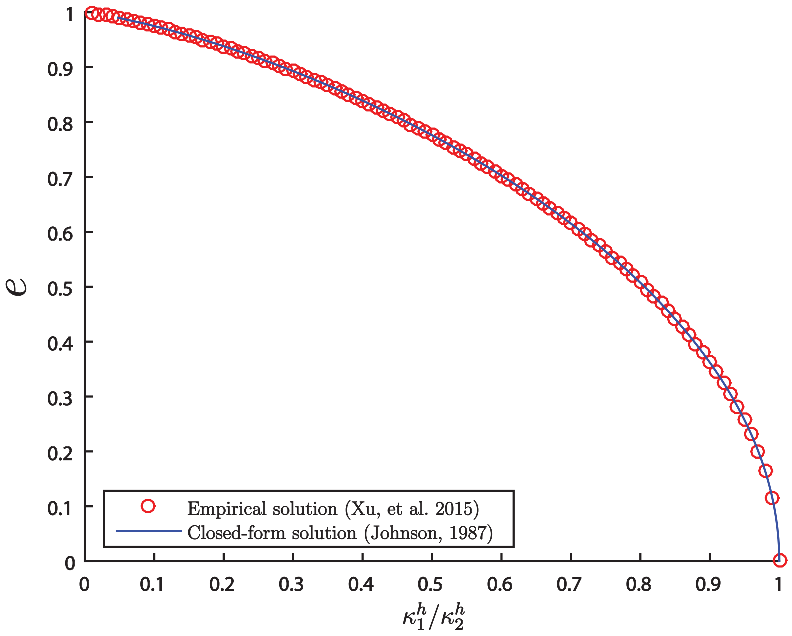

Figure 4.2: Plot of e vs. κ_1^h/κ_2^h of the empirical solution in Eq. (4.11) and the closed-form solution in Eq. (4.10).

4.2.2 Hertzian Circular Contact Model

When the principal curvatures are the same, i.e., $\kappa_1^h = \kappa_2^h = \kappa^h$, the applied normal surface displacement has an axisymmetric form:

$$\bar{w}(r) = \delta - \frac{1}{2}\kappa^h r^2,$$

which is defined using cylindrical coordinates where $r = \sqrt{x^2 + y^2}$. The corresponding asperities with axisymmetric shape are illustrated in Fig. 4.1(c) (with geometric/mean curvature).

For a given penetration δ, the contact area, A_i, and the contact load, P_i, are [3]:

$$A_i(\delta, \kappa^h) = \pi(\kappa^h)^{-1}\delta, \tag{4.12}$$

$$P_i(\delta, \kappa^h) = \frac{4}{3}E^*(\kappa^h)^{-1/2}\delta^{3/2}. \tag{4.13}$$

Unlike the Hertzian elliptical contact model, the Hertzian circular contact model is straightforward when δ is known. This is why the Hertzian circular contact model is widely used in the statistical contact model, even though the axisymmetric parabolic asperities rarely exist upon Gaussian surfaces [5].

4.2.3 Hertzian Mildly Elliptical Contact Model (Geometric Curvature)

For a mildly elliptical contact, Johnson [3] found $F_1(e)$ and $F_2(e)$ in Eqs. (4.8) and (4.9) decay slowly from unity as $\sqrt{\kappa_2^h/\kappa_1^h}$ is increased, see Fig. 4.4 in [3]. Noticing the analogies between Eqs. (4.6) and (4.12) (also Eqs. (4.7) and (4.13)), the mildly elliptical contact is equivalent to a circular contact if κ^h in Eqs. (4.12) and (4.13) is replaced by $\kappa_g^h = \sqrt{\kappa_1^h \kappa_2^h}$ [5], i.e.,

$$A_i(\delta, \kappa_g^h) = \pi(\kappa_g^h)^{-1}\delta, \tag{4.14}$$

$$P_i(\delta, \kappa_g^h) = \frac{4}{3}E^*(\kappa_g^h)^{-1/2}\delta^{3/2}. \tag{4.15}$$

The geometry of such asperity is still axisymmetric with geometric curvature, see Fig. 4.1(c).

4.2.4 Hertzian Mildly Elliptical Contact Model (Mean Curvature)

As $\kappa_2^h/\kappa_1^h \to 1^+$, Eq. (2.30) yields $\kappa_m^h \approx \kappa_g^h$. Replacing κ_g^h in Eqs. (4.14) and (4.15) by $\kappa_m^h = (\kappa_1^h + \kappa_2^h)/2$, the contact area, A_i, and the contact load, P_i, are [6]

$$A_i(\delta, \kappa_m^h) = \pi(\kappa_m^h)^{-1}\delta, \tag{4.16}$$

$$P_i(\delta, \kappa_m^h) = \frac{4}{3}E^*(\kappa_m^h)^{-1/2}\delta^{3/2}. \tag{4.17}$$

This approximation is expected to be valid when the principal curvatures are mildly different. Therefore, it is referred to as the Hertzian mildly elliptical contact model.

4.2.5 Remarks

Due to the complexity of the Hertzian elliptical contact theory, two mildly elliptical contact models are proposed based on the Hertzian circular contact theory. The approximation is extremely easy to achieve by replacing the curvature κ^h in the circular contact model with either the mean curvature κ_m^h or the geometric curvature κ_g^h. This idea can also be used to extend the circular adhesive contact model (e.g., the JKR model [7] and the Maugis-Dugdale model [8]) to the elliptical contact. Through the same approximation, the elliptical crack problem can also be simplified using the penny-shaped crack model. This will be discussed in the next chapter.

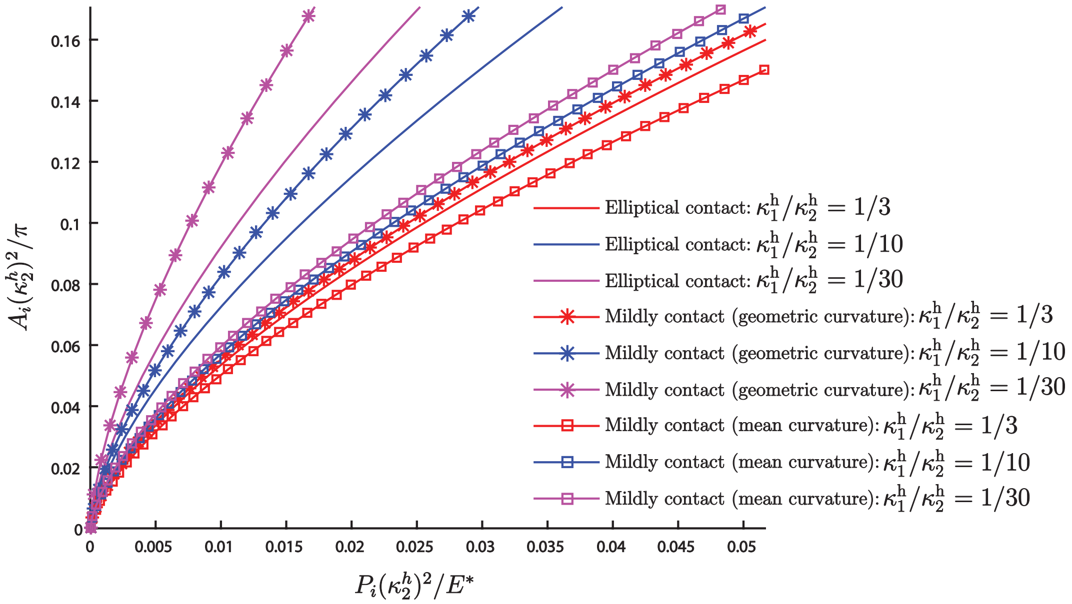

Figure 4.3: The plots of dimensionless contact area, $A_i(\kappa_2^h)^2/\pi$, vs. the dimensionless contact load, $P_i(\kappa_2^h)^2/E^*$, determined by (1) the Hertzian elliptical contact model, (2) the Hertzian mildly contact (mean curvature) model and (3) the Hertzian mildly elliptical contact (geometric curvature) model. The dimensionless penetration, $\delta\kappa_2^h$, varies within $[0, 0.1]$. The ratios (κ_1^h/κ_2^h) considered are $1/3$, $1/10$ and $1/30$. The colored figure is available online.

In the rest of the section, the accuracy of two approximated elliptical models using the mean curvature and the geometrical curvatures are tested. The relations of dimensionless contact area, $A_i(\kappa_2^h)^2/\pi$, to dimensionless contact load, $P_i(\kappa_2^h)^2/E^*$, determined by different elliptical contact models associated with different κ_2^h/κ_1^h are shown in Fig. 4.3. Several important observations are summarized below:

- An obvious gap can be found between two Hertzian mildly elliptical models and the Hertzian elliptical model. The gap is increased as κ_2^h/κ_1^h is increased.

- The mildly elliptical model with the geometrical curvature is a better approximation to the elliptical model than the one using mean curvature.

4.3 Multi-Asperity Contact Models

As shown in Section 4.1, the contact ratio, A^*, and the average contact pressure, $\bar{p}$, are related to the ensemble average of the area, A_i, and load, P_i, of the single contacting asperity. Depending on the different forms of the asperity contact model and the probability density function, a series of statistical models are developed in the past literatures. Some representative statistical models are introduced in this section.

4.3.1 Adapted Greenwood and Williamson (GW) model

In the original GW model, the asperity height is assumed to follow the Gaussian distribution. Then, the corresponding PDF is only a function of the asperity height, ξ^h, and is written as:

$$\Phi^h(\xi^h) = \frac{1}{\sqrt{2\pi}\sigma_s^h}\text{exp}\left[-\frac{\left(\xi^h - m^h\right)^2}{2\sigma_s^h}\right], \tag{4.18}$$

where σ_s^h is the root mean square (rms) of the asperity height. m^h is the distance between the mean asperity level and the mean level of the rough surface.

Eqs. (4.12) and (4.13) are used as the single asperity contact model:

$$A_i(\delta) = \pi(\kappa^h)^{-1}\delta, \tag{4.19}$$

$$P_i(\delta) = \frac{4}{3}E^*(\kappa^h)^{-1/2}(\delta)^{3/2}, \tag{4.20}$$

where $\delta = \xi^h - d$ is the interference between the contacting asperity ($\xi^h > d$) and the rigid flat. Another important assumption made in the original GW model is that all the asperities share the same radius of curvature ($R^h = 1/\kappa^h$).

Substituting Eqs. (4.19), (4.20) and (4.18) into Eqs. (4.2) and (4.3), the final forms of the GW model are [1]:

$$A^*(d) = \eta^h \int_d^\infty A_i(\xi^h - d)\Phi^h(\xi^h)d\xi^h, \tag{4.21}$$

$$\bar{p}(d) = \eta^h \int_d^\infty P_i(\xi^h - d)\Phi^h(\xi^h)d\xi^h. \tag{4.22}$$

A similar statistical model was developed by Zhuravlev [9] almost 20 years before the GW model. The formulation of A and P is very similarly to Eqs. (4.21) and (4.22) except that two PDFs are used to model the interaction between two rough surfaces. As we mentioned before in Section 2.5, the inputs of the GW model can be determined by the McCool's inputs [10], see Eqs. (2.43)-(2.46).

Nayak [11] pointed out that the PDF of the asperities in the function of ξ^{h*} approaches a Gaussian distribution only when $\alpha^h \to \infty$. Thus, instead of using the Gaussian distribution in Eq. (4.18), it si more accurate that $\Phi^h(\xi^{h*})$ in Eqs. (4.21) and (4.22) is replaced by the PDF in Eq. (2.42). As a matter of fact, m^h and σ_s^h become redundant in the adapted GW model. Another reason of using the PDF in Eq. (2.42) is that the dimensionless variables applied to the original GW model are not consistent with those used in the other statistical models introduced in the later sections [12].

Replacing A_i, P_i, η^h and R^h in Eqs. (4.21) and (4.22) by Eqs. (4.12), (4.13), (2.43) and (2.45) , we have the final form of the adapted GW model:

$$A^*(d^*) = \frac{\sqrt{\pi}}{16\sqrt{3}}\sqrt{\alpha^h}\int_{d^*}^{\infty}\left(\xi^{h*} - d^*\right)\Phi^h(\xi^{h*})d\xi^{h*}, \tag{4.23}$$

$$\bar{p}(d^*) = \frac{E^*}{9\sqrt{2}(\pi)^{3/4}}(\alpha^h)^{3/4}\sqrt{m_2^h}\int_{d^*}^{\infty}\left(\xi^{h*} - d^*\right)^{3/2}\Phi^h(\xi^{h*})d\xi^{h*}, \tag{4.24}$$

where $d^* = d/\sqrt{m_0^h}$ is the dimensionless surface separation. Defining the dimensionless pressure: $\bar{p}^* = \bar{p}/\sqrt{m_0^p}$ and using the identity in Eq. (2.52), i.e., $m_0^p = \frac{1}{2}(E^*)^2 m_2^h$, we can rewrite Eq. (4.24) as:

$$\bar{p}^*(d^*) = \frac{1}{9(\pi)^{3/4}}(\alpha^h)^{3/4}\int_{d^*}^{\infty}\left(\xi^{h*} - d^*\right)^{3/2}\Phi^h(\xi^{h*})d\xi^{h*}. \tag{4.25}$$

It is obvious that the relation of A^* to d^*, as well as $\bar{p}^*$ to d^*, only depend on the bandwidth parameter α^h.

This adapted GW model is very similar to the one proposed by Carbone [13] except that the radius of the asperities are still constant instead of a function of ξ^h in Carbone's model.

4.3.2 The Nayak-Bush Model

Bush [6] developed a statistical model by using the Hertzian spherical contact model in Eqs. (4.16) and (4.17) along with the PDF, $\Phi^h(\xi^{h*}, \kappa_m^{h*})$, in Eq. (2.40):

$$\begin{aligned} A^*(d^*) =& \eta^h \int_{d^*}^{\infty} \int_0^{\infty} A_i(\xi^h - d, \kappa_m^h) \Phi^h(\xi^{h*}, \kappa_m^{h*}) d\kappa_m^{h*} d\xi^{h*}, \\ \bar{p}(d^*) =& \eta^h \int_{d^*}^{\infty} \int_0^{\infty} P_i(\xi^h - d, \kappa_m^h) \Phi^h(\xi^{h*}, \kappa_m^{h*}) d\kappa_m^{h*} d\xi^{h*}. \end{aligned}$$

Replacing A_i, P_i and η^h in the above equations by Eqs. (4.12), (4.13) and (2.43), the final forms of the Nayak-Bush model are as follows:

$$A^*(d^*) = \frac{1}{6\sqrt{3}} \sqrt{\alpha^h} \int_{d^*}^{\infty} \int_0^{\infty} \left(\xi^{h*} - d^*\right) (\kappa_m^{h*})^{-1} \Phi^h(\xi^{h*}, \kappa_m^{h*}) d\kappa_m^{h*} d\xi^{h*}, \tag{4.26}$$

$$\bar{p}^*(d^*) = \frac{2\sqrt{2}}{9\sqrt{3}\pi} (\alpha^h)^{3/4} \int_{d^*}^{\infty} \int_0^{\infty} \left(\xi^{h*} - d^*\right)^{3/2} (\kappa_m^{h*})^{-1/2} \Phi^h(\xi^{h*}, \kappa_m^{h*}) d\kappa_m^{h*} d\xi^{h*}. \tag{4.27}$$

4.3.3 The Greenwood Model

Greenwood [5] combined the Hertzian mildly parabolic contact, in Eqs. (4.14) and (4.15), and the PDF, $\Phi^h(\xi^{h*}, \kappa_g^{h*})$, in Eq. (2.41), to form the following statistical model:

$$\begin{aligned} A^*(d^*) =& \eta^h \int_{d^*}^{\infty} \int_0^{\infty} A_i(\xi^h - d, \kappa_g^h) \Phi^h(\xi^{h*}, \kappa_g^{h*}) d\kappa_g^{h*} d\xi^{h*}, \\ \bar{p}(d^*) =& \eta^h \int_{d^*}^{\infty} \int_0^{\infty} P_i(\xi^h - d, \kappa_g^h) \Phi^h(\xi^{h*}, \kappa_g^{h*}) d\kappa_g^{h*} d\xi^{h*}. \end{aligned}$$

Replacing A_i, P_i and η^h in the above equations by Eqs. (4.14), (4.15) and (2.43), the final forms of the Greenwood model are obtained:

$$A^*(d^*) = \frac{1}{6\sqrt{3}} \sqrt{\alpha^h} \int_{d^*}^{\infty} \int_0^{\infty} \left(\xi^{h*} - d^*\right) (\kappa_g^{h*})^{-1} \Phi^h(\xi^{h*}, \kappa_g^{h*}) d\kappa_g^{h*} d\xi^{h*}, \tag{4.28}$$

$$\bar{p}^*(d^*) = \frac{2\sqrt{2}}{9\sqrt{3}\pi} (\alpha^h)^{3/4} \int_{d^*}^{\infty} \int_0^{\infty} \left(\xi^{h*} - d^*\right)^{3/2} (\kappa_g^{h*})^{-1/2} \Phi^h(\xi^{h*}, \kappa_g^{h*}) d\kappa_g^{h*} d\xi^{h*}. \tag{4.29}$$

4.3.4 Bush, Gibson and Thomas (BGT) Model

Bush et al. [14] developed the original BGT model based on a PDF in the function of the asperity height, ξ^h, and the semi-major and semi-minor radius of the bearing area of the asperity. In order to have the consistent formulations with the previous statistical models, the following BGT model utilizes the PDF in Eq. (2.39) along with the Hertzian elliptical contact model proposed in Eqs. (4.6) and (4.7):

$$\begin{aligned}
A^*(d^*) =& \eta^h \int_{d^*}^{\infty} \int_0^{\kappa_2^{h*}} \int_0^{\infty} A_i(\xi^h - d, \kappa_1^h, \kappa_2^h) \Phi^h(\xi^{h*}, \kappa_1^{h*}, \kappa_2^{h*}) d\kappa_2^{h*} d\kappa_1^{h*} d\xi^{h*}, \\
\bar{p}(d^*) =& \eta^h \int_{d^*}^{\infty} \int_0^{\kappa_2^{h*}} \int_0^{\infty} P_i(\xi^h - d, \kappa_1^h, \kappa_2^h) \Phi^h(\xi^{h*}, \kappa_1^{h*}, \kappa_2^{h*}) d\kappa_2^{h*} d\kappa_1^{h*} d\xi^{h*},
\end{aligned}$$

where $\kappa_1^{h*} \leq \kappa_2^{h*}$.

Replacing A_i, P_i and η^h in the above equations by Eqs. (4.6), (4.7) and (2.43) into the above equations, the final forms of an equivalent BGT model are obtained:

$$A^*(d^*) = \frac{1}{6\sqrt{3}} \sqrt{\alpha^h} \int_{d^*}^{\infty} \int_0^{\kappa_2^{h*}} \int_0^{\infty} \left(\xi^{h*} - d^*\right) \left(\kappa_1^{h*} \kappa_2^{h*}\right)^{-1/2} F_1^2(e)/F_2(e) \Phi^h(\xi^{h*}, \kappa_1^{h*}, \kappa_2^{h*}) d\kappa_2^{h*} d\kappa_1^{h*} d\xi^{h*}, \tag{4.30}$$

$$\begin{aligned}
\bar{p}^*(d^*) =& \frac{2\sqrt{2}}{9\sqrt{3}\pi} (\alpha^h)^{3/4} \times \\
& \int_{d^*}^{\infty} \int_0^{\kappa_2^{h*}} \int_0^{\infty} \left(\xi^{h*} - d^*\right)^{3/2} \left(\kappa_1^{h*} \kappa_2^{h*}\right)^{-1/4} F_2^{-3/2}(e) \Phi^h(\xi^{h*}, \kappa_1^{h*}, \kappa_2^{h*}) d\kappa_2^{h*} d\kappa_1^{h*} d\xi^{h*}.
\end{aligned} \tag{4.31}$$

where e can be determined by the fit shown in Eq. (4.11).

4.3.5 Asymptotic BGT Model when d^* is Large

An important asymptotic relation between A^* and $\bar{p}^*$, as well as d^* and $\bar{p}^*$, was originally obtained by Bush et al. [13, 14] when d^* is large:

$$A^* = \frac{1}{4}\mathrm{erfc}\left(\frac{d^*}{\sqrt{2}}\right), \tag{4.32}$$

$$\bar{p} = E^* \frac{\sqrt{m_2^h}}{2\sqrt{2}\pi}\frac{1}{d^*}\exp\left(-\frac{d^{*2}}{2}\right). \tag{4.33}$$

According to the asymptotic expansion of erfc(x) [13]:

$$\mathrm{erfc}(x) = \frac{\exp(-x^2)}{x\sqrt{\pi}}\sum_{n=0}^{\infty}(-1)^n\frac{(2n-1)!!}{(2x^2)^n},$$

where $(2n-1)!!$ is the double factorial. For a very large dimensionless separation, d^*, Eq. (4.33) becomes

$$\bar{p} = \frac{E^*\sqrt{m_2^h}}{4\sqrt{\pi}}\mathrm{erfc}\left(\frac{d^*}{\sqrt{2}}\right).$$

Substituting the above identity into Eq. (2.53), we have

$$\bar{p}^* = \frac{1}{2\sqrt{2}\sqrt{\pi}}\mathrm{erfc}\left(\frac{d^*}{\sqrt{2}}\right). \tag{4.34}$$

An alternative derivation of the asymptotic BGT model can follow the so-called "GW modified" model proposed by Carbone [13]. GW modified model is revisited in Chapter 4 to derive the asymptotic relations between $\bar{A}^*$ and $\bar{p}^*$, as well as $\bar{g}^*$ and $\bar{p}^*$, at the nearly complete contact stage.

Combining the asymptotic relations, Eqs. (4.32) and (4.34), we have the most important form of the asymptotic BGT model

$$A^* = \sqrt{\frac{\pi}{2}}\bar{p}^*, \tag{4.35}$$

which implies a linear relation between A^* and $\bar{p}^*$ which is independent of the roughness when d^* is very large.

4.4 Numerical Results

In this section, the numerical results of the statistical models, namely, (i) the GW model, (ii) the Nayak-Bush model, (iii) the Greenwood model and (iv) the BGT model are compared with each others. Except for the adapted GW model, the other statistical models involve high-dimensional integration, especially the BGT model. The Gauss quadrature [15], commonly used in the numerical integration in the FEM/BEM, is applied. The line, area and volume integrals applied to the statistical models are briefly discussed below:

Line integral In the adapted GW model and the asymptotic BGT model, the line integrals in A^* and $\bar{p}^*$ have the common form as follows:

$$\int_{d^*}^{\infty} f(\xi^{h*}) d\xi^{h*}.$$

Using the change of variable: $x = 1/\xi^{h*}$, the integral with the finite limit is achieved:

$$\int_{0}^{1/d^*} \frac{1}{x^2} f(x) dx$$

The domain, $x \in [0, 1/d^*]$, is divided into N_x line elements and the integral within each element is achieved by using the Gauss quadrature with four integral points [15]:

$$\begin{aligned}\int_{x_1}^{x_2} f(x)dx =& \frac{x_2 - x_1}{2} \int_{-1}^{1} f\left(\frac{x_2 - x_1}{2} x + \frac{x_2 + x_1}{2}\right) dx, \\ =& \frac{x_2 - x_1}{2} \sum_{i=1}^{4} w_i f\left(\frac{x_2 - x_1}{2} x_i + \frac{x_2 + x_1}{2}\right)\end{aligned} \tag{4.36}$$

where the Gaussian quadrature abscissae and weight can be found in [15].

Double integral In the Nayak-Bush model and the Greenwood model, the double integrals in A^* and $\bar{p}^*$ have the common form as follows:

$$\int_{d^*}^{\infty} \int_{0}^{\infty} f(\xi^{h*}, \kappa) d\kappa d\xi^{h*},$$

where κ can be either κ_m^{h*} or κ_g^{h*}. Using the change of variables: $x = 1/\xi^{h*}$ and $y = \exp(-\kappa)$, the integral with the finite limit is achieved:

$$\int_0^{1/d^*} \int_0^1 \frac{1}{x^2 y} f(x,y) dy dx.$$

The domain, $(x,y) \in [0, 1/d^*] \times [0,1]$, is divided into $N_x \times N_y$ rectangular elements. The double integral in each rectangular element is calculated by using Gauss quadrature in y direction first and then x direction:

$$\begin{aligned}\int_{x_1}^{x_2} \int_{y_1}^{y_2} f(x,y) dy dx =& \frac{(x_2 - x_1)(y_2 - y_1)}{4} \sum_{i=1}^{4} \sum_{j=1}^{4} \\ & w_i w_j f\left(\frac{x_2 - x_1}{2} x_i + \frac{x_2 + x_1}{2}, \frac{y_2 - y_1}{2} y_j + \frac{y_2 + y_1}{2} \right). \end{aligned} \tag{4.37}$$

Volume integral In the BGT model, the volume integrals in A^* and $\bar{p}^*$ have the common form as follows:

$$\int_{d^*}^{\infty} \int_0^{\kappa_2^{h*}} \int_0^{\infty} f(\xi^{h*}, \kappa_1^{h*}, \kappa_2^{h*}) d\kappa_2^{h*} d\kappa_1^{h*} d\xi^{h*},$$

Using the change of variables: $x = 1/\xi^{h*}$, $y = \kappa_1^{h*}/\kappa_2^{h*}$ and $z = \exp(-\kappa_2^{h*})$, the inetgral with the finite limit is achieved:

$$\int_0^{1/d^*} \int_0^1 \int_0^1 \frac{-\ln(z)}{x^2 z} f(x,y,z) dz dy dx.$$

The domain, $(x,y,z) \in [0, 1/d^*] \times [0,1] \times [0,1]$, is divided into $N_x \times N_y \times N_z$ brick elements. The volume integral in each rectangular element is calculated as:

$$\begin{aligned}\int_{x_1}^{x_2} \int_{y_1}^{y_2} \int_{z_1}^{z_2} f(x,y,z) dz dy dx = & \frac{(x_2 - x_1)(y_2 - y_1)(z_2 - z_1)}{8} \sum_{i=1}^{4} \sum_{j=1}^{4} \sum_{k=1}^{4} \\ w_i w_j w_k f\left(\frac{x_2 - x_1}{2} x_i + \frac{x_2 + x_1}{2}, \frac{y_2 - y_1}{2} y_j + \frac{y_2 + y_1}{2}, \frac{z_2 - z_1}{2} z_k + \frac{z_2 + z_1}{2} \right). \end{aligned} \tag{4.38}$$

To illustrate the validity of the numerical results solved by the Gauss quadrature proposed above, the numerical results of (1) the Nayak-Bush model, (2) the Greenwood model and (3) the BGT model are compared with that reported by Carbone and Bottiglione [16] in Table. 4.1 and Table. 4.2. In the adapted GW model: $N_x = 1000$. In the Nayak-Bush model and the Greenwood model: $N_x = 1000$ and $N_y = 1000$. In the BGT model: $N_x = 50$, $N_y = 50$ and $N_z = 50$. An excellent agreement is found except for one possible typo in Carbone and Bottiglione's results (see $d^* = 1.5$ in the column of BGT model).

Table 4.1: The values of A^* and $\sqrt{\pi/2}\,\bar{p}^*$ associated with the dimensionless surface separation d^* determined by the BGT and the Greenwood model. Note that $\bar{p}/(E^*\sqrt{m_2^h/\pi})$ used in [16] is exactly $\sqrt{\pi/2}\,\bar{p}^*$. The mismatch is highlighted in red and one obvious difference could be a typo in [16].

d^*	BGT Model				The Greenwood Model			
	A^*		$\sqrt{\pi/2}\,\bar{p}^*$		A^*		$\sqrt{\pi/2}\,\bar{p}^*$	
	Dissertation	[16]	Dissertation	[16]	Dissertation	[16]	Dissertation	[16]
$\alpha^h = 2$								
0	1.644×10^{-1}	1.644×10^{-1}	2.270×10^{-1}	2.270×10^{-1}	1.674×10^{-1}	1.674×10^{-1}	2.218×10^{-1}	2.218×10^{-1}
0.5	1.080×10^{-1}	1.080×10^{-1}	1.368×10^{-1}	1.368×10^{-1}	1.098×10^{-1}	1.098×10^{-1}	1.339×10^{-1}	1.339×10^{-1}
1	6.039×10^{-2}	6.039×10^{-2}	7.102×10^{-2}	7.102×10^{-2}	6.129×10^{-2}	6.129×10^{-2}	6.967×10^{-2}	6.967×10^{-2}
1.5	2.750×10^{-2}	2.750×10^{-2}	3.060×10^{-2}	3.600×10^{-2}	2.785×10^{-2}	2.785×10^{-2}	3.010×10^{-2}	3.010×10^{-2}
2	9.940×10^{-3}	9.940×10^{-3}	1.066×10^{-2}	1.066×10^{-2}	1.004×10^{-2}	1.004×10^{-3}	1.052×10^{-2}	1.052×10^{-2}
2.5	2.824×10^{-3}	2.825×10^{-3}	2.962×10^{-3}	2.962×10^{-3}	2.848×10^{-3}	2.848×10^{-3}	2.931×10^{-3}	2.931×10^{-3}
3.0	6.301×10^{-4}	6.301×10^{-4}	6.519×10^{-4}	6.519×10^{-4}	6.341×10^{-4}	6.341×10^{-4}	6.463×10^{-4}	6.463×10^{-4}
$\alpha^h = 10$								
0	2.040×10^{-1}	2.040×10^{-1}	3.680×10^{-1}	3.680×10^{-1}	2.079×10^{-1}	2.089×10^{-1}	3.588×10^{-1}	3.588×10^{-1}
0.5	1.174×10^{-1}	1.174×10^{-1}	1.950×10^{-1}	1.950×10^{-1}	1.195×10^{-1}	1.195×10^{-1}	1.902×10^{-1}	1.902×10^{-1}
1	5.809×10^{-2}	5.809×10^{-2}	8.940×10^{-2}	8.940×10^{-2}	5.912×10^{-2}	5.912×10^{-2}	8.730×10^{-2}	8.730×10^{-2}
1.5	2.415×10^{-2}	2.415×10^{-2}	3.471×10^{-2}	3.471×10^{-2}	2.456×10^{-2}	2.456×10^{-2}	3.393×10^{-2}	3.393×10^{-2}
2	8.269×10^{-3}	8.269×10^{-3}	1.120×10^{-2}	1.120×10^{-2}	8.403×10^{-2}	8.403×10^{-3}	1.096×10^{-2}	1.096×10^{-2}
2.5	2.297×10^{-3}	2.297×10^{-3}	2.956×10^{-3}	2.956×10^{-3}	2.333×10^{-3}	2.333×10^{-3}	2.896×10^{-3}	2.896×10^{-3}
3.0	5.120×10^{-4}	5.120×10^{-4}	6.308×10^{-4}	6.308×10^{-4}	5.194×10^{-4}	5.194×10^{-4}	6.188×10^{-4}	6.188×10^{-4}

Table 4.2: The values of A^* and $\sqrt{\pi/2}\,\bar{p}^*$ associated with the dimensionless surface separation d^* determined by the Nayak-Bush model.

d^*	$\alpha^h = 2$				$\alpha^h = 10$			
	A^*		$\sqrt{\pi/2}\,\bar{p}^*$		A^*		$\sqrt{\pi/2}\,\bar{p}^*$	
	Dissertation	[16]	Dissertation	[16]	Dissertation	[16]	Dissertation	[16]
0	1.449×10^{-1}	1.449×10^{-1}	2.089×10^{-1}	2.089×10^{-1}	1.785×10^{-1}	1.785×10^{-1}	3.361×10^{-1}	3.361×10^{-1}
0.5	9.593×10^{-2}	9.593×10^{-1}	1.266×10^{-1}	1.266×10^{-1}	1.030×10^{-1}	1.030×10^{-1}	1.785×10^{-1}	1.785×10^{-1}
1	5.425×10^{-2}	5.425×10^{-2}	6.624×10^{-2}	6.624×10^{-2}	5.121×10^{-2}	5.121×10^{-2}	8.209×10^{-2}	8.209×10^{-2}
1.5	2.507×10^{-2}	2.507×10^{-2}	2.881×10^{-2}	2.881×10^{-2}	2.139×10^{-2}	2.139×10^{-2}	3.198×10^{-2}	3.198×10^{-2}
2	9.210×10^{-3}	9.210×10^{-3}	1.014×10^{-2}	1.014×10^{-2}	7.367×10^{-3}	7.367×10^{-3}	1.036×10^{-2}	1.036×10^{-2}
2.5	2.657×10^{-3}	2.657×10^{-3}	2.844×10^{-3}	2.844×10^{-3}	2.059×10^{-3}	2.069×10^{-3}	2.745×10^{-3}	2.745×10^{-3}
3.0	6.003×10^{-4}	6.003×10^{-4}	6.307×10^{-4}	6.307×10^{-4}	4.617×10^{-4}	4.617×10^{-4}	5.883×10^{-4}	5.883×10^{-4}

According to Section 4.3, the relation A^* to d^* (also $\bar{p}^*$ to d^*) only depends on α^h. Fig. 4.4 illustrates the relation of A^* to $\bar{p}^*$ determined by numerous statistical models where $\alpha^h = 2$ (Fig. 4.4(a)) and $\alpha^h = 10$ (Fig. 4.4(b)) with $d^* \in [0, 3]$. When $\alpha^h = 2$, the relations predicted by all the statistical models (except for the adapted GW model) are almost identical ($A^* <$

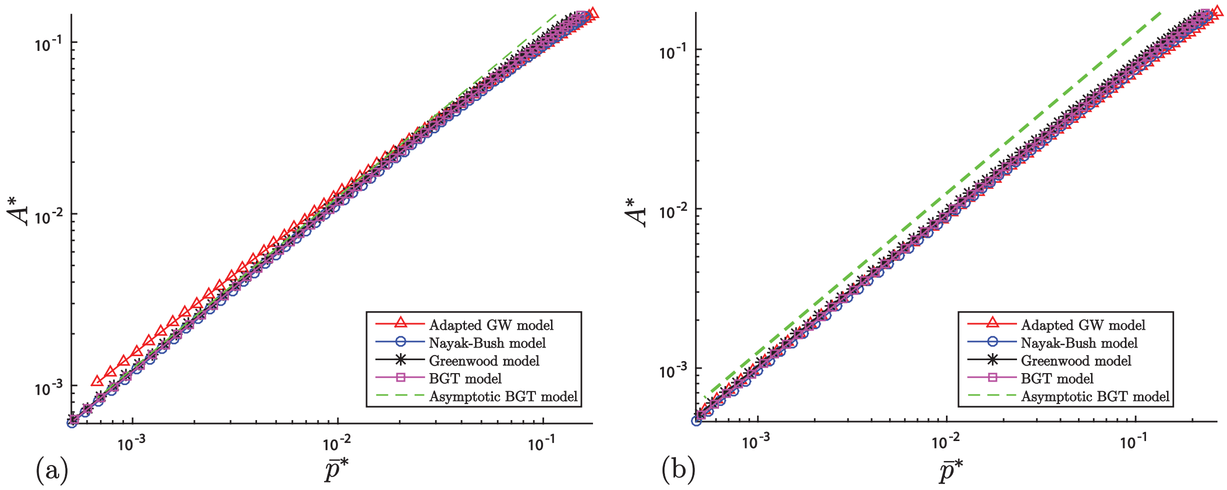

Figure 4.4: Plots of A^* vs. $\bar{p}^*$ associated with (a) $\alpha^h = 2$ and (b) $\alpha^h = 10$.

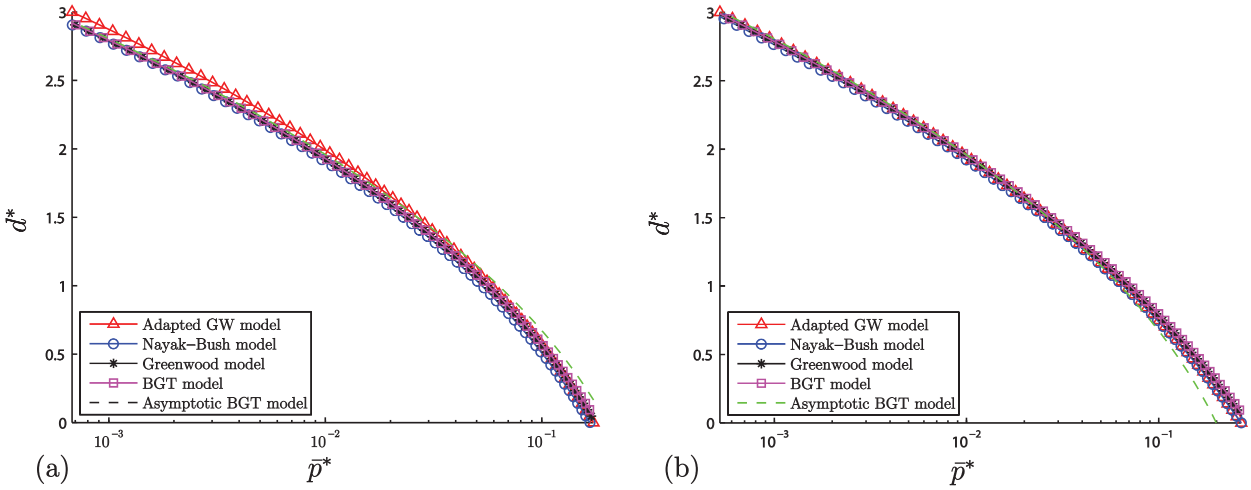

Figure 4.5: Plots of d^* vs. $\bar{p}^*$ associated with (a) $\alpha^h = 2$ and (b) $\alpha^h = 10$.

0.02). When $\alpha^h = 10$, all the statistical models obviously deviate from the asymptotic BGT model. The corresponding relations of d^* to $\bar{p}^*$ are shown in Fig. 4.5. Good agreement between the asymptotic BGT model and the rest of the statistical models can be observed, especially at higher range of $\bar{p}^*$. The slope of A^* vs. $\bar{p}^*$ curve, $\kappa = dA^*/d\bar{p}^*$, is plotted against $\bar{p}^*$ in Fig. 4.6. When $\alpha^h = 2$, all the statistical models, except for the adapted GW model, are gradually approaching the limit predicted by the asymptotic BGT model. The mismatch of the slope of the adapted GW model is also reflected in Fig. 4.4(a). When $\alpha^h = 10$, all the statistical models have the tendency of deviating from the asymptotic limit, see Fig. 4.4(b). The overall value of κ is decreased as α^h is increased. According to Yastrebov et al., [17, 18], approaching the asymptotic limit is a very slow procedure where $d^* \to \infty$.

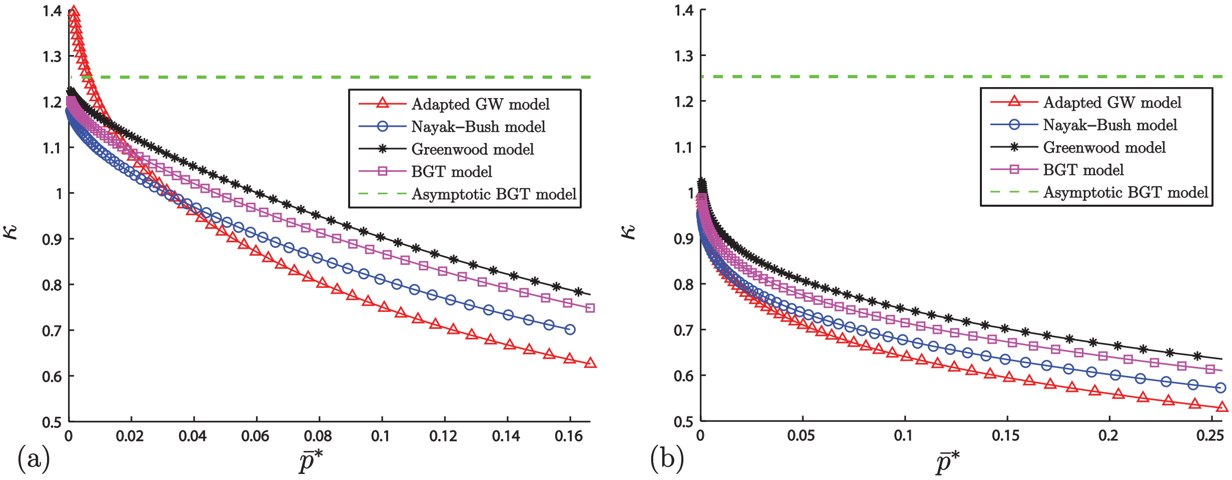

Figure 4.6: Plots of κ vs. $\bar{p}^*$ associated with (a) $\alpha^h = 2$ and (b) $\alpha^h = 10$.

4.5 Conclusions

In this chapter, a general frame of the statistical model of early contact is briefly introduced in the beginning. The average contact pressure is so small that the rough surface contact problem can be decomposed into numerous asperity normal contact problems. The Hertzian elliptical contact model and two Hertzian mildly elliptical contact models are introduced as the asperity contact models. The agreement between the mildly elliptical contact model and the elliptical model is deteriorated as the curvature ratio κ_2^h/κ_1^h increases. After combining the asperity contact models with the appropriate PDFs, four statistical models, namely, the adapted GW model, the Nayak-Bush model, the Greenwood model and the BGT model, are systematically introduced. Unlike the statistical models introduced in past literatures, the relation, A^* vs. d^*, as well as the dimensionless $\bar{p}^*$ vs. d^*, of all statistical models are found to be only dependent on the bandwidth parameter, α^h. The line, area and volume integrals involved in the statistical models are solved by the Gauss quadrature. The accuracy of the numerical integrals is confirmed by the comparison with the data reported by Carbone and Bottiglione [13].

References

[1] Greenwood, J.A. and Williamson, J.B.P., 1966. Contact of nominally flat surfaces. Proceedings of the Royal Society of London A: Mathematical, Physical and Engineering Sciences, **295**(1442), pp.300-319.

[2] Hertz, H., 1896. *Miscellaneous papers*. Macmillan.

[3] Johnson, K.L., 1987. *Contact Mechanics*. Cambridge University Press.

[4] Xu, Y., Rostami, A. and Jackson, R.L., 2015. Elastic contact between a geometrically anisotropic bisinusoidal surface and a rigid base. ASME Journal of Tribology, **137**(2), p.021402.

[5] Greenwood, J.A., 2006. A simplified elliptic model of rough surface contact. Wear, **261**(2), pp.191-200.

[6] Bush, A.W., 1982, Contact mechanics, in: Thomas, T.R.(Ed), *Rough Surfaces*, First ed. Longman, London.

[7] Johnson, K.L., Kendall, K. and Roberts, A.D., Surface energy and the contact of elastic solids. Proc. R. Soc. London A., **324**(1558), pp.301-313.

[8] Maugis, D., 1992. Adhesion of spheres: the JKR-DMT transition using a Dugdale model. Journal of colloid and interface science, **150**(1), pp.243-269.

[9] Zhuravlev, V.A., 2007. On the question of theoretical justification of the Amontons-Coulomb law for friction of unlubricated surfaces. Proceedings of the Institution of Mechanical Engineers, Part J: Journal of Engineering Tribology, **221**(8), pp.893-898.

[10] McCool, J.I., 1986. Comparison of models for the contact of rough surfaces. Wear, **107**(1), pp.37-60.

[11] Nayak, P.R., 1971. Random process model of rough surfaces. ASME Journal of Lubrication Technology **93**, pp.398-407.

[12] Xu, Y., Jackson, R.L. and Marghitu, D.B., 2014. Statistical model of nearly complete elastic rough surface contact. International Journal of Solids and Structures, **51**(5), pp.1075-1088.

[13] Carbone, G., 2009. A slightly corrected Greenwood and Williamson model predicts asymptotic linearity between contact area and load. Journal of the Mechanics and Physics of Solids, **57**(7), pp.1093-1102.

[14] Bush, A.W., Gibson, R.D. and Thomas, T.R., 1975. The elastic contact of a rough surface. Wear, **35**(1), pp.87-111.

[15] Zienkiewicz, O.C., Taylor, R.L., and Zhu, J.Z., 2008, *The finite element method: its basis and fundamentals*, Sixth edition, Elsevier, Singapore.

[16] Carbone, G. and Bottiglione, F., 2008. Asperity contact theories: Do they predict linearity between contact area and load?. Journal of the Mechanics and Physics of Solids, **56**(8), pp.2555-2572.

[17] Yastrebov, V.A., Anciaux, G. and Molinari, J.F., 2012, Contact between representative rough surfaces. Physical Review E, **86**(3), p.035601.

[18] Yastrebov, V.A., Anciaux, G. and Molinari, J.F., 2015. From infinitesimal to full contact between rough surfaces: evolution of the contact area. International Journal of Solids and Structures, **52**, pp.83-102.

Chapter 5

Statistical Models of Nearly Complete Contact

In Chapter 4, the statistical models of early contact in the past literatures are studied systematically. Unlike Chapter 4, the stage of the nearly complete contact where the real area of contact is nearly the same as the nominal contact is explored in the current chapter. At this stage, the non-contact area consists of numerous non-contact regions of elliptical/circular shape. Each of the non-contact region can be visualized as an elliptical/circular (half) “cracks”. This hypothesis is supported by the direct observation of the contact area distribution, Fig. 3.9(d), and the interfacial distribution, Fig. 3.10(d).

5.1 Introduction

The statistical model of early contact is extensively studied ever since the pioneering work of Zhuravlev [1] and Greenwood and Williamson [2]. Up till recently, Xu et al. [3] proposed a general statistical model which can be applied to another extreme of the rough surface contact, i.e., the *nearly complete contact*. At this stage, the real area of contact is almost identical to the nominal contact area, i.e., $A^* \to 1$. On the contact interface, the non-contact area is composed of numerous no-contact regions which are visualized as “islands” surrounded by the “sea” of contact area, see Fig. 5.1. From Figs. 3.9(d) and Fig. 3.10(d), it is expected that the non-contact regions are approximately elliptical and circular.

The contact pressure distribution, $p(x, y)$, at nearly complete contact within the contact area can be approximated by the contact pressure, $p_c(x, y)$, at complete contact where the entire rough boundary, $z = -h(x, y)$, is in contact with the rigid flat. In the complete contact, the

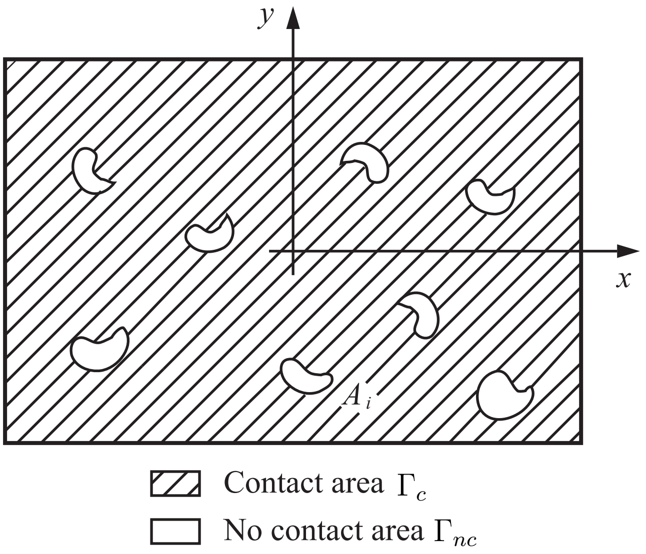

Figure 5.1: Schematic representation of the distributions of the contact area and the non-contact area within a finite rectangular region. Reprinted from International Journal of Solids and Structures, Xu, Y., Jackson, R.L., and Marghitu, D.B., Statistical model of nearly complete elastic rough surface contact, **51**, pp.1078, 2014, with permission from Elsevier.

normal displacement of the boundary is known as: $\bar{w}(x, y) = h(x, y) + C$ where C is the rigid body displacement due to the average pressure $\bar{p}$. Assuming that (i) the boundary $z = -h(x, y)$ is smooth up to the class C^1, i.e., the derivatives $\partial h/\partial x$ and $\partial h/\partial y$ exist and are continuous everywhere, and (ii) the local slopes are several order of magnitude smaller than the unity, then the rough half-space can be approximated as a half-space. Therefore, the contact pressure, $p_c(x, y)$, at complete contact can be formulated by Eq. (2.47) [20, 21]. Since the contact is adhesionless, $\bar{p}$ of the complete contact should satisfy[1]:

$$\bar{p} \geq |\min(p_c)|.$$

Fig. 5.2(a) schematically illustrates the deformed contact interface, as well as the contact pressure distribution, $p(x, y)$, at the nearly complete contact when $(\bar{p} - |\min(p_c)|) \to 0^-$. Fig.

---

[1] Many analytical models raised up the concern about whether a complete contact (perfect seal) can be achieved bewteen the rough surfaces under a finite $\bar{p}$. A popular point of view is that $\bar{p}$ under complete contact is infinite (e.g., Manners [4]; Ciavarella et al. [5]; Persson [6]; Manners and Greenwood [7]; Jackson [8]). This unexpectedly high pressure may be caused by the idealization of the rough surface using various models (e.g., rough surfaces with exponential auto-correlation [4], Weierstrass-Mandelbrot function [5] and fractal surfaces with prescribed PSD [6–8]). A recent theoretical study by Kudish et al [9] has shown that a rough surface can be completely flattened under a finite $\bar{p}$ if it is smooth up to class C^2, i.e., the second order derivatives of $h(x, y)$ exist and continuous everywhere.

5.2(b) shows the complete contact under the same average pressure $\bar{p}$ and the contact pressure would be

$$p_1(x, y) = \bar{p} + p_c(x, y), \tag{5.1}$$

if the complete contact is achieved under sufficient adhesion, see Fig. 5.2(b). Two contact pressure distributions, namely, $p(x, y)$ and $p_1(x, y)$, are exactly the same over the entire interface except at the vicinity of the non-contact regions. In order to achieve the traction-free boundary condition inside the non-contact regions in Fig. 5.2(a), the pressurized crack problem shown in Fig. 5.2(c) is superposed to the complete contact problem in Fig. 5.2(b). In the crack problem, numerous flat cracks, which are pressurized by the normal traction $p_2(x, y) = -p_1(x, y)$, are embedded inside an infinite body on $z = 0$ plane. Due to the symmetry of the crack problem, only the upper half ($z > 0$) is illustrated in Fig. 5.2(c).

Based on the decomposition of the contact problem shown in Fig. 5.2, it is clear that the distribution of the non-contact regions is correlated with that of the tensile portions of $p_1(x, y)$ and this correlation is clearly illustrated in Fig. 5.3(a). recalling the definition of "pressure surface" in the beginning of Section 2.6, the above correlation can be rephrased as follows: the distribution of the non-contact regions can be correlated with that of the asperities of the "pressure surface" which are higher than $\bar{p}$, see Fig. 5.3(b).

According to the definition of the asperity in Section. 2.4, the geometry of a parabolic asperity can be uniquely represented by a vector of random variables: $(\xi^p, \kappa_1^p, \kappa_2^p)$

If the size of non-contact region (crack size) $A_i(\xi^p, \kappa_1^p, \kappa_2^p)$ and the trapped volume $V_i(\xi^p, \kappa_1^p, \kappa_2^p)$ are known, then the non-contact ratio $1 - A^*$ and the average interfacial gap $\bar{g}$ under a certain $\bar{p}$ can be obtained by following the statistical models of early contact (see Chapter 4):

$$1 - A^*(\bar{p}) = \eta^p \int_{\bar{p}}^{\infty} \int_0^{\kappa_2^p} \int_0^{\infty} A_i(\xi^p, \kappa_1^p, \kappa_2^p) \Phi^p(\xi^p, \kappa_1^p, \kappa_2^p) d\kappa_2^p d\kappa_1^p d\xi^p. \tag{5.2}$$

$$\bar{g}(\bar{p}) = \eta^p \int_{\bar{p}}^{\infty} \int_0^{\kappa_2^p} \int_0^{\infty} V_i(\xi^p, \kappa_1^p, \kappa_2^p) \Phi^p(\xi^p, \kappa_1^p, \kappa_2^p) d\kappa_2^p d\kappa_1^p d\xi^p. \tag{5.3}$$

The integrals in Eqs. (5.2) and (5.3) represent the ensemble average of the area and the trapped volume of a single non-contact region, respectively. The validity of Eqs. (5.2) and (5.3) implies

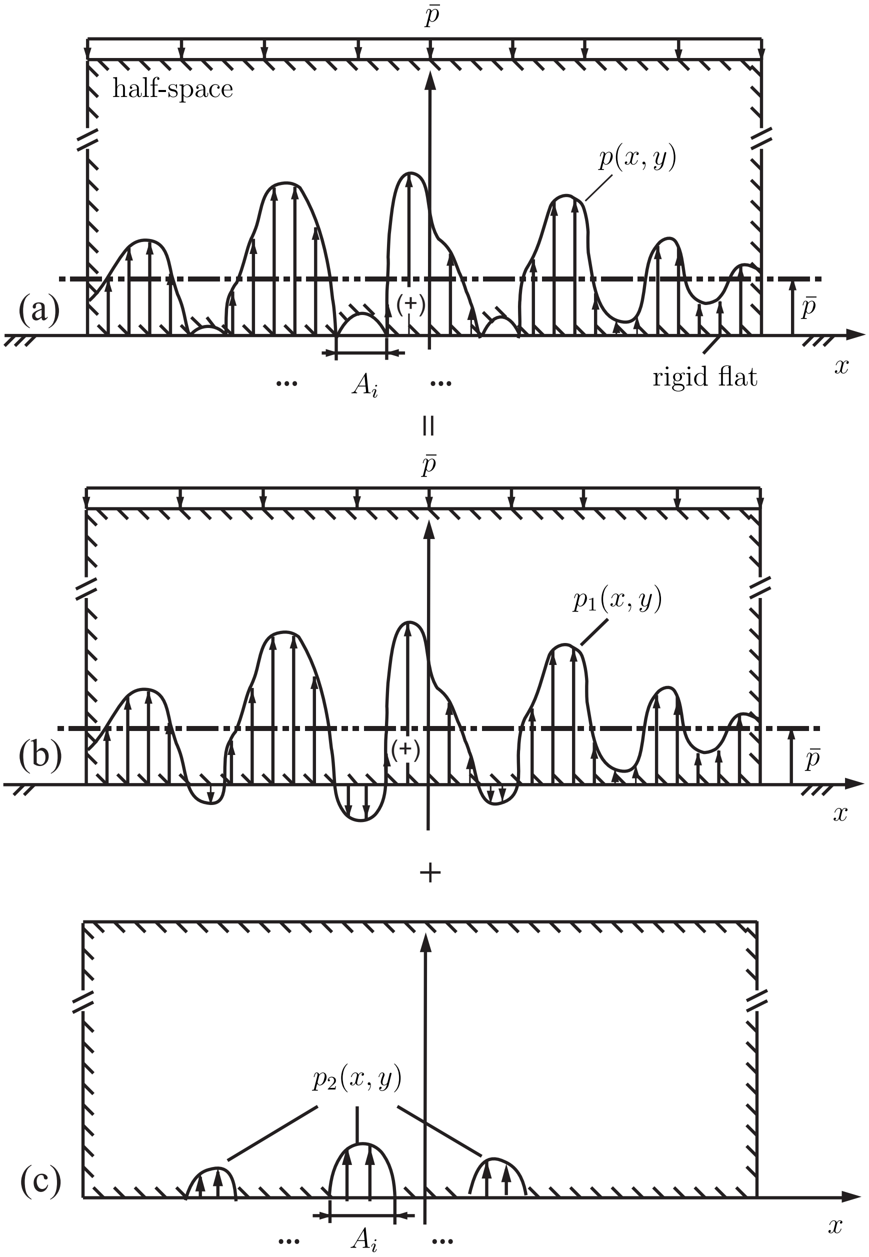

Figure 5.2: Decomposition of the (a) nearly complete contact into (b) a complete contact and (c) pressurized cracks problem. Adapted from International Journal of Solids and Structures, Xu, Y., Jackson, R.L., and Marghitu, D.B., Statistical model of nearly complete elastic rough surface contact, **51**, pp. 1078, 2014, with permission from Elsevier.

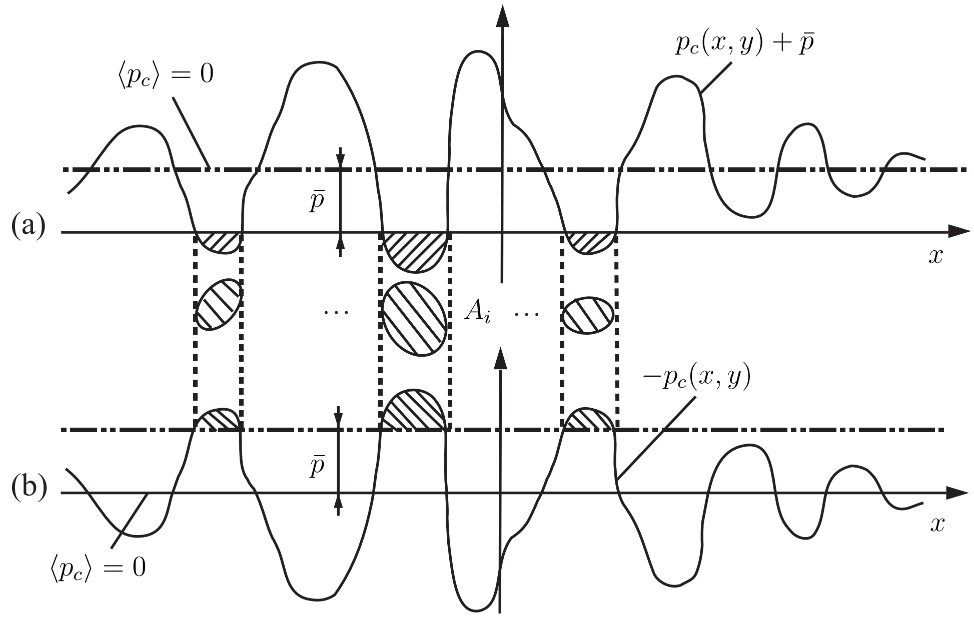

Figure 5.3: (a) Correlation between the distributions of the asperity of $p_c(x,y)$ and the crack; (b) Correlation between the distribution of the asperity of $-p_c(x,y)$ and the crack. Reprinted from International Journal of Solids and Structures, Xu, Y., Jackson, R.L., and Marghitu, D.B., Statistical model of nearly complete elastic rough surface contact, **51**, pp. 1078, 2014, with permission from Elsevier.

that the neighboring non-contact regions are distantly located so that each non-contact region (pressurized crack) can be studied individually and their results can be superposed.

The statistical characterization of the "pressure surface" has already been addressed in Section 2.6. The pressurized crack problem is studied in Section 5.2. The final formulation of various statistical models associated with different joint PDFs and crack models are given in Section 5.3. The Persson model and its relation to the statistical models of the nearly complete contact is discussed in detail in Section. 5.4. Numerical results of some selected cases solved by the statistical models and the Persson model are compared in Section 5.5.

5.2 Single Pressurized Crack Model

The decomposition of the contact problem at the vicinity of a single non-contact region is illustrated in Fig. 5.4. The contact pressure and the deformed interface at the vicinity of a non-contact region are shown in Fig. 5.4(a). In the complete contact (Fig. 5.4(b)), the vicinity of the non-contact region is subjected to $p_1(x,y)$. Similar to the geometry of the asperity of the rough surface discussed in Eq. (2.26), the geometry of the asperity of the "pressure surface"

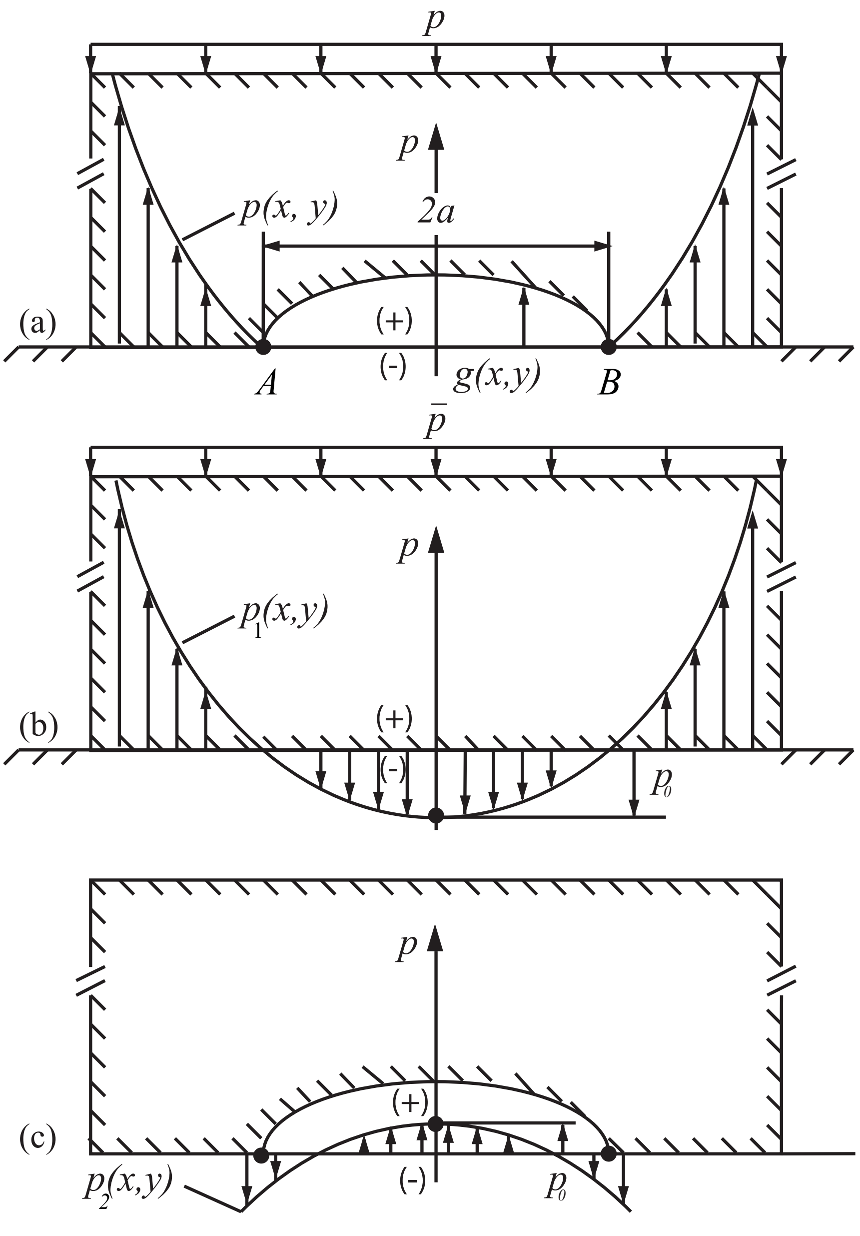

Figure 5.4: Schematic representation of the decomposition at the vicinity of the single non-contact region. The cross-section area is along the major axis. Adapted from International Journal of Solids and Structures, Xu, Y., Jackson, R.L., and Marghitu, D.B., Statistical model of nearly complete elastic rough surface contact, **51**, pp. 1078, 2014, with permission from Elsevier.

can also be formulated in the parabolic form:

$$p_1(x, y) = -p_0 + \frac{\kappa_1^p}{2}x^2 + \frac{\kappa_2^p}{2}y^2, \tag{5.4}$$

where (κ_1^p, κ_2^p) are two principle curvatures $\kappa_1^p < \kappa_2^p$. From Section 5.1, it is obvious that $p_0 = \xi^p - \bar{p}$. To enable the stress-free boundary condition within the elliptical non-contact region in Fig. 5.4(a), we need to superpose a pressurized elliptical crack problem, which is shown in Fig. 5.4(c). The crack is embedded in an infinite space and lies on $z = 0$ plane with its center at the origin. The infinite space in Fig. 5.4(c) is stress-free at far end. The upper and lower crack surface are subjected to the normal traction: $p_2(x, y) = -p_1(x, y)$ within the elliptical region Ω:

$$\Omega = \{(x, y, 0)|x = a\rho\cos(\phi), y = b\rho\sin(\phi), 0 \leq \rho < 1, 0 \leq \phi < 2\pi\}, \tag{5.5}$$

where

$$\rho = \sqrt{\left(\frac{x}{a}\right)^2 + \left(\frac{y}{b}\right)^2}.$$

a and b are the semi-major radius and semi-minor radius of the ellipse, see Fig. 5.5. Due to the symmetry of the problem about the plane $z = 0$, only the upper half of the crack is shown in Fig. 5.4(c). In Section 5.2.1, the general pressurized elliptical problem is solved analytically.

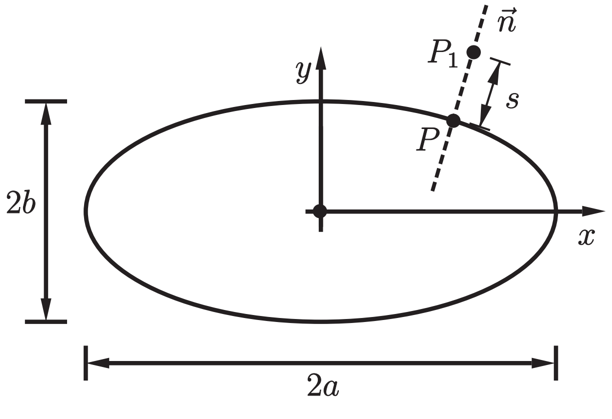

Figure 5.5: Schematic representation of a elliptical crack.

The crack area and the trapped volume inside the elliptical crack are derived in the closed-forms. To further simplify the solutions, two pressurized penny-shaped crack problems are proposed where the crack surfaces are subjected to the axisymmetric $p_2(r)$ with the mean and geometrical curvature κ_g^p and κ_m^p. This simplification is very similar to that used in the asperity contact discussed in Section 4.2.

5.2.1 Elliptical Crack

The pressurized elliptical crack problems under various forms of $p_2(x, y)$ have been solved by many researchers (Green and Sneddon [10], Kassir and Sih [11], Shah and Kobayashi [12], Sneddon [13], Martin [14], Atroshchenko [15], etc). In this section, the methodology and the results of Martin [14] are briefly introduced.

Due to the asymmetry of the elliptical crack and the normal traction, the mode-I stress intensity factor (SIF) is varied with ϕ on the crack front, i.e., $K_I(\phi)$. Let $P = (a\cos(\phi), b\sin(\phi), 0)$ and $P_1 = (a\rho\cos(\phi), b\rho\sin(\phi), 0)$ be the points on the crack front and outside ($\rho > 1$) the crack region Ω, respectively, see Fig. 5.5. Assuming P_1 lies on the normal vector of the ellipse passing the point P and the distance between P_1 and P is s, then the mode-I SIF[2] can be defined as [13, 14]:

$$\begin{aligned} K_I(\phi) &= \lim_{s\to 0^+} \sqrt{2\pi s}\sigma_{zz}(a\rho\cos(\phi), b\rho\sin(\phi), 0), \\ &=(ab)^{1/2}\left[a^2\sin^2(\phi) + b^2\cos^2(\phi)\right]^{-1/4} \lim_{\rho\to 1^+}\left[(\rho^2-1)^{1/2}\sigma_{zz}(a\rho\cos(\phi), b\rho\sin(\phi), 0)\right], \end{aligned} \tag{5.6}$$

where σ_{zz} is the normal stress components perpendicular to xy plane.

Using the polynomial form proposed by Krenk [16], the boundary conditions: $\sigma_{zz}(x, y, 0) = -p(x, y)$ inside Ω ($\rho < 1$) and $w(x, y, 0) = 0$ outside Ω ($\rho > 1$) are automatically satisfied. Then, $\sigma_{zz}(x, y, 0)$ outside Ω ($\rho > 1$) and the upper/lower crack opening displacement $g(x, y) = w(x, y, 0)$ inside Ω ($\rho < 1$) can be solved in an inverse manner.

The mode-I SIF due to the traction $p(x, y)$ is then (see Eqs. (7.2) and (7.10) in [14])

$$K_I(\phi) = \sqrt{\pi}\left[a^2\sin^2(\phi) + b^2\cos^2(\phi)\right]^{1/4}\left\{\frac{p_0}{\mathbf{E}(e)}\left(\frac{a}{b}\right)^{1/2} - \frac{8}{15}\left(\frac{b}{a}\right)^{1/2}\left[B_0(e) + B_2(e)\cos(2\phi)\right]\right\}, \tag{5.7}$$

---

[2] Eq. (5.6) is different from the definition in [14] by a multiplier of $\sqrt{\pi}$.

where e is the eccentricity of the elliptical crack:

$$e = \sqrt{1 - \left(\frac{b}{a}\right)^2}.$$

$\mathbf{E}(e)$ is the complete elliptical integral of the second kind. $B_0(e)$ and $B_2(e)$ are in the function of e only:

$$\begin{aligned} B_0(e) =& \frac{1}{8\Omega(e)} \left(\kappa_1^p a^2 + \kappa_2^p b^2\right) \left[3\Omega(e) + 2I_{00}^c(e) I_{22}^c(e)\right] / I_{00}^c(e) + \\ & \frac{1}{4} \left(\kappa_1^p a^2 - \kappa_2^p b^2\right) I_{02}^c(e), \qquad (5.8) \\ B_2(e) =& \frac{1}{8\Omega(e)} \left[\left(\kappa_1^p a^2 + \kappa_2^p b^2\right) I_{02}^C + \left(\kappa_1^p a^2 - \kappa_2^p b^2\right) I_{00}^c(e)\right], \qquad (5.9) \end{aligned}$$

where

$$\Omega = I_{00}^c(e) I_{22}^c(e) - I_{02}^c(e) I_{20}^c(e).$$

$I_{00}^c(e)$, $I_{22}^c(e)$, $I_{02}^c(e)$ and $I_{20}^c(e)$ are the functions of eccentricity, e, only [14]:

$$I_{00}^c(e) = 2\mathbf{E}(e), \tag{5.10}$$

$$I_{02}^c(e) = I_{20}^c(e) = \begin{cases} \frac{2}{3e^2} \left[(2 - e^2)\mathbf{E}(e) - 2(1 - e^2)\mathbf{K}(e)\right] & \text{where} \quad e \in (0, 1], \\ 0 \quad \text{where} \quad e = 0. \end{cases} \tag{5.11}$$

$$I_{22}^c(e) = \begin{cases} \frac{1}{15e^4} \left[(14e^4 + 16e^2 - 16)\mathbf{E}(e) + 8(2 - e^2)(1 - e^2)\mathbf{K}(\mathbf{e})\right] & \text{where} \quad e \in (0, 1], \\ \frac{\pi}{2} \quad \text{where} \quad e = 0, \end{cases} \tag{5.12}$$

where $\mathbf{K}$ is the complete elliptical integral of the first kind.

Based on the statistical model of nearly complete contact discussed in Section. 5.1, the random variables ($p_0 = p - \bar{p}, \kappa_1^p, \kappa_2^p$) are known for each crack problem. The objective of this section is to determine the associated semi-minor radius b and semi-major radius a, as well as the crack area, A_i, and the trapped volume, V_i. For the penny-shaped crack, two types of boundary conditions are proposed by Johnson et al. [20], namely, (1) zero SIF: $K_I = 0$ and (2)

$g = 0,\ \partial g/\partial r = 0$ at the crack front. This is shown by Xu et al. [3,23] that these two boundary conditions result in the same crack radius. In the rest of the section, the zero SIF condition is adopted to solve the pressurized crack problem. In the Section 5.2.6, the later conditions are examined.

At the contact edges (crack fronts), the contact pressure decays to zero as long as no adhesive attraction and geometrical singularity exist. Thus, it is natural to expect that $K_I = 0$ regardless of ϕ. For a non-trivial solution of a and b, we have the following two relations:

$$B_2(e) = 0, \tag{5.13}$$

$$\frac{p_0}{\mathbf{E}(e)}\left(\frac{a}{b}\right)^{1/2} - \frac{8}{15}\left(\frac{b}{a}\right)^{1/2} B_0(e) = 0. \tag{5.14}$$

According to Eq. (5.13), the nonlinear relation of the κ_1^p/κ_2^p to e can be determined explicitly from Eqs. (5.9) and (5.13):

$$\frac{\kappa_1^p}{\kappa_2^p} = (1-e^2)\left[(2e^2-1)\mathbf{E}(e) + (1-e^2)\mathbf{K}(e)\right] / \left[(1+e^2)\mathbf{E}(e) - (1-e^2)\mathbf{K}(e)\right]. \tag{5.15}$$

It is interesting to notice that the eccentricity, e, of the elliptical crack depends only on the κ_1^p/κ_2^p. An empirical solution of e in the function of κ_1^p/κ_2^p can be obtained through the curve-fit:

$$\sqrt{1-e^2} = \exp\left[-0.00681 \times \log^2(\kappa_1^p/\kappa_2^p) + 0.3953 \times \log(\kappa_1^p/\kappa_2^p)\right]. \tag{5.16}$$

The good agreement between Eqs. (5.15) and (5.16) can be found when they are plotted as shown in Fig. 5.6.

According to Eq. (5.14), the area of the elliptical crack, $A = \pi ab$, can be determined as:

$$A_i(p_0, \kappa_1^p, \kappa_2^p) = 3\pi(\kappa_g^p)^{-1} p_0 F_1(e), \tag{5.17}$$

where

$$F_1(e) = 5\left[\frac{3}{2} + \frac{I_{00}^c(e) I_{22}^c(e)}{\Omega(e)} - I_{02}^c(e)\right]^{-1}\left[\sqrt{\kappa_1^p/\kappa_2^p} + \sqrt{\kappa_2^p/\kappa_1^p}(1-e^2)\right]^{-1}. \tag{5.18}$$

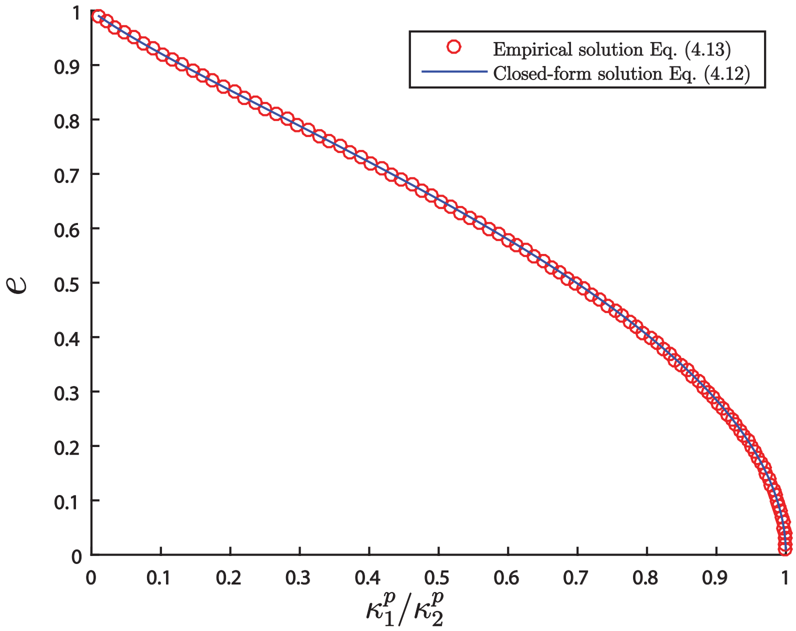

Figure 5.6: Plots of e vs. κ_1^p/κ_2^p by Eqs. (5.15) and (5.16).

Note that e can be determined by Eq. (5.15) or (5.16). A plot of $F_1(e)$ against e is shown in Fig. 5.7.

Additionally, the closed-form solution of the (upper) crack opening displacement[3] [14] is also available:

$$g(x,y) = g(\rho) = \frac{2b}{9\mathbf{E}(e)E^*}\left[9p_0 - \frac{1}{2}\left(\kappa_1^p a^2 + \kappa_2^p b^2\right)\left(1+2\rho^2\right)\right]\sqrt{1-\rho^2}. \tag{5.19}$$

The corresponding trapped volume V_i can be determined by

$$V_i = \int_0^b g(r/b)C(r)dr, \tag{5.20}$$

where $C(r)$ is the perimeter of the ellipse (r: semi-minor radius) concentric to the elliptical crack front:

$$C(r) = \frac{4r}{\sqrt{1-e^2}}\mathbf{E}(e). \tag{5.21}$$

---

[3] Martin [14] only gave the general form of $w(x,y,0^+)$. The final form of $w(x,y,0^+)$ due to the parabolic form of $p(x,y)$ was given by Martin [14].

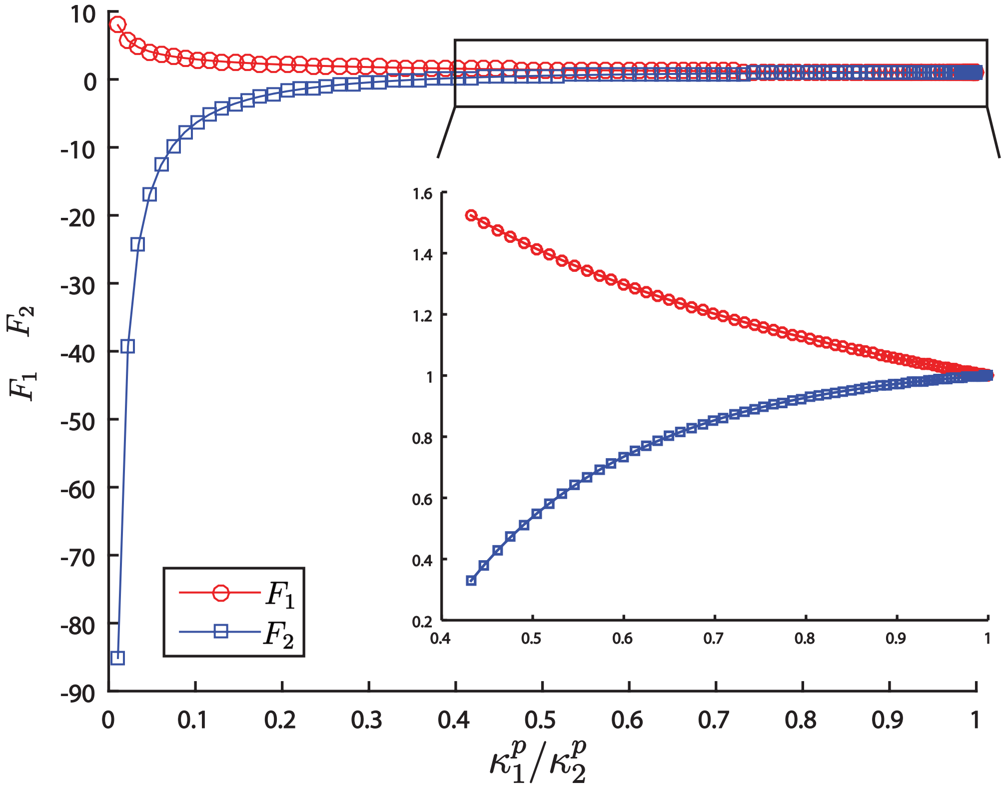

Figure 5.7: Plots of functions $F_1(e)$ and $F_2(e)$ vs. e

Substituting Eqs. (5.21) and (5.19) into Eq. (5.20) and integrating, we have

$$V_i = \frac{8ab^2}{3E^*}\left[p_0 - \frac{1}{10}\left(\kappa_1^p a^2 + \kappa_2^p b^2\right)\right]. \tag{5.22}$$

Substituting Eq. (5.17) into the above equation, we can obtain the final form of V_i:

$$V_i(p_0, \kappa_1^p, \kappa_2^p) = \frac{16\sqrt{3}}{5E^*}(\kappa_g^p)^{-3/2} p_0^{5/2} F_2(e), \tag{5.23}$$

where

$$F_2(e) = \frac{5}{2}(1-e^2)^{1/4} F_1(e)^{3/2}\left\{1 - \frac{3}{10}F_1(e)\left(1-e^2\right)^{-1/2}\left[\sqrt{\kappa_1^p/\kappa_2^p} + \sqrt{\kappa_2^p/\kappa_1^p}(1-e^2)\right]\right\}. \tag{5.24}$$

A plot of $F_2(e)$ can be found in Fig. 5.7. The discussion of $F_1(e)$ and $F_2(e)$ in Fig. 5.7 can be found in Section 5.2.6.

5.2.2 Penny-Shaped Crack

When $a \to b$, the elliptical crack is degraded to a penny-shaped crack. Due to the symmetry of the penny-shaped crack, the pressurized penny-shaped crack problem has been extensively studied (e.g., Sneddon [17], Barenblatt [18], Sneddon and Lowengrub [19]). Green's function can be used to calculate the mode-I SIF [3, 7, 18, 20]. Sneddon's solution [17] is available to calculate the (upper) crack opening displacement $w(x, y, 0^+)$. An alternative is to find the asymptotic behavior of the pressurized elliptical crack when $e \to 0^+$, i.e., $a \to b$. The asymptotic analysis is also served as a validation of the pressurized elliptical model. In the rest of this section, the latter method is used and the results are exactly the same as the Green's function used in Xu et al. [3].

Since $\mathbf{E}(0) = \mathbf{K}(0) = \pi/2$ as $e \to 0$, Eq. (5.15) is degraded to $\kappa_1^p = \kappa_2^p = \kappa^p$. Substituting $e = 0$ and $\kappa_1^p = \kappa_2^p = \kappa^p$ into Eq. (5.7), we can have

$$K_I = \frac{2\sqrt{b}}{\sqrt{\pi}} \left(p_0 - \frac{1}{3}\kappa^p b^2 \right), \tag{5.25}$$

which is the same as that formulated using the Green's function (see Eq. (13) in [3][4]).

Substituting $e = 0$ and $\kappa_1^p = \kappa_2^p = \kappa^p$ into Eq. (5.19), the (upper) crack opening displacement is

$$g(\rho) = \frac{4b}{9\pi E^*} \left(9p_0 - \kappa^p b^2 - 2\kappa^p b^2 \rho^2 \right) \sqrt{1 - \rho^2}, \tag{5.26}$$

which is the same as Eq. (B.1) in [3] based on the Sneddon's solution [17, 20].

As $e \to 0$, $F_1(0) \to 1$ and $F_2(0) \to 1$. According to Eqs. (5.17) and (5.23), the area of penny-shaped crack and the corresponding trapped volume of a penny-shaped crack are

$$A_i(p_0, \kappa^p) = 3\pi(\kappa^p)^{-1} p_0, \tag{5.27}$$

$$V_i(p_0, \kappa^p) = \frac{16\sqrt{3}}{5E^*} (\kappa^p)^{-3/2} p_0^{5/2}, \tag{5.28}$$

which are the same as Eq. (17) and Eq. (25) in [3], respectively.

---

[4] The curvature used in Eq. (13) in [3] is half of the corresponding curvature in Eq. (5.25).

5.2.3 Mildly Elliptical Crack (Geometric Curvature)

Comparing Eqs. (5.27) and (5.28) of the penny-shaped crack with Eqs. (5.17) and (5.23) of the elliptical one, we may find that $F_1(e)$ and $F_2(e)$ in Eqs. (5.17) and (5.23) are the only corrective terms when $\kappa_1^p < \kappa_2^p$. According to Fig. 5.7, $F_1(e)$ and $F_2(e)$ deviate from the unity as $\sqrt{\kappa_1^p/\kappa_2^p}$ is gradually decreased from unity. Following the approximation used in Section 4.2.3, the corresponding crack size and the trapped volume of a mildly elliptical crack can be approximated by:

$$A_i(p_0, \kappa_g^p) = 3\pi(\kappa_g^p)^{-1}p_0, \tag{5.29}$$

$$V_i(p_0, \kappa_g^p) = \frac{16\sqrt{3}}{5E^*}(\kappa_g^p)^{-3/2}p_0^{5/2}. \tag{5.30}$$

Note that Eq. (5.29) is the same as Eq. (16) in [3] and Eq. (5.30) is equivalent to Eq. (24) in [3] as long as $\kappa_1^p \to \kappa_2^p$. In [3], the solutions (e.g., the SIF, K_I, and the crack opening displacement, $g(r)$) of the penny-shaped crack are directly transformed to the solutions of the elliptical crack by replacing r with $\rho = \sqrt{x^2/a^2 + y^2/b^2}$. Consequently, Eqs. (16) and (24) in [3] are also an approximate solution only valid for the mildly elliptical crack.

5.2.4 Mildly Elliptical Crack (Mean Curvature)

For a Gaussian rough surface, Greenwood [22] showed that the hemi-spherical asperity ($\kappa_1^h = \kappa_1^h$) is nearly impossible to occur and two principle curvatures of nearly all asperities should be different. Since the "pressure surface" is Gaussian as long as the corresponding rough surface is Gaussian [3]. Therefore, nearly all the cracks are elliptical and are pressurized by the parabolic normal traction with different principle curvatures, $\kappa_1^p < \kappa_2^p$. Following the simplification applied to the Hertzian contact theory, a mildly elliptical crack model can be proposed based on the penny-shaped crack model where κ^p is replaced by the mean curvature: $\kappa_m^p = (\kappa_1^p + \kappa_2^p)/2$,

$$A_i(p_0, \kappa_m^p) = 3\pi(\kappa_m^p)^{-1}p_0, \tag{5.31}$$

$$V_i(p_0, \kappa_m^p) = \frac{16\sqrt{3}}{5E^*}(\kappa_m^p)^{-3/2}p_0^{5/2}. \tag{5.32}$$

5.2.5 Comparisons

The crack area and the trapped volume are normalized as $A_i\kappa_2^p/(\pi E^*)$ and $V_i(\kappa_2^p)^{3/2}/(E^*)^{3/2}$. The relation between the dimensionless A_i and V_i associated with different κ_1^p/κ_2^p are shown in Fig. 5.8. Some important observations are summarized below:

- As κ_1^p/κ_2^p is decreased, the elliptical and the mildly elliptical crack models start to deviate from the (nearly) penny-shaped crack model ($\kappa_1^p/\kappa_2^p = 1/1.2$) with different paces. The elliptical crack model deviates more aggressively than the mildly elliptical crack models.
- The mildly elliptical crack models are good approximations to the elliptical crack model only within a narrow range of $\kappa_1^p/\kappa_2^p \approx [1, 1.2]$. This can be explained by the stronger non-linearity, i.e., $V_i \approx O(A_i^{5/2})$. Recalling the Hertzian contact discussed in Section 4.2, Hertzian contact does not have such a strong non-linearity between A_i and P_i, i.e., $P_i \approx O(A_i^{3/2})$.
- Compared with the mildly elliptical crack with the mean curvature, the mildly elliptical crack with the geometrical curvature is a relatively better approximation to the elliptical crack model.

5.2.6 Remarks

In Section 5.2, the crack area, as well as the trapped volume, are determined based on the fact that the mode-I SIF, $K_I(\phi)$, should be zero everywhere on the crack front. In this remark, we shall focus on another boundary condition mentioned earlier. Johnson et al. [20] pointed out that the crack should be closed smoothly on the crack front i.e., $g(\rho = 1) = 0$ and $\partial g/\partial\rho|_{\rho-1} = 0$. The first condition ($g(\rho = 1) = 0$) is automatically satisfied according to Eq. (5.19). In order to have $\partial g/\partial\rho|_{\rho=1} = 0$, the terms in side the square bracket in front of the singular term: $(1-\rho^2)^{-1/2}$ in Eq. (5.19) should be vanishing. After some manipulations, an expression of the crack area A similar to Eq. (5.17) is obtained:

$$A = 3\pi(\kappa_g^p)^{-1}p_0F_3(e), \tag{5.33}$$

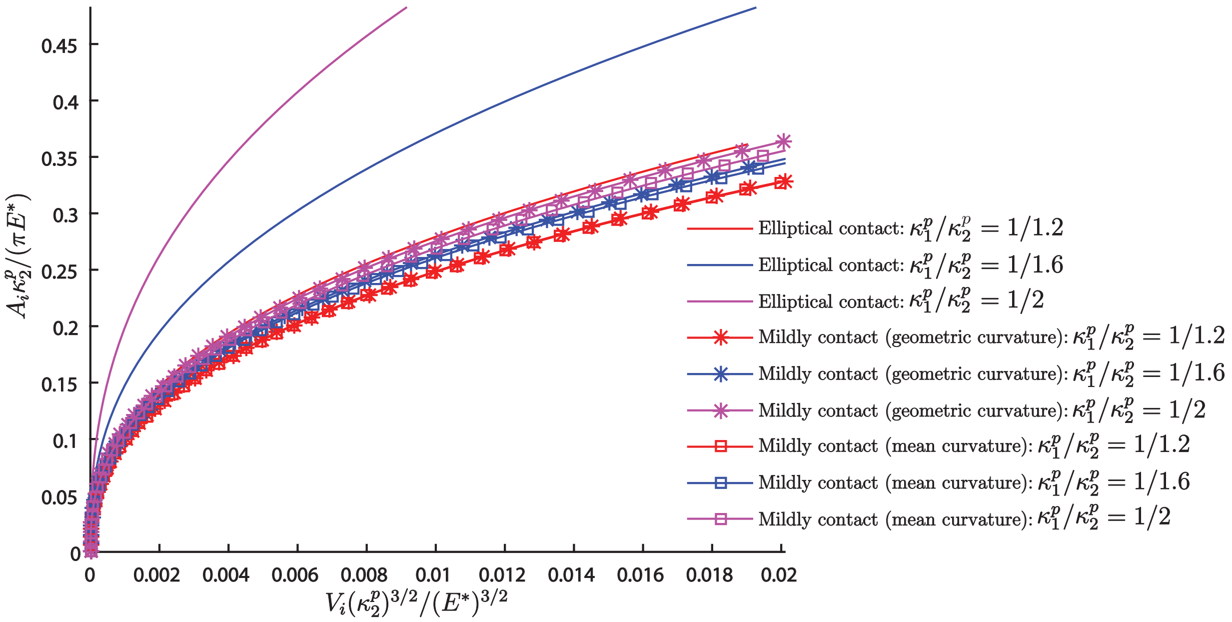

Figure 5.8: The plots of dimensionless contact area, $A_i\kappa_2^p/(\pi E^*)$, vs. the dimensionless trapped volume, $V(\kappa_2^p)^{3/2}/(E^*)^{3/2}$, determined by (1) the elliptical crack model, the mildly elliptical crack model with (2) the geometrical curvature and (3) the mean curvature. The dimensionless pressure, p_0/E^*, varies within $[0, 0.1]$. The ratios κ_1^p/κ_2^p are $1/1.2$, $1/1.6$ and $1/2$. The colored figure is available online.

where

$$F_3(e) = 2(1-e^2)^{-1/2}\left[\sqrt{\kappa_1^p/\kappa_2^p} + \sqrt{\kappa_2^p/\kappa_1^p}(1-e^2)\right]^{-1}. \tag{5.34}$$

Eq. (5.17) and Eq. (5.33) are not the same since $F_1(e) \neq F_3(e)$.

readers may already notice that the trapped volume determined by Eq. (5.33) would be negative if $\kappa_1^p/\kappa_2^p \to 0$. This is confirmed by the plots of $F_1(e)$ and $F_2(e)$ in Fig. 5.7. $F_2(e)$ is monotonically decreased from unity when $\kappa_1^p = \kappa_2^p$ towards negative infinity as $\kappa_1^p/\kappa_2^p \to 0$. Since the elliptical crack is subjected to $p_2(x, y)$ which is a mixture of compressive (at the central part) and the tensile (close to the crack front) traction, the negative trapped volume at small ratio of $\kappa_1^p/\kappa_2^p = 0$ is a sure sign that the *penetration* occurs between the upper and lower crack surfaces. Since the crack surface contact is not included in the current elliptical crack model (neither do any available elliptical crack models), the current elliptical crack model is *ill-defined*. This is the main reason why $K_I(\phi) = 0$ and $\partial g/\partial\rho|_{\rho=1} = 0$ cannot be satisfied simultaneously. If the crack surface contact is included, the resulting crack area may be more complicated than an ellipse.

For the penny-shaped crack ($a \to b$), $K_I = 0$ and $\partial g/\partial r|_{r=b} = 0$ can be satisfied simultaneously (see Johnson et al. [20], Xu et al. [3] and Greenwood [23]). Due to the ill-defined nature of the current elliptical crack model, only the penny-shaped crack model and the mildly elliptical models with mean and geometric curvatures are used in the statistical model of nearly complete contact. According to Fig. 5.8, this compromise may be a source of error to the statistical models developed in the next section.

5.3 Multi-Cracks Contact Model

Similar to the multi-asperity contact model in Section 4.3, this section is named as the "multi-cracks contact model" to emphasize the core concept of the statistical model in which the non-contact area and the average interfacial gap are the superposition of the corresponding results of the crack problems. Depending on the various forms of PDFs shown in Section 2.5 and different crack models discussed in Section 5.2, totally three statistical models are proposed. All statistical models of early contact, except for the BGT model, have an equivalent model at nearly complete contact. The failure of adaptation of the BGT model at the nearly complete contact is because the current elliptical crack model discussed in Section 5.2.1 is ill-defined.

5.3.1 Adapted Greenwood-Williamson (GW) model

Similar to the adapted GW model at early contact (see Section. 4.3.1), the asperities of the "pressure surface" are also assumed to share the same radius: $R^p = 1/\kappa^p$. Thus, using the penny-shaped crack model in Eqs. (5.27) and (5.28) and PDF in Eq. (2.42), Eq. (5.2) and (5.3) can be rewritten as:

$$1 - A^*(\bar{p}^*) = \eta^p \int_{\bar{p}^*}^{\infty} A_i(\xi^p - \bar{p}, \kappa^p)\Phi^p(\xi^{p*})d\xi^{p*}, \tag{5.35}$$

$$\bar{g}(\bar{p}^*) = \eta^p \int_{\bar{p}^*}^{\infty} V_i(\xi^p - \bar{p}, \kappa^p)\Phi^p(\xi^{p*})d\xi^{p*}, \tag{5.36}$$

where η^p and $\kappa^p (= 1/R^p)$ can be determined McCool's solutions in Eqs. (2.43) and (2.45) based on the moments, m_n^p, of the "pressure surface". Defining the dimensionless variable: $\bar{g}^* = \bar{g}/\sqrt{m_0^h}$, and replacing A_i, V_i, η^p and κ^p by Eqs. (5.27), (5.28), (2.43) and (2.45), the final forms of the adapted GW model are obtained as follows:

$$1 - A^*(\bar{p}^*) = \frac{\sqrt{3}}{16}\sqrt{\pi}\sqrt{\alpha^p}\int_{\bar{p}^*}^{\infty}(\xi^{p*} - \bar{p}^*)\Phi^p(\xi^{p*})d\xi^{p*}, \tag{5.37}$$

$$\bar{g}^*(\bar{p}^*) = \frac{3}{20\sqrt{2}}(\pi)^{-1/4}(\alpha^p)^{1/4}(\alpha^h)^{-1/2}\int_{\bar{p}^*}^{\infty}(\xi^{p*} - \bar{p}^*)^{5/2}\Phi^p(\xi^{p*})d\xi^{p*}. \tag{5.38}$$

5.3.2 The Nayak-Bush Model

Similar to the Nayak and Bush model of early contact (see Section. 4.3.2), the asperity of the "pressure surface" is assumed to be axisymmetric with the summit curvature κ_m^p. Using the mildly elliptical crack model in Section. 5.2.4 and the joint PDF, $\Phi^p(\xi_1^{p*}, \kappa_m^{p*})$, in Eq. (2.40), Eq. (5.2) and (5.3) can be rewritten as [3]:

$$1 - A^*(\bar{p}^*) = \eta^p\int_{\bar{p}^*}^{\infty}\int_0^{\infty}A_i(\xi^p - \bar{p}, \kappa_m^p)\Phi^p(\xi^{p*}, \kappa_m^{p*})d\kappa_m^{p*}d\xi^{p*}, \tag{5.39}$$

$$\bar{g}(\bar{p}^*) = \eta^p\int_{\bar{p}^*}^{\infty}\int_0^{\infty}V_i(\xi^p - \bar{p}, \kappa_m^p)\Phi^p(\xi^{p*}, \kappa_m^{p*})d\kappa_m^{p*}d\xi^{p*}. \tag{5.40}$$

Substituting A_i, V_i and η^p (Eqs. (5.27), (5.28) and (2.43)) into the above equations, the final forms of the Nayak-Bush model are obtained as follows:

$$1 - A^*(\bar{p}^*) = \frac{1}{2\sqrt{3}}\sqrt{\alpha^p}\int_{\bar{p}^*}^{\infty}\int_0^{\infty}(\xi^{p*} - \bar{p}^*)(\kappa_m^{p*})^{-1}\Phi^p(\xi^{p*}, \kappa_m^{p*})d\kappa_m^{p*}d\xi^{p*}, \tag{5.41}$$

$$\bar{g}^*(\bar{p}^*) = \frac{4\sqrt{3}}{15\pi}(\alpha^p)^{1/4}(\alpha^h)^{-1/2}\int_{\bar{p}^*}^{\infty}\int_0^{\infty}(\xi^{p*} - \bar{p}^*)^{5/2}(\kappa_m^{p*})^{-3/2}\Phi^p(\xi^{p*}, \kappa_m^{p*})d\kappa_m^{p*}d\xi^{p*}. \tag{5.42}$$

5.3.3 The Greenwood Model

Similar to the Greenwood model of early contact (see Section. 4.3.3), the asperities of the "pressure surface" are assumed to be mildly elliptical, i.e., $\kappa_1^p/\kappa_2^p \to 1$. Using the mildly elliptical crack in Section 5.2.3 and the joint PDF, $\Phi^p(\xi^{p*}, \kappa_g^{p*})$, in Eq. (2.41), then Eq. (5.2) and (5.3) can be rewritten as [3]:

$$1 - A^*(\bar{p}^*) = \eta^p \int_{\bar{p}^*}^{\infty} \int_0^{\infty} A_i(\xi^p - \bar{p}, \kappa_g^p) \Phi^p(\xi^{p*}, \kappa_g^{p*}) d\kappa_g^{p*} d\xi^{p*}, \tag{5.43}$$

$$\bar{g}(\bar{p}^*) = \eta^p \int_{\bar{p}^*}^{\infty} \int_0^{\infty} V_i(\xi^p - \bar{p}, \kappa_g^p) \Phi^p(\xi^{p^*}, \kappa_g^{p*}) d\kappa_g^{p*} d\xi^{p*}. \tag{5.44}$$

Substituting A_i, V_i and η^p (Eqs. (5.29), (5.30) and (2.43)) into the above equations, the final forms of GW model are obtained as follows:

$$1 - A^*(\bar{p}^*) = \frac{1}{2\sqrt{3}} (\alpha^p)^{1/2} \int_{\bar{p}^*}^{\infty} \int_0^{\infty} (\xi^{p*} - \bar{p}^*)(\kappa_g^{p*})^{-1} \Phi^p(\xi^{p*}, \kappa_g^{p*}) d\kappa_g^{p*} d\xi^{p*}, \tag{5.45}$$

$$\bar{g}^*(\bar{p}^*) = \frac{4\sqrt{3}}{15\pi} (\alpha^p)^{1/4} (\alpha^h)^{-1/2} \int_{\bar{p}^*}^{\infty} \int_0^{\infty} (\xi^{p*} - \bar{p}^*)^{5/2} (\kappa_g^{p*})^{-3/2} \Phi^p(\xi^{p*}, \kappa_g^{p*}) d\kappa_g^{p*} d\xi^{p*}. \tag{5.46}$$

Eqs. (5.45) and 5.46 are equivalent to the ones derived by Xu et al. [3]. In their original formulation, the principle curvatures are used as the random variables.

5.3.4 The Ciavarella Asymptotic Model

Carbone [43] proposed a statistical model to solve the rough surface contact at early stage. Carbone model was extended by Ciavarella [44, 45] to obtain the asymptotic relation between A^* and $\bar{p}^*$ when $\bar{p}^*$ is very large. In this section, the Ciavarella asymptotic solution is revisited in a different approach and the same asymptotic relation between $\bar{g}^*$ and $\bar{p}^*$ is also obtained.

The Carbone model is very similar to the Nayak-Bush except that the PDF of the asperity only depends on the summit height, ξ^{h*}. Therefore, the statistical expectation of the dimensionless mean asperity curvature with the dimensionless summit height ξ^{h*}, i.e., $\kappa_m^{h*}(\xi^{h*})$, determined by Nayak [47] is utilized:

$$\kappa_m^{h*}(\xi^{h*}) = \frac{\int_0^{\infty} \kappa_m^{h*} \Phi^h(\xi^{h*}, \kappa_m^{h*}) d\kappa_m^{h*}}{\int_0^{\infty} \Phi^h(\xi^{h*}, \kappa_m^{h*}) d\kappa_m^{h*}}. \tag{5.47}$$

The closed form of $\kappa_m^{h*}(\xi^{h*})$ can be found in [43, 47]. Similarly, the statistical expectation of $\kappa_m^{p*}(\xi^{p*})$ has the same expression with different superscript.

Following the Nayak-Bush model of nearly complete contact, the non-contact ratio and the average interfacial gap can be formulated as

$$1 - A^*(\bar{p}^*) = \frac{1}{2\sqrt{3}}\sqrt{\alpha^p}\int_{\bar{p}^*}^{\infty} (\xi^{p*} - \bar{p}^*)\left[\kappa_m^{p*}(\xi^{p*})\right]^{-1}\Phi^p(\xi^{p*})d\xi^{p*}, \tag{5.48}$$

$$\bar{g}^*(\bar{p}^*) = \frac{4\sqrt{3}}{15\pi}(\alpha^p)^{1/4}(\alpha^h)^{-1/2}\int_{\bar{p}^*}^{\infty} (\xi^{p*} - \bar{p}^*)^{5/2}\left[\kappa_m^{p*}(\xi^{p*})\right]^{-3/2}\Phi^p(\xi^{p*})d\xi^{p*}. \tag{5.49}$$

As ξ^{p*} is very large, then asymptotic expressions of $\Phi^p(\xi^{p*})$ and $\kappa_m^{p*}(\xi^{p*})$ are [43]

$$\Phi^p(\xi^{p*}) \approx \frac{3\sqrt{3}}{\sqrt{2\pi}}\frac{(\xi^{p*})^2}{\alpha^p}\exp\left[-\frac{(\xi^{p*})^2}{2}\right], \tag{5.50}$$

$$\kappa_m^{p*}(\xi^{p*}) \approx \frac{\xi^{p*}}{\sqrt{\alpha^p}}. \tag{5.51}$$

Substituting the above asymptotic expressions into Eqs. (5.48) and (5.49), we can have

$$1 - A^*(\bar{p}^*) = \frac{3}{2\sqrt{2\pi}}\int_{\bar{p}^*}^{\infty} \xi^{p*}(\xi^{p*} - \bar{p}^*)\exp\left[-\frac{(\xi^{p*})^2}{2}\right]d\xi^{p*}, \tag{5.52}$$

$$\bar{g}^*(\bar{p}^*) = \frac{12}{5\sqrt{2}(\pi)^{3/2}}(\alpha^h)^{-1/2}\int_{\bar{p}^*}^{\infty} (\xi^{p*})^{1/2}(\xi^{p*} - \bar{p}^*)^{5/2}\exp\left[-\frac{(\xi^{p*})^2}{2}\right]d\xi^{p*}. \tag{5.53}$$

Using the change of variable, Eq. (5.52) can be simplified to [43]

$$1 - A^*(\bar{p}^*) = \frac{3}{4}\mathrm{erfc}\left(\frac{\bar{p}^*}{\sqrt{2}}\right). \tag{5.54}$$

5.4 The Persson Model

Persson and his co-workers successfully applied the Persson model [6] which he originally developed for the sliding contact of a viscoelastic rubber against a rough rigid flat to many aspects of tribology, i.e., seal [25–27, 35], rough interface lubrication [28–31], heat transfer between rough interfaces [29], adhesive contact [32–35], rubber friction [36], etc. For the nominally flat rough surface contact, the Persson model yields a strikingly simple but still qualitatively accurate form of the real area of contact [7] and the average interfacial gap [32].

Starting from the probability of the pressure at complete contact, Persson derived a diffusion equation of the probability of the contact pressure. Due to the unusual mathematical format and the mechanics symbols used in Persson's original work [6], many researchers find it hard to understand. Thus, an equivalent diffusion equation derived by Manners and Greenwood [7] are used instead:

$$\frac{\partial P}{\partial (m_0^p)} = \frac{1}{2}\frac{\partial^2 P}{\partial p^2}, \tag{5.55}$$

where the probability density of the contact pressure, p, is denoted by P. The Persson model is referred to as a multi-scale model because it quantitatively describes the evolution of the PDF of the contact pressure as more higher frequency scales are included. Let us use the fractal surface associated with the PSD in Eq. (2.18) as an example. Then, for a fixed upper and lower frequency limits: k_s and k_l, the expression of m_0^p is (see Eq. (2.56))

$$m_0^p = (E^*)^2 \frac{1}{8}\frac{(2\pi)^3 C}{1-H}\left(\kappa_s^{2-2H} - \kappa_l^{2-2H}\right).$$

If k_l is fixed, more higher frequency scales are included in the diffusion equation if the magnification ratio: $\xi = k_s/k_l$ becomes larger. Thus, m_0^p is a measure of the multi-scale nature of the rough surface. As $m_0^p \to \infty$, it is a sign that all frequency scales are included in the multi-scale model[5].

The initial conditions of diffusion equation (Eq. (5.55)) when applied to the nominally rough surface contact are proposed by Persson [6] as

$$P(\forall p, m_0^p = 0) = \delta(p - \bar{p}), \tag{5.56}$$

$$P(p = 0, \forall m_0^p) = 0. \tag{5.57}$$

---

[5] The statistical models, thus, can also be considered as multi-scale model since the moments depend on k_s and k_l.

where $\delta(\bullet)$ is the Dirac function. The largest wavelength of current rough boundary is infinite, i.e., $k_l = 0$. According Eq. (2.56), as $m_0^p \to 0$, then $k_s \to k_l = 0$ and the rough boundary turns to be a flat: $z = 0$. As a matter of fact, the contact pressure distribution is uniform: $p(x, y) = \bar{p}$ and this is exactly described by Eq. (5.56). In the meantime, another initial condition, Eq. (5.57), implies that $P(p, m_0^p)$ is the probability density of the positive contact pressure within the contact area, Ω_c, only. However, the validity of this initial conditions are still under debate [37–41].

Eq. (5.55), together with the initial conditions (Eqs. (5.56) and (5.57)), has a unique solution [6, 7]

$$P(p, m_0^p) = \frac{1}{\sqrt{2\pi m_0^p}} \left\{ \exp\left[-\frac{(p-\bar{p})^2}{2m_0^p} \right] - \exp\left[-\frac{(p+\bar{p})^2}{2m_0^p} \right] \right\}, \tag{5.58}$$

which is the difference between a Gaussian distribution and its mirror about $p = 0$. The contact ratio, A^*, can be evaluated by integrating Eq. (5.58) over $p \in [0, \infty]$ [7]:

$$1 - A^*(\bar{p}^*) = \operatorname{erfc}\left(\frac{\bar{p}^*}{\sqrt{2}} \right), \tag{5.59}$$

where erfc$(\bullet)$ is the complementary error function. The average interfacial gap, $\bar{g}$, can be determined based on the elastic energy due to the applied traction [32], see Appendix E for more detail.

As $\bar{p}$ is increased to infinity, then the second exponential term in Eq. (5.58) is vanishing and the PDF is degraded to the Gaussian distribution. In the Persson model, the complete contact only occurs when $\bar{p}$ reaches infinity, see Eq. (5.59). This is a sign that the contact pressure at complete contact follows Gaussian distribution. Manners and Greenwood [7] found the diffusion equation (Eq. (5.55)) is automatically satisfied if the contact pressure is Gaussian. Therefore, the corresponding rough interface should not only be a self-affine fractal, but also a Gaussian surface. Recalling the statistical model at nearly complete contact discussed in Section 5.1, the contact pressure at complete contact is Gaussian process and the statistical models proposed in Section 5.3 are only valid at the nearly complete contact. This similarity inspired the following exploration on the analogy between the Persson model and the statistical models of nearly complete contact:

Comparing Eq. (5.54) with Eq. (5.59), the non-contact ratio of the statistical model is exactly the same as the Persson model except for the different coefficients in front of erfc$(\bullet)$ [44–46]. Since erfc$(\bar{p}^* = 0) = 1$, then A^* in Eq. (5.59) satisfies $A^*(\bar{p}^* = 0) = 0$ while Eq. (5.54) does not. It is clear from this asymptotic analysis that the Persson model is fundamentally equivalent to the statistical model at nearly complete contact. The difference is caused by the initial condition Eq. (5.57) which guarantees that the Persson model is also qualitatively reasonable at the lower load range, specially $A^*(\bar{p}^* = 0) = 0$. However, this is achieved by sacrificing the accuracy.

5.5 Numerical Results

In this section, the analytical models discussed in the previous sections, namely, (i) the adapted GW model, (ii) the Nayak-Bush model, (iii) the Greenwood model of the nearly complete contact (iv) the Ciavarella asymptotic model and (v) the Persson model are compared with each other. For the relation between the contact ratio, A^*, and the contact pressure, $\bar{p}^*$, all the aforementioned models only rely on the band-width parameter, α^p, except for the asymptotic model where a roughness-independent relation is obtained. Thus, two representative rough surfaces with $\alpha^p = 2$ and $\alpha^p = 10$ are used in the comparison. Similarly, the relations $\bar{g}^*$ to $\bar{p}^*$ of the statistical models rely on α^p and α^h only, except for the asymptotic model where the corresponding relation only relies on α^h. However, the Persson model for the average interfacial gap, see Appendix A., relies on H, k_s and k_l. Thus, the comparisons of the relation of $\bar{g}^*$ to $\bar{p}^*$ are only restricted to the statistical models of nearly complete contact. More numerical results related to the Persson model of the average interfacial gap can be found in Chapter E. The line and double integrals involved in the statistical models are determined by the Gauss quadrature shown in Section. 4.4.

Fig. 5.9(a-b) show the A^* to $\bar{p}^*$ relation of all the analytical models associated with $\alpha^p = 2$ and $\alpha^p = 10$. When $\alpha^p = 2$, all the analytical models are almost identical at higher load range when $\alpha^p = 2$, except for the adapted GW model, see Fig. 5.9(a). When $\alpha^p = 10$ (Fig.

5.9(b)), the Ciavarella aymptotic model deviates from the rest of the statistical models. In both cases ($\alpha^p = 2$ and 10), the Persson model overestimates (underestimates) the non-contact area (contact area). The results of statistical models are dispersed with the lower bound and upper bound predicted by the Greenwood model and the asymptotic model, respectively. Fig. 5.9(c-d) shows $\bar{g}^*$ to $\bar{p}^*$ relation of all the statistical models. Similar trends shown in Fig. 5.9(a-b) are repeated in Fig. 5.9(c-d). The Ciavarella asymptotic model shows more dramatic deviation from the rest of the statistical model. This may be explain by the fact that the asymptotic model is only valid at a larger load.

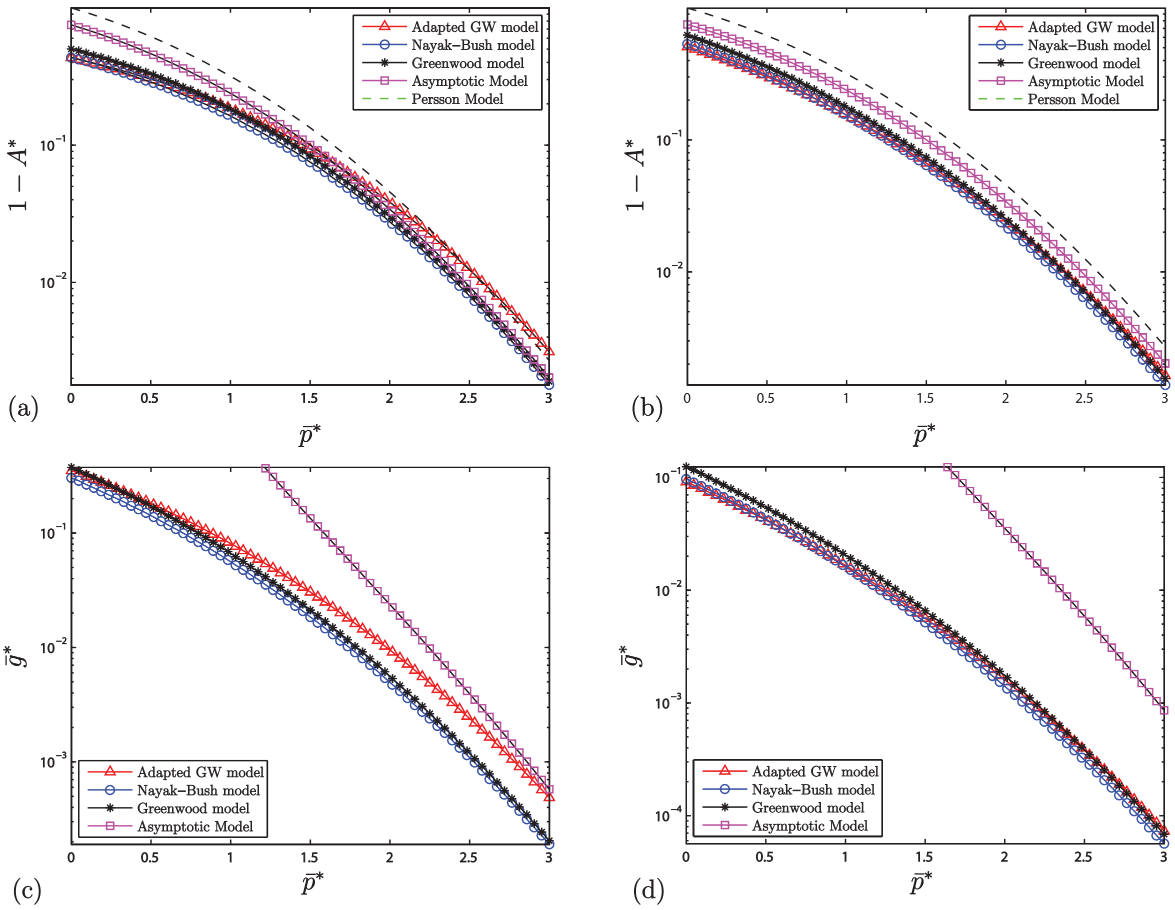

Figure 5.9: Plots of the relations A^* to $\bar{p}^*$ (a-b) and $\bar{g}^*$ to $\bar{p}^*$ (c-d) determined by the statistical models and the Persson model. $\alpha^p = 2$ (a, c) and $\alpha^p = 10$ (b, d). $\alpha^h = 2$.

5.6 Conclusions

In this chapter, a general frame of the statistical model of nearly complete contact is given in details. The rough surface contact at the nearly complete range is decomposed into a complete contact and an infinite body embedded by numerous coplanar pressurized elliptical cracks. The elliptical crack model, two mildly elliptical crack models and the penny-shaped crack model are given. It is found that the elliptical crack model without crack surface contact is ill-defined. Thus, only the penny-shaped crack model and two mildly elliptical crack model are valid. Combining the crack models with the suitable PDFs, four statistical models are discussed. The Persson model is briefly discussed and the analogy between the Persson model and the statistical model of nearly complete contact is explored in detail. The analogy implies that the accuracy of the Persson model at the range of nearly complete contact is sacrificed in order to achieve the boundary condition $A^*(\bar{p}^* \to 0) = 0$. The relation A^* vs. $\bar{p}^*$, as well as $\bar{g}^*$ vs. $\bar{p}^*$, predicted by the statistical models and the Persson model are given.

References

[1] Zhuravlev, V.A., 2007. On the question of theoretical justification of the Amontons-Coulomb law for friction of unlubricated surfaces. Proceedings of the Institution of Mechanical Engineers, Part J: Journal of Engineering Tribology, **221**(8), pp.893-898.

[2] Greenwood, J.A. and Williamson, J.B.P., 1966. Contact of nominally flat surfaces. Proceedings of the Royal Society of London A: Mathematical, Physical and Engineering Sciences, **295**(1442), pp.300-319.

[3] Xu, Y., Jackson, R.L. and Marghitu, D.B., 2014. Statistical model of nearly complete elastic rough surface contact. International Journal of Solids and Structures, **51**(5), pp.1075-1088.

[4] Manners, W., 2000. Pressure required to flatten an elastic random rough profile. International Journal of Mechanical Sciences, **42**(12), pp.2321-2336.

[5] Ciavarella, M., Demelio, G., Barber, J.R. and Jang, Y.H., 2000, Linear elastic contact of the Weierstrass profile. Proceedings of the Royal Society of London A: Mathematical, Physical and Engineering Sciences, **56**(1994), pp.387-405

[6] Persson, B.N., 2001. Theory of rubber friction and contact mechanics. The Journal of Chemical Physics, **115**(8), pp.3840-3861.

[7] Manners, W. and Greenwood, J.A., 2006. Some observations on Persson's diffusion theory of elastic contact. Wear, **261**(5), pp.600-610.

[8] Jackson, R.L., 2010. An analytical solution to an Archard-type fractal rough surface contact model. Tribology Transactions, **53**(4), pp.543-553.

[9] Kudish, I.I., Cohen, D.K. and Vyletel, B., 2013. Perfect Mechanical Sealing in Rough Elastic Contacts: Is It Possible?. ASME Journal of Applied Mechanics, **80**(1), p.014504.

[10] Green, A.E. and Sneddon, I.N., 1950, The distribution of stress in the neighbourhood of a flat elliptical crack in an elastic solid. Mathematical Proceedings of the Cambridge Philosophical Society, **46**(01), pp. 159-163.

[11] Kassir, M.K. and Sih, G.C., 1967, Griffith's theory of brittle fracture in three dimensions. International Journal of Engineering Science, **5**(12), pp.899-918.

[12] Shah, R.C. and Kobayashi, A.S., 1971, Stress intensity factor for an elliptical crack under arbitrary normal loading. Engineering Fracture Mechanics, **3**(1), pp.71-96.

[13] Sneddon, I.N., 1979. The stress intensity factor for a flat elliptical crack in an elastic solid under uniform tension. International Journal of Engineering Science, **17**(2), pp.185-191.

[14] Martin, P.A., 1986. Orthogonal polynomial solutions for elliptical cracks under shear loadings. The Quarterly Journal of Mechanics and Applied Mathematics, **39**(4), pp.519-534.

[15] Atroshchenko, E., 2010. Stress intensity factors for elliptical and semi-elliptical cracks subjected to an arbitrary mode-I loading. Ph.D. dissertation, University of Waterloo, Canada.

[16] Krenk, S., 1979. A circular crack under asymmetric loads and some related integral equations. ASME Journal of Applied Mechanics, **46**(4), pp.821-826.

[17] Sneddon, I., 1946, The distribution of stress in the neighbourhood of a crack in an elastic solid. Proceedings of the Royal Society of London A: Mathematical, Physical and Engineering Sciences **187**(1009), pp.229-260.

[18] Barenblatt, G.I., 1962. The mathematical theory of equilibrium cracks in brittle fracture. Advances in Applied Mechanics, **7**, pp.55-129.

[19] Sneddon, I.N. and Lowengrub, M., 1969. *Crack problems in the classical theory of elasticity*, John Willey & Sons. New York.

[20] Johnson, K.L., Greenwood, J.A. and Higginson, J.G., 1985. The contact of elastic regular wavy surfaces. International Journal of Mechanical Sciences, **27**(6), pp.383-396.

[21] Stanley, H.M. and Kato, T., 1997. An FFT-based method for rough surface contact. ASME Journal of Tribology, **119**(3), pp.481-485.

[22] Greenwood, J.A., 2006. A simplified elliptic model of rough surface contact. Wear, **261**(2), pp.191-200.

[23] Greenwood, J.A., 2015. On the almost-complete contact of elastic rough surfaces: The removal of tensile patches. International Journal of Solids and Structures, **56**, pp.258-264.

[24] Persson, B.N.J., and Yang, C., 2008, Theory of the leak-rate of seals, Journal of Physics: Condensed Matter, **20**, p.315011.

[25] Lorenz, B., and Persson, B.N.J., 2009, Leak rate of seals: Comparison of theory with experiment, EPL, **86**, p.44006.

[26] Lorenz, B. and Persson, B.N.J., 2010. On the dependence of the leak rate of seals on the skewness of the surface height probability distribution. European Physics Letters, **90**(3), p.38002.

[27] Lorenz, B. and Persson, B.N.J., 2010. Leak rate of seals: Effective-medium theory and comparison with experiment. The European Physical Journal E, **31**(2), pp.159-167.

[28] Persson, B.N.J. and Scaraggi, M., 2009. On the transition from boundary lubrication to hydrodynamic lubrication in soft contacts. Journal of Physics: Condensed Matter, **21**(18), p.185002.

[29] Persson, B.N.J., 2010. Fluid dynamics at the interface between contacting elastic solids with randomly rough surfaces. Journal of Physics: Condensed Matter, **22**(26), p.265004.

[30] Lorenz, B. and Persson, B.N.J., 2010. Time-dependent fluid squeeze-out between solids with rough surfaces. The European Physical Journal E, **32**(3), pp.281-290.

[31] Lorenz, B. and Persson, B.N.J., 2011. Fluid squeeze-out between rough surfaces: comparison of theory with experiment. Journal of Physics: Condensed Matter, **23**(35), p.355005.

[32] Persson, B.N.J., 2007. Relation between interfacial separation and load: a general theory of contact mechanics. Physical Review Letters, **99**(12), p.125502.

[33] Persson, B.N.J., 2003. On the mechanism of adhesion in biological systems. The Journal of Chemical Physics, **118**(16), pp.7614-7621.

[34] Carbone, G., Mangialardi, L. and Persson, B.N.J., 2004. Adhesion between a thin elastic plate and a hard randomly rough substrate. Physical Review B, **70**(12), p.125407.

[35] Persson, B.N.J., 2008. Capillary adhesion between elastic solids with randomly rough surfaces. Journal of Physics: Condensed Matter, **20**(31), p.315007.

[36] Selig, M., Lorenz, B., Henrichmller, D., Schmidt, K., Ball, A. and Persson, B., 2014. Rubber friction and tire dynamics: A comparison of theory with experimental data. Tire Science and Technology, **42**(4), pp.216-262.

[37] Hyun, S., Pei, L., Molinari, J.F. and Robbins, M.O., 2004. Finite-element analysis of contact between elastic self-affine surfaces. Physical Review E, **70**(2), p.026117.

[38] Hyun, S. and Robbins, M.O., 2007. Elastic contact between rough surfaces: Effect of roughness at large and small wavelengths. Tribology International, **40**(10), pp.1413-1422.

[39] Putignano, C., Afferrante, L., Carbone, G. and Demelio, G., 2012. The influence of the statistical properties of self-affine surfaces in elastic contacts: A numerical investigation. Journal of the Mechanics and Physics of Solids, **60**(5), pp.973-982.

[40] Yastrebov, V.A., Anciaux, G. and Molinari, J.F., 2014. The contact of elastic regular wavy surfaces revisited. Tribology Letters, **56**(1), pp.171-183.

[41] Dapp, W.B., Prodanov, N. and Mser, M.H., 2014. Systematic analysis of Perssons contact mechanics theory of randomly rough elastic surfaces. Journal of Physics: Condensed Matter, **26**(35), p.355002.

[42] Bush, A.W., Gibson, R.D. and Thomas, T.R., 1975. The elastic contact of a rough surface. Wear, **35**(1), pp.87-111.

[43] Carbone, G., 2009. A slightly corrected Greenwood and Williamson model predicts asymptotic linearity between contact area and load. Journal of the Mechanics and Physics of Solids, **57**(7), pp.1093-1102.

[44] Ciavarella, M., 2015. Adhesive rough contacts near complete contact. International Journal of Mechanical Sciences, **104**, pp.104-111.

[45] Ciavarella, M., 2016. Rough contacts near full contact with a very simple asperity model. Tribology International, **93**, pp.464-469.

[46] Xu, Y., and Jackson, R.L., 2017, Statistical Models of Nearly Complete Elastic Rough Surface Contact-Comparison with Numerical Solutions, Tribology International, **105**, pp.274-291.

[47] Nayak, P.R., 1971. Random Process Model of Rough Surfaces. ASME Journal of Lubrication Technology, **93**, pp.398-407.

Chapter 6

Statistical Models of Nearly Complete Adhesive Contact

In this chapter, the statistical models of nearly complete contact is extended to include the adhesion between the rough surface and the rigid flat. Inspired by Chapter 5, the non-contact area in the nearly complete adhesive contact can be divided into numerous (half) adhesive "cracks". The statistical modeling used in Chapter 5 is adopted in this chapter. One major difference is the hysteresis at the adhesive crack level and the rough surface contact level.

6.1 Introduction

Adhesion is referred to as the attraction between the contact interfaces due to the surface energy. The study of the adhesive contact received considerable attention in the 1970s resulting in two classic models, namely, the JKR model [1] (after Johnson, Kendall and Roberts) and the DMT model [2] (after Derjaguin, Muller and Toporov). These models were proposed for the adhesive spherical contact. Tabor [3] successfully explained the difference between the JKR and DMT model by a new parameter:

$$\mu = \left[\frac{Rw^2}{(E^*)^2 z_0^3}\right]^{1/3},$$

which is commonly referred to as Tabor's parameter. R is the effective radius of the contact pair. w is the surface energy. z_0 is the equilibrium separation of the atoms. The JKR model is valid for the case with low μ, i.e., the sphere is stiff with a small radius and low surface energy. The adhesive contacts associated with low μ are said to be in the JKR limit. On the contrary, the adhesive contacts associated with high μ are considered in the DMT limit in which the sphere is soft with large radius and high surface energy. After finding the analogy between the adhesive contact and the fracture mechanics [4], Maugis [5] proposed the Maugis-Dugdale model resorting to the concepts of the fracture mechanics, e.g., Griffith crack [6], Barenblatt cohesive crack [7], J-integral [8], etc. The Maugis-Dugdale model is capable of transitioning from the DMT limit to the JKR limit as the Maugis parameter (similar to the Tabor's parameter) is monotonically increased from zero to infinity. Several improved adhesive models have also been proposed [9–11]. A complete adhesion map of the spherical contact is proposed by Johnson and Greenwood [12] and a detailed review of the historical development of the adhesive asperity contact theory is done by Barthel [13].

The study of the rough surface adhesive starts from the pioneering work of Fuller and Tabor [14] where the Hertzian contact theory in the GW model is replaced by the JKR model. Similarly, the other statistical models combining the GW model with other adhesive asperity contact models are proposed (e.g., the DMT model in [15]; Maugis-Dugdale model in [16, 17]; double Hertzian model [9] in [18]). Since the roughness has the multi-scale structure, the multi-scale model is also applied to study the effect of the multi-scale nature on the adhesive contact [21–23]. For a better accuracy, the numerical models play a major role in exploring the rough adhesive contact [24–29]. Recently, a contact mechanics challenge for the adhesive rough surface contact was launched by Müser and Dapp [30]. The results of various analytical models and numerical results are compared with each other in [31].

At early contact, the attractive force between the rough surfaces is hard to detect and has a negligible effect on the contact status. This is because the adhesion between the surfaces are progressively broken down by the roughness and only exist on the tips of the asperities [14, 32]. However, the effect of adhesion would be dominant at the case of nearly complete contact since the real area of contact is nearly identical to the nominal contact area [33, 34]. In this chapter, the adhesive rough surface contact in the loading and unloading stage is modeled using the statistical approach with the special focus on the stage of nearly complete contact.

In order to simplify the adhesive contact modeling at the nearly complete stage, two major assumptions are introduced:

- **Assumption 1**. the short range repulsive stress within the contact area is replaced by the hard wall repulsion, i.e., only the contact pressure is taken into consideration;

- **Assumption 2**. the long range adhesive stress at the non-contact area is approximated by a band of an adhesive zone close to the contact edge. The intensity of the adhesive stress, σ_0, is uniform within the adhesive zone and this is referred to as the Dugdale model [5].

Following the decomposition of the non-adhesive rough contact in Section 5.1, the adhesive nearly complete contact is the superposition of a complete contact problem and an infinite body embedded by the coplanar adhesive cracks on the $z = 0$ plane. Fig. 5.2 for the non-adhesive problem can be reused to illustrate the decomposition of the coresponding adhesive problem. According to the assumption 1 listed above, the contact pressure, $p(x, y)$, within the contact area does not altered significantly, except at the contact boundary, by the adhesive stress at the non-contact area. The contact pressure at complete contact, $p_1(x, y)$, is exactly the same as that in Eq. (5.1). Upper surface of each adhesive crack shown in Fig. 5.2(c) is subjected to $p_2(x, y)$, as well as the uniform adhesive stress of the intensity σ_0. It is expected that the area of each non-contact region, A_i, and the corresponding trapped volume V_i are smaller than that of the non-adhesive case. The non-contact ratio, A^*, and the average interfacial gap, $\bar{g}$, can be formulated using the statistical approach by Eqs. (5.2) and (5.3). The detailed expressions of A^* and $\bar{g}$ for each model will be given after various adhesive crack models are discussed.

6.2 Penny-Shaped Adhesive Crack Models

As it is mentioned in Chapter 5, nearly all the non-contact regions are elliptical. In order to reduce the complexity of the presentation, the simpler penny-shaped adhesive crack is studied first. Starting from the penny-shaped adhesive crack model, the elliptical adhesive crack model is approximated in a same manner as that in the elliptical asperity contact model (Section 4.2) and the non-adhesive elliptical crack model (Section 5.2). In this section, an analysis similar to that applied by Maugis [5, 36] to the adhesive Hertzian contact is adjusted in the study of the adhesive crack model. Thus, the adhesive crack model studied in this section is also referred to as the Maugis-Dugdale model.

A schematic representation of a penny-shaped adhesive crack is shown in Fig. 6.1. The upper and lower crack surfaces are subjected to an axisymmetric normal traction as follows

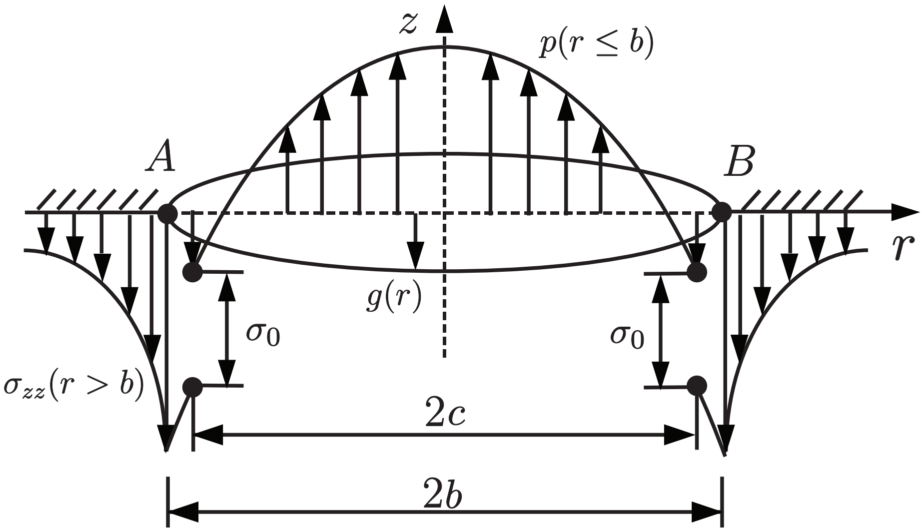

Figure 6.1: Schematic representation of a penny-shaped cohesive crack embedded in an elastic infinite body with uniform adhesive stress within the adhesive zone: $r \in [c, b]$. The crack surfaces are subjected to $p(r)$. Only the state of stresses acting on $z > 0$ part are shown. The discontinuity of $p(r)$ at $r = c$ is due to the superposition of the uniform adhesive stress.

($\kappa_1^p = \kappa_2^p = \kappa^p$):

$$p(r) = \begin{cases} p_0 - \dfrac{\kappa^p}{2} r^2 & r \leq c, \\ p_0 - \sigma_0 - \dfrac{\kappa^p}{2} r^2 & c < r \leq b, \end{cases} \tag{6.1}$$

where a discontinuous point can be found at $r = c$ due to the uniform adhesive (positive) stress of the Dugdale model. As a matter of fact, the upper/lower crack opening displacement (COD), $g(r)$, is also discontinuous at $r = c$. The original Maugis-Dugdale model [5] of Hertzian contact also suffers the discontinuity of the normal surface displacement outside the contact area and it can be avoided by the double-Hertzian model proposed by Greenwood and Johnson [9]. Similarly, the discontinuous COD may be fixed by using a continuous adhesive law.

The Dugdale model is the simplest one among all the adhesive laws [37] and is proposed originally for the small scale yielding at the vicinity of the tip of the plane crack [38]. The adhesive zone in the penny-shaped crack is an annular region with an outer and inner radius, b and c, respectively (Fig. 6.1). A constant adhesive stress is distributed over the annular region.

According to Barenblatt [5,7,36], this adhesive stress should be the theoretical stress:

$$\sigma_0 = 1.03\frac{w}{z_0}, \tag{6.2}$$

if the Lennard-Jones (LJ) potential is used. w is the surface energy which is assumed to be constant over the adhesive crack surfaces. z_0 is the equilibrium separation of the atoms. Theoretically, the Young's modulus can be determined based on the LJ potential [36]:

$$\sigma_0 = 0.06E. \tag{6.3}$$

The validity of using the Dugdale model to approximate the LJ potential is confirmed in the spherical contact [20,39], in the cylindrical contact [40] and in the slightly wavy plane contact [41]. Additionally, Barthel [13] pointed out that the finer details of the adhesive law have a minor effect on the adhesive contact system.

Next, a new group of dimensionless variables is defined below:

$$\begin{aligned} p^* =& p_0/\left[\frac{\pi^2(E^*)^2w^2\kappa^p}{72}\right]^{1/5}, \quad b^* = b/\left[\frac{81\pi E^* w}{16(\kappa^p)^2}\right]^{1/5}, \\ m =& c/b, \quad G^* = G/w. \end{aligned} \tag{6.4}$$

Similarly, the corresponding crack area, A_i, and the trapped volume, V_i, are normalized by

$$A_i^* = A_i/\left[\frac{81\pi E^* w}{16(\kappa^p)^2}\right]^{2/5}, \quad V_i^* = V_i/\left[\frac{3w}{2\kappa^p}\right]. \tag{6.5}$$

A dimensionless variable similar to Tabor's parameter [3] is defined below:

$$\sigma_0^* = \sigma_0/\left[\frac{\pi^2(E^*)^2w^2\kappa^p}{72}\right]^{1/5}. \tag{6.6}$$

As it will be shown in the rest of the section, the adhesive crack transits from the non-adhesive limit to the JKR limit as σ_0^* varies monotonically from 0 to ∞.

6.2.1 Non-Adhesive Limit

In the non-adhesive limit where w is vanishing, Tabor's parameter, σ_0^*, approaches 0. Recalling Eq. (5.25), the requirement of the zero singularity at the crack tip results in (see Eq. (5.25))

$$p_0 = \frac{1}{3}\kappa^p b^2. \tag{6.7}$$

The crack area and the trapped volume are already developed in Eqs. (5.27) and (5.28) and are rewritten below for the readers' convenience:

$$\begin{aligned} A_i &= 3\pi(\kappa^p)^{-1}p_0, \\ V_i &= \frac{16\sqrt{3}}{45}\pi(p_0)^{5/2}. \end{aligned}$$

Substituting the dimensionless groups in Eqs. (6.4) and (6.5) into the above three equations, the dimensionless forms of p_0, A_i and V_i are

$$p^* = \frac{3}{2}(b^*)^2, \tag{6.8}$$

$$A_i^* = \frac{2}{3}\pi p^*, \tag{6.9}$$

$$V_i^* = \frac{16\sqrt{3}}{45}\pi(p^*)^{5/2}. \tag{6.10}$$

In the original Maugis-Dugdale model [5], as the Tabor's parameter is decreased, the asymptotic contact area and the contact load approach the DMT limit which is slightly different from the Hertzian theory (non-adhesive limit). Similarly, the DMT limit of A_i and V_i may also exist in the adhesive crack model. The derivation of the DMT limit in the Hertzian contact [2, 5, 42] relies on the assumption that (i) the cohesion zone is extended to infinity and (ii) the interfacial gap (outside the contact area) and the contact pressure (inside the contact area) are the same as that in the Hertzian theory. Then the total load in the DMT limit is lower than that in Hertzian contact theory by an amount equaling the adhesive force outside the contact area. Since the adhesive zone only covers a finite region, only the second assumption can be applied to the adhesive crack problem and it results in the same A_i and V_i as that in the non-adhesive limit. Therefore, the DMT limit is the same as the non-adhesive limit in the adhesive crack model.

6.2.2 JKR Limit

In the adhesive contact, the concept of the JKR limit is referred to as the contact status where the adhesive zone outside the contact area is vanishing [1]. In the fracture mechanics, the edges of the adhesive contact in the JKR limit is equivalent to the Griffith crack [4, 6] where the singularity of the normal stress is allowed. Due to the vanishing of the adhesion zone, the normal traction on the crack surfaces is degraded into $p(r) = p_0 - \dfrac{\kappa^p}{2} r^2$ where $r \leq b$ and the corresponding SIF is [33]:

$$K_I = \frac{2\sqrt{b}}{\sqrt{\pi}} (p_0 - \frac{1}{3}\kappa^p b^2). \tag{6.11}$$

The strain energy release rate of a Griffith crack is (only upper portion is taken into consideration) [33]

$$G = w = \frac{K_I^2}{2E^*}. \tag{6.12}$$

Combining Eq. (6.11) and (6.12), the crack radius can be solved from the following nonlinear equation [33]

$$p_0 = \frac{1}{3}\kappa^p b^2 + \sqrt{\frac{\pi E^* w}{2b}}. \tag{6.13}$$

Substituting the dimensionless group in Eq. (6.4) into Eq. (6.13), the governing equation[1] of the JKR limit is obtained:

$$p^* = \frac{3}{2}(b^*)^2 + \sqrt{\frac{2}{b^*}}. \tag{6.14}$$

The minimum value of p^* is can be found from $dp^*/db^* = 0$:

$$p^*_{\text{min}} = \frac{3}{2}\left(\frac{\sqrt{2}}{6}\right)^{4/5} + \sqrt{2}\left(\frac{\sqrt{2}}{6}\right)^{-1/5} \approx 2.3602. \tag{6.15}$$

---

[1] Eq. (6.14) can be adapted into

$$\frac{3}{2}t^5 - p^* t + \sqrt{2} = 0 \quad \text{where} \quad t = \sqrt{b^*},$$

and solved by the polynomial solver for the radius b^*.

Substituting the dimensionless group in Eq. (6.4), the dimensionless strain energy release rate, G^*, in the JKR limit is

$$G^* = \frac{1}{8}b^* \left[2p^* - 3(b^*)^2\right]^2. \tag{6.16}$$

For the fixed load condition (p^* is constant) and $p^* > p^*_{\text{min}}$, the stability of the adhesive crack in the JKR limit is governed by $dG^*/db^* \leq 0$, i.e.,

$$\frac{3(b^*)^2}{2} \leq p^* \leq \frac{15(b^*)^2}{2}, \tag{6.17}$$

and the adhesive crack becomes unstable if the above criterion is not satisfied.

The dimensionless crack area can be determined based on the definition after b^* is solved from Eq. (6.14):

$$A_i^* = \pi(b^*)^2. \tag{6.18}$$

The interfacial gap, $g(r)$, in the JKR limit can be determined in Case I as shown in the Appendix B as:

$$g(r) = \frac{4}{\pi E^*}\left[p_0 - \frac{1}{9}\kappa^p(2r^2 + b^2)\right]. \tag{6.19}$$

The trapped volume, V_i, is obtained after the integration of $g(r)$ over the area of the open crack in the polar coordinates:

$$V_i = \frac{8}{3E^*}b^3\left[p_0 - \frac{1}{5}\kappa^p b^2\right], \tag{6.20}$$

and, after the normalization using the dimensionless group in Eq. (6.4), the dimensionless trapped volume is:

$$V_i^* = 2\pi(b^*)^3\left[p^* - \frac{9}{10}(b^*)^2\right]. \tag{6.21}$$

6.2.3 Maugis-Dugdale Model

The Maugis-Dugdale model represents the adhesive crack varying between the JKR limit and the non-adhesive limit. The adhesive crack schematically shown in Fig. 6.1 can be decomposed into a adhesive crack in the JKR limit and a penny-shaped crack subjected to the uniform tensile stress, σ_0, within the adhesive zone, $r \in [c, b]$. According to the analytical solutions tabulated in Appendix D, The normal stress, $\sigma_{zz}(r)$, COD, $g(r)$, and the stress intensity factor (SIF), K_I, can be obtained through the use of superposition:

$$K_I = \frac{2}{\sqrt{\pi b}}\left[p_0 b - \frac{\kappa^p}{3}b^3 - \sigma_0\sqrt{b^2-c^2}\right], \tag{6.22}$$

$$\begin{aligned}\sigma_{zz}(r \geq b) =& \frac{b}{\pi}\frac{K_I}{\sqrt{r^2-b^2}} - \frac{2}{\pi}(p_0 - \frac{\kappa^p}{2}r^2)\tan^{-1}\left(\frac{b}{\sqrt{r^2-b^2}}\right) - \\ & \frac{\sigma_0}{\pi}\tan^{-1}\left(\frac{r^2-2b^2+c^2}{2\sqrt{b^2-c^2}\sqrt{r^2-b^2}}\right) - \frac{b\kappa^p}{\pi}\sqrt{r^2-b^2} + \frac{\sigma_0}{2},\end{aligned} \tag{6.23}$$

$$g(r \leq b) = \frac{4}{\pi E^*}\left\{\sqrt{b^2-r^2}\left[p_0 - \frac{1}{9}\kappa^p(2r^2+b^2)\right] - \sigma_0\int_{\max(r,c)}^{b}\frac{\sqrt{t^2-c^2}}{\sqrt{t^2-r^2}}dt\right\}. \tag{6.24}$$

The adhesive crack must satisfy:

- **Condition 1**. vanishing singularity at crack tip [7]: $K_I = 0$. This requirement also enables the continuity of the normal stress at the vicinity of the crack tip: $\sigma_{zz}(r \to b^+) = \sigma_{zz}(r \to b^-)$.
- **Condition 2**. crack equilibrium[2]:$G = \sigma_0 g(c) = w$.

Substituting Eqs. (6.22) and (6.24) into the above two conditions result in the following two governing equations:

$$p_0 b - \frac{1}{3}\kappa^p b^3 - \sigma_0\sqrt{b^2-c^2} = 0, \tag{6.26}$$

$$\frac{4}{\pi E^*}\sigma_0\left\{\sqrt{b^2-c^2}\left[p_0 - \frac{1}{9}\kappa^p(2c^2+b^2)\right] - \sigma_0(b-c)\right\} - w = 0. \tag{6.27}$$

Note that Eqs. (6.26) and (6.27) are independent [5], i.e., the normal stress continuity can be maintained even though the crack is unstable. This important observation will be used later.

---

[2] The same form has been derived by Maugis [5] using J-integral [8]. However, the original J-integral is only valid for the plane crack. An alternative way is to starting from the definition of the surface energy [9]:

$$w = \int_0^\infty \sigma_{zz}(g)dg \approx \int_0^{\max(g)} \sigma_{zz}(g)dg = \int_a^c \sigma_{zz}(r)\frac{dg}{dr}dr = \sigma_0 g(c), \tag{6.25}$$

where $\sigma_{zz}(r < c) = 0$ and $\sigma_{zz}(c \leq r \leq a) = \sigma_0$. Here we assume $\max(u_z)$ could be treated as infinitely large comparing with the equilibrium separation, z_0.

Substituting the dimensionless group in Eqs. (6.4) and (6.6) into Eqs. (6.26) and (6.27), the normalized forms of two governing equations are:

$$\frac{3}{2}(b^*)^2 + \sigma_0^*\sqrt{1-m^2} - p^* = 0, \tag{6.28}$$

$$\frac{1}{2}\sqrt{1-m^2}(2m^2+1)(b^*)^3 - \left[p^*\sqrt{1-m^2} - (1-m)\sigma_0^*\right] b^* + \frac{1}{\sigma_0^*} = 0. \tag{6.29}$$

Similar to the JKR limit, the governing equations of the Maugis-Dugdale model are non-linear, too. For a given p^*, the unknowns b^* and m are dependent on Tabor's parameter, σ_0^*. Generally, b^* and m in the above set of dimensionless equations have the maximum of two real roots.

For a *fixed load condition* (i.e., p^* is constant), the stability of the adhesive crack in the static equilibrium can be determined based on the Griffith's crack theory [6], i.e., stable crack for $\partial G^*/\partial b^* \leq 0$ and unstable crack for $\partial G^*/\partial b^* > 0$ where G^* can be obtained from Eq. (6.29):

$$G^* = \sigma_0^*\left[p^*\sqrt{1-m^2} - (1-m)\sigma_0^*\right] b^* - \frac{1}{2}\sigma_0^*\sqrt{1-m^2}(2m^2+1)(b^*)^3, \tag{6.30}$$

and

$$\begin{aligned}\left(\frac{\partial G^*}{\partial b^*}\right)\bigg|_{p^*} =&\sigma_0^*\left[p^*\sqrt{1-m^2} - (1-m)\sigma_0^*\right] + \sigma_0^* b^*\left[\sigma_0^* - p^*\frac{m}{\sqrt{1-m^2}}\right]\frac{\partial m}{\partial b^*} - \\ &\frac{3}{2}\sigma_0^*\sqrt{1-m^2}(2m^2+1)(b^*)^2 + \frac{1}{2}\sigma_0^*\frac{m}{\sqrt{1-m^2}}\frac{\partial m}{\partial b^*}(2m^2+1)(b^*)^3 - \\ &2\sigma_0^* m\sqrt{1-m^2}(b^*)^3\frac{\partial m}{\partial b^*},\end{aligned} \tag{6.31}$$

where the partial derivatives $\frac{\partial m}{\partial b^*}$ is directly obtained from Eq. (6.28)

$$\frac{\partial m}{\partial b^*} = \frac{3b^*}{m(\sigma_0^*)^2}\left[p^* - \frac{3}{2}(b^*)^2\right]. \tag{6.32}$$

The dimensionless crack area, A_i^*, follows the same form in the JKR limit, see Eq. (6.18). The trapped volume is determined based on the interfacial gap, $g(r)$, in Eq. (6.24). The closed form evaluation of the last integral in Eq. (6.24) can be found in Eqs. (D.12) and (D.13) in

Appendix D. Therefore, the simplest form of the trapped volume is formulated below:

$$V_i = \frac{8}{3E^*} b^3 \left[p_0 - \frac{1}{5} \kappa^p b^2 \right] - \frac{4\sigma_0 b^3}{3\pi E^*} \left[\sqrt{1-m^2} + m^3 F_3(m) \right], \tag{6.33}$$

where

$$\begin{aligned} F_3(m) =& m + m^{-1} - \sqrt{m^{-2}-1} - 2 \ + 3 \int_m^1 k^{-4} \left[\mathbf{E}(\varphi_2, k) - \mathbf{E}(k) - \mathbf{F}(\varphi_2, k) + \mathbf{K}(k) \right] dk + \\ & 3 \int_m^1 k^{-2} \left[\mathbf{F}(\varphi_2, k) - \mathbf{K}(k) \right] dk. \end{aligned} \tag{6.34}$$

The calculation of V_i involves the integral of the incomplete/complete elliptic integral with respect to the modulus. Very few closed-form solution can be found in the past literature [43]. Therefore, the Gauss quadrature is used.

Consequently, the dimensionless trapped volume, V_i^*, is

$$V_i^* = 2\pi (b^*)^3 \left[p^* - \frac{9}{10} (b^*)^2 \right] - (b^*)^2 \sigma_0^* \left[\sqrt{1-m^2} + m^3 F_3(m) \right]. \tag{6.35}$$

The first term on the right hand side of Eq. (6.35) is the same as the dimensionless volume, V_i^*, in the JKR limit, see Eq. (6.10). The second term is related to the loss of volume due to the adhesive traction.

6.2.4 Full Adhesion Limit: $c = 0$

The Maugis-Dugdale transition discussed above implicitly assumes that the adhesion zone is restricted within the annulus: $0 < c \leq r \leq b$ [44,45]. As $c \to 0$ ($m \to 0^+$), the adhesive zone is extended to the entire crack surface and it is referred to as the full adhesion limit. This limit can only occur in the adhesive crack since the crack radius is finite and has nothing to do with the DMT limit because Tabor's parameter, σ_0^*, is not necessarily vanishing. If the continuity of the normal stress is still held, then the dimensionless crack size, b^*, can be directly solved from Eq. (6.28):

$$b^* = \sqrt{\frac{2}{3} (p^* - \sigma_0^*)} = \left[\frac{2}{3} (p^* - \sigma_0^*) \right]^{2/3}, \tag{6.36}$$

where $p^* \geq 1$. When σ_0^* is small, the full adhesion limit approaches the non-adhesive limit shown in Eq. (6.8).

G^* can be obtained by substituting $m = 0$ and Eq. (6.36) into Eq. (6.30):

$$G^* = \sigma_0^* \left[\frac{2}{3}(p^* - \sigma_0^*) \right]^{3/2} . \tag{6.37}$$

Since $\partial G^*/\partial b^* = 3\sigma_0^*(b^*)^2 > 0$, the static equilibrium of the cohesive crack cannot maintained in the full adhesion limit. Therefore, the adhesive crack in the full adhesion limit is in closure ($G^* > 1$), in propagation ($G^* < 1$) and in the static equilibrium ($G^* = 1$). As it is mentioned earlier that Eqs. (6.28) and (6.29) are coupled, the unstable crack would not affect condition zero K_I represented by Eq. (6.36).

6.3 Penny-Shaped Adhesive Crack Models - Numerical Results

The solutions, b^* and m, solved from the system of equations, Eqs. (6.28) and (6.29), and in the full cohesion limit are illustrated in Figs. 6.2 and 6.3 associated with different p^* and Tabor's parameter, σ_0^*. The loading stage of the adhesive crack is related to the loading stage of the rough surface contact where the dimensionless radius of adhesive crack, b^*, and the dimensionless pressure, p^*, monotonically decreases. Similarly, b^* and p^* increases monotonically in the unloading stage of the adhesive crack. Only one loading-unloading cycle are illustrated in Figs. 6.2 and 6.3. For the sake of clarity, Figs. 6.2(a) and 6.3(a) associated with $\sigma_0^* = 5$ are used as the representative results of the evolution of b^* and m since all the important branches are visible. The rest of the figures associated with lower values of σ_0^* will be explained later.

The entire loading stage (marked by the solid line with an arrow) can be divided into four branches, namely, A-G, G-B, B-C and C-D. In the A-G branch, non-negative roots of Maugis-Dugdale model (b^* and m) are unique and decreases monotonically with the decreasing of p^*. The A-G branch is stable since $\partial G^*/\partial b^* \leq 0$ (see also the legend in Figs. 6.2(a) and 6.3(a)). When $p^* < p_G^*$, the Maugis-Dugdale model has dual (non-negative) roots, namely, the branches G-B and E-B. The loading stage follows branch G-B since (1) it is a stable branch and (2) b^*, as well as m, is continuous at point G. At point B, a negative perturbation of p^* at $p^* = p_B^*$ results

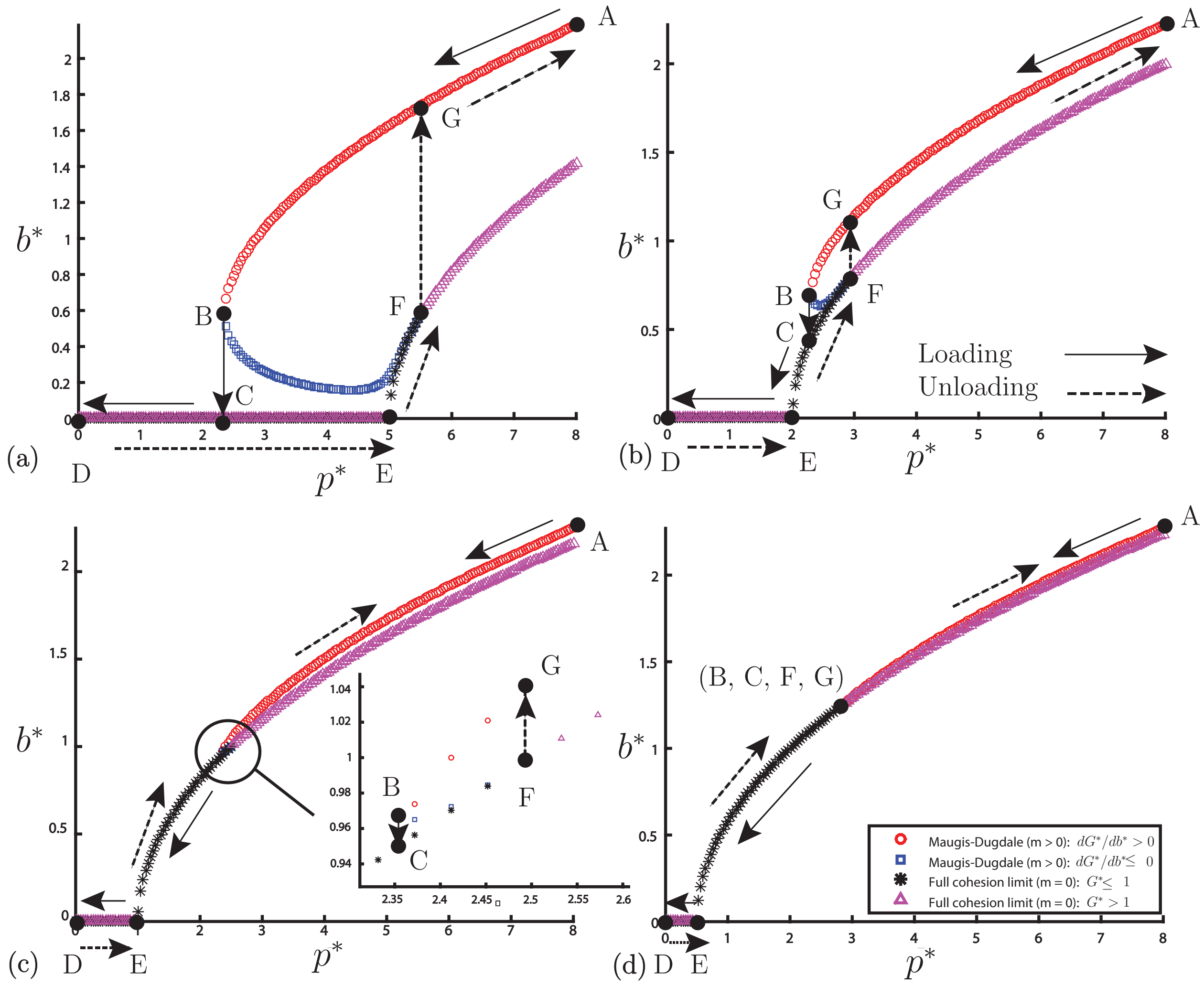

Figure 6.2: Evolution of b^* of a adhesive crack during one loading-unloading cycle with (a) $\sigma_0^* = 5$, (b) $\sigma_0^* = 2$, (c) $\sigma_0^* = 1$ and (d) $\sigma_0^* = 0.5$. The unloading stage starts from $p^* = 0$.

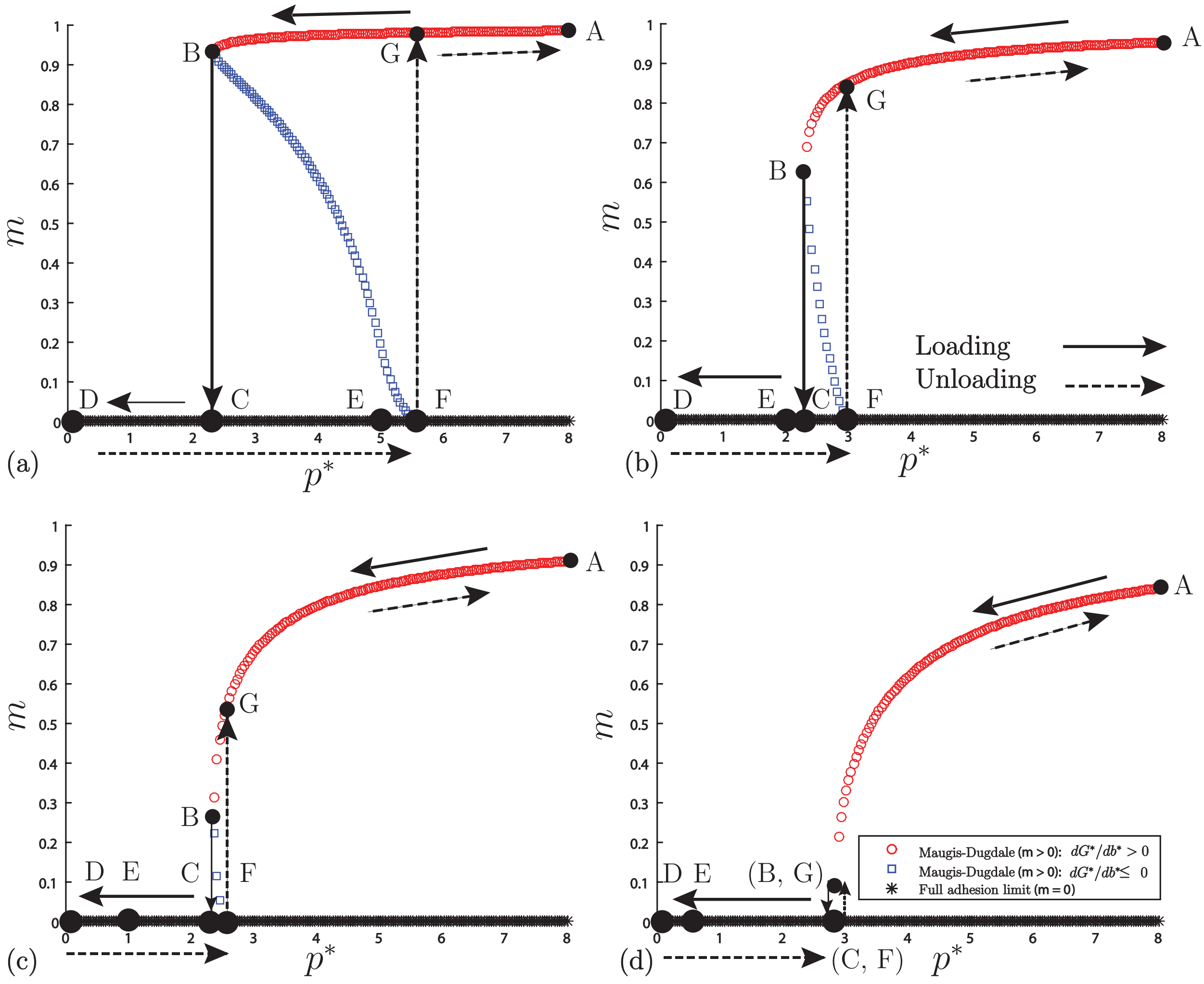

Figure 6.3: Evolution of m of a adhesive crack during one loading-unloading cycle with (a) $\sigma_0^* = 5$, (b) $\sigma_0^* = 2$, (c) $\sigma_0^* = 1$ and (d) $\sigma_0^* = 0.5$. The unloading stage starts from $p^* = 0$.

in the snap-in, i.e., an instantaneous closure of the adhesive crack within the B-C branch where p^* is kept constant. Within the C-D branch, the adhesive crack remains closed, see Fig. 6.2(a), and the adhesive zone is instantaneously extended to the entire crack surface, see Fig. 6.3(a).

The entire unloading stage can be divided into four branches, namely, D-E, E-F, F-G and G-A. The adhesive crack remains closed within the D-E branch until point E is reached where the adhesive crack is nucleated. The corresponding p^* at E can be solved analytically from the full cohesion limit:

$$p_E^* = \sigma_0^*. \tag{6.38}$$

Along the E-F branch, the adhesive crack is propagating ($G^* < 1$) with $m = 0$ until point F is reached. F is the intersection of the full cohesion limit and the unstable branch of the Maugis-Dugdale transition. Therefore, the root, $p^* = p_F^*$, results in $G^* = 1$ in the full cohesion limit and p_F^* is available in the closed-form:

$$p_F^* = \sigma_0^* + \frac{3}{2}(\sigma_0^*)^{-2/3}. \tag{6.39}$$

Because point F is instable, the pull-off occurs, i.e., the adhesive crack is propagating instantaneously where p^* is kept constant within the branch F-G. This instable propagation stops at the next stable stage at point G of the Maugis-Dugdale model. After point G ($p^* > p_G^*$), the unloading and loading stages are reversible since it is in the static equilibrium. Consequently, the hysteresis/energy dissipation of the adhesive crack associated with $\sigma_0^* = 5$ occurs within $p^* \in [p_B^*, p_F^*]$.

When $\sigma_0^* = 2$, the unstable points B and F are approaching to each other in Fig. 6.2(b). At the unstable point B, an instantaneous jump onto the full adhesion limit (instead of a snap-in) occurs. Following the C-E branch, the crack is completely closed when $p^* < p_E^*$. The unloading stage follows the same branches in Fig. 6.2(a) and 6.3(a). It is obvious that the energy dissipation only occurs within a smaller range, see Fig. 6.2(b). The decrease of the hysteresis range is confirmed in the rest of the figures in Fig. 6.2 where σ_0^* is even smaller. This trend shows that Tabor's parameter, σ_0^*, is correlated with the hysteresis/energy dissipation of the single adhesive crack.

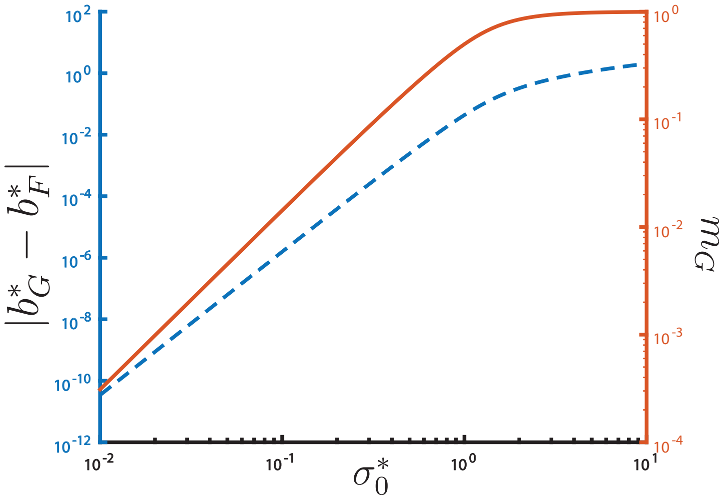

Figure 6.4: The dual roots of the Maugis-Dugdale transition when $p^* = p_F^*$. The dashed curve is associated with b^*. The colored figure is available online.

When $\sigma_0^* = 1$, the instantaneous jump at points B and F can still be visualized in the detailed plot in Fig. 6.2(c). However, as σ_0^* is decreased to 0.5, the points B, C, F and G are visually coincident, see Fig. 6.2(d). To investigate the validity of this observation, a program is developed to find the possible dual (non-negative) roots at points F and G (i.e., b_F^*, b_G^*, m_F and m_G) at $p^* = p_F^*$ and the corresponding results are in Fig. 6.4. Since the full cohesion limit is applied at F, see Fig. 6.3, then $m_F = 0$. The absolute difference, $|b_F^* - b_G^*|$ and m_G are plotted against σ_0^*. As σ_0^* decreases from 10 to 0.01, the dual roots, b_F^* and b_G^*, as well as m_F and m_F, still exist with a decreasing difference. It is expected that the difference of the dual roots becomes zero when $\sigma_0^* \to 0$ (the rigorous proof is currently not available). According to Rolle's theorem, the unstable point B exists (e.g., $b_B^* \in [b_F^*, b_G^*]$ and $m_B \in [m_F, m_G]$). Therefore, the instantaneous jump always occurs at point B regardless of $\sigma_0^* > 0$. As the surface energy w approaches zero, it is expected, from the trend observed in Figs. 6.2, that (b^*, p^*) at B, C, F and G are infinite and the reversible portion of the Mangis-Dugdale model is vanishing. This irregular phenomenon is due to the fact that b^* and p^* are normalized by w. If the dimensional variables are used, the loading-unloading cycle should be reversible with points, B, C, F and G, at $(0, 0)$.

Important observations of the hysteresis loading-unloading loop of the adhesive crack are summarized blow:

Loading stage:

1. the snap-in (instantaneous closure) of the adhesive crack occurs when $p^* = \min(p_B^*, \sigma_0^*)$;
2. the instantaneous jump onto the full cohesion limit occurs if $p^* = p_c^*$ and $p_B^* > p_E^*$.

Unloading stage:

1. the adhesive crack has hysteresis loading-unloading cycle as long as the unloading stage starts at $p^* < p_B^*$;
2. the unloading and loading stages are reversible within $[p_F^*, \infty]$ after the instantaneous jump at $p^* = p_F^*$ from the full cohesion limit to the Maugis-Dugdale transition.

It should be noticed that the unloading stages, illustrated in Figs. 6.2 and 6.3, all start from $p^* = 0$. If the adhesive crack is unloaded at a positive minimum, $p_D^* > 0$, we may have the following three possibilities:

- $p_D^* < p_E^*$: the adhesive crack is unloaded from closure and the unloading stage follows the same path in Fig. 6.2 (i.e., D-E-F-G-A);
- $p_E^* < p_D^* < p_B^*$: the cohesive crack is unloaded from a positive size in the cohesion limit and follows by the unloading path: D-F-G-A.
- $p_D^* \geq p_B^*$: the adhesive crack is unloaded with a finite crack size followed by a reversible unloading stage, i.e., loading-unloading cycle is no longer hysteresis .

After the removal of the redundant roots in Fig. 6.2, b^* vs. p^* curves associated with different σ_0^*, as well as the non-adhesive (DMT) limit and the JKR limit, are illustrated in Fig. 6.5(a) (loading stage) and Fig. 6.5(b) (unloading stage). Note that the unloading stage starts after p^* reaches zero. It is clear that the Maugis-Dugdale model has the tendency to approach the non-adhesive (DMT) limit and the JKR limit as $\sigma_0^* \to 0$ and $\sigma_0^* \to \infty$.

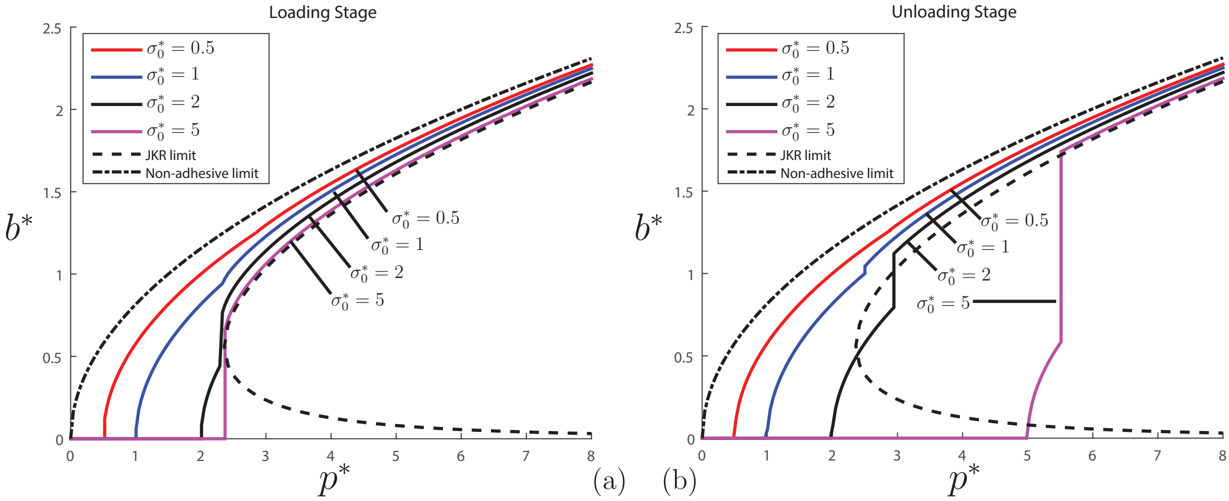

Figure 6.5: b^* vs. p^* associated with different σ_0^* at (a) loading (b^* decreases) and (b) unloading stage (b^* increases). p^* reaches zero at the end of loading stage. The colored figure is available online.

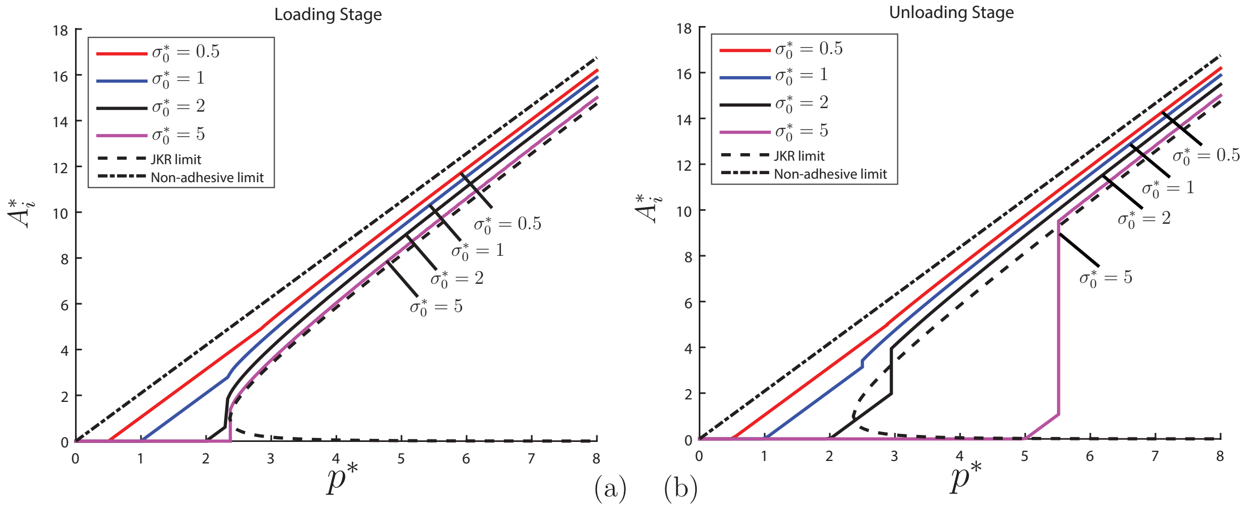

Figure 6.6: A_i^* vs. p^* associated with different σ_0^* at (a) loading (A_i^* decreases) and (b) unloading stage (A_i^* increases). p^* reaches zero at the end of loading stage. The colored figure is available online.

The corresponding A^* vs. p^* curves, as well as the asymptotic solutions when $\sigma_0^* \to 0$ and $\sigma_0^* \to \infty$, are plotted in Fig. 6.6. As σ_0^* increases, A^* vs. p^* transits from the non-adhesive (DMT) limit to the JKR limit. Similar transition can be observed for V_i^* vs. p^* in Fig. 6.7.

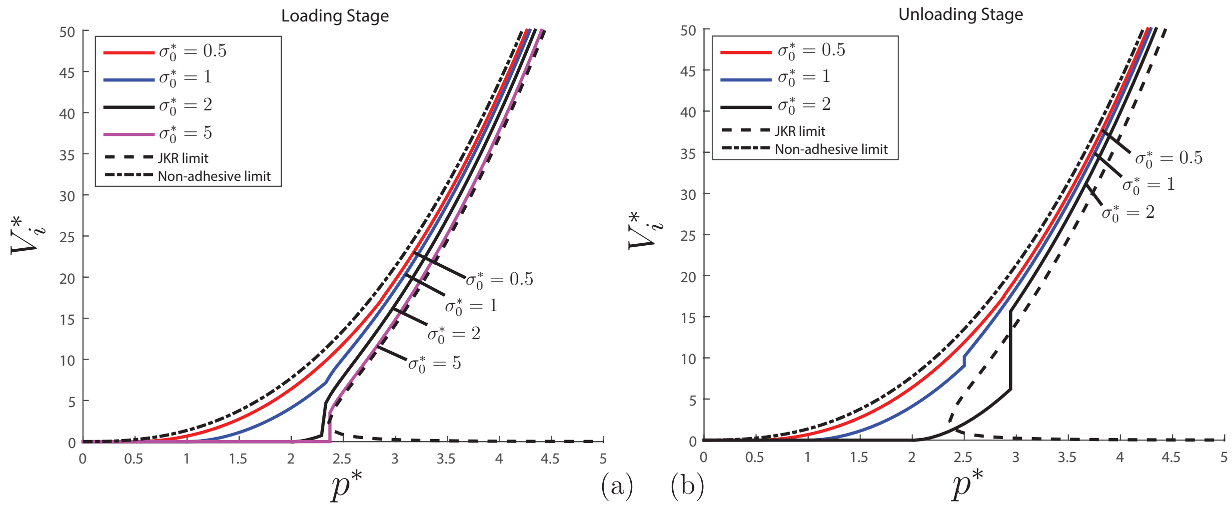

Figure 6.7: V_i^* vs. p^* associated with different σ_0^* at (a) loading (V_i^* decreases) and (b) unloading stage (V_i^* increases). p^* reaches zero at the end of loading stage. The colored figure is available online.

6.4 Elliptical Crack

In the previous chapters, an approximation to the Hertzian elliptical contact based on the Hertzian circular theory is demonstrated. For a mildly elliptical asperity (κ_1^h is close to κ_2^h), two Hertzian mildly elliptical contact models are proposed by replacing the curvature, κ^h, in the Hertzian circular contact model with the mean curvature, κ_m^h, and the geometric curvature, κ_g^h, respectively. Similarly, this approximation is applied to the elliptical non-adhesive crack.

For an elliptical adhesive crack, two mildly elliptical adhesive crack models are proposed based on the penny-shaped adhesive model. The curvature, κ^p, used in Eqs. 6.26 and 6.27, is replaced by the geometric curvature, $\kappa_g^p = \sqrt{\kappa_1^p \kappa_2^p}$, and the mean curvature, $\kappa_m^p = (\kappa_1^p + \kappa_2^p)/2$, respectively. Following Section 6.2, the dimensional b, A_i and V_i associated with the geometric/mean curvature can be numerically solved in a same manner.

6.5 Multi-Cracks Contact Model

Following the non-adhesive statistical models discussed in Section 5.3, totally four adhesive statistical models of nearly complete contact can be developed depending on the types of adhesive crack models and the PDFs which are tabulated in Table. 6.1. For each adhesive rough contact model, a corresponding non-adhesive model can be found in the previous chapter. Except for the forms of A_i and V_i, the formulation of the contact ratio, A^*, and the dimensionless average interfacial gap, $\bar{g}^*$, are exactly the same.

Table 6.1: Four adhesive statistical models with different crack models and PDFs.

Models	Adhesive crack model	PDF
Adapted GW model	Penny-shaped model	$\Phi^p(\xi^{p*})$
Nayak-Bush model	Mildly elliptical model (mean curvature)	$\Phi^p(\xi^{p*}, \kappa_m^{p*})$
Greenwood model	Mildly elliptical model (geometric curvature)	$\Phi^p(\xi^{p*}, \kappa_g^{p*})$
Asymptotic model	Penny-shaped model	$\Phi^p(\xi^{p*})$

For the sake of simplicity, only the adapted GW model are developed below.

6.5.1 Adapted GW Model

The statistical model of the adhesive rough contact is built upon the non-adhesive one discussed in Chapter 5.3.1 and the adapted GW model with adhesion is:

$$1 - A^*(\bar{p}^*) = \eta^p \int_{\bar{p}^*}^{\infty} A_i(\xi^p - \bar{p}, \kappa^p, \frac{\sigma_0}{E^*})\Phi^p(\xi^{p*})d\xi^{p*}, \tag{6.40}$$

$$\bar{g}^*(\bar{p}^*) = \frac{1}{\sqrt{m_0^h}}\eta^p \int_{\bar{p}^*}^{\infty} V_i(\xi^p - \bar{p}, \kappa^p, \frac{\sigma_0}{E^*})\Phi^p(\xi^{p*})d\xi^{p*}. \tag{6.41}$$

From the governing equations, Eqs. (6.4) and (6.5), the unknowns, b and m, are only dependent on $(\xi^p - \bar{p}, \kappa^p, \sigma_0/E^*)$ and so do A_i and V_i. The asperity density, η^p, and the constant curvature, κ^p, can be calculated based on McCool's solution in Eqs. (2.43) and (2.45) with a different superscript "p":

$$\eta^p = \frac{1}{6\sqrt{3}\pi}\frac{m_4^p}{m_2^p}, \tag{6.42}$$

$$\kappa^p = \frac{8}{3}\left(\frac{\pi}{m_4^p}\right)^{-1/2}. \tag{6.43}$$

The only difference between the adhesive and non-adhesive models is the single crack area and the corresponding trapped volume. In the previous section, the crack area and the trapped volume are derived in the following dimensionless forms:

$$A_i^* = A_i / \left[\frac{81\pi E^* w}{16(\kappa^p)^2}\right]^{2/5}, \quad V_i^* = V_i / \left(\frac{3w}{2\kappa^p}\right).$$

Note that the adhesive crack model is driven by the dimensionless pressure, $p^* = (\xi^p - \bar{p}) / \left[\frac{\pi^2 (E^*)^2 w^2 \kappa^p}{72}\right]^{1/5}$, see Eq. (6.4). This normalization is different from that used in the non-adhesive contact model where $\xi^{p*} = \xi^p / \sqrt{m_0^p}$. A transformation between p^* and ξ^{p*} is found below:

$$p^* = (\xi^{p*} - \bar{p}^*) C, \tag{6.44}$$

where the constant C is

$$C = \sqrt{m_0^p} / \left[\frac{\pi^2 (E^*)^2 w^2 \kappa^p}{72}\right]^{1/5}. \tag{6.45}$$

Consequently, the non-adhesive formulations shown above can be easily adapted to the following general forms when the dimensionless forms of A_i and V_i are used:

$$1 - A^*(\bar{p}^*) = C_1 \int_{\bar{p}^*}^{\infty} A_i^*(\sigma_0^*, p^*) \Phi^p(\xi^{p*}) d\xi^{p*}, \tag{6.46}$$

$$\bar{g}^*(\bar{p}^*) = C_2 \int_{\bar{p}^*}^{\infty} V_i^*(\sigma_0^*, p^*) \Phi^p(\xi^{p*}) d\xi^{p*}, \tag{6.47}$$

where

$$C_1 = \eta^p \left[\frac{81\pi E^* w}{16(\kappa^p)^2}\right]^{2/5}, \tag{6.48}$$

$$C_2 = \frac{\eta^p}{\sqrt{m_0^h}} \frac{3w}{2\kappa^p}. \tag{6.49}$$

Due to the snap-in of the adhesive cracks and the hysteresis occurs in the unloading stage, the above general form should be rewritten in the loading and unloading stage, separately. A similar adhesive model in the JKR limit including the loading-unloading hysteresis is recently proposed by Ciavarella et al. [34].

Loading stage

In the loading stage, A_i^* and V_i^* are zero due to the snap-in of the adhesive crack when $p^* \leq$

$p_L^* = \min(p_B^*, \sigma_0^*)$ (for example, Fig. 6.2(a)). Consequently, p_L^* should be used as the lower bound of the integrals in the statistical model since A_i^* and V_i^* are zero when $p^* < p_L^*$. As a matter of fact, final forms of $1 - A^*$ and $\bar{g}^*$ in the loading stage are

$$1 - A^*(\bar{p}^*) = C_1 \int_{p_L^*/C+\bar{p}^*}^{\infty} A_i^*(\sigma_0^*, p^*)\Phi^p(\xi^{p*})d\xi^{p*}, \tag{6.50}$$

$$\bar{g}^*(\bar{p}^*) = C_2 \int_{p_L^*/C+\bar{p}^*}^{\infty} V_i^*(\sigma_0^*, p^*)\Phi^p(\xi^{p*})d\xi^{p*}, \tag{6.51}$$

where the lower bound of ξ^{p*} is determined based on Eq. (6.44).

Once the maximum load $\bar{p}^* = \bar{p}^*_{\text{max}}$ is reached at the end of the loading stage, each adhesive crack enters the unloading stage with different p^*. Then, the non-contact ratio in Eq. (6.46) can be rewritten as:

$$1-A^*(\bar{p}^*_{\text{max}}) = C_1 \left[\underbrace{\int_{\bar{p}^*_{max}}^{p_B^*/C+\bar{p}^*_{max}} A_i^*(\sigma_0^*, p^*)\Phi^p(\xi^{p*})d\xi^{p*}}_{\text{irreversible portion}} + \underbrace{\int_{p_B^*/C+\bar{p}^*_{max}}^{\infty} A_i^*(\sigma_0^*, p^*)\Phi^p(\xi^{p*})d\xi^{p*}}_{\text{reversible portion}} \right]. \tag{6.52}$$

A similar formulation can also be obtained for $\bar{g}^*$. The cracks involved in the first integral of Eq. (6.52) are closed after snap-in. Therefore, the first integral is zero. Similarly, the remainder of the cracks (in the second integral of Eq. (6.52)) are still opened and governed by the Maugis-Dugdale model. The reason why the first and second term on the right hand side of Eq. (6.52) are named the "irreversible portion" and the "reversible portion", respectively, is given below.

Unloading stage

In the unloading stage, the dimensionless average contact pressure, $\bar{p}^*$, monotonically decreases from $\bar{p}^*_{max}$. According to the summary of the observation generalized in the end of Section 6.3, the cracks unloaded from the close status and open status have the irreversible and reversible loading-unloading cycle, respectively. This is the main reason that the first and second integral are referred to as the "irreversible portion" and "*reversible portion*".

In order to track the reversible cracks in the unloading stage, the integral limits of the corresponding integral are the same as that in the "reversible portion" in Eq. (6.52). The rest of the adhesive cracks are all irreversible. Then, the corresponding non-contact ratio in the unloading stage becomes

$$1 - A^*(\bar{p}^*) = C_1 \left[\int_{p_E^*/C+\bar{p}^*}^{p_B^*/C+\bar{p}_{max}^*} A_i^*(\sigma_0^*, p^*)\Phi^p(\xi^{p*})d\xi^{p*} + \int_{p_B^*/C+\bar{p}_{max}^*}^{\infty} A_i^*(\sigma_0^*, p^*)\Phi^p(\xi^{p*})d\xi^{p*} \right]. \tag{6.53}$$

A_i^* in the first integral of Eq. (6.53) remains zero when $p^* < p_E^*$ and is solved by the Maugis-Dugdale model when $p^* > p_F^*$. A_i^* in the second integral should be solved by the Maugis-Dugdale model alone. Since part of the cracks in the first integrals are either in closure or in the full cohesion limit and the corresponding value of A_i^* in the unloading stage is lower than that in the loading stage, see Figs. 6.2 and 6.6. This is a clear sign that the non-contact ratio, $1 - A^*$, in the unloading stage is less than that in the loading stage.

Similarly, the average interfacial gap in the unloading stage can be written as:

$$\bar{g}^*(\bar{p}^*) = C_2 \left[\int_{p_E^*/C+\bar{p}^*}^{p_B^*/C+\bar{p}_{max}^*} V_i^*(\sigma_0^*, p^*)\Phi^p(\xi^{p*})d\xi^{p*} + \int_{p_B^*/C+\bar{p}_{max}^*}^{\infty} V_i^*(\sigma_0^*, p^*)\Phi^p(\xi^{p*})d\xi^{p*} \right]. \tag{6.54}$$

Up till now, the adhesive contact model is built in the loading and unloading stage based on the adapted GW model in the non-adhesive limit. However, it is not clear which inputs have the major effect on the results, namely, A^* and $\bar{g}^*$ for a given dimensionless pressure, $\bar{p}^*$. In the rest of the section, the parameters used in the above statistical models, namely, σ_0^*, C, C_1, C_2, are reorganized and the multi-scale nature of the Tabor's parameter, σ_0^*, is also explored.

In order to simplify the formulation, three dimensionless moments of the "pressure surface" are defined:

$$m_i^{p*} = m_i^p/(E^*)^2, \quad i = 0, 2, 4. \tag{6.55}$$

As shown in Section 6.3, σ_0^* is an indicator showing (i) how hysteresis the loading-unloading cycle of the adhesive crack is and (ii) the status of adhesive contact towards the non-adhesive limit and JKR limit. At the first glance, σ_0^* may only be used for the single crack just like the Tabor's parameter for the single asperity contact. However, κ^p (Eq. (6.43)) in σ_0^* is a multi-scale parameter since (i) m_4^p is related to the rough surface and (ii) it depends on the scales included in the roughness (Eq. (2.58)). Thus, σ_0^* is also dependent of the roughness and the same conclusion is also drawn by Ciavarella [33] using the statistical model with the adhesive crack in the JKR limit.

Substituting κ^p (Eq. (6.43)) into the dimensionless σ_0^* in Eq. (6.4), we can get the following form

$$\sigma_0^* = \left(\frac{3}{\sqrt{\pi}}\right)^{3/5} (z_0)^{-2/5} \left(\frac{\sigma_0}{E^*}\right)^{3/5} (m_4^{p*})^{-1/10}. \tag{6.56}$$

The transformation scale, C, (Eq. (6.45)) can be expanded similarly:

$$C = \left(\frac{3}{\sqrt{\pi}}\right)^{3/5} (z_0)^{-2/5} \left(\frac{\sigma_0}{E^*}\right)^{-2/5} \sqrt{m_0^{p*}}(m_4^{p*})^{-1/10}. \tag{6.57}$$

Substituting Eq. (6.57), η^p (the form is similar to Eq. (2.43) with different superscript: p) and κ^p (Eq. (6.43)), then the constant, C_1, in front of the integral of A^* becomes

$$C_1 = \frac{\sqrt{3}}{8\pi}(6\pi^2)^{2/5}(z_0)^{2/5} \left(\frac{\sigma_0}{E^*}\right)^{2/5} (m_2^{p*})^{-1}(m_4^{p*})^{3/5}. \tag{6.58}$$

Similarly, C_2 is reformulated as:

$$C_2 = \frac{\sqrt{3}}{32\sqrt{\pi}} z_0 \left(\frac{\sigma_0}{E^*}\right) (m_2^{p*})^{-1}\sqrt{m_4^{p*}} m_0^h. \tag{6.59}$$

Now it is clear that, for a given dimensionless pressure, $\bar{p}^*$, (i) the non-contact ratio $1 - A^*$ depends on m_0^{p*}, m_2^{p*}, m_4^{p*}, z_0 and $\frac{\sigma_0}{E^*}$ and (ii) the average interfacial gap $\bar{g}^*$ depends on m_0^{p*}, m_2^{p*}, m_4^{p*}, m_0^{h*}, z_0 and $\frac{\sigma_0}{E^*}$. In the non-adhesive case, $1 - A^*$ only depends on α^p and $\bar{g}^*$ on α^p and α^h.

6.6 Numerical Results

In this section, the adhesive rough surface contact between a Gaussian surface and a rigid flat is studied using the statistical model proposed in Section 6.5.1. The moments of the Gaussian surfaces are given in Table. 6.2 where $\alpha^h = \alpha^p = 2$. Ideally, the theoretical strength is only 6% of the Young's modulus, E, according to the LJ potential, see Eq. (6.3). In the practice, however, the theoretical strength is less then 6% of the Young's modulus because of the defects and roughness on the interfaces. For the most of the engineering material, $E^* \approx E$. Three different values of $\dfrac{\sigma_0}{E^*}$ are used, namely, $1/20$, $1/50$ and $1/100$. The adhesive contact status in the non-adhesive limit ($\sigma_0^* \to 0$), JKR limit ($\sigma_0^* \to \infty$) are also explored.

Table 6.2: Moments of rough surface

$m_0^h[m^2]$	m_2^h	$m_4^h[1/m^2]$	m_6^h	m_0^{p*}	m_2^{p*}	m_4^{p*}
8.35×10^{-19}	2×10^{-4}	9.58×10^{10}	6.67×10^{25}	1×10^{-4}	3.19×10^{10}	2×10^{25}

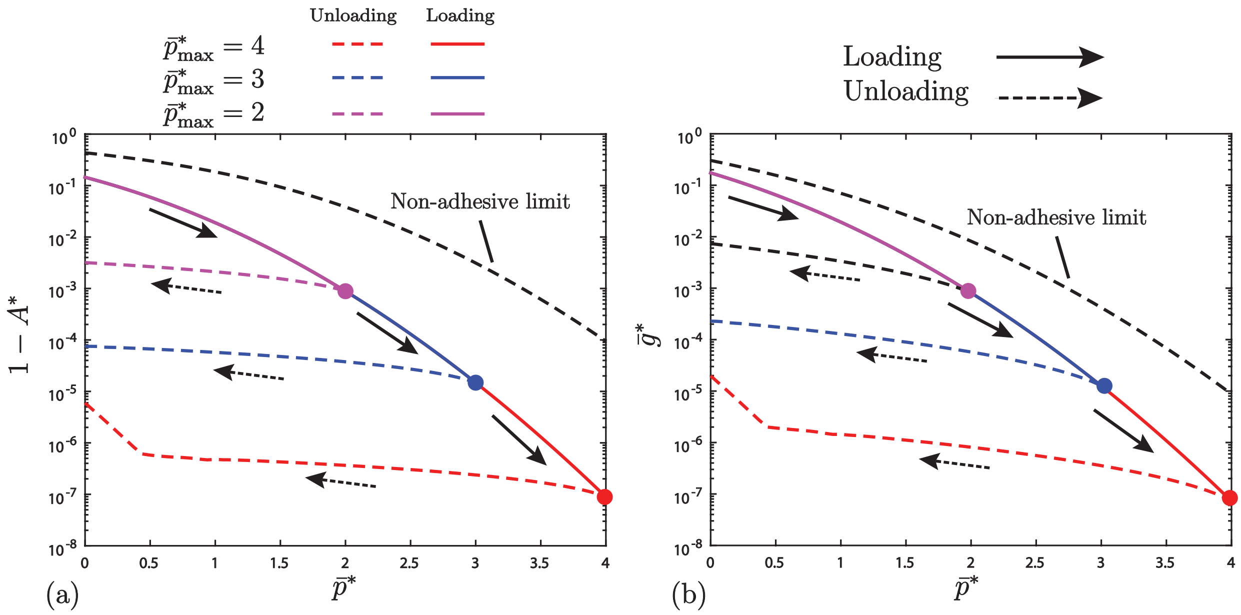

Figure 6.8: One loading-unloading cycle of (a) the non-contact ratio, $1-A^*$, and (b) the average interfacial gap, $\bar{g}^*$, associated with different $\bar{p}^*_{max} = 2,\ 3$ and 4. The colored figure is available online.

Consider a fixed $\sigma_0/E^* = 1/20$. If the adhesive rough contact is unloaded at different maximum $\bar{p}^*$ at the loading stage: $p^*_{\max} = 2,\ 3,\ 4$, the loading portions of $1 - A^*$ and $\bar{g}^*$ are partially overlapped, see Fig. 6.8. The unloading portions of associated with $\bar{p}^*_{\max} = 4$ are different from the rest and it consists two distinct regions. At larger $\bar{p}^*$, the non-contact ratio, in Fig. 6.8(a), increases relatively slow due to the fact that the reversible portion in Eq. (6.53) are negligible. A large portion of cracks are still in closure or in the full adhesion limit where the non-contact area is lower than that of the Maugis-Dugdale regime. As more and more cohesive cracks are nucleated at lower $\bar{p}^*$, the increase of non-contact ratio $1 - A^*$ is accelerated. The above reasoning can be used to explained the similar phenomenon for $\bar{g}^*$ in Fig. 6.8(b). No accelerated unloading portions are observed associated with $\bar{p}^*_{\text{max}} = 2$ and 3 because the reduction of $\bar{p}^*$ from $\bar{p}^*_{\text{max}}$ is not sufficient. We can also notice that all loading-unloading curves of adhesive rough contact lie under the non-adhesive limit. This is a sign that the statistical model proposed in Section 6.5.1 reasonably captures the increase of contact ratio due to the adhesion.

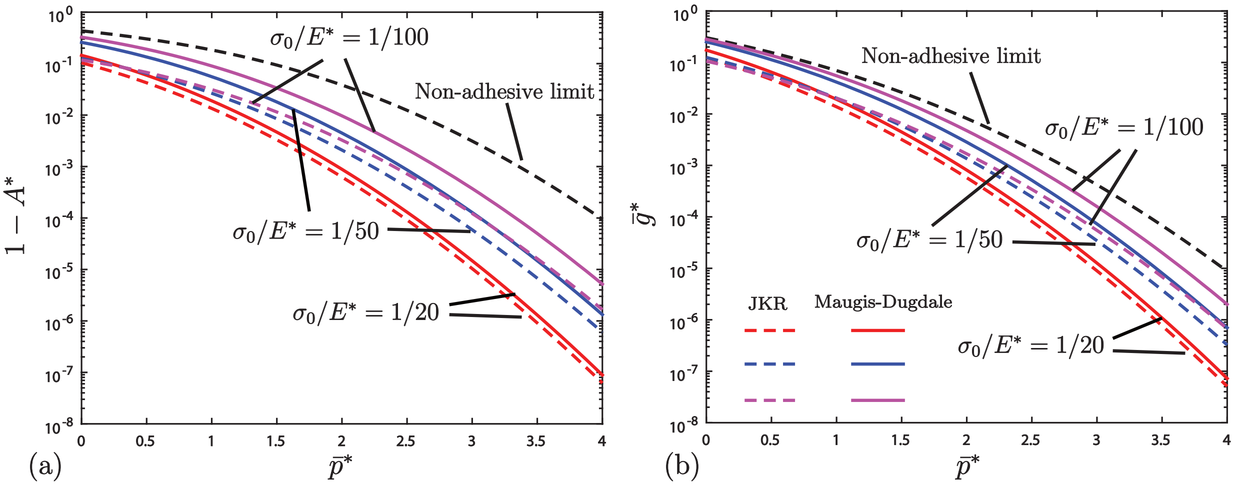

(a) (b)

Figure 6.9: (a) The non-contact ratio, $1 - A^*$, and the average interfacial gap, $\bar{g}^*$, of the rough surface #1 associated with various $\sigma_0/E^* = 1/20,\ 1/50,\ 1/100$ in the loading stage. Black dashed line indicates non-adhesive limit results. Dashed line with other color represents the results in the JKR limit.

If the unloading stage starts from $\bar{p}^* = \bar{p}^* = 4$ and σ_0/E^* decreases from $1/20$ to $1/100$, we should expect to see the corresponding non-contact ratio, $1 - A^*$, and the average interfacial gap, $\bar{g}^*$, predicted by the adhesive statistical model should gradually approach the non-adhesive limit results due to the reduction of the surface energy. This is confirmed in Fig. 6.9 for loading stage and Fig. 6.10 for unloading stage. For each value of σ_0/E^*, the corresponding $1 - A^*$ and $\bar{g}^*$ in the JKR limit are also given in Figs. 6.9 and 6.10. The results in the JKR limit are calculated based on the work of Ciavarella et al. [48]. Contrary to the non-adhesive limit, the results of statistical model gradually deviate from the JKR limit. Additionally, we may notice that the results of unloading stage are more dramatically affected by the changing of σ_0/E^*.

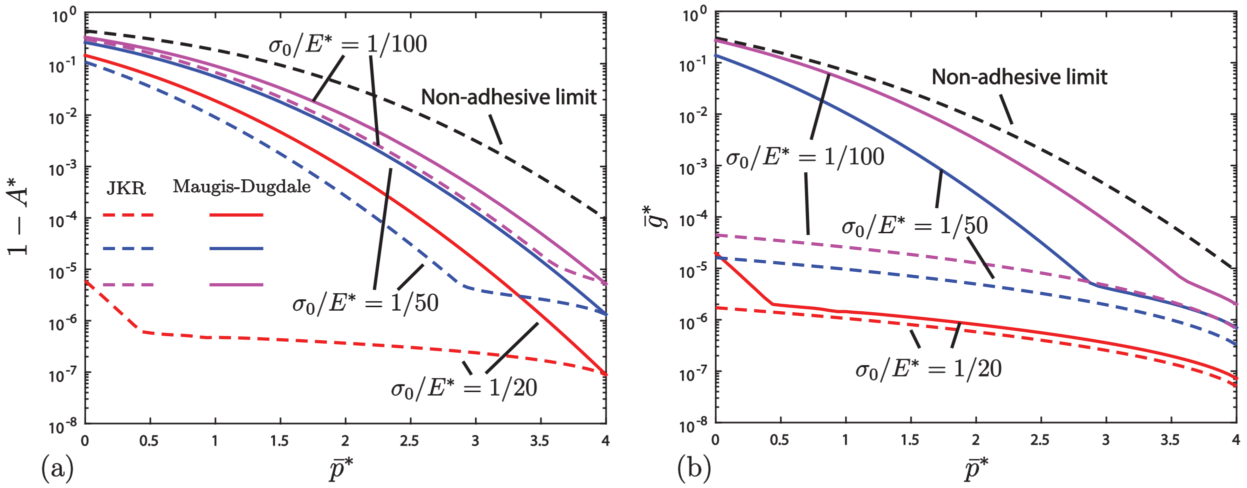

Figure 6.10: (a) The non-contact ratio, $1-A^*$, and the average interfacial gap, $\bar{g}^*$, of the rough surface $\#1$ associated with various $\sigma_0/E^*=1/20,\ 1/50,\ 1/100$ in the unloading stage. Black dashed line indicates non-adhesive limit results. Dashed line with other color represents the results in the JKR limit.

Finally, the hysteresis loop of the adhesive rough surface contact in one loading-unloading cycle associated with different σ_0/E^* are plotted in Fig. 6.11. The dissipated energy in one loading-unloading cycle can be estimated by the subtraction of the area underneath the loading (solid lien) and unloading (dashed line) stages in Fig. 6.11(b). It is reasonable to see that, as σ_0/E^* decreases, the dissipated energy becomes nearly vanishing.

6.7 Conclusions

In this chapter, the single penny-shaped adhesive crack is modeled first similar to the Maugis-Dugdale model in the adhesive Hertzian contact. The corresponding Tabor's parameter, σ_0^*, which enables the adhesive crack to transit from the non-adhesive (DMT) limit to the JKR limit as σ_0^* is varied from 0 to ∞. Unlike the adhesive Hertzian contact, the cohesion may extended to the entire crack surface and it is referred to as the full cohesion limit. The hysteresis loop of the crack area and the trapped volume in the loading-unloading cycle of the adhesive cycle is studied. It is found that a strong hysteresis loop is associated with a high Tabor's parameter, σ_0^*. The elliptic crack can be approximated by the penny-shaped crack using either the geometric curvature or the mean curvature. The adhesive adapted GW model at nearly complete contact is developed using the penny-shaped adhesive crack to predict the non-contact

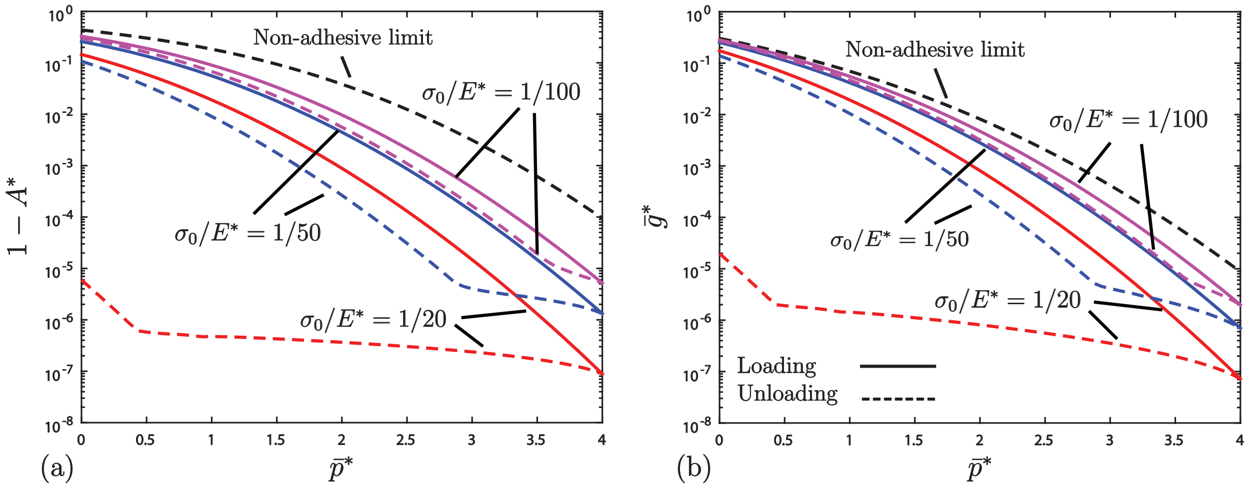

Figure 6.11: One loading-unloading cycle of (a) the non-contact ratio, $1-A^*$, and the average interfacial gap, $\bar{g}^*$, of the rough surface #1 associated with various $\sigma_0/E^* = 1/20,\ 1/50,\ 1/100$.

ratio and the average interfacial gap. For the fixed equilibrium separation of atoms, z_0, and bandwidth parameter, α^h and α^p, the numerical results shows that the stickiness of the rough surface is governed by σ_0/E^*, m_0^{p*} and m_4^{p*}. Either one of the parameters: p_0^* and C can be used to predict the stickiness of the rough surface contact.

References

[1] Johnson, K.L., Kendall, K. and Roberts, A.D., 1971. Surface energy and the contact of elastic solids. Proceedings of the Royal Society of London A: Mathematical, Physical and Engineering Sciences, **324**(1558), pp.301-313.

[2] Derjaguin, B.V., Muller, V.M. and Toporov, Y.P., 1975. Effect of contact deformations on the adhesion of particles. Journal of Colloid and Interface Science, **53**(2), pp.314-326.

[3] Tabor, D., 1977. Surface forces and surface interactions. Journal of Colloid and Interface Science, **58**(1), pp.2-13.

[4] Maugis, D., and Barquins, M., 1978, Fracture mechanics and the adherence of viscoelastic bodies, Journal of Physics D: Applied Physics, **10**, pp.1989-2023.

[5] Maugis, D., 1992. Adhesion of spheres: the JKR-DMT transition using a Dugdale model. Journal of Colloid and Interface Science. **150**(1), pp.243-269.

[6] Griffith, A.A., 1920. The phenomena of rupture and flow in solids. Phyilosophical Transactions of the Royal Society A: Mathematical, Physical and Engineering Science, **221**, pp.163-198.

[7] Barenblatt, G.I., 1962. The mathematical theory of equilibrium cracks in brittle fracture. Advances in Applied Mechanics, **7**(1), pp. 55-129.

[8] Rice, J.R., 1968. A path independent integral and the approximate analysis of strain concentration by notches and cracks. ASME Journal of Applied Mechanics, **35**(2), pp.379-386.

[9] Greenwood, J.A., and Johnson, K.L., 1998, An alternative to the Maugis model of adhesion between elastic spheres, Journal of Physics D: Applied Physics, **31**, pp.3279-3290.

[10] Carpick, R.W., Ogletree, D.F. and Salmeron, M., 1999. A general equation for fitting contact area and friction vs load measurements. Journal of Colloid and Interface Science, **211**(2), pp.395-400.

[11] Schwarz, U.D., 2003. A generalized analytical model for the elastic deformation of an adhesive contact between a sphere and a flat surface. Journal of Colloid and Interface Science, **261**(1), pp.99-106.

[12] Johnson, K.L. and Greenwood, J.A., 1997. An adhesion map for the contact of elastic spheres. Journal of Colloid and Interface Science, **192**(2), pp.326-333.

[13] Barthel, E., 1998, On the Description of the adhesive contact of spheres with arbitrary interaction potentials Journal of Colloid and Interface Science, **200**, pp.718.

[14] Fuller, K.N.G. and Tabor, D., 1975, The effect of surface roughness on the adhesion of elastic solids. Proceedings of the Royal Society of London A: Mathematical, Physical and Engineering Sciences, **345**(1642), pp.327-342.

[15] Maugis, D., 1996. On the contact and adhesion of rough surfaces. Journal of Adhesion Science and Technology, **10**(2), pp.161-175.

[16] Adams, G.G., Müftü, S. and Azhar, N.M., 2003. A scale-dependent model for multi-asperity contact and friction. ASME Journal of Tribology, **125**(4), pp.700-708.

[17] Morrow, C., Lovell, M. and Ning, X., 2003. A JKRDMT transition solution for adhesive rough surface contact. Journal of Physics D: Applied Physics, **36**(5), p.534.

[18] Zhang, W., Jin, F., Zhang, S. and Guo, X., 2014. Adhesive contact on randomly rough surfaces based on the double-Hertz model. ASME Journal of Applied Mechanics, **81**(5), p.051008.

[19] Muller, V. M., Derjaguin, B. V. and Toporov, Y. P. 1983. On two methods of calculation of the force of sticking of an elastic sphere to a rigid plane. Colloids and Surfaces. **7**, pp.251-259.

[20] Greenwood, J.A., 1997, Adhesion of elastic spheres. Proceedings of the Royal Society of London A: Mathematical, Physical and Engineering Sciences, **453**(1961), pp.1277-1297.

[21] Persson, B.N.J., 2002. Adhesion between an elastic body and a randomly rough hard surface. The European Physical Journal E: Soft Matter and Biological Physics, **8**(4), pp.385-401.

[22] Jackson, R.L., 2011. A model for the adhesion of multiscale rough surfaces in MEMS, IEEE 43rd Southeastern Symposium, pp.257-262.

[23] Afferrante, L., Ciavarella, M. and Demelio, G., 2015. Adhesive contact of the Weierstrass profile. Proceedings of the Royal Society of London A: Mathematical, Physical and Engineering Sciences, **471**(2182), p.20150248.

[24] Yang, C., Persson, B.N.J., Israelachvili, J. and Rosenberg, K., 2008. Contact mechanics with adhesion: Interfacial separation and contact area. European Physics Letters, **84**(4), p.46004.

[25] Carbone, G., Scaraggi, M. and Tartaglino, U., 2009. Adhesive contact of rough surfaces: comparison between numerical calculations and analytical theories. The European Physical Journal E, **30**(1), pp.65-74.

[26] Medina, S. and Dini, D., 2014. A numerical model for the deterministic analysis of adhesive rough contacts down to the nano-scale. International Journal of Solids and Structures, **51**(14), pp.2620-2632

[27] Pastewka, L. and Robbins, M.O., 2014. Contact between rough surfaces and a criterion for macroscopic adhesion. Proceedings of the National Academy of Sciences, **111**(9), pp.3298-3303.

[28] Carbone, G., Pierro, E. and Recchia, G., 2015. Loading-unloading hysteresis loop of randomly rough adhesive contacts. Physical Review E, **92**(6), pp.062404.

[29] Müser, M.H., 2015. A dimensionless measure for adhesion and effects of the range of adhesion in contacts of nominally flat surfaces. Tribology International. **100**, pp.41-47.

[30] Müser, M.H. and Dapp, W.B., 2015. The contact mechanics challenge: Problem definition. arXiv preprint arXiv:1512.02403.

[31] Müser, M.H., Dapp, W.B., Bugnicourt, B., Sainsot, B., LesaffreTon, Lubrecht, T.A., Persson, B.N.J., Harris, K., Bennett, A., Schulze, K., Rohde, S., IfjuW, P., Sawyer, W.G., Angelini, T., Esfahani, H.A., Kadkhodaei, M., Akbarzadeh, S., Wu, J.J., Vorlaufer, G., Vernes, A., Solhjoo, S., Vakis, A.I., Jackson, R.L., Xu, Y., Streator, J., Rostami, A., Dini, D., Medina, S., Carbone, G., Bottiglione, F., Afferrante, L., Monti, J., Pastewka, L., Robbins, M.O., Greenwood, J.A., 2017. Meeting the Contact-Mechanics Challenge. Tribology Letters, **65**(4), p.118.

[32] Johnson, K.L., 1987. *Contact mechanics*. Cambridge University Press.

[33] Ciavarella, M., 2015. Adhesive Rough Contacts near Complete Contact. International Journal of Mechanical Science, **104**, pp.104-111.

[34] Ciavarella, M., Xu, Y. and Jackson, R.L., 2018. Some Closed-Form Results for Adhesive Rough Contacts Near Complete Contact on Loading and Unloading in the Johnson, Kendall, and Roberts Regime. ASME Journal of Tribology, **140**(1), p.011402.

[35] Greenwood, J.A., 2006. A simplified elliptic model of rough surface contact. Wear, **261**(2), pp.191-200.

[36] Maugis, D., 2000, *Contact, adhesion and rupture of elastic solids*, Springer, Berlin.

[37] Sun, C.T., and Jin, Z.H., 2012, *Fracture mechanics*. Academic Press. pp.230-235.

[38] Dugdale, D.S., 1960. Yielding of Steel Sheets Containing Slits. Journal of the Mechanics and Physics of Solids. **8**, pp.100-104.

[39] Müser, M.H., 2014. Single-asperity contact mechanics with positive and negative work of adhesion: Influence of finite-range interactions and a continuum description for the squeeze-out of wetting fluids. Beilstein Journal of Nanotechnology, **5**(1), pp.419-437.

[40] Wu, J.J., 2009. Adhesive contact between a cylinder and a half-space. Journal of Physics D: Applied Physics, **42**(15), p.155302.

[41] Wu, J.J., 2012. Numerical simulation of the adhesive contact between a slightly wavy surface and a half-space. Journal of Adhesion Science and Technology, **26**(1-3), p.331-351.

[42] Pashley, M.D., 1984. Further consideration of the DMT model for elastic contact. Colloids and surfaces, **12**, pp. 69-77.

[43] Cvijovic, D., and Klinowski, J., 1994, On the integration of incomplete elliptic integrals, Proceedings of the Royal Society of London A: Mathematical, Physical and Engineering Sciences, **444**(1922), pp.525-532.

[44] Jin, F., Guo, X. and Wan, Q., 2016. Revisiting the MaugisDugdale Adhesion Model of Elastic Periodic Wavy Surfaces. Journal of Applied Mechanics, 83(10), p.101007.

[45] Jin, F., Wan, Q. and Guo, X., 2016. A double-Westergaard model for adhesive contact of a wavy surface. International Journal of Solids and Structures, **102**, pp.66-76.

[46] Xu, Y., Jackson, R.L., Marghitu, D.B., 2014. Statistical Model of Nearly Complete Elastic Rough Surface Contact. International Journal of Solids and Structures. **51**, pp.1075-1088.

[47] Nayak, P.R., 1971. Random Process Model of Rough Surfaces. ASME Journal of Lubrication Technology. **93**, pp.398-407.

[48] Ciavarella, M., 2017, A note on the possibility of roughness enhancement of adhesion in Persson's theory, International Journal of Mechanical Sciences, **121**, pp.119-122.

[49] Ciavaarella, M., 2016, On Pastewka and Robbins criterion for macroscopic adhesion of rough surfaces, ASME Journal of Tribology, **139**, p.031404.

Chapter 7

Comparison of the Statistical Models with the Numerical Models

In this chapter, a comprehensive comparison is performed between (1) the statistical models of early contact, (2) the statistical models of nearly complete contact, (3) the Persson model and (4) the BEM where the adhesion is not included. Similar comparisons have been done by many researchers, e.g., Hyun et al. [1], Campañá and Müser [2], Jackson and Green et al. [3], Putignano et al. [4], Yastrebov et al. [5, 6], etc. However, the roughness either generated by the algorithm (e.g., [1]) or measured by the profilometry (e.g., [3]) cannot guarantee that the rough surface is isotropic, Gaussian and fractal at the same time. One such rough surface generation algorithm is developed in Section 7.1. This algorithm is further tested in Section 7.2 to show the Gaussianity and the isotropy of the generated rough surfaces. After a brief discussion of the inputs (e.g., the loading history, roughness data and the statistical parameters) of the BEM, statistical models and the Persson model in Section 7.3, the comparisons between the predicted values of A^* and $\bar{g}^*$ are given in Section 7.4. The discussion and the conclusion are given in Section 7.5 and 7.6.

7.1 Rough Surface Generation

In many rough surface contact models, e.g., the finite element (FE) model [1], the boundary element (BE) model [7] and Jackson-Streator model [8], the contact interface is modeled as rough boundary. The rough surface is either measured by the profilometer or created by the computer simulation. Many rough surface algorithms are proposed in the past literatures (e.g., Weierstrass-Mandelbrot (WM) function [9], successive random midpoint [10], Hu and Tonder [11] and Wu [12]). The researchers prefer to generate the rough surfaces by the computer simulation since the statistical parameters of the generated rough surfaces are controllable. Another reason is that it can quickly generate multiple surfaces which are *statistically similar*, i.e., the corresponding moments, m_n^h, are the same. Since rough surfaces are a random process, the statistically similar surfaces have an *infinite* number of realizations. For a controlled manufacturing process, the engineering surfaces of the same parts of the products may also be statistically similar.

In this section, an algorithm of generating rough surfaces, recently developed by Xu and Jackson [15], is introduced in detail. This algorithm can guarantee that the generated surfaces are approximately *isotropic*, *Gaussian* and *fractal*. This is motivated by the objective of this chapter to compare different analytical models which are built upon certain restrictions of rough surfaces. The statistical models need the rough surface to be isotropic and Gaussian. The Persson model requires the surface to be fractal. The new approach is developed based on the algorithms proposed by Hu and Tonder [11] and Wu [12].

The fractal and the isotropy can be satisfied if we assume that the rough surface has the axisymmetric power spectrum density (PSD) shown in Eq. (2.18) where $k_l = k_r$. The values of k_s and k_l in (2.18) are directly assigned. The constant, C, in the PSD represents the amplitude of the roughness and can be indirectly assigned by prescribing m_2^h (see Eq. (2.22)):

$$C = \frac{4(1-H)m_2^h}{(2\pi)^3\left[k_s^{2-2H} - k_l^{2-2H}\right]}. \tag{7.1}$$

In order to guarantee that $h(x,y)$ is Gaussian, the rough surface is initialized by a Gaussian surface, $h_0(x,y)$, generated by the Gaussian generator. Then, through the following convolution:

$$h(x,y) = \int_{-\infty}^{\infty}\int_{-\infty}^{\infty} f(x-x', y-y')h_0(x',y')dx'dy', \tag{7.2}$$

and $h(x,y)$ should also be Gaussian [11]. Applying the Fourier transform in Eqs. (2.1) and (2.2) to the above convolution, we have

$$\mathcal{F}[h](k_x,k_y) = \mathcal{F}[f](k_x,k_y)\mathcal{F}[h_0](k_x,k_y). \tag{7.3}$$

Resorting to Eq. (2.9), the absolute value of the transfer function can be determined as:

$$|\mathcal{F}[f](k_x, k_y)| = \sqrt{S^h(k_x, k_y)/S[h_0](k_x, k_y)}. \tag{7.4}$$

In order to utilize the inverse Fourier transform to reconstruct the rough surface, $h(x, y)$, the spectrum of $f(x, y)$ has the following complex form [12]:

$$\mathcal{F}[f](k_x, k_y) = |\mathcal{F}[f](k_x, k_y)| \left[\cos(\theta) + i \sin(\theta)\right], \tag{7.5}$$

where θ is the random phase varied between 0 and 2π. Since $h(x, y)$ is real, $\mathcal{F}[f](k_x, k_y)$ must follow *Hermitian symmetry*[1], i.e.,

$$\mathcal{F}[f](-k_x, -k_y) = \text{conj}\left(\mathcal{F}[f](k_x, k_y)\right),$$

where conj(•) is the complex conjugate operator.

7.2 Isotropy and Gaussianity of Rough Surfaces and the Corresponding "Pressure Surface"

Table 7.1: 17 surface groups.

Case	Group #	k_l[1/m]	k_s[1/m]	H	Case	Group #	k_l[1/m]	k_s[1/m]	H
1	1	16	64	0.8	3	9	1	64	0.8
	2	16	128	0.8		10	1	128	0.8
	3	16	256	0.8		11	1	256	0.8
	4	16	512	0.8		12	1	512	0.8
2	5	4	64	0.8	4	13	4	128	0.1
	6	4	128	0.8		14	4	128	0.3
	7	4	256	0.8		15	4	128	0.5
	8	4	512	0.8		16	4	128	0.7
						17	4	128	0.9

---

[1] $|\mathcal{F}[f](k_x, k_y)|$ is symmetric about axes: $k_x = 0$ and $k_y = 0$. In Wu's paper [12], Hermitian symmetry is achieved by forcing the random phase, $\theta(k_x, k_y)$, in Hermitian symmetry.

In the previous section, an algorithm of rough surface generation is proposed. Theoretically, the rough surface, as well as the corresponding "pressure surface", should be isotropic, fractal and Gaussian. The fractal surface is satisfied for each realization since the PSD in Eq. (2.18) is explicitly embedded in the surface generation algorithm. In this section, the isotropy and the Gaussianity of the generated rough surfaces and the corresponding "pressure surface" are explored.

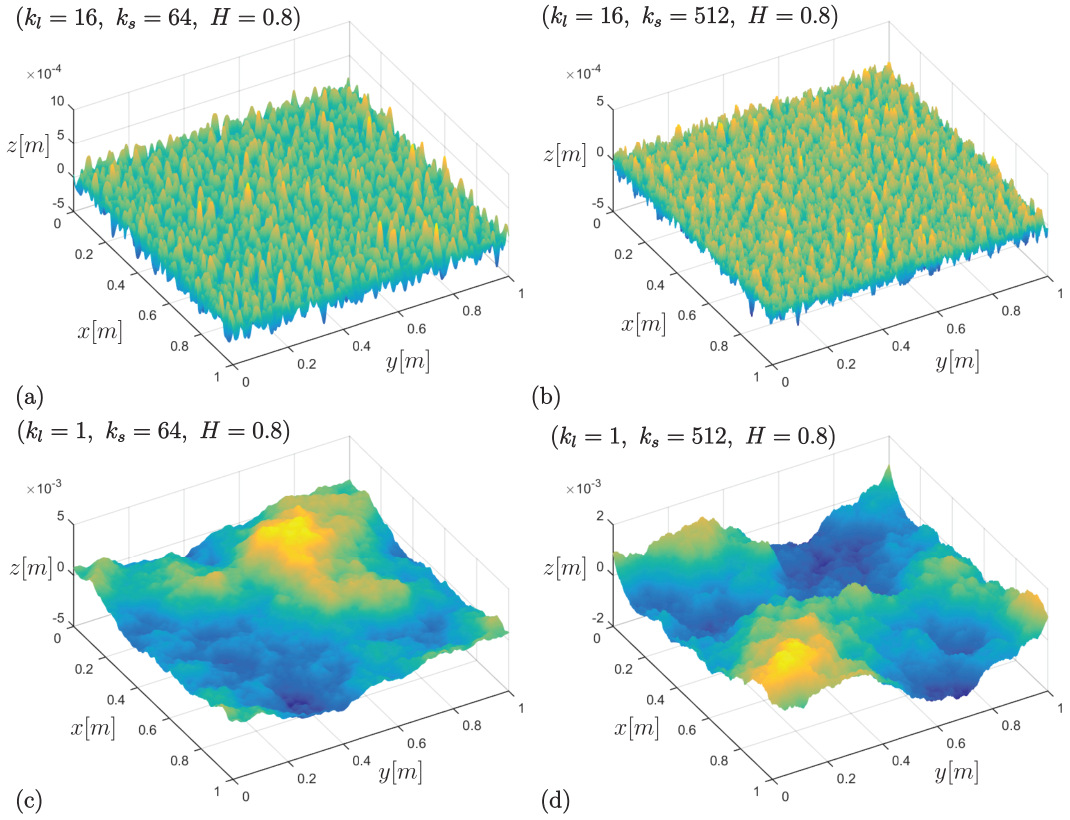

Figure 7.1: Plots of one realization of the surface group (a) #1, (b) #4, (c) #9 and (d) #12. The colored figure is available online.

Because the generated rough surfaces are used in the BEM and all computational resources have limited memory, the number of sampling points is restricted to $N_x \times N_y = 1024 \times 1024$ in this chapter. The x- and y-intervals of the sampling points are held constant. The sampling lengths in the x and y axes are $L_x = 1$ and $L_y = 1$, respectively. The moment, $m_0^{p*} = m_0^p / E^*$, is set to a constant 1×10^{-4} (equivalently, $m_2^h = 2 \times 10^{-4}$). The reason for this assignment is that the root mean square (rms) slope should be small so that the domain can be reasonably approximated by a half-space which is a fundamental assumption in the BEM model proposed in Chapter 3. The rough surfaces are generated based on the PSD in Eq. (2.18) where $k_r = k_l$. Therefore, one parameter combination (k_l, k_s, H) uniquely represents one rough surface group which contains an infinite number of statistically similar realizations due to the random phase introduced in the spectrum.

A total of 17 rough surface groups associated with different (k_l, k_s, H) are generated, see Table 7.1. Those groups are divided into four cases. Each case contains multiple groups where only one variable in (k_l, k_s, H) is changed and the other two are held constant. In cases $1-3$, the upper cut-off wavenumber is changed associated with constant k_s and H. In case 4, only H is changed. For each surface group, 1000 surfaces are generated. The corresponding "pressure surfaces" are determined by FFT based on Eq. (2.47). Figs. 7.1(a-d) illustrates four rough surfaces from surface groups $\#1$, $\#4$, $\#9$ and $\#12$, respectively.

7.2.1 Isotropy

The isotropy of a surface means that the statistics are identical along any direction [17, 18]. In this study, the isotropy is examined based on the similarity of the mean moments (over 1000 realizations) measured in the x and y directions. The corresponding standard deviations are calculated to show the dispersions of the moments over 1000 surfacess. The moments are numerically calculated based on the definitions in Eq. (2.13):

$$m_{n0}^{h(p)} = \left\langle \left(\frac{\partial^{(n/2)} h}{\partial x^{(n/2)}} \right)^2 \right\rangle \quad n = 0, 2, 4, 6 \cdots \text{ (for } x\text{)}, \tag{7.6}$$

$$m_{0n}^{h(p)} = \left\langle \left(\frac{\partial^{(n/2)} h}{\partial y^{(n/2)}} \right)^2 \right\rangle \quad n = 0, 2, 4, 6 \cdots \text{ (for } y\text{)}, \tag{7.7}$$

where the derivatives of order n at calculated using the central differentiation of the corresponding derivatives of order $n-1$. Only the moments essential to the statistical models are calculated, namely, m_n^h $(n = 2,\ 4,\ 6)$ and m_n^{p*} $(n = 2,\ 4)$.

Table 7.2 shows the average values and the std of the m_{n0}^h and m_{0n}^h $(n = 2,\ 4,\ 6)$ of 17 rough surfaces. The differences between m_{n0}^h and m_{0n}^h are insignificant comparing their mean values. The corresponding std of the moments are less than the mean value, at least, by one

Table 7.2: Moments of rough surfaces of 17 rough surface groups

Group #	m^h_{20}	m^h_{02}	$m^h_{40}[m^{-2}]$	$m^h_{04}[m^{-2}]$	$m^h_{60}[m^{-4}]$	$m^h_{06}[m^{-4}]$
1	1.97×10^{-4}	1.97×10^{-4}	9.00	9.02	6.59×10^5	6.59×10^5
	$\pm 6.47 \times 10^{-8}$	$\pm 6.62 \times 10^{-8}$	± 0.0028	± 1.39	± 410.87	± 393.61
2	1.91×10^{-4}	1.91×10^{-4}	27.01	26.97	6.94×10^6	6.94×10^6
	$\pm 5.09 \times 10^{-8}$	$\pm 5.07 \times 10^{-8}$	± 0.0057	± 2.74	$\pm 2.46 \times 10^3$	$\pm 2.41 \times 10^3$
3	1.73×10^{-4}	1.73×10^{-4}	78.90	79.85	5.43×10^7	5.43×10^7
	$\pm 3.67 \times 10^{-8}$	$\pm 3.58 \times 10^{-8}$	± 0.011	± 5.49	$\pm 1.16 \times 10^4$	$\pm 1.19 \times 10^4$
4	1.35×10^{-4}	1.35×10^{-4}	172.77	172.97	1.20×10^8	1.20×10^8
	$\pm 2.52 \times 10^{-8}$	$\pm 2.47 \times 10^{-8}$	± 0.014	± 8.48	$\pm 1.62 \times 10^4$	$\pm 1.56 \times 10^4$
5	2.00×10^{-4}	2.00×10^{-4}	5.92	5.88	4.19×10^5	4.19×10^5
	$\pm 8.44 \times 10^{-8}$	$\pm 8.32 \times 10^{-8}$	± 0.0019	± 0.87	± 253.58	± 260.08
6	1.94×10^{-4}	1.94×10^{-4}	20.48	20.44	5.23×10^6	5.23×10^6
	$\pm 6.47 \times 10^{-8}$	$\pm 6.28 \times 10^{-8}$	± 0.0043	± 2.07	$\pm 1.85 \times 10^3$	$\pm 1.81 \times 10^3$
7	1.79×10^{-4}	1.79×10^{-4}	66.15	66.10	4.49×10^7	4.49×10^7
	$\pm 4.66 \times 10^{-8}$	$\pm 4.66 \times 10^{-8}$	± 0.0088	± 4.54	$\pm 9.56 \times 10^3$	$\pm 9.86 \times 10^3$
8	1.43×10^{-4}	1.43×10^{-4}	151.37	151.35	1.05×10^8	1.05×10^8
	$\pm 3.55 \times 10^{-8}$	$\pm 3.45 \times 10^{-8}$	± 0.01	± 7.73	$\pm 1.39 \times 10^4$	$\pm 1.38 \times 10^4$
9	2.05×10^{-4}	2.05×10^{-4}	4.90	4.91	3.47×10^5	3.47×10^5
	$\pm 1.07 \times 10^{-7}$	$\pm 1.00 \times 10^{-7}$	± 0.0016	± 0.69	± 210.45	± 209.32
10	1.99×10^{-4}	1.99×10^{-4}	17.94	17.93	4.58×10^6	4.58×10^6
	$\pm 8.35 \times 10^{-8}$	$\pm 8.20 \times 10^{-8}$	± 0.0039	± 1.84	$\pm 1.58 \times 10^3$	$\pm 1.56 \times 10^3$
11	1.73×10^{-4}	1.73×10^{-4}	79.90	79.85	5.43×10^7	5.43×10^7
	$\pm 3.67 \times 10^{-8}$	$\pm 3.58 \times 10^{-8}$	± 0.011	± 5.49	$\pm 1.16 \times 10^4$	$\pm 1.19 \times 10^4$
12	1.49×10^{-4}	1.49×10^{-4}	141.29	141.45	9.83×10^7	9.83×10^7
	$\pm 4.54 \times 10^{-8}$	$\pm 4.66 \times 10^{-8}$	± 0.012	± 6.93	$\pm 1.33 \times 10^4$	$\pm 1.27 \times 10^4$
13	1.86×10^{-4}	1.86×10^{-4}	43.30	43.32	1.32×10^7	1.32×10^7
	$\pm 3.83 \times 10^{-8}$	$\pm 3.91 \times 10^{-8}$	± 0.0087	± 4.66	$\pm 4.26 \times 10^3$	$\pm 4.34 \times 10^3$
14	1.87×10^{-4}	1.87×10^{-4}	37.95	38.12	1.11×10^7	1.11×10^7
	$\pm 4.08 \times 10^{-8}$	$\pm 4.18 \times 10^{-8}$	± 0.0079	± 4.01	$\pm 3.79 \times 10^3$	$\pm 3.62 \times 10^3$
15	1.90×10^{-4}	1.90×10^{-4}	31.55	31.49	8.83×10^6	8.83×10^6
	$\pm 4.61 \times 10^{-8}$	$\pm 4.66 \times 10^{-8}$	± 0.0068	± 3.28	$\pm 3.02 \times 10^3$	$\pm 3.02 \times 10^3$
16	1.93×10^{-4}	1.93×10^{-4}	24.26	24.29	6.41×10^6	6.41×10^6
	$\pm 5.74 \times 10^{-8}$	$\pm 5.79 \times 10^{-8}$	± 0.0055	± 2.52	± 453.48	$\pm 2.22 \times 10^3$
17	1.96×10^{-4}	1.96×10^{-4}	16.78	16.79	4.12×10^6	4.12×10^6
	$\pm 7.68 \times 10^{-8}$	$\pm 6.97 \times 10^{-8}$	± 0.0037	± 1.64	$\pm 1.49 \times 10^3$	$\pm 1.26 \times 10^3$

order of magnitude. It is clear that the similarities between m^h_{n0} and m^h_{0n} $(n = 2, 6)$ exist not only in the average sense, but also for each surface. The std of m^h_{04} is surprisingly larger than that of m^h_{40} by three order of magnitude and the reason is not clear. This difference may result in a slight difference between m^h_{04} and m^h_{40} of each surface

Table 7.3 shows the average values and the std of the m^{p*}_{n0} and m^{p*}_{0n} $(n = 2,\ 4)$ of 17 rough surfaces. The std of m^{p*}_{04} is just one order of magnitude less than the mean value which may result in differences between m^{p*}_{04} and m^{p*}_{40} in some surfaces. The similarities between the m^{p*}_{n0} and m^{p*}_{0n} $(n = 2,\ 4)$ are obvious in the average sense.

Table 7.3: Moments of “pressure surface” of 17 rough surface groups.

Group #	$m_{20}^{p*}[m^{-2}]$	$m_{02}^{p*}[m^{-2}]$	$m_{40}^{p*}[m^{-4}]$	$m_{04}^{p*}[m^{-4}]$
1	2.98 $\pm 8.62 \times 10^{-4}$	2.98 $\pm 8.62 \times 10^{-4}$	2.04×10^5 ± 59.42	2.05×10^5 $\pm 3.56 \times 10^4$
2	2.98 $\pm 8.62 \times 10^{-4}$	2.98 $\pm 8.62 \times 10^{-4}$	2.37×10^6 ± 464.04	2.36×10^6 $\pm 2.80 \times 10^5$
3	23.08 ± 0.0028	23.08 ± 0.0028	2.68×10^7 $\pm 3.09e3$	2.68×10^7 $\pm 2.10 \times 10^6$
4	36.05 ± 0.0027	36.05 ± 0.0027	1.95×10^8 $\pm 1.57e4$	1.95×10^8 $\pm 1.07 \times 10^7$
5	1.96 $\pm 5.88 \times 10^{-4}$	1.96 $\pm 5.89 \times 10^{-4}$	1.30×10^5 ± 38.98	1.29×10^5 $\pm 2.27 \times 10^4$
6	6.59 ± 0.0013	6.59 ± 0.0013	1.78×10^6 ± 349.18	1.78×10^6 $\pm 2.10 \times 10^5$
7	19.11 ± 0.0023	19.11 ± 0.0023	2.22×10^7 $\pm 2.55e3$	2.22×10^7 $\pm 1.74 \times 10^6$
8	31.59 ± 0.0025	31.59 ± 0.0023	1.71×10^8 $\pm 1.41e4$	1.71×10^8 $\pm 9.71 \times 10^6$
9	1.62 $\pm 4.85 \times 10^{-4}$	1.62 $\pm 4.80 \times 10^{-4}$	1.08×10^5 ± 32.32	1.08×10^5 $\pm 1.75 \times 10^4$
10	5.77 ± 0.0011	5.77 ± 0.0011	1.56×10^6 ± 310.56	1.56×10^6 $\pm 1.85 \times 10^5$
11	23.08 ± 0.0028	23.08 ± 0.0028	2.68×10^7 $\pm 3.09 \times 10^3$	2.68×10^7 $\pm 2.10 \times 10^6$
12	29.49 ± 0.0022	29.49 ± 0.0022	1.59×10^8 $\pm 1.29 \times 10^4$	1.60×10^8 $\pm 8.73 \times 10^6$
13	13.83 ± 0.0025	13.83 ± 0.0025	4.55×10^6 ± 853.19	4.55×10^6 $\pm 5.45 \times 10^5$
14	12.14 ± 0.0022	12.14 ± 0.0023	3.83×10^6 ± 751.55	3.84×10^6 $\pm 4.63 \times 10^5$
15	10.12 ± 0.0019	10.12 ± 0.0019	3.03×10^6 ± 606.88	3.02×10^6 $\pm 3.62 \times 10^5$
16	7.80 ± 0.0015	7.80 ± 0.0015	2.19×10^6 ± 453.48	3.02×10^6 $\pm 3.62 \times 10^5$
17	5.41 ± 0.0011	5.41 ± 0.0011	1.40×10^6 ± 280.11	1.40×10^6 $\pm 1.62 \times 10^5$

As a summary, the isotropy of the generated rough surface and the corresponding “pressure surface” can not be satisfied strictly in each surface associated with the same PSD. However, the isotropy is achieved in an average sense.

7.2.2 Gaussianity

In the statistical models developed in Chapters 4 and 5, the frequently used joint PDFs of the asperity are

$$\Phi^{h(p)}(\xi^{h(p)*}), \quad \Phi^{h(p)}(\xi^{h(p)*}, \quad \kappa_m^{h(p)*}), \quad \Phi^{h(p)}(\xi^{h(p)*}, \kappa_g^{h(p)*}) \text{ and } \Phi^{h(p)}(\xi^{h(p)*}, \kappa_1^{h(p)*}, \kappa_2^{h(p)*}).$$

where $\xi^{h(p)}$, $\kappa_m^{h(p)}$ and $\kappa_g^{h(p)}$ are the asperity height, mean and geometrical asperity curvature of the rough surface ("pressure surface"), respectively. More detailed description of these random variable can be found in Section 2.4. The corresponding closed-form solutions can be found in Eqs. (2.42), (2.41), (2.40) and (2.39), respectively. In this section, the Gaussianity of the generated rough surface is checked by the similarity between the PDFs of the generated rough surface/"pressure surface" and the corresponding closed-form solutions. The asperities in the rough surface and the "pressure surface" are identified using the *eight-nearest-neighbors* [19] which states that an asperity has the maximum height among all of its eight nearest sampling points. However, the comparisons between the joint PDFs with more than one random variable are hard to illustrate. For the sake of the simplicity, only the PDFs of the asperity, $\Phi^{h(p)}(\xi^{h(p)*})$ and $\Phi^{h(p)}(\kappa_m^{h(p)*})$, of the generated rough surface are compared with that of the Gaussian surface. The closed-form of $\Phi^h(\xi^{h*})$ can be found in Eq. (2.42). The closed-form of $\Phi^h(\kappa_m^{h*})$ for the Gaussian surface is derived by Greenwood [20]:

$$\Phi(\kappa_m^{h*}) = \frac{3}{2\sqrt{\pi}} \left\{ \left[3(\kappa_m^{h*})^2 - 2\right] \exp\left[-\frac{3}{4}(\kappa_m^{h*})^2\right] + 2\exp\left[-\frac{9}{4}(\kappa_m^{h*})^2\right] \right\}, \tag{7.8}$$

and the PDF of the "pressure surface" can be easily adapted by replacing the superscript "h" by "p".

Additionally, to evaluate if the surface is Gaussian process, the moments of the generated rough surface and the corresponding "pressure surface" are compared with the closed-form solutions: Eqs. (2.21) - (2.24) and Eqs. (2.56) - (2.58). If the generated rough surface is strictly Gaussian, then the moments of the generated rough surface and the corresponding "pressure surface" should be identical with the closed-form solutions. The moments, $m_n^{h(p)}$ ($n > 0$), of the generated rough surfaces are the mean value of the corresponding moments in the x and y directions.

Three comparisons are illustrated below. The first comparison is related to the PDFs of the surface groups $\#1-\#4$ in case 1 shown in Table 7.1, where only the upper cut-off wavenumber is changed. The second one is related to the PDFs of the surface groups $\#1$, $\#5$ and $\#9$ where only the lower cut-off wavenumber is changed. The final comparison is related to the PDFs of the surface groups $\#13-\#17$ in case 4 where the Hurst dimension, H, is changed.

Changing k_s

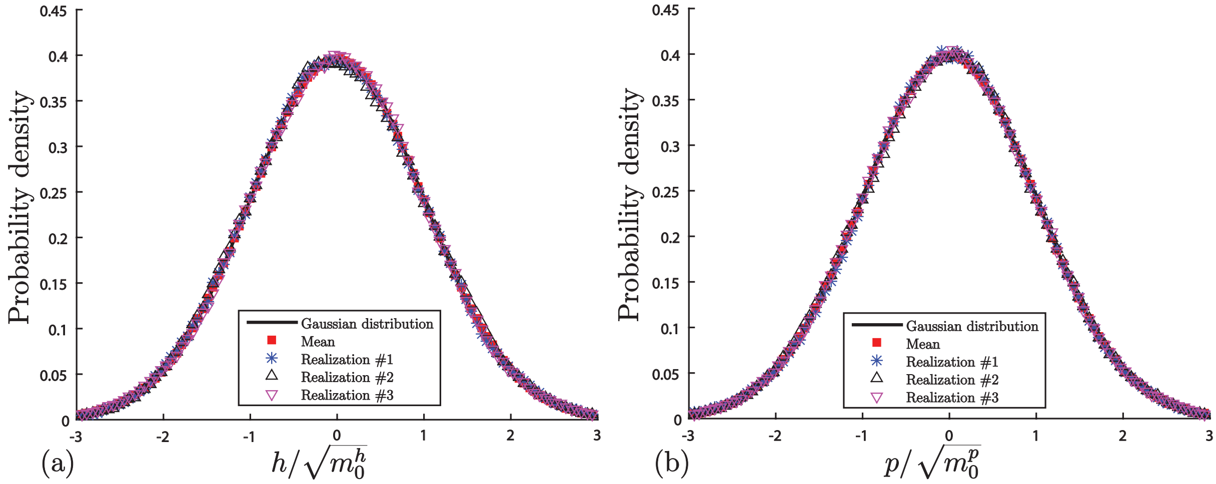

Figure 7.2: The probability density distribution of the rough surface height and the "pressure surface" magnitude of surface group $\#1$.

The rough surface height and the corresponding "pressure distribution" magnitude should follow the Gaussian distribution and it is confirmed in Fig. 7.2 for surface group $\#1$ where $(k_l, k_s, H) = (16, 64, 0.8)$. The agreement is not only in the average sense but also may be in each surface, at least in three surfaces shown in Fig. 7.2. Similar agreement is also found in the other three surface groups ($\#2-\#4$).

From the cheering results shown in Fig. 7.2, we may expect that the good agreement should also exist for the asperity height and asperity mean curvature distributions. In Fig. 7.3(a-b) where $k_s = 64$, $\Phi^h(\kappa_m^{h*})$ and $\Phi(\kappa_m^h)$ have a good agreement with the closed-form

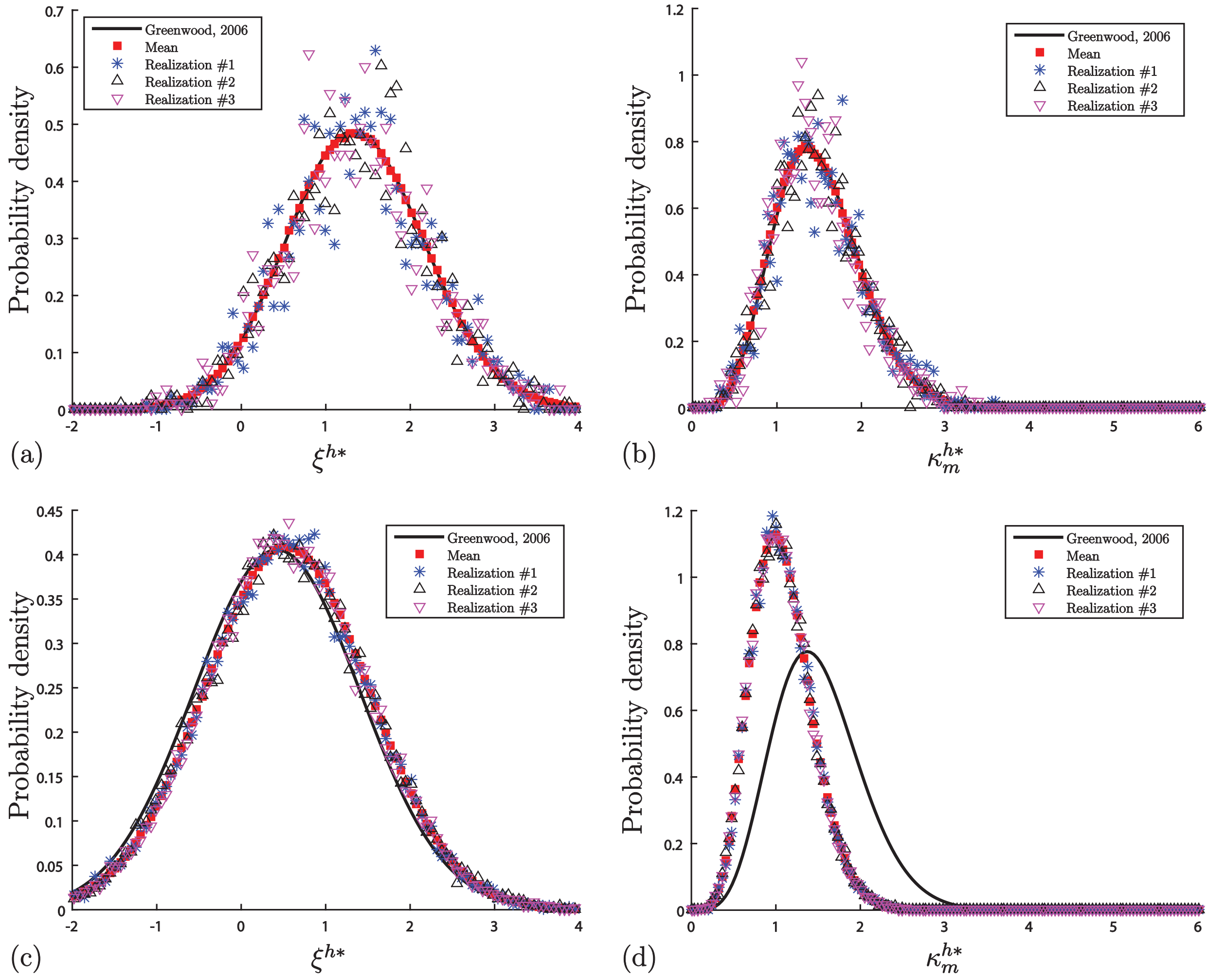

Figure 7.3: The probability density distribution of the asperity height, ξ^{h*}, and asperity mean curvature, ξ^{p*}, of the rough surface group $\#1$ (a-b) and $\#4$ (c-d).

solutions in an average sense. The corresponding probability density distributions of three selected surfaces in surface group $\#1$ oscillate about the closed-form solutions. As k_s increases to 512 in Fig. 7.3(c-d), the probability density distributions of three generated surfaces nearly converge into one master distribution with insignificant oscillation. This implies that the dispersions of $\Phi^h(\kappa_m^h)$ and $\Phi(\kappa_m^h)$ over 1000 surfaces become insignificant with higher upper cut-off wavenumber k_s. However, the agreement between the mean probability densities and the corresponding closed-form solutions are deteriorated. According to the other surface groups in case 1, the good agreement of the probability density distribution is gradually deteriorated as k_s is increased from 64 to 512, especially for that of the asperity curvature. All the above phenomenons are repeated in Fig. 7.4 for the "pressure surface". The deteriorations of the

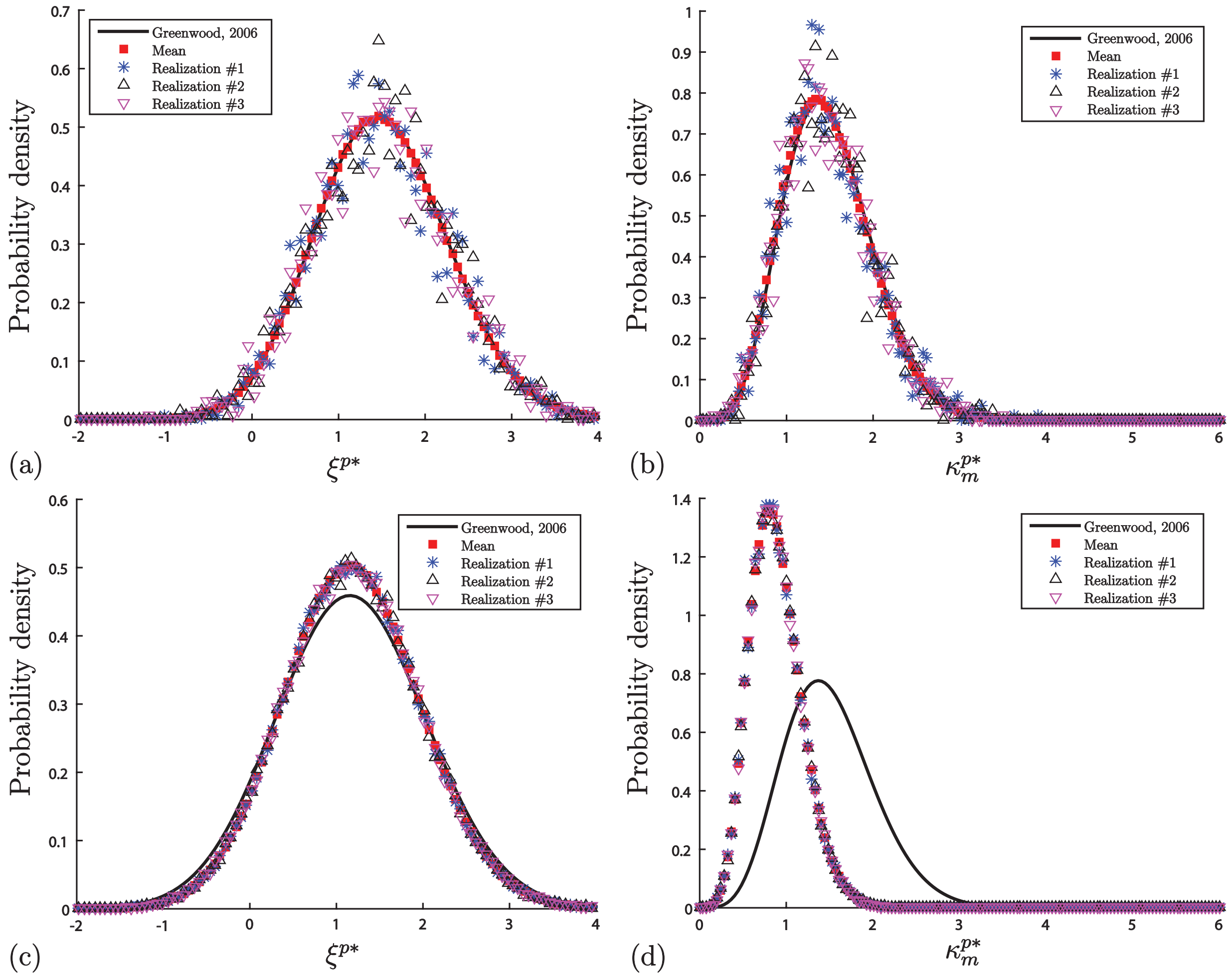

Figure 7.4: The probability density distribution of the asperity height, ξ^{h*}, and asperity mean curvature, ξ^{p*}, of the “pressure surface” in the rough surface group #1 (a-b) and #4 (c-d). The colored figure is available online.

agreement between the probability density distribution are also observed in case 2 and 3 where only k_s is monotonically increased. The mean curvature distributions, $\Phi^h(\kappa_m^{h*(p*)})$, are more sensitive to the change of k_s

Due to its complexity, the joint PDFs of the generated rough surface and the “pressure surface” are not compared with the corresponding closed-form solutions. The agreement between the joint PDFs can still be examined indirectly by checking the agreements between the moments of the generate rough surface/“pressure surface” and the corresponding closed-form solutions. Th eresults of surface groups $\#1-\#4$ are tabulated in Table 7.4. Except for the surface group #1, the moments of the other rough surface groups do not have a good agreement

Table 7.4: Moments of the rough surface and the "pressure surface" in groups $\#1-4$. "Num" means the mean values of the generated rough surface.

Group $\#$	$m_0^h[m^2]$		m_2^h		$m_4^h[m^{-2}]$		$m_6^h[m^{-4}]$	
	Eq. (2.21)	Num	Eq. (2.22)	Num	Eq. (2.23)	Num	Eq. (2.24)	Num
1	1.19×10^{-8}	1.20×10^{-8}	2.00×10^{-4}	1.97×10^{-4}	9.16	9.01	6.97×10^{5}	6.59×10^{5}
2	7.35×10^{-9}	7.44×10^{-9}	2.00×10^{-4}	1.91×10^{-4}	28.44	26.99	8.42×10^{6}	6.94×10^{6}
3	4.81×10^{-9}	4.87×10^{-9}	2.00×10^{-4}	1.73×10^{-4}	96.40	79.38	1.14×10^{8}	5.43×10^{7}
4	3.29×10^{-9}	3.32×10^{-9}	2.00×10^{-4}	1.35×10^{-4}	344.88	172.87	1.62×10^{9}	1.20×10^{8}
Group $\#$			m_0^{p*}		$m_2^{p*}[m^{-2}]$		$m_4^{p*}[m^{-4}]$	
			Eq. (2.56)	Num	Eq. (2.57)	Num	Eq. (2.58)	Num
1			1.00×10^{-4}	1.00×10^{-4}	3.05	2.98	2.09×10^{5}	2.05×10^{5}
2			1.00×10^{-4}	1.00×10^{-4}	9.48	8.69	2.53×10^{6}	2.37×10^{6}
3			1.00×10^{-4}	1.00×10^{-4}	32.13	23.08	3.41×10^{7}	2.69×10^{7}
4			1.00×10^{-4}	1.00×10^{-4}	114.96	36.05	4.87×10^{8}	1.95×10^{8}

with the corresponding closed-form solution and the agreement deteriorates as k_s increases. The differences are more significant for the higher order moments (e.g., m_6^h) associated with higher order derivatives of asperity height. The deteriorations of the agreement between the moments are also observed for surface groups in case 2 and 3 where only k_s monotonically increases. In a summary, Figs. 7.3 and 7.4 and Table 7.4 imply that the generated rough surfaces are no longer a Gaussian process at higher upper cut-off wavenumber k_s.

The non-Gaussian asperity height/mean curvature distribution of generated rough surfaces associated with higher k_s is due to the fact that the sampling resolution, Δ (x/y-interval of the sample points), is not dominantly larger than the shortest wavelength ($1/k_s$). If $\Delta \rightarrow 1/k_s$, then each asperity is sampled with an insufficient number of sampling points. The asperity height and the mean curvature can not be measured accurately. Due to the insufficient number of sampling points on each asperity, the profile of each asperity is equivalently smoothed with a smaller mean curvature. This may be the reason why the higher probability density of the generated rough surfaces in Figs. 7.3(d) and 7.4(d) are associated with the smaller curvature, see Figs. 7.3(d) and 7.4(d). By increasing the sampling numbers, Xu and Jackson [15] showed that the mismatch of the asperity height/mean curvature distribution may be relieved.

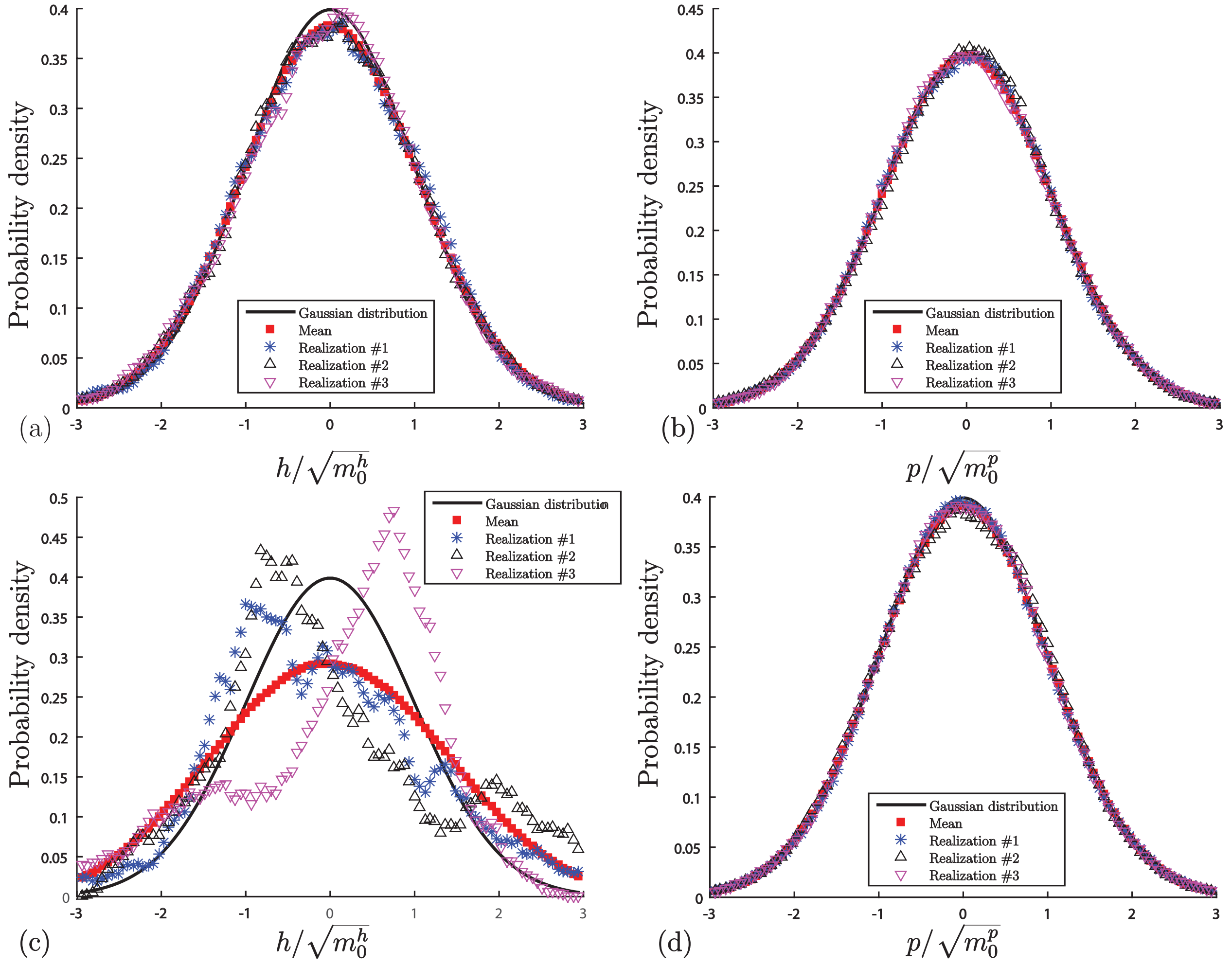

Figure 7.5: The probability density distributions of the rough surface height and the “pressure surface” magnitude of surface group $\#5$ and $\#9$.

Table 7.5: Moments of the rough surface and the “pressure surface” in groups $\#1$, $\#5$ and $\#9$. “Num” means the mean values of the generated rough surface.

Group #	$m_0^h[m^2]$		m_2^h		$m_4^h[m^{-2}]$		$m_6^h[m^{-4}]$	
	Eq. (2.21)	Num	Eq. (2.22)	Num	Eq. (2.23)	Num	Eq. (2.24)	Num
1	1.19×10^{-8}	1.20×10^{-8}	2.00×10^{-4}	1.97×10^{-4}	9.16	9.01	6.97×10^{5}	6.59×10^{5}
5	7.70×10^{-8}	8.37×10^{-8}	2.00×10^{-4}	1.91×10^{-4}	6.02	5.90	4.43×10^{5}	4.19×10^{5}
9	5.91×10^{-7}	1.02×10^{-6}	2.00×10^{-4}	1.73×10^{-4}	4.99	4.91	3.67×10^{5}	3.47×10^{5}
Group #			m_0^{p*}		$m_2^{p*}[m^{-2}]$		$m_4^{p*}[m^{-4}]$	
			Eq. (2.56)	Num	Eq. (2.57)	Num	Eq. (2.58)	Num
1			1.00×10^{-4}	1.00×10^{-4}	3.05	2.98	2.09×10^{5}	2.05×10^{5}
5			1.00×10^{-4}	1.01×10^{-4}	2.01	1.96	1.33×10^{5}	1.30×10^{5}
9			1.00×10^{-4}	1.00×10^{-4}	1.66	1.62	1.10×10^{5}	1.08×10^{5}

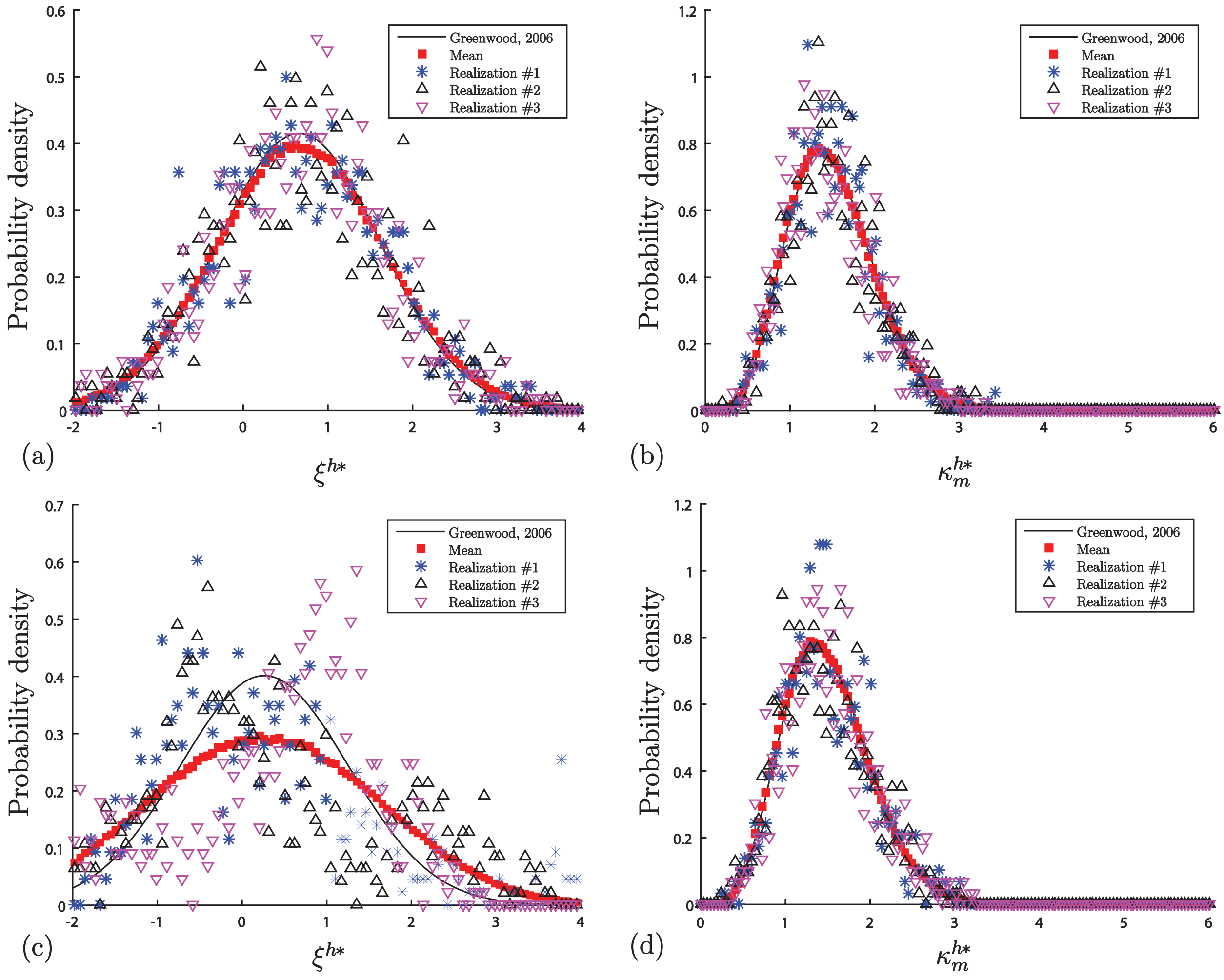

Figure 7.6: The probability density distribution of the asperity height, ξ^{h*}, and asperity mean curvature, κ_m^{h*}, of the rough surface group #5 (a-b) and #9 (c-d).

Changing k_l

In order to explore the effect of the lower cut-off frequency on the Guassianity of the generated rough surface, three rough surfaces, namely, the surface groups #1 ($k_l = 16$), #5 ($k_l = 4$) and #9 ($k_l = 1$), are selected where $k_s = 128$ and $H = 0.8$ are fixed. The probability density distributions of the surface height with $k_l = 4$ shown in Fig. 7.5(a) slightly deviate from the Gaussian distribution at the vicinity of $h = 0$. When $k_l = 1$, the probability density distribution shown in Fig. 7.5(c) completely deviates from the Gaussian distribution not only for each surface but also in the average sense. Recalling the probability density distribution with $k_l = 16$

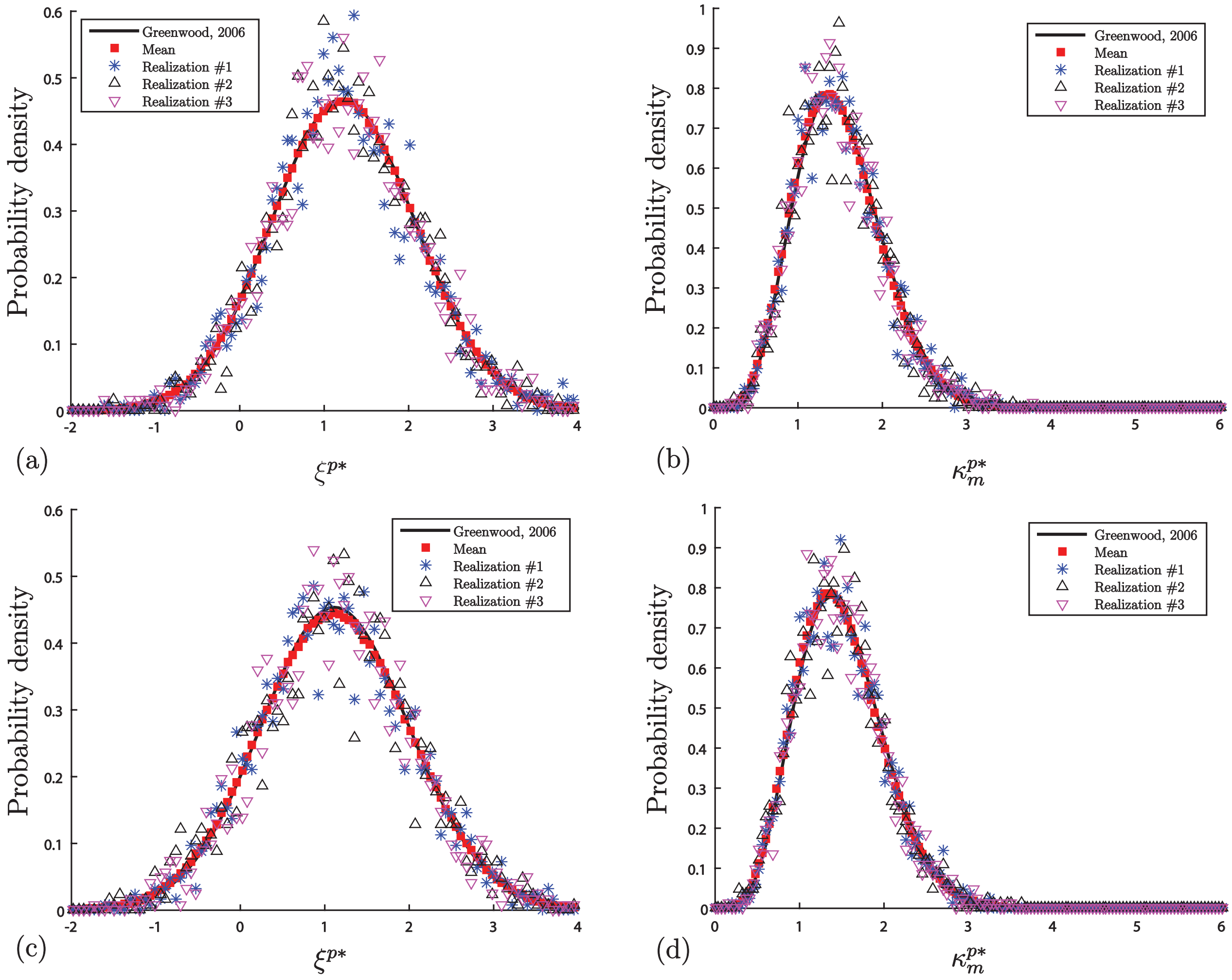

Figure 7.7: The probability density distribution of the asperity height, ξ^{h*}, and asperity mean curvature, κ_m^{p*}, of the "pressure surface" in the rough surface group $\#5$ (a-b) and $\#9$ (c-d).

in Fig. 7.2(a), we can expect that the probability density distributions of the surface heights (either in an average sense or in each realization) gradually deviate from the Gaussian distribution. Surprisingly, the probability density distributions of the "pressure surface" magnitude shown in Fig. 7.5(b) and Fig. 7.5(d) have a good agreement with the Gaussian distribution not only in an average sense but also for each surface, regardless of k_l. Two reasons govern this unexpected mismatch. As k_l decreases to the unity, more and more lower frequency (longer wavelength) components are introduced. Recalling the PSD of the generated rough surface in Eq. (2.18), the lower frequency components are associated with higher PSD. It is those higher values of PSD within the lower frequency range that result in a non-Gaussian distribution of the rough surface. Since *the Gaussian surface can be regarded as being the sum of an infinite number* *of infinitesimally small, uncorrelated, sinusoidal waves* [18], the bias of the PSD (square of the amplitude of the sinusoidal components) towards the lower frequency components causes infinitesimally small amplitudes only occur within the higher frequency range. The above explanations may not be true for the "pressure surface", since the corresponding PSD, $S^p(k)$, is different (see Eq. (2.48)):

$$S^p(k) = \begin{cases} Ck^{-2H} & k \in [k_l, k_s), \\ 0 & \text{otherwise}. \end{cases} \tag{7.9}$$

It is obvious that the slope of S^p vs. k is less than that of S^h vs. k, especially when H is vanishing. Consequently, the Gaussianity of the "pressure surface" magnitude is less sensitive to the change of k_l. This insensitiveness is confirmed in Fig. 7.5(b) and Fig. 7.5(d) where $k_l = 4$ and 1, respectively. In Fig. 7.5(d), only an insignificant mismatch is found at the vicinity of $p = 0$.

The asperity height distribution of the rough surface also has a mismatch with the closed-form solution associated with lower k_l, see Fig. 7.6(a) and 7.6(c). The worst agreement is observed in Fig. 7.6(c) when $k_l = 1$. This is a direct consequence due to the non-Gaussian distribution of the rough surface shown in Figs. 7.5(a) and 7.5(c). The good match of the asperity mean curvature distribution of the generated rough surface can be found in Fig. 7.6(b) and Fig. 7.6(d). The good agreement can also be observed in Fig. 7.7(a-d) for the asperity height and the mean curvature of the "pressure surface" because of its unbiased PSD. The comparisons shown above are also consistent with the moments in Table 7.5 where m_0^h is the only moment which has an obvious mismatch.

As a summary, the overall effect of reducing lower cut-off wavenumber k_l is to deteriorate the Gaussianity of the rough surface and the "pressure surface". The distribution of the surface height and the asperity height of the roughness is more sensitive to the changing of k_l then that of the "pressure surface" due to the biased PSD, $S^h(k)$. The mean curvature distribution, as well as the higher derivatives distribution, of both the roughness and the "pressure surface" are nearly invariant of k_s.

Changing H

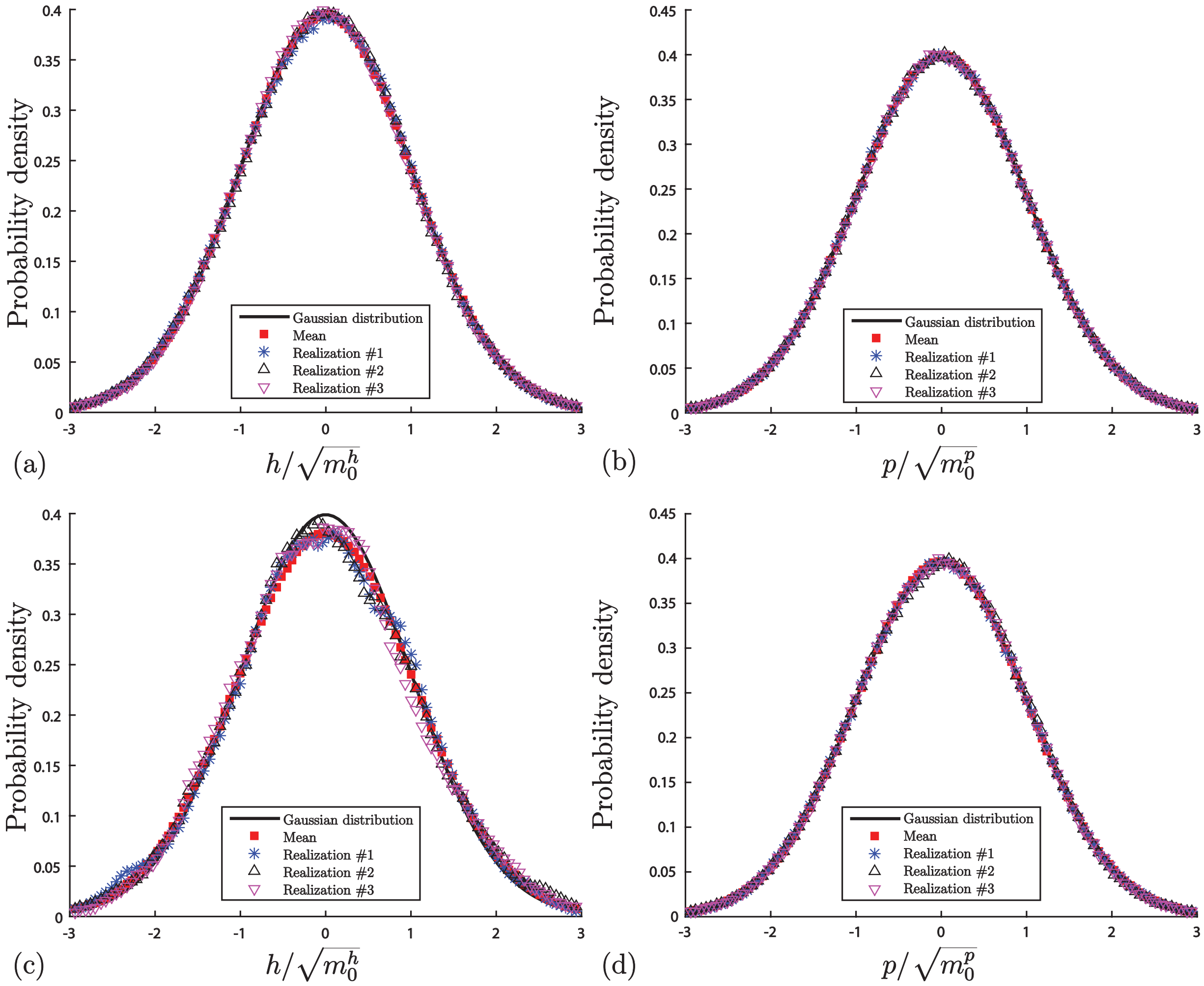

Figure 7.8: The probability density distributions of the rough surface height and the "pressure surface" magnitude of surface group #13 and #17.

In order to explore the effect of H on the Gaussianity of the generated rough surface and the "pressure surface", the upper and lower cut-off wavenumbers are fixed: $k_s = 128$ and $k_l = 4$. The Hurst dimension, H, has a minor effect on the Gaussianity of the generated rough surface and the corresponding "pressure surface" in the average sense as H is changed from 0.1 to 0.9, see Figs. 7.8(a-d), 7.9(a-d), 7.10(a-d). The Gaussianity of the "pressure surface" is nearly insensitive to H, as shown in Figs. 7.8(b,d), 7.9(b,d), 7.10(b, d), but with a deteriorate trend with increasing H. Similar observations can also be found associated with the rough surface group with $H = 0.3,\ 0.5$ and 0.7. The existing mismatch is mainly contributed by the

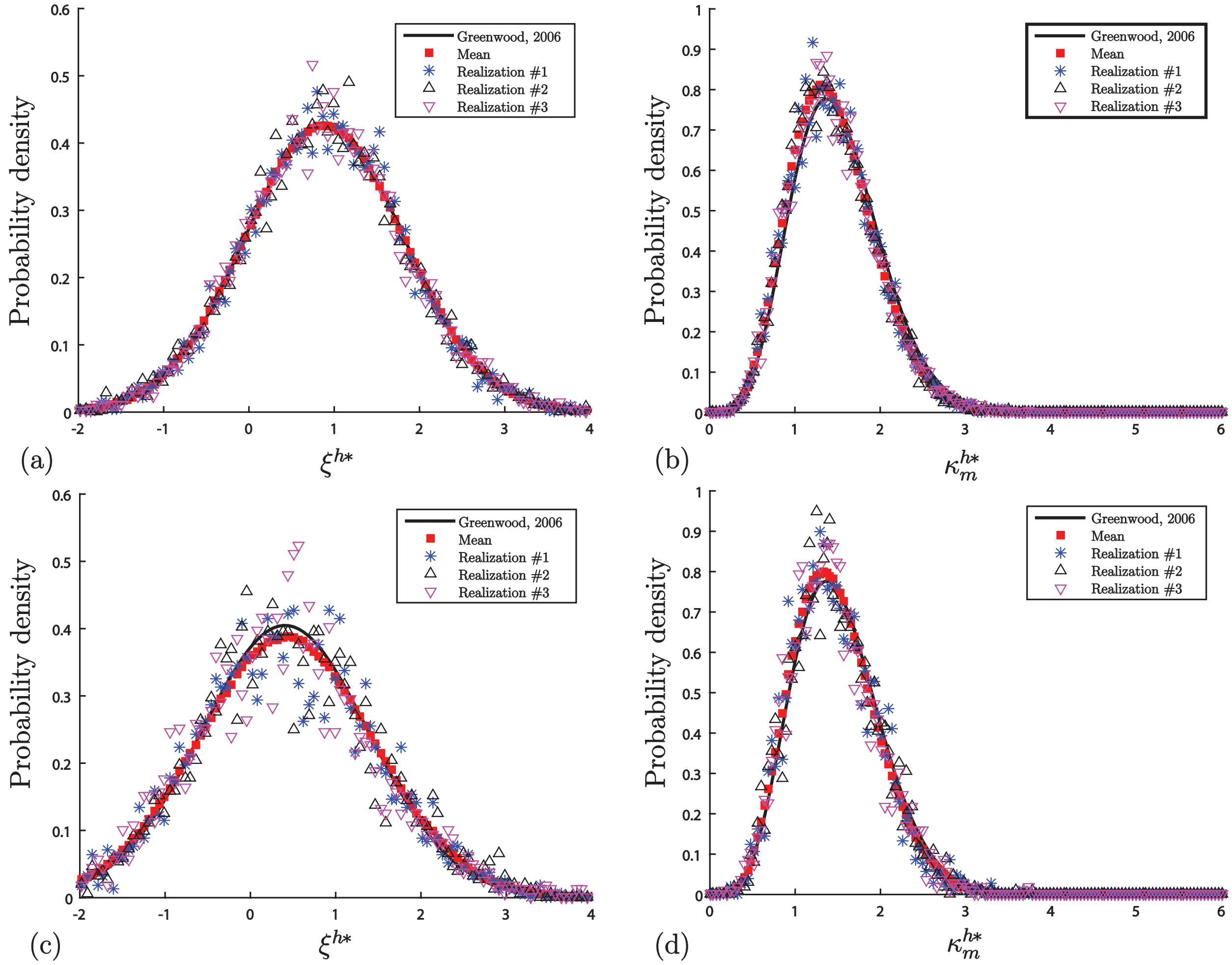

Figure 7.9: The probability density distribution of the asperity height, ξ^{h*}, and asperity mean curvature, ξ^{p*}, of the rough surface group #13 (a-b) and #17 (c-d).

relatively low $k_l = 128$ and relatively high k_s. The comparisons of the moments are tabulated in Table 7.6 and it indicates a negligible effect of H on the moments.

Remarks

After the parameter study in the above sections, a rule of thumb can be generalized on how to generate a nearly Gaussian surface using the surface generation algorithm proposed in Section 7.1:

$$k_l \gg \frac{1}{L_{x(y)}} \quad \text{and} \quad k_s \ll \frac{1}{\Delta_{x(y)}} = \frac{N_{x(y)}}{L_x}. \tag{7.10}$$

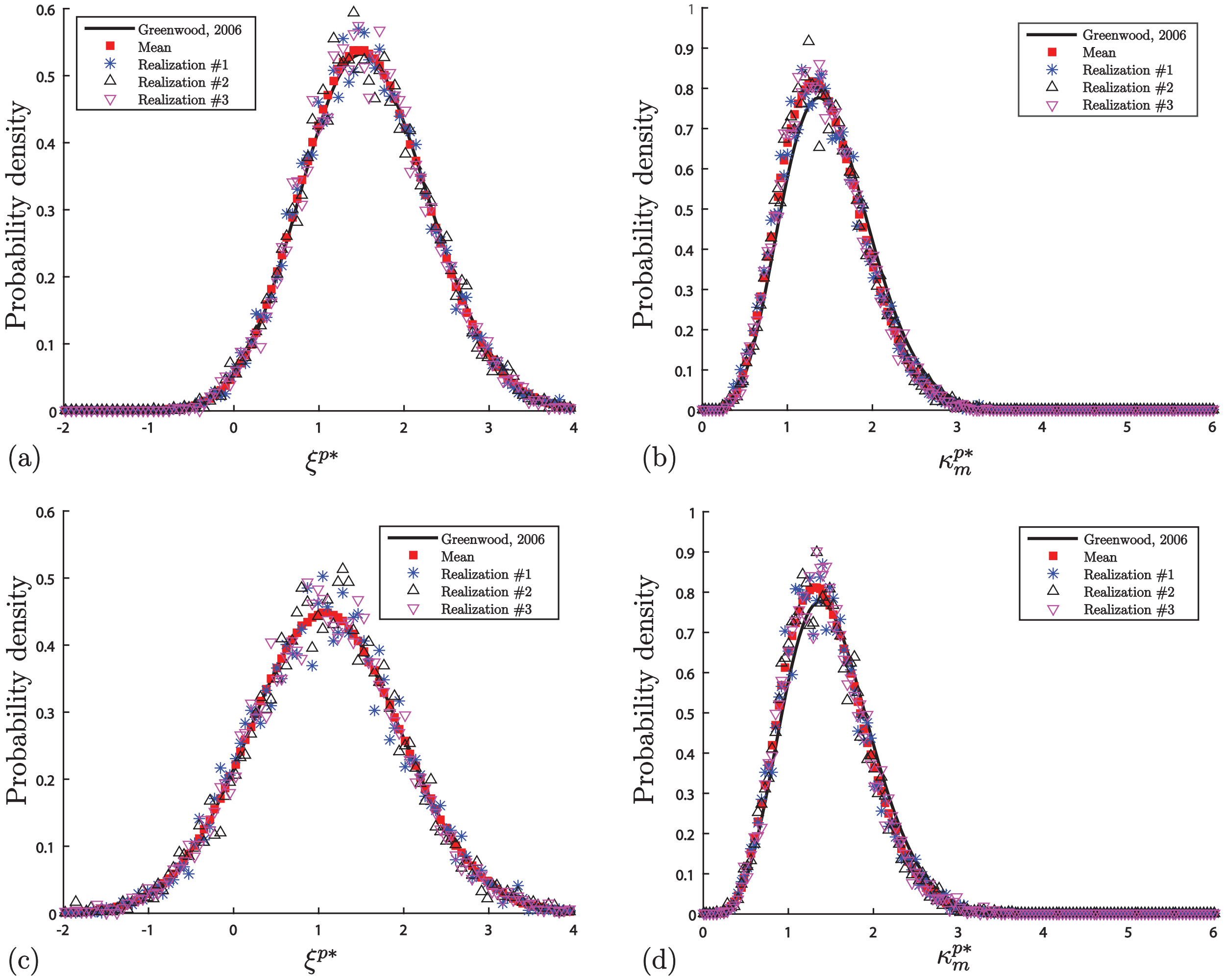

Figure 7.10: The probability density distribution of the asperity height, ξ^{h*}, and asperity mean curvature, ξ^{p*}, of the “pressure surface” in rough surface group #13 (a-b) and #17 (c-d).

The first criterion relieves the biased PSD through removing the longer wavelength components. This is very essential to the Gaussianity of the surface and asperity height distribution. The latter criterion guarantees that the single asperities and the other local features are sufficiently sampled. This criterion is a key requirement of the Gaussianity of the mean curvature distribution and the other higher order derivatives distribution.

Based on the above criterion, the only (nearly) Gaussian surfaces among all 17 surface groups are rough surface groups #1 and #2. Unfortunately, the comparisons associated with the statistical models, the Persson model and BEM in many articles [1–6], do not check the isotropy and the Gaussianity of the rough surface. This may be result an unreasonable conclusion when the criterion in Eq. (7.10) is not satisfied.

Table 7.6: Moments of the rough surface and the “pressure surface” in groups $\#13-17$. “Num” means the mean values of the generated rough surface.

Group #	$m_0^h[m^2]$		m_2^h		$m_4^h[m^{-2}]$		$m_6^h[m^{-4}]$	
	Eq. (2.21)	Num	Eq. (2.22)	Num	Eq. (2.23)	Num	Eq. (2.24)	Num
13	5.58×10^{-9}	5.70×10^{-9}	2.00×10^{-4}	1.86×10^{-4}	46.05	43.31	1.63×10^{7}	1.32×10^{7}
14	1.02×10^{-8}	1.06×10^{-8}	2.00×10^{-4}	1.87×10^{-4}	40.27	38.04	1.37×10^{7}	1.11×10^{7}
15	1.98×10^{-8}	2.09×10^{-8}	2.00×10^{-4}	1.90×10^{-4}	33.38	31.52	1.08×10^{7}	8.83×10^{6}
16	3.85×10^{-8}	4.14×10^{-8}	2.00×10^{-4}	1.93×10^{-4}	25.59	24.28	7.80×10^{7}	6.41×10^{6}
17	2.44×10^{-7}	7.71×10^{-8}	2.00×10^{-4}	1.96×10^{-4}	17.63	16.79	4.98×10^{6}	4.12×10^{6}
Group #			m_0^{p*}		$m_2^{p*}[m^{-2}]$		$m_4^{p*}[m^{-2}]$	
			Eq. (2.56)	Num	Eq. (2.57)	Num	Eq. (2.58)	Num
13			1.00×10^{-4}	1.00×10^{-4}	15.35	13.83	4.88×10^{6}	4.55×10^{6}
14			1.00×10^{-4}	1.00×10^{-4}	13.42	12.14	4.10×10^{6}	3.84×10^{6}
15			1.00×10^{-4}	1.00×10^{-4}	11.13	10.12	3.24×10^{6}	3.03×10^{6}
16			1.00×10^{-4}	1.00×10^{-4}	8.53	7.80	2.34×10^{6}	2.19×10^{6}
17			1.00×10^{-4}	1.01×10^{-4}	5.88	5.41	1.49×10^{6}	1.40×10^{6}

7.3 A Brief Description of All Models

All the analytical and numerical models compared in this chapter are briefly introduced in this section.

Rough Surfaces According to the rule of thumb proposed in Eq. 7.10 and 17 rough surface groups tabulated in Table 7.1, only 50 surfaces from rough surface groups $\#1$ and $\#2$, respectively, are selected randomly as the inputs of various statistical models, the Persson model and Polonsky and Keer model. In Section 7.2, we have shown that a generated rough surface can never be exactly Gaussian surface. In order to have consistent rough interfaces in both the statistical models and the Polonsky and Keer model, the bandwidth parameters, α^h and α^p, used as the sole inputs of the statistical models should be evaluated from the generated Gaussian surfaces, i.e., the rough surface groups: $\#1 - \#2$ [15].

Table 7.7: Bandwidth parameters, α^h and α^p, of the rough surface groups $\#1$ and $\#2$.

Group #	α^h	α^p
1	2.7861 ± 0.2144	2.3146 ± 0.2144
2	5.4853 ± 0.2787	3.1357 ± 0.1854

Boundary Element Model The Polonsky and Keer model with periodic boundary conditions is selected. The reason is explicitly explained by Xu and Jackson [15]. The Polonsky and Keer model is driven by the dimensionless average contact pressure, $\bar{p}^* = \bar{p}/\sqrt{m_0^p}$, which monotonically increases from 0 to 4 where complete contact is almost achieved. The entire loading history is divided into three stages, namely, (i) the early contact stage: $\bar{p}^* \in (0, 0.2]$, (ii) the medium stage: $\bar{p}^* \in (0.2, 2]$ and (ii) the nearly complete contact stage: $\bar{p}^* \in (2, 4]$. A specific number of sub-steps have been assigned to each stage, namely, $n_1 = 30$, $n_2 = 45$ and $n_3 = 20$. The loading histories at early contact and the nearly complete contact are uniformly discretized and the loading step in the medium stage is gradually increased. An explicit expression of the discretized loading history, $\bar{p}^*$, of $n = n_1 + n_2 + n_3$ sub-steps below:

$$\bar{p}_i^* = \begin{cases} i\Delta_1, & 0 < i \le n_1 \\ \exp\left[\ln(0.2) + \Delta_2(i - n_1)\right], & n_1 < i \le n_1 + n_2 \\ 2 + \Delta_3(i - n_1 - n_2), & n_1 + n_2 < i \le n \end{cases} \tag{7.11}$$

where $\Delta_1 = 0.067$, $\Delta_2 = 0.0512$ and $\Delta_3 = 0.1$. The minimum $\bar{p}^*$ is 0.065 and, based on the asymptotic BGT model in Eq. (4.35), the corresponding minimum contact ratio is $A^* \approx 0.0814$. When the average contact pressure, $\bar{p}^*$, is below 0.065, only a few asperities are in contact with the rigid flat. Due to an insufficient number of contacting asperities and insufficient number of nodes within each asperity contact area [1], the estimation of the contact ratio, A^*, and the average interfacial gap, $\bar{g}^*$ based on the BEM results cannot be accurate. Similarly, this conclusion is also true when $\bar{p}^*$ is extremely high [16] where each non-contact region is not sufficient sampled. The contact ratio is determined by the ratio of the number of nodes associated with positive pressure to the total number of nodes. The average interfacial gap is determined by Eq. (3.36). The convergence of the average interfacial gap, the contact pressure, and the contact area at each load stage is determined by the criterion consisting of Eqs. (3.47), (3.48), (3.49) and (3.51) given in Section 3.7.3. The contact ratio and the average interfacial gap are the mean value over the corresponding results of 50 surfaces. The error bar is used to represent the standard deviation of these 50 surfaces.

Statistical Models of Early Contact The statistical models of early contact, namely, (i) the adapted GW model (see Section. 4.3.1), (ii) the Nayak-Bush model (Section. 4.3.2), (iii) the Greenwood model (Section. 4.3.3), (iv) the BGT model (Section. 4.3.4) and (v) the asymptotic BGT model (Section. 4.3.4), are driven by the dimensionless surface separation, $d^* = d/\sqrt{m_0^h}$. The surface separation monotonically decreases from 3 to 0 within 65 steps with constant step-size, i.e.,

$$d_i^* = 3 - 0.0469 \times (i-1), \quad i = 1, ..., 65.$$

The outputs of the statistical models are $\bar{p}^*$ and the contact ratio A^*. At early contact where $\bar{p}^* \to 0^+$, the average interfacial gap is approximately the same as the surface separation, i.e., $\bar{g}^* \approx d^*$ [15].

Statistical Models of Nearly Complete Contact The statistical models of nearly complete contact, namely, (i) the adapted GW model (Section. 5.3.1), (ii) the Nayak-Bush model (Section. 5.3.2), (iii) the Greenwood model (Section. 5.3.3) and (iv) the Ciavarella asymptotic model (Section. 5.3.4), are driven by the dimensionless average contact pressure, $\bar{p}^*$, which monotonically increases from $\bar{p}^* = 0$ to $\bar{p}^* = 4$ within 65 substeps:

$$\bar{p}_i^* = 0.625 \times (i-1), \quad i = 1, ..., 65.$$

Persson's model The Persson model for the real area of contact (Eq. (5.59)) and the average interfacial gap discussed in Appendix E are used.

7.4 Numerical Results

7.4.1 Overall Results

In this section, the results of the statistical models at the early contact and the nearly complete contact are compared with that of the Polonsky and Keer model. The objective is to show (i) their accuracies within the load range: $\bar{p}^* \in [0, 4]$, and (ii) the limitations of two types of statistical models. For the sake of a clear presentation, only the Greenwood model and the asymptotic BGT models are selected among all the analytical models.

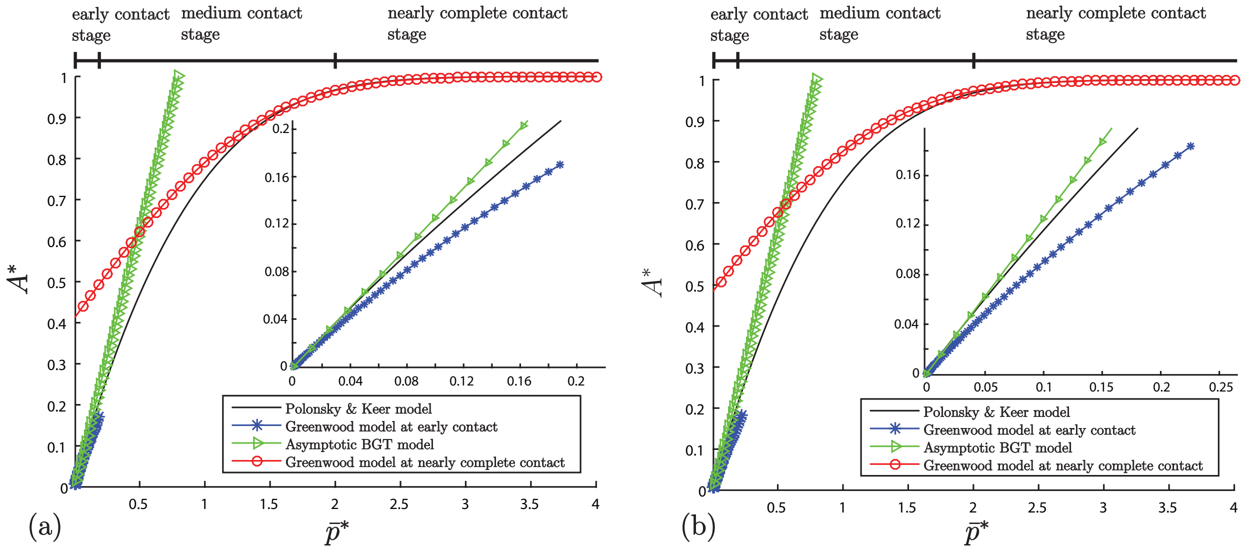

Figure 7.11: The contact ratio, A^*, vs. the dimensionless contact pressure, $\bar{p}^*$, throughout the entire loading history. Surface group (a) #1 $(k_l, k_s, H) = (16, 64, 0.8)$ and (b) #2 $(k_l, k_s, H) = (16, 128, 0.8)$.

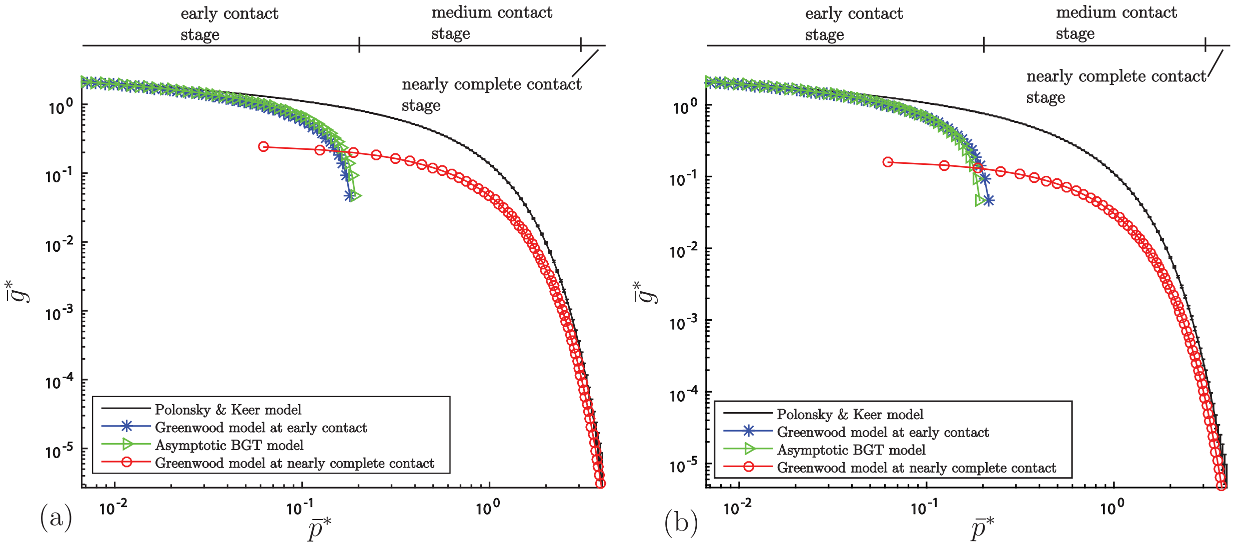

Figure 7.12: The average interfacial gap, $\bar{g}^*$, vs. the dimensionless contact pressure, $\bar{p}^*$, throughout the entire loading history. Surface group (a) #1 $(k_l, k_s, H) = (16, 64, 0.8)$ and (b) #2 $(k_l, k_s, H) = (16, 128, 0.8)$.

Commonly, the statistical models of early contact are only considered valid when the contact ratio is infinitesimally small and it is confirmed in Fig. 7.11(a-b). The Greenwood model of early contact and the asymptotic BGT model gradually deviate from the BEM results as A^* increases from zero. The relation, A^* vs. $\bar{p}^*$, of the Greenwood model and the BEM results seem to converge to a linear relation predicted by the asymptotic BGT when A^*(or $\bar{p}^*$)

is vanishing. It will be shown in Section 7.4.2 that the slopes are not exactly the same. As $\bar{p}^*$ further increases, the asymptotic BGT model, as well as the Greenwood model of early contact, would eventually predict the complete contact under an extremely low $\bar{p}^*$. The Greenwood model of nearly complete contact shown in Fig. 7.11 does not have a good prediction at the early contact stage and the medium stage, especially the contact ratio does not converge to zero when $\bar{p}^* \to 0$. At the nearly complete contact stage ($\bar{p}^* > 2$), the Greenwood model has an excellent agreement with the Polonsky and Keer model through the entire nearly complete contact stage.

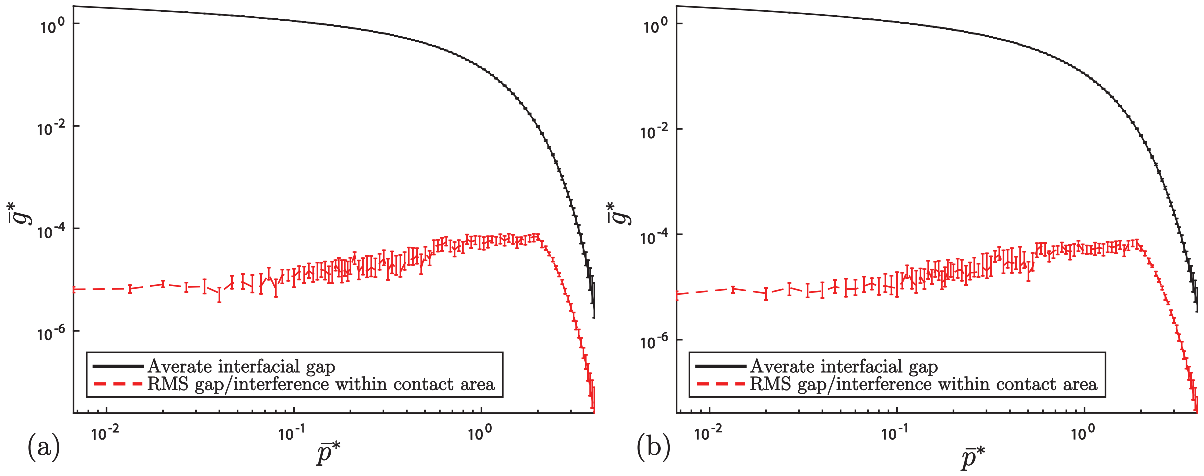

Figure 7.13: The plots of average interfacial gap, $\bar{g}^*$, and the root mean square gap/interference within the contact area. Surface group (a) #1 $(k_l, k_s, H) = (16, 64, 0.8)$ and (b) #2 $(k_l, k_s, H) = (16, 128, 0.8)$. The colored figure is available online.

Similar observations are found in Fig. 7.12 where two types of the statistical models have a good agreement with the Polonsky and Keer model at the early and nearly complete contact stages, respectively. Noticing that the surface group #2 is less Gaussian (see Table. 7.4), the prediction of the Greenwood model at nearly complete contact becomes less accurate compared with the BEM results and it is shown in Figs. 7.11 and 7.12. As mentioned in Chapter 3, the zero interference/gap cannot be satisfied exactly at the contacting points in the BEM. The mean average interfacial gap, $\bar{g}^*$, of two rough surface groups are found to be several order of magnitude larger than the root mean square (rms) gap within the contact area throughout the entire loading history, see Fig. 7.13. This shows that the predictions of $\bar{g}^*$ by the BEM are not affected by the numerical error within the contact area.

7.4.2 Early Contact

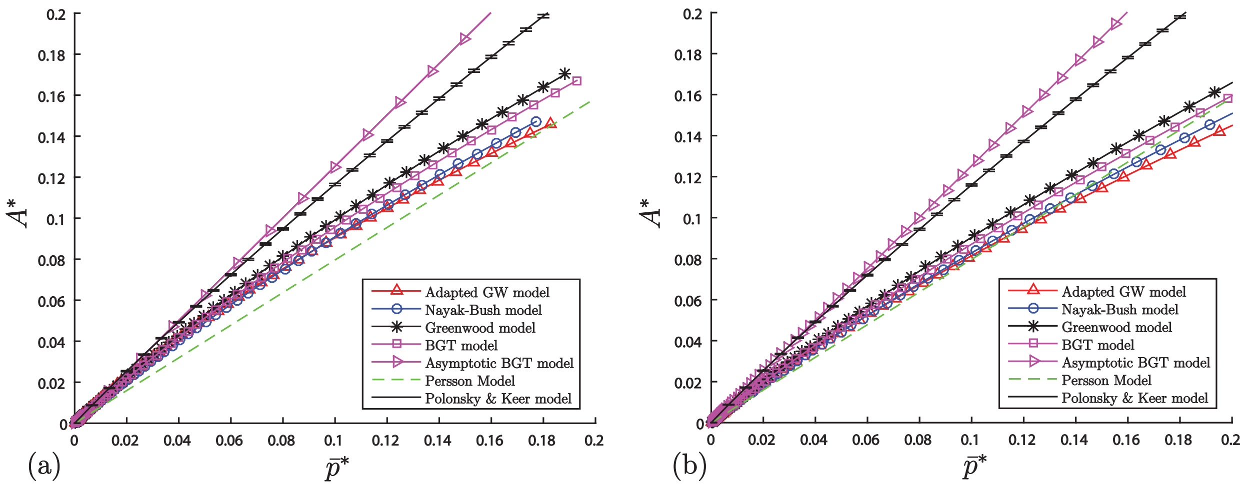

Figure 7.14: The contact ratio, A^*, vs. the dimensionless contact pressure, $\bar{p}^*$, at the early contact stage. Surface group (a) $\#1$ $(k_l, k_s, H) = (16, 64, 0.8)$ and (b) $\#2$ $(k_l, k_s, H) = (16, 128, 0.8)$. The predictions of Polonsky and Keer model are plotted with the error bar which is negligibly small in the figure.

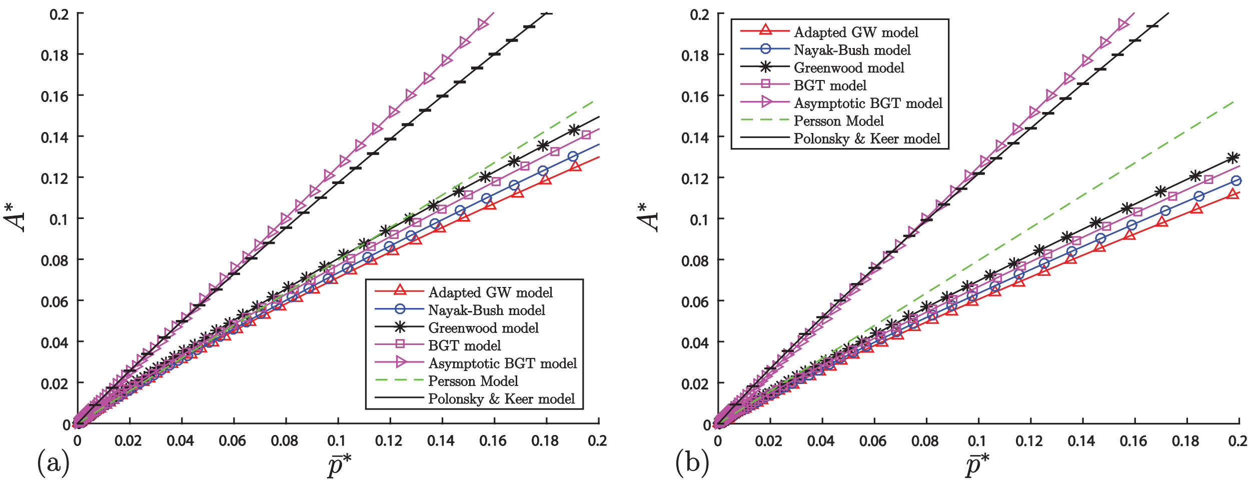

Figure 7.15: The contact ratio, A^*, vs. the dimensionless contact pressure, $\bar{p}^*$, at the early contact stage. Surface group (a) $\#3$ $(k_l, k_s, H) = (16, 256, 0.8)$ and (b) $\#4$ $(k_l, k_s, H) = (16, 512, 0.8)$. The predictions of Polonsky and Keer model are plotted with the error bar which is negligibly small in the figure.

The stage of the early contact is restricted within $\bar{p}^* \in [0, 0.2]$. A comprehensive comparison of the contact ratio and average interfacial gap predicted by the BEM, statistical model and the Persson model is rare in the literature, except for the work done by Yastrebov et al. [5] in which only the contact ratio is discussed. The (joint) probability density function of the rough surfaces used in the current study has better approximation to that of a Gaussian surface and this better approximation makes the comparison fair for the statistical models. Additionally, more statistical models are joined the comparison.

The asymptotic BGT model has an excellent agreement with the Polonsky and Keer model throughout the entire range of the early contact stage for both surface groups, see Fig. 7.14(a-b). The contact ratio, A^*, shown in Fig. 7.14 predicted by the Persson model and the other statistical models are underestimated. Similar observation has also been reported by Yastrebov et al. [5]. The other statistical models quickly deviate from the Polonsky and Keer model as $\bar{p}^*$ increases from zero. As k_s increases, the agreement between the Polonsky and Keer model and the other statistical models (except for the asymptotic BGT model) deteriorates. This is related to the fact that the Gaussianity of the generated rough surfaces become worse when k_s increases. This postulation is confirmed by Fig. 7.15 in which k_s of the generated rough surface further increases to (a) 256 and (b) 512. The Persson model, however, is invariant of the change of k_s and has a better prediction of A^* when rough surface is non-Gaussian. For a Gaussian rough surface, the statistical models may have a better accuracy than the Persson model. The comparison of the instantaneous slope, κ, of A^* vs. $\bar{p}^*$ curves shown in Fig. 7.16 also support the above postulation where k predicted by the statistical models are closer to the BEM results in Fig. 7.16(a). As $\bar{p}^*$ further decreases to zero, κ of the advanced statistical models (e.g., the BGT model, the Greenwood model and the Nayak-Bush model) will converge to the asymptotic BGT model. The Polonsky and Keer model may not be able to have the same trend since the contacting points are not sufficiently sampled, unless the rough surface is sampled with finer resolution. This is a clear sign that a more Gaussian rough surface would result in a closer agreement between the contact ratios predicted by the BEM and the statistical models. Additionally, as pointed out by Yastrebov et al. [5,6], the contact ratio calculated based on the positive contact pressure is overestimated. This fact may also help to bring the BEM and the statistical model even closer.

Unfortunately, the prediction of the average interfacial gaps, $\bar{g}^*$, by the statistical models do not have a good agreement with the BEM results, even when $\bar{p}^*$ is small. The disagreement

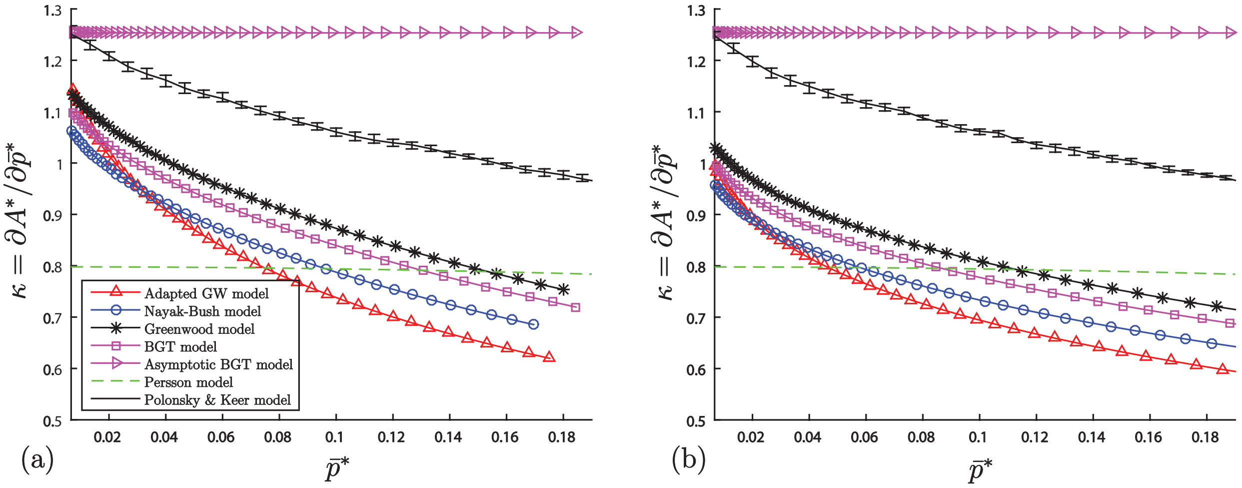

Figure 7.16: The derivative $\kappa = \partial A^*/\partial \bar{p}^*$ vs. the dimensionless contact pressure, $\bar{p}^*$, at the early contact stage. Surface group (a) #1 $(k_l, k_s, H) = (16, 64, 0.8)$ and (b) #2 $(k_l, k_s, H) = (16, 128, 0.8)$.

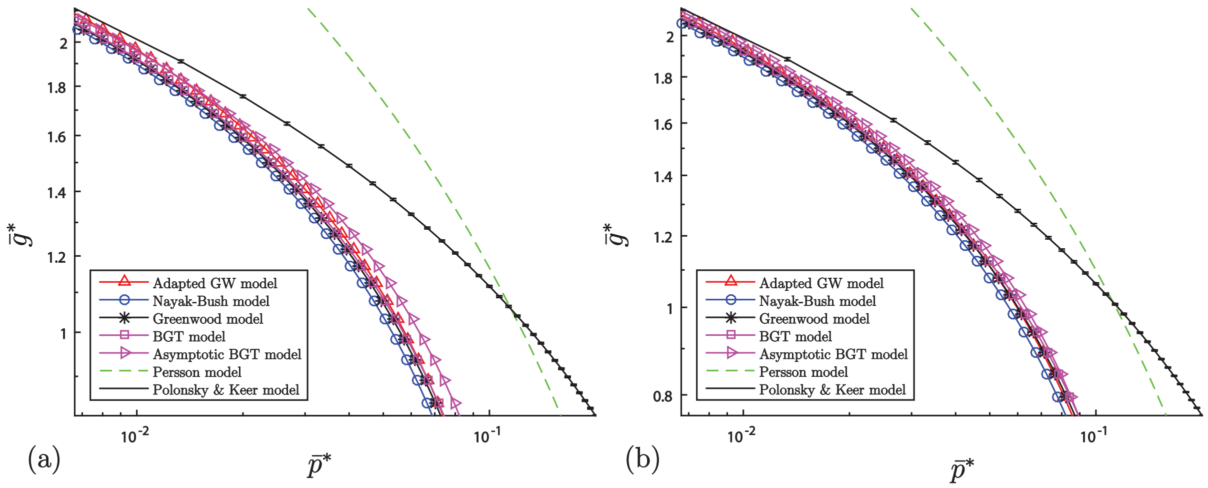

Figure 7.17: The contact ratio, $\bar{g}^*$, vs. the dimensionless contact pressure, $\bar{p}^*$, at the early contact stage. Surface group (a) #1 $(k_l, k_s, H) = (16, 64, 0.8)$ and (b) #2 $(k_l, k_s, H) = (16, 128, 0.8)$.

is contributed by the two factor: (1) the generated rough surface used in the BEM is not sufficiently sampled and (2) the approximation of the average interfacial gap, i.e., $\bar{g}^* \approx \bar{d}^*$, is not accurate within the given range of $\bar{p}^*$. It is expected to have a better agreement within a vanishing $\bar{p}^*$. However, the BEM may not be valid in this extreme case since the contacting asperities in the BEM may not be sampled sufficiently. Noticing that the Persson model is completely different from the results of the BEM and statistical models.

7.4.3 Nearly Complete Contact

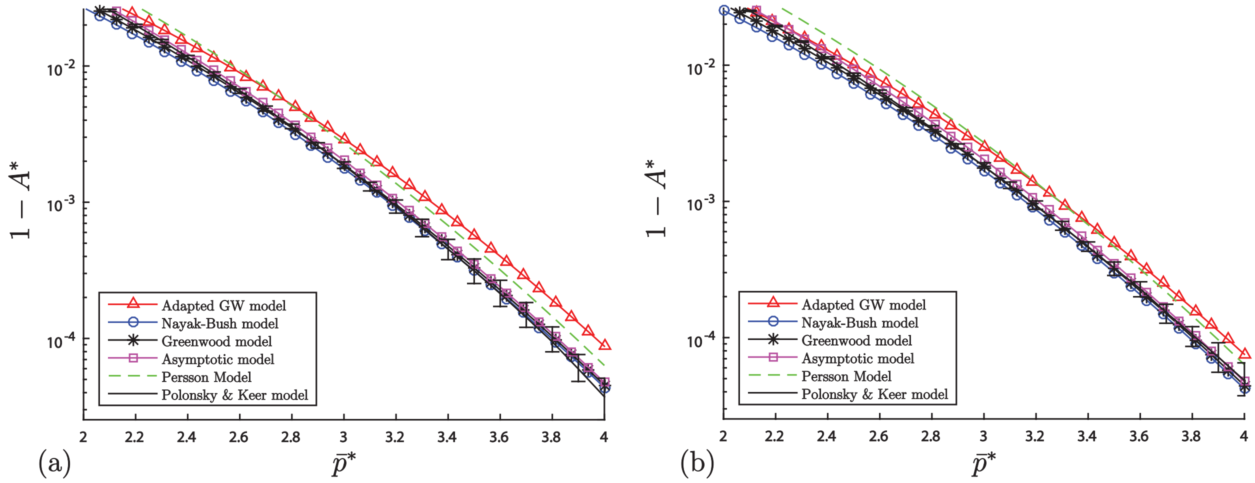

(a) (b)

Figure 7.18: The contact ratio, A^*, vs. the dimensionless contact pressure, $\bar{p}^*$, at the nearly complete contact stage. Surface group (a) #1 $(k_l, k_s, H) = (16, 64, 0.8)$ and (b) #2 $(k_l, k_s, H) = (16, 128, 0.8)$.

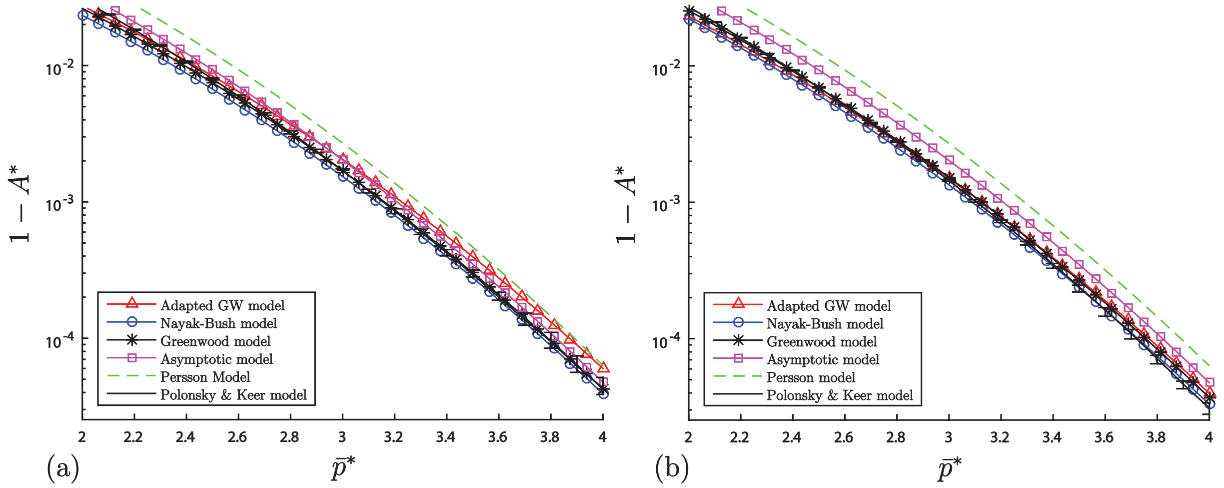

(a) (b)

Figure 7.19: The contact ratio, A^*, vs. the dimensionless contact pressure, $\bar{p}^*$, at the early contact stage. Surface group (a) #3 $(k_l, k_s, H) = (16, 256, 0.8)$ and (b) #4 $(k_l, k_s, H) = (16, 512, 0.8)$.

The stage of the nearly complete contact is restricted to $\bar{p}^* \in [2, 4]$. The Ciavarella asymptotic model, the Nayak-Bush model and the Greenwood model have an excellent agreement with the Polonsky and Keer model in Fig. 7.18. The adapted GW model and the Persson model overestimate the non-contact ratio, $1 - A^*$. Compared with the corresponding results at early

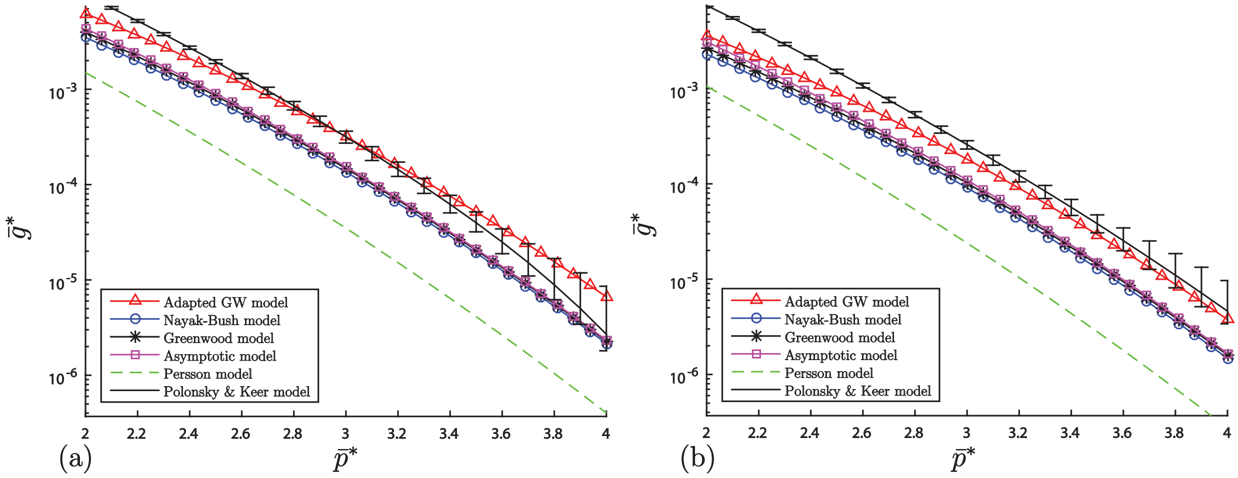

(a) (b)

Figure 7.20: The average interfacial gap, $\bar{g}^*$, vs. the dimensionless contact pressure, $\bar{p}^*$, at the nearly complete contact stage. Surface group (a) #1 $(k_l, k_s, H) = (16, 64, 0.8)$ and (b) #2 $(k_l, k_s, H) = (16, 128, 0.8)$.

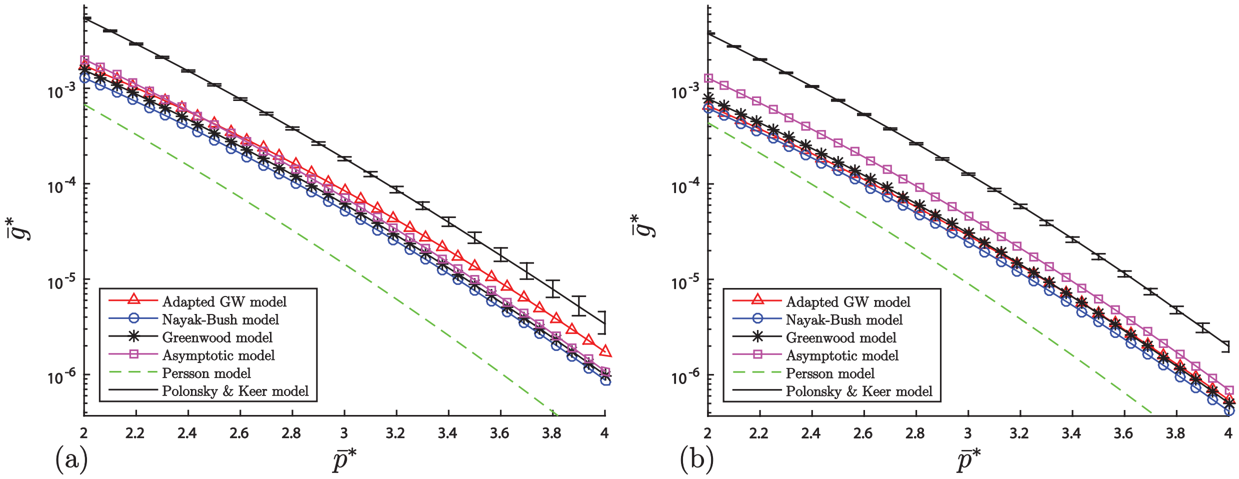

(a) (b)

Figure 7.21: The average interfacial gap, $\bar{g}^*$, vs. the dimensionless contact pressure, $\bar{p}^*$, at the nearly complete contact stage. Surface group (a) #3 $(k_l, k_s, H) = (16, 256, 0.8)$ and (b) #4 $(k_l, k_s, H) = (16, 512, 0.8)$.

contact in Figs. 7.14 and 7.15, the predictions of $1 - A^*$ by the Nayak-Bush model and the Greenwood model shown in Figs. 7.18 and 7.19 are nearly insensitive to the deterioration of the Gaussianity as k_s increases from 64 to 512. Accuracy of the adapted GW model and the Ciavarella asymptotic models are improved when k_s increases and decreases, respectively. The Persson model overestimates $1 - A^*$ in all four cases in Figs. 7.18 and 7.19 regardless of k_s.

The predictions of $\bar{g}^*$ by all the statistical models shown in Fig. 7.20 are not in a good agreement with the BEM results for two rough surface groups. In Figs. 7.20 and 7.21, the Persson model underestimates the predictions of $\bar{g}^*$ by nearly one order of magnitude for all four rough surface groups. Unlike the predictions of the contact ratio, the predictions of $\bar{g}^*$ by statistical models are highly sensitive to the deterioration of the Gaussianity of the rough surface. In Figs. 7.20 and 7.21, the BEM results of $\bar{g}^*$ gradually deviate from the predictions of the statistical model as k_s increases from 64 to 512. This phenomenon is confirmed by Figs. 7.21(a-b) for the rough surface groups associated with $k_s = 256$ and $k_s = 512$.

7.5 Discussions

In Section 7.4, the numerical results of $1 - A^*$ and $\bar{g}^*$ predicted by the BEM (Polonsky and Keer model), the statistical models and the Persson model are compared with each other. The most important observation is that the agreement between the Polonsky and Keer model and the statistical models relies strongly on the Gaussianity of the generated rough surface (in an average sense). Within the given load range, the statistical models deviate more from the BEM results if the Gaussianity of the generated rough surfaces used in the BEM is deteriorated. This trend repeatedly appears more or less in the predictions of A^*, $\bar{g}^*$ and κ at early contact and the predictions of $1 - A^*$ and $\bar{g}^*$ at the nearly complete contact. In other words, this trend implies that the statistical models are more accurate when the rough surface is more Gaussian. However, in the real world, the roughness from the engineering surfaces are not strictly Gaussian [13, 14], nor are the generated rough surfaces by the algorithm developed in this chapter. Consequently, it is always expected to have a mismatch between the BEM results and the statistical models even within its suggested range of application, unless the non-Gaussian statistical models are proposed.

The numerical results of the Polonsky and Keer model are just an approximation associated with the discretized rough interface which is nearly Gaussian. A rigorous comparison may need an infinite number of sampling points. As shown by Yastrebov et al. [6], the prediction of A^* is gradually converged as the total number of sampling points increases from 256×256 to 4096×4096 and the changing of A^* is insignificant when number of sampling points are higher. This convergent trend may also be true for $\bar{g}^*$. Thus, more accurate BEM results can be achieved when a larger number of sampling points are used. Recalling the BEM results of $1 - A^*$ associated with ascending k_s shown in Figs. 7.18-7.21, the standard deviation of the BEM results (over 50 surfaces) gradually decreases as more higher frequency components are introduced. A similar descending trend can be found in the BEM results (A^* and $\bar{g}^*$) in the entire loading range. The introduction of the higher frequency components reduces the dispersion of the contact results of different realizations. Because real rough surfaces are always rough down to the atomic scale, the corresponding statistically similar rough surfaces may achieve nearly the same contact ratio, A^*, and the average interfacial gap, $\bar{g}^*$.

The Persson model claimed to be accurate at the nearly complete contact [21]. From the comparison with the statistical models and the BEM, however, A^* and $\bar{g}^*$ are underestimated by the Persson model at early (Figs. 7.14 and 7.17) and nearly complete contact (Figs. 7.18 and 7.20). Similar conclusions are also drawn by Xu and Jackson [15]. The Persson model (for contact ratio) has been shown in Section 5.3.4 that it is very similar to the asymptotic form of the statistical model at nearly complete contact with a different constant. This different constant can guarantee the contact ratio, A^*, in Persson's model decays to zero when $\bar{p}^*$ is vanishing and this boundary condition cannot be satisfied in the statistical models of nearly complete contact, see Fig. 7.11. Based on this reason, the Persson model at early contact is just an approximation and it is not surprise why $\bar{g}^*$ vs. $\bar{p}^*$ predicted by the Persson model is completely off. More detailed reasons why the Persson model overestimate the contact ratio can be found in the Sections 5.3.4 and 5.4.

The last point discussed in the section is related to the application of the statistical models to the real world applications. The statistical model of early contact, especially the GW model [22], is very popular in the industry and the academy to predict the contact ratio. Most of the time, the statistical models, especially the GW model [22], are misused since the rough surface is not Gaussian [13,14]. As shown in Figs. 7.14 and 7.15, a less Gaussian rough surface results in a significant underestimate of A^* by the statistical model at the early contact. This is also true for the statistical models of nearly complete contact. For the non-Gaussian surface, the corresponding PDF may not have the closed-form solutions as shown in Section 2.5. However, the framework of the statistical models (mainly due to Greenwood and Williamson [22]) should be invariant of the types of the rough surface even though it is originally designed for the Gaussian process. To overcome the difficulty brought by the non-Gaussian surface in the real world, the PDF can be evaluated numerically for each rough surface and the same frameworks discussed in Sections 4.1 and 5.1 can be followed to obtain the final solutions.

In the real world, the contact ratio, A^*, is usually between a vanishing value and the unity. The limited application ranges ($A^* \to 0$ and $A^* \to 1$) for the statistical models at early contact and the nearly complete contact prevent its application to the real world rough contact problems. In the next chapter, a curve-fit solution of the contact ratio, A^*, based on the statistical model of nearly complete contact is developed. This curve-fit solution is valid for the entire loading history, i.e., from the first touch to the complete contact.

7.6 Conclusions

In this chapter, the validity of the statistical models developed in Chapter 4 and 5 are conprehensively tested at the stages of early contact and nearly complete contact, respectively. The roughness input of the BEM is generated by a new algorithm which can guarantee the rough surface is nearly isotropic, fractal and Gaussian at the same time. According to the test done in Section 7.2 for 17 generated rough surface groups (each contains 1000 surfaces), the isotropy and the Gaussianity are nearly satisfied in an average sense by the generated rough surface if the rule of thumb proposed in Eq. (7.10) is satisfied. Two generated rough surface groups are used for the later comparison. The Persson model does not have a good agreement with the BEM at the early and nearly complete contact. The statistical models and the Persson model at early contact only have a closed agreement with the BEM for A^* and $\bar{g}^*$ when $\bar{p}^*$ is vanishing. The statistical models at nearly complete contact, especially the Greenwood model and the Nayak-Bush model, have excellent agreement with the BEM for A^* throughout the entire nearly complete contact stage. The average interfacial gap, $\bar{g}^*$, predicted by the statistical model at nearly complete contact gradually deviates from the BEM as the Gaussianity is deteriorated through the introduction of the higher frequency components. A similar phenomenon is also observed at the early contact for A^* and $\bar{g}^*$. This trend implies that a better agreement of $\bar{g}^*$ can be achieved if a better Gaussianity of the generated rough surface can be achieved.

References

[1] Hyun, S., Pei, L., Molinari, J.F. and Robbins, M.O., 2004. Finite-element analysis of contact between elastic self-affine surfaces. Physical Review E, **70**(2), p.026117.

[2] Campañá, C. and Müser, M.H., 2007. Contact mechanics of real vs. randomly rough surfaces: A Green's function molecular dynamics study. EPL, **77**(3), p.38005.

[3] Jackson, R.L. and Green, I., 2011. On the modeling of elastic contact between rough surfaces. Tribology Transactions, **54**(2), pp.300-314.

[4] Putignano, C., Afferrante, L., Carbone, G. and Demelio, G., 2012. The influence of the statistical properties of self-affine surfaces in elastic contacts: A numerical investigation. Journal of the Mechanics and Physics of Solids, **60**(5), pp.973-982.

[5] Yastrebov, V.A., Anciaux, G. and Molinari, J.F., 2015. From infinitesimal to full contact between rough surfaces: evolution of the contact area. International Journal of Solids and Structures, **52**, pp.83-102.

[6] Yastrebov, V.A., Anciaux, G. and Molinari, J.F., 2017. On the accurate computation of the true contact-area in mechanical contact of random rough surfaces. Tribology International, **114**, pp.161-171.

[7] Borri-Brunetto, M., Carpinteri, A., Chiaia, B., 1998. Lacunarity of the Contact Domain between Elastic Bodies with Rough Boundaries. In: Frantziskonis, G. (Ed) Probamat 97, Probabilities and Materials. Kluwer, Dordrecht.

[8] Jackson, R.L., Streator, J.L., 2006. A multiscale model for contact between rough surfaces. Wear. **261**, pp.1337-1347.

[9] Yan, W. and Komvopoulos, K., 1998. Contact analysis of elastic-plastic fractal surfaces. Journal of Applied Physics, **84**(7), pp.3617-3624.

[10] Voss, R.F., 1985. Random fractal forgeries. In the Fundamental algorithms for computer graphics (pp. 805-835). Springer Berlin Heidelberg.

[11] Hu, Y.Z. and Tonder, K., 1992. Simulation of 3-D random rough surface by 2-D digital filter and Fourier analysis. International Journal of Machine Tools and Manufacture, **32**(1-2), pp.83-90.

[12] Wu, J.J., 2000. Simulation of rough surfaces with FFT. Tribology International, **33**(1), pp.47-58.

[13] Borri, C., Paggi, M., 2015. Topological Characterization of Antireflective and Hydrophobic Rough Surfaces: Are Random Process Theory and Fractal Modeling Applicable? Journal of Physics D: Applied Physics, **48**, p.045301.

[14] Borodich, F.M., Pepelyshev, A. and Savencu, O., 2016. Statistical approaches to description of rough engineering surfaces at nano and microscales. Tribology International, **103**, pp.197-207.

[15] Xu, Y., and Jackson, R.L., 2017, Statistical models of nearly complete elastic rough surface contact-comparison with numerical solutions, Tribiology International, **105**, pp.274-291

[16] Xu, Y., Jackson, R.L., Marghitu, D.B., 2014. Statistical model of nearly complete elastic rough surface contact. International Journal of Solid and Structures, **51**, pp.1075-1088.

[17] Nayak, P.R., 1971. Random process model of rough surfaces. ASME Journal of Lubrication Technology, **93**, pp.398-407.

[18] Manners, W. and Greenwood, J.A., 2006. Some observations on Persson's diffusion theory of elastic contact. Wear, **261**(5), pp.600-610.

[19] Sayles, R.S., and Thomas, T.R., 1979. Measurement of the Statistical Microgeometry of Engineering Surfaces. ASME Journal of Lubrication Technology, **101**, pp.409-417.

[20] Greenwood, J.A., 2006. A simplified elliptic model of rough surface contact. Wear. **261**, pp.191-200.

[21] Persson, B.N., 2001. Theory of rubber friction and contact mechanics. The Journal of Chemical Physics, **115**(8), pp.3840-3861.

[22] Greenwood, J.A. and Williamson, J.B.P., 1966. Contact of nominally flat surfaces. Proceedings of the Royal Society of London A: Mathematical, Physical and Engineering Sciences, **295**(1442), pp.300-319.

Chapter 8

A Complete Statistical Model for Contact Ratio

8.1 Motivation

In the previous chapter, the validity of the statistical models at the early and nearly complete contact are confirmed by the Polonsky and Keer model (i.e., BEM). The predictions of the contact ratio by the statistical models and the BEM have a good agreement. However, these two types of statistical models can only predict the asymptotic contact ratio when $\bar{p}^*$ is infinitesimally small and very large, see Fig. 7.11. As $\bar{p}^*$ enters the intermediate range from the early contact stage, the framework under which the statistical models are developed is no longer valid because of the *asperity coalescence* [1, 2] and the *asperity interaction* [3–7]. Asperity coalescence is due to the finite distance between the neighboring contacting asperities. As $\bar{p}^*$ increases, the neighboring contacting asperities are coalesced into larger contact patches with irregular shapes. The asperity interaction is referred to the coupling between the neighboring contacting asperities due to the elasticity of the substrate. Because of the asperity coalescence and the asperity interaction, each contacting asperity can no longer be studied individually and the final real area of contact and the contact load can no longer be expressed as the superposition of the corresponding results of single asperity contact.

Similar conclusions can also be drawn for the statistical models at the nearly complete contact when $\bar{p}^*$ enters the intermediate range from the nearly complete contact stage. Due to the finite distance between the neighboring pressurized cracks, the *crack coalescence* occurs to form the non-contact patches with irregular shapes. Additionally, each pressurized crack cannot be modeled individually due to the *crack interaction*. Therefore, the non-contact area and the trapped volume cannot be expressed as the superposition of the corresponding results of pressurized cracks.

Some efforts are dedicated to extend the statistical models at early contact to the intermediate load range through including the asperity coalescence [1, 2] and the asperity interaction [3–7]. Among those efforts, some can directly applied to the statistical models at nearly complete contact. In this chapter, an alternative approach is followed to improve the accuracy of the contact ratio predicted by the statistical models within the intermediate range of $\bar{p}^*$. Here, we assume the rough interface is isotropic, Gaussian and self-affine fractal. A curve-fit equation based on the BEM results and the statistical models of nearly complete contact is found to bridge two asymptotic solutions of contact ratio at early complete contact ($A^* \to 0^+$) and nearly complete contact ($A^* \to 1^-$), respectively.

8.2 Generated Rough Surfaces

For the validity of the BEM results, the rough surfaces used in the BEM should all be isotropic and Gaussian at the same time. This may be achieved by the surface generation algorithm developed in the previous chapter as long as the following rule of thumb is satisfied:

$$k_l \gg \frac{1}{L_{x(y)}} \quad \text{and} \quad k_s \ll \frac{1}{\Delta_{x(y)}} = \frac{N_{x(y)}}{L_x}. \tag{8.1}$$

In Chapter 7, 17 rough surface groups (each consists of 1000 surfaces) show an excellent isotropy in an average sense, see Table. 7.2 and Table. 7.3. However, only two out of 17 rough surface groups are found to be Gaussian in an average sense[1]. In this chapter, ten more Gaussian rough surface groups ($\#18 - \#27$) are generated and the important parameters used in the surface generation are tabulated in Table 8.4.

The mean PDFs of each surface group, e.g., $\Phi^{h(p)}(\xi^{h*(p*)})$ and $\Phi^{h(p)}(\kappa_m^{h*(p*)})$, show good agreement with that of the Gaussian process. The mean moments of each rough surface group

---

[1] A rough surface group is considered to be Gaussian if the average PDFs, $\Phi^{h(p)}(\xi^{h*(p*)})$ and $\Phi^{h(p)}(\kappa_m^{h*(p*)})$, with one random variable have good agreement with that of a Gaussian process, Eqs. (2.42) and (7.8). The accuracy of the PDFs with multiple random variables can be indirectly checked through the comparisons of the moments.

Table 8.1: Ten Gaussian surface groups.

Group #	k_l[1/m]	k_s[1/m]	H	$N_x \times N_y$	Group #	k_l[1/m]	k_s[1/m]	H	$N_x \times N_y$
18	16	64	0.1	1024×1024	23	16	128	0.1	2048×2048
19	16	64	0.3	1024×1024	24	16	128	0.3	2048×2048
20	16	64	0.5	1024×1024	25	16	128	0.5	2048×2048
21	16	64	0.7	1024×1024	26	16	128	0.7	2048×2048
22	16	64	0.9	1024×1024	27	16	128	0.9	2048×2048

Table 8.2: Mean moments and bandwidth parameter of the rough surface group over 1000 realizations. “Num” means the mean values of the generated rough surface.

Group #	$m_0^h[m^2]$		m_2^h		$m_4^h[m^{-2}]$		α^h	
	Eq. (2.21)	Num	Eq. (2.22)	Num	Eq. (2.23)	Num	Eq. (2.25)	Num
18	7.75×10^{-9}	7.79×10^{-9}	2.00×10^{-4}	1.96×10^{-4}	12.46	12.27	2.41	2.50
19	8.74×10^{-9}	8.81×10^{-9}	2.00×10^{-4}	1.96×10^{-4}	11.56	11.39	2.53	2.60
20	9.89×10^{-9}	9.99×10^{-9}	2.00×10^{-4}	1.97×10^{-4}	10.61	10.47	2.63	2.70
21	1.12×10^{-8}	1.13×10^{-8}	2.00×10^{-4}	1.97×10^{-4}	9.64	9.52	2.70	2.77
22	1.26×10^{-8}	1.28×10^{-8}	2.00×10^{-4}	1.98×10^{-4}	8.68	8.57	2.74	2.81
23	2.94×10^{-9}	2.95×10^{-9}	2.00×10^{-4}	1.96×10^{-4}	47.06	46.24	3.46	3.55
24	3.79×10^{-9}	3.81×10^{-9}	2.00×10^{-4}	1.96×10^{-4}	42.21	41.63	4.00	4.11
25	4.95×10^{-9}	4.99×10^{-9}	2.00×10^{-4}	1.97×10^{-4}	36.98	36.41	4.56	4.68
26	6.46×10^{-9}	6.53×10^{-9}	2.00×10^{-4}	1.98×10^{-4}	31.27	30.89	5.05	5.16
27	8.33×10^{-9}	8.43×10^{-9}	2.00×10^{-4}	1.98×10^{-4}	25.66	25.37	5.34	5.44

Table 8.3: Mean moments and the bandwidth parameter of the corresponding “pressure surface” over 1000 realizations. “Num” means the mean values of the generated rough surface.

Group #	m_0^{p*}		$m_2^{p*}[m^{-2}]$		$m_4^{p*}[m^{-4}]$		α^p	
	Eq. (2.56)	Num	Eq. (2.57)	Num	Eq. (2.58)	Num	Eq. (2.59)	Num
18	1.00×10^{-4}	1.00×10^{-4}	4.15	4.03	3.32×10^5	3.25×10^5	1.92	2.00
19	1.00×10^{-4}	1.00×10^{-4}	3.85	3.75	2.97×10^5	2.91×10^5	2.00	2.08
20	1.00×10^{-4}	1.00×10^{-4}	3.54	3.44	2.61×10^5	2.57×10^5	2.09	2.17
21	1.00×10^{-4}	1.00×10^{-4}	3.21	3.13	2.26×10^5	2.22×10^5	2.19	2.27
22	1.00×10^{-4}	1.00×10^{-4}	2.89	2.82	1.92×10^5	1.89×10^5	2.30	2.38
23	1.00×10^{-4}	1.00×10^{-4}	15.69	15.26	4.99×10^6	4.88×10^6	2.03	2.10
24	1.00×10^{-4}	1.00×10^{-4}	14.01	13.70	4.30×10^6	4.23×10^6	2.17	2.25
25	1.00×10^{-4}	1.00×10^{-4}	12.30	11.99	3.59×10^6	3.53×10^6	2.37	2.46
26	1.00×10^{-4}	1.00×10^{-4}	10.42	10.18	2.87×10^6	2.83×10^6	2.64	2.73
27	1.00×10^{-4}	1.00×10^{-4}	8.55	8.37	2.20×10^6	2.16×10^6	3.00	3.10

are numerically determined and compared with the corresponding closed-form solutions (Eqs. (2.21-2.23)) in Table 8.2. Similarly, the mean moments of the corresponding pressure surfaces are also tabulated together with the closed-form solutions (Eqs. (2.56-2.58)) in Table 8.3. The standard deviations of the moments and bandwidth parameters are negligible compared with the corresponding mean values. Comparing Tables 8.2 and 8.3 with Tables 7.4 and 7.6 reported in Chapter 7, we can conclude that a significant improvement of the Gaussianity of the generated rough surface can be achieved in the average sense if the rule of thumb in Eq. (7.10) is adopted. However, minor differences can still be found in all the moments and the bandwidth parameter in Tables 8.2 and 8.3. This indicates that the mean PDFs of multiple random variables of the generated rough surface are slightly different from that of the Gaussian process. This inaccuracy may be insignificant in the current study since the difference shown in Tables 8.2 and 8.3 are at least one order of magnitude smaller than the corresponding values.

8.3 BEM Results

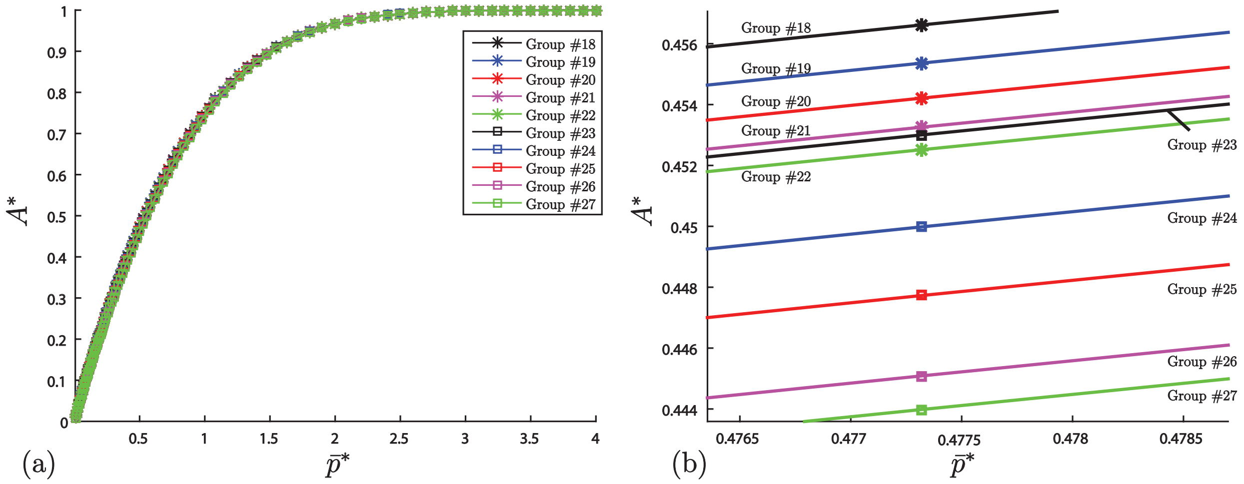

Figure 8.1: Mean contact ratio, A^*, vs. the dimensionless pressure, $\bar{p}^* = \bar{p}/\sqrt{m_0^p}$, for all 10 rough surface groups. (a) Full plot and (b) detailed plot at a certain intermediate pressure. The colored figure is available online.

The BEM results of A^* and $\bar{g}^*$ associated with 10 rough surface groups (each consists 50 surfaces) are solved by the Polonsky and Keer model. Fig. 8.1(a) illustrates that the mean A^* vs. $\bar{p}^*$ relations associated with 10 rough surface groups are converged into a master curve which is nearly insensitive to the changes of the statistics of the rough surface groups. Similar

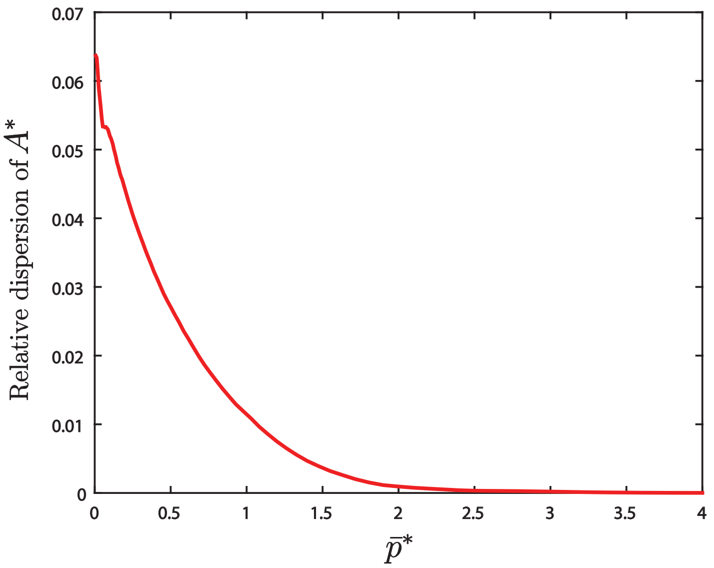

Figure 8.2: The distribution of the maximum dispersion of A^* among 10 rough surface groups

observations have been reported previously by many authors [8–11]. However, minor differences between the curves can still be observed with a finer scale in Fig. 8.1(b). For a fixed upper cut-off wavenumber, k_s, the contact ratio decreases as the increase of Hurst dimension, H. However, a larger k_s (rough surface groups $\#23 - \#27$) may result in more dramatic decrease of A^* against the increase of H. For the fixed pressure, $\bar{p}^*$, the dispersion of the contact ratio, A^*, among ten rough surface groups is quantified by the absolute difference between the maximum and minimum A^*. Define the relative dispersion of A^* at a fixed $\bar{p}^*$ as the ratio of the dispersion to the mean A^* of 10 rough surface groups. The distribution of the relative dispersion of A^* is illustrated in Fig. 8.2. Two interesting observations are summarized below:

1. The prediction of A^* is relatively sensitive to the change of the mean statistics of the rough surface groups at light and intermediate load range ($\bar{p}^* < 2$);
2. The contact ratio, A^*, is nearly independent of the mean statistics of the rough surface groups at nearly complete contact range ($\bar{p}^* \geq 2$);
3. The relative dispersion of A^* is at least one order of magnitude less than the unity throughout the entire range of $\bar{p}^*$.

The slight change of A^* among 10 rough surface groups may also due to the ranges of the statistics of the rough surface and the corresponding “pressure surface” in Tables 8.2 and 8.3

which do not cover a large span of order of magnitudes. As readers may already notice at the beginning of this section that the difference of each rough surface group is mainly due to the different Hurst dimension H if the number of sampling points is fixed to either 1024×1024 or 2048×2048. Changing of H is a compromising procedure in order to achieve the overall Gaussianity of each generated rough surface group. Recalling the observations in Chapter 7, the Gaussianity of each rough surface group, in an average sense, is only insensitive to the change of H. According to the rule of thumb in Eq. (7.10), the choices of k_l and k_s are related to the sampling length, $L_x(L_y)$, and the number of sampling points, $N_x(N_y)$, respectively. Additionally, the ratio of k_s/k_l is greatly maximized to include more frequency components in each realization. Therefore, for a fixed number of sampling points, k_s and k_l are fixed. As a matter of fact, for a larger span of the statistics and the bandwidth parameters, the “safest” approach is to increase the number of sampling points. However, if the sampling points are larger than 2046×2046, an unrealistic amount of computational time (50 surfaces for each rough surface group) and memory usage will be experienced inevitably. In the future, the numerical results associated with larger number of sampling points are needed to prove whether a master curve can be used to represent A^* vs. $\bar{p}^*$ of a Gaussian rough surface with various statistics.

On a contrary, the relations of the average interfacial gap, $\bar{g}^*$, vs. $\bar{p}^*$ associated with 10 rough surface groups do not converge into a master curve, see Fig. 8.3(a). The log-log plot in Fig. 8.3(a) gives a delusion that the dispersion of $\bar{g}^*$ is dramatic at the light load stage. From the plot of the relative dispersion of $\bar{g}^*$ in Fig. 8.3(b), we may found that the dispersion of $\bar{g}^*$ is more severe at heavy load range. However, the overall relative dispersion is larger than the unity which indicates that the relation $\bar{g}^*$ vs. $\bar{p}^*$ strongly depends on the statistics of the Gaussian rough surface.

8.4 Results of Statistical Models

The above observations can, more or less, be confirmed also by the results of the statistical model of early and of nearly complete contact. Only the Greenwood models of the early contact and of the nearly complete contact are used as a representative model. The Greenwood model of

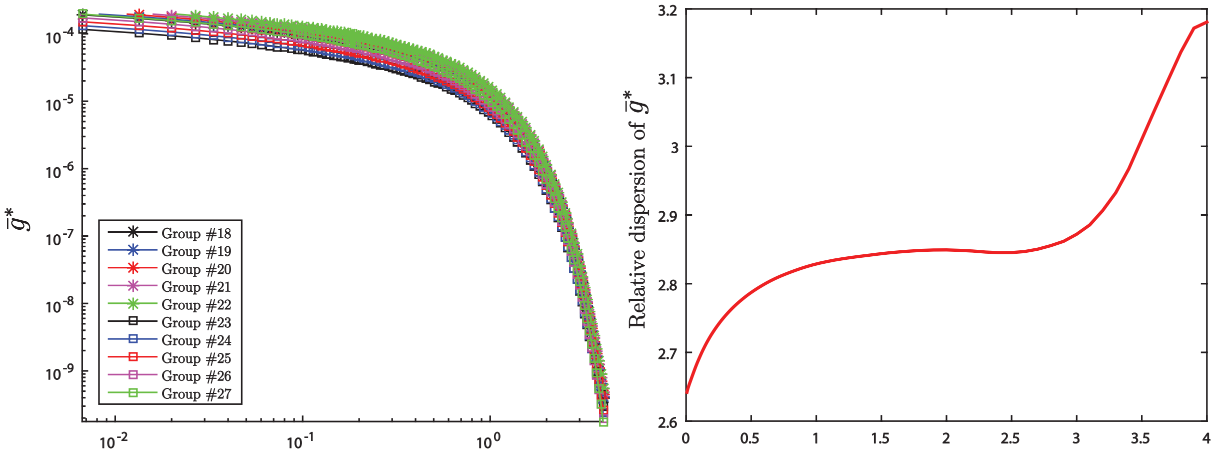

(a) (b)

Figure 8.3: (a) Mean average interfacial gap, $\bar{g}^* = \bar{g}/\sqrt{m_0^h}$, vs. the dimensionless pressure, $\bar{p}^* = \bar{p}/\sqrt{m_0^p}$, for all 10 rough surface groups and (b) the distribution of the maximum dispersion of $\bar{g}^*$ among 10 rough surface groups

the early contact only relies on the bandwidth parameter, α^h, and a sequence of values are used: $\alpha^h = 2,\ 5,\ 10,\ 50,\ 100$. The Greenwood model of the nearly complete contact only relies on the bandwidth parameters, α^h and α^p. A sequence of values of $\alpha^p = 2,\ 5,\ 10,\ 50,\ 100$ is used while $\alpha^h = 2$.

In light load condition as shown in Fig. 8.4(a), especially when $\bar{p}^* \to 0$, the curves of A^* vs. $\bar{p}^*$ associated with various α^h quickly deviates from each other. For $\bar{g}^*$ vs. $\bar{p}^*$, the dramatic dispersion does not occur, especially at lower α^h, see Fig. 8.4(b). This is consistent with Figs. 8.1 and 8.2.

In heavy load condition, the relation of $1 - A^*$ to $\bar{p}^*$ is nearly independent of the change of α^p, see Fig. 8.5(a). This is consistent with that observed in Figs. 8.1 and 8.2. In Fig. 8.5(b), it is shown that the extent of the dispersion of $\bar{g}^*$ is more significant than $1 - A^*$.

8.5 Curve-Fit Solution of A^*

In this section, a possible curve-fit solutions of the contact ratio, A^*, based on the statistical models at nearly complete contact and the BEM results are proposed.

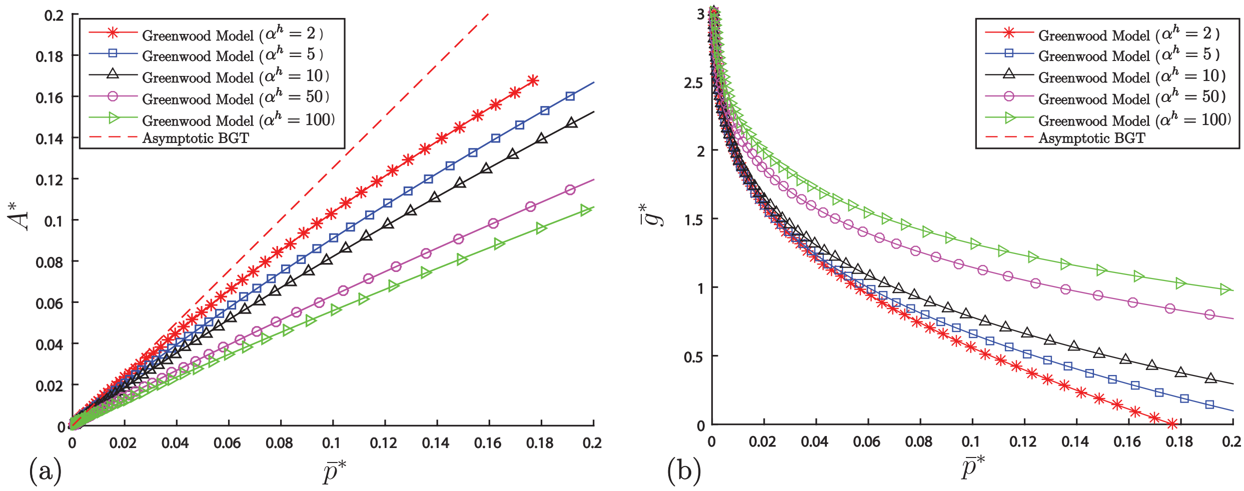

Figure 8.4: Results of Greenwood model at early contact associated with different $\alpha^h = 2,\ 5,\ 10,\ 50$ and 100.

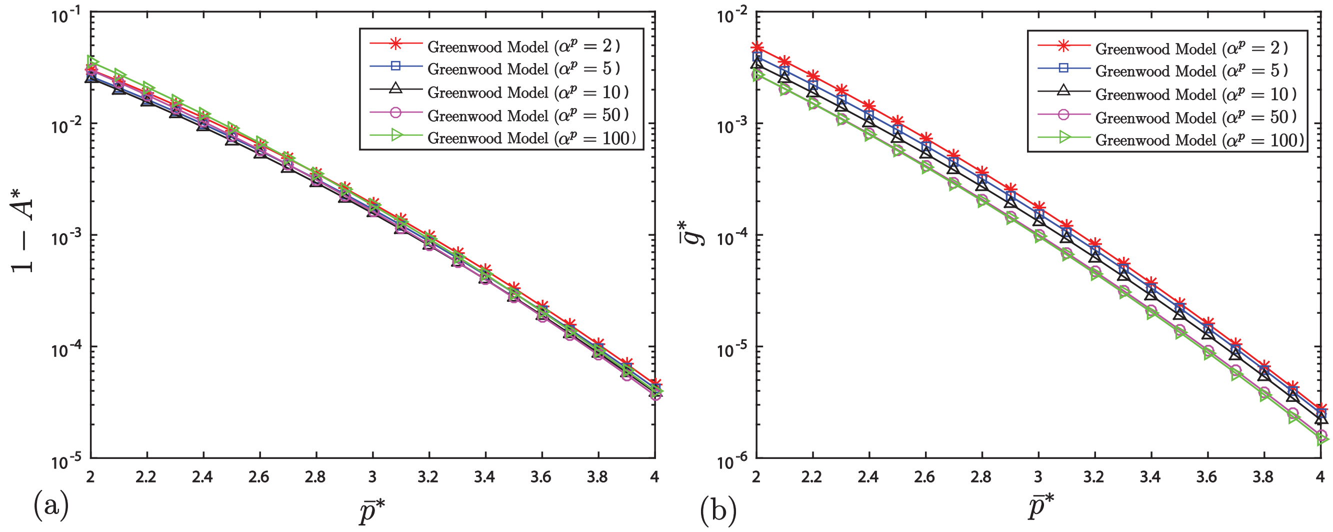

Figure 8.5: Results of Greenwood model at nearly complete contact associated with different $\alpha^p = 2,\ 5,\ 10,\ 50$ and 100 and $\alpha^h = 2$.

The contact ratio of the Greenwood model is used as an example (see Eq. (5.45)) and is rewritten below:

$$A^*(\bar{p}^*) = 1 - \frac{1}{2\sqrt{3}}(\alpha^p)^{1/2}\int_{\bar{p}^*}^{\infty}\int_0^{\infty}(\xi^{p*} - \bar{p}^*)(\kappa_g^{p*})^{-1}\Phi^p(\xi^{p*}, \kappa_g^{p*})d\kappa_g^{p*}d\xi^{p*}.$$

where the PDF, $\Phi^p(\xi^p, \kappa_g^{p*})$, is available in Eq. (2.41). Let $I(\bar{p}^*)$ represents the contact ratio predicted by the Greenwood model. A piece-wise function is proposed to approximate the

BEM results:

$$A^*(\bar{p}^*) = \begin{cases} I(\bar{p}^*) f(\bar{p}^*) & \bar{p}^* \in [0, 2], \\ I(\bar{p^*}) & \bar{p}^* \in (2, \infty). \end{cases} \tag{8.2}$$

The strategy of the above curve-fit is to use the Greenwood model "as is" in the range of nearly complete contact: $\bar{p}^* \in [2, \infty]$. In the lower range, the Greenwood model is corrected by

$$f(\bar{p}^*) = a \exp(b\, \bar{p}^*) + c \exp(d\, \bar{p}^*). \tag{8.3}$$

This function is a summation of two exponential functions of $\bar{p}^*$ and it does not depends on the statistics of the rough surface. The number of free variables (i.e., a, b, c and d) can be reduced through the following boundary conditions:

- $A^*(\bar{p}^* \to 0) \to 0$;
- $A^*(\bar{p}^* \to 2) \to I(2)$.

The former condition requires the vanish of contact ratio, A^*, at zero load and it results in $a = -c$. The latter condition achieves the continuity at $\bar{p}^* = 2$ and requires $c = 1/\left(\exp(2d) - \exp(2b)\right)$. Now, only two free variables are left (i.e., c and d). Recalling the asymptotic BGT model at early contact, the asymptotic derivative $\partial A^*/\partial \bar{p}^*$ at $\bar{p}^* = 0$ is $\sqrt{\pi/2}$. Unfortunately, this boundary condition cannot be achieved with the given function f above, but may be work with the other form of f. However, more constraints may cause the failure of the curve-fit procedure using the optimization. Fortunately, the corresponding slope of the curve-fit solution is fairly close to $\sqrt{\pi/2}$ in Fig. 8.6(b).

The curve fitting toolbox in MATLAB® is used to find b and d for all ten groups and the curve-fit results are tabulated in Table 8.4. The inputs (i.e., α^h and α^p) of the Greenwood model of each surface group are from Tables 8.2 and 8.3. The BEM results of the contact ratio associated with all ten rough surface groups are illustrated in Fig. 8.1(a) and A^* vs. $\bar{p}^*$ is nearly independent of the statistics of the rough surface groups, at least for all ten rough surface groups. This invariance is also shown in the curve-fitting variables: $a = -1.913 \pm 0.0332$, $b = 1.130 \pm 0.0301$ and $c = -0.0490 \pm 0.0128$. The curve-fit A^* has an excellent match

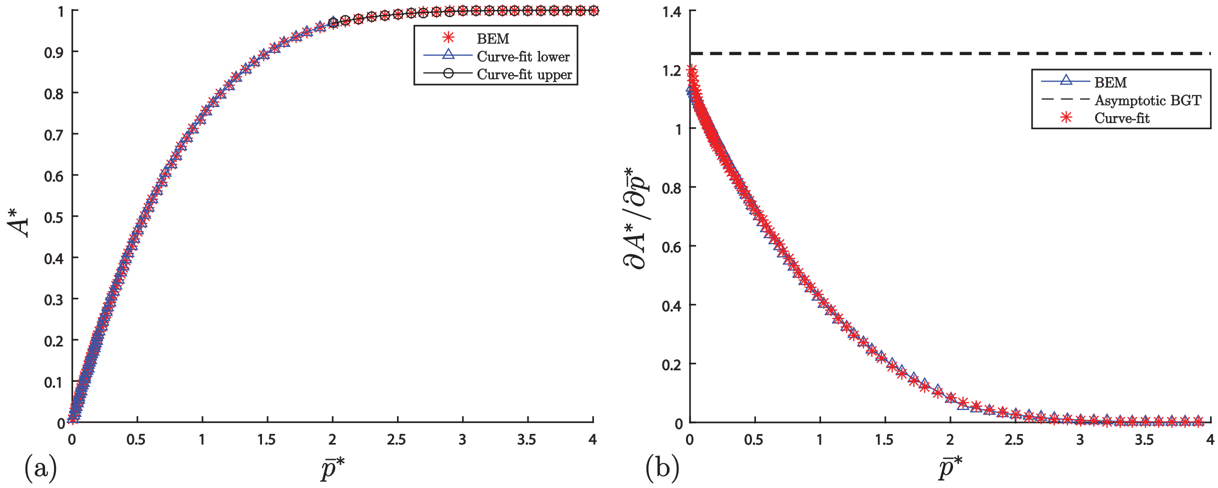

Figure 8.6: (a) The contact ratio of rough surface group #27 predicted by the curve-fit solution and the BEM; (b) the slope, $\partial A^*/\partial \bar{p}^*$, of rough surface group #27 predicted by the curve-fit solution, the BEM and the asymptotic BGT model.

with the corresponding BEM result throughout the entire range of load for all 10 groups and the comparison associated with the surface group #27 can be found in Fig. 8.6(a). The slope, $\partial A^*/\partial \bar{p}^*$, is also illustrated in Fig. 8.6(b). The asymptotic slope of the curve-fit result is close to $\sqrt{\pi/2}$.

Table 8.4: Ten Gaussian surface groups.

Group #	b	c	d	Group #	b	c	d
18	−1.923	1.160	−0.062	23	−1.870	1.169	−0.065
19	−1.924	1.150	−0.058	24	−1.863	1.156	−0.059
20	−1.931	1.138	−0.053	25	−1.873	1.133	−0.049
21	−1.943	1.123	−0.047	26	−1.897	1.103	−0.037
22	−1.959	1.108	−0.040	27	−1.949	1.065	−0.021

8.6 Conclusions

In the previous section, a curve-fit function, Eq. (8.2), based on the Greenwood model at nearly complete contact is found to calculate the contact ratio throughout the entire loading range from the initial touch till the first complete contact. This does not mean that the usage of Eq. (8.2) is only restricted to the Greenwood model. The other statistical model at nearly complete contact may also benefit from the general form of curve-fit function to achieve a better accuracy at lower load range. Recalling the form of the curve-fit function in Eq. (8.2), it is assumed to be dependent on the dimensionless pressure, $\bar{p}^*$, and is independent of the roughness. From the curve-fit results tabulated in Table 8.4, the variations of the curve-fit parameters (i.e., b, c and d) have insignificant standard deviations for 10 rough surface groups and the above hypothesis is confirmed. However, care is needed for the application of the curve-fit function since it is only based upon a small groups of rough surface covering a finite range of the statistics of the rough surfaces. Since the contact ratio formulation of the Greenwood model only relies on the bandwidth parameter, α^p, we may expect that the curve-fit function associated with the parameters in Table 8.4 are only valid for small bandwidth parameter $\alpha^p < 3$. For higher α^p, the curve-fit solution needs further validation.

References

[1] Eid, H. and Adams, G.G., 2007. An elasticplastic finite element analysis of interacting asperities in contact with a rigid flat. Journal of Physics D: Applied Physics, **40**(23), p.7432.

[2] Afferrante, L., Carbone, G. and Demelio, G., 2012. Interacting and coalescing Hertzian asperities: a new multiasperity contact model. Wear, **278**, pp.28-33.

[3] Zhao, Y., Chang, L., 2001. A model of asperity interactions in elasticplastic contact of rough surfaces. ASEM Journal of Tribology, **123**, pp.857864.

[4] Ciavarella, M., Greenwood, J.A., Paggi, M., 2008. Inclusion of interaction in the Greenwood and Williamson contact theory. Wear **265**, pp.729734.

[5] Yeo, C.D., Katta, R.R., Lee, J. and Polycarpou, A.A., 2010. Effect of asperity interactions on rough surface elastic contact behavior: Hard film on soft substrate. Tribology International, **43**(8), pp.1438-1448.

[6] Chandrasekar, S., Eriten, M. and Polycarpou, A.A., 2013. An improved model of asperity interaction in normal contact of rough surfaces. ASME Journal of Applied mechanics, **80**(1), p.011025.

[7] Yashima, S., Romero, V., Wandersman, E., Frétigny, C., Chaudhury, M.K., Chateauminois, A. and Prevost, A.M., 2015. Normal contact and friction of rubber with model randomly rough surfaces. Soft Matter, **11**(5), pp.871-881.

[8] Hyun, S. and Robbins, M.O., 2007. Elastic contact between rough surfaces: Effect of roughness at large and small wavelengths. Tribology International, **40**(10), pp.1413-1422.

[9] Campañá, C. and Müser, M.H., 2007. Contact mechanics of real vs. randomly rough surfaces: A Green's function molecular dynamics study. EPL (Europhysics Letters), **77**(3), p.38005.

[10] Putignano, C., Afferrante, L., Carbone, G. and Demelio, G., 2012. The influence of the statistical properties of self-affine surfaces in elastic contacts: A numerical investigation. Journal of the Mechanics and Physics of Solids, **60**(5), pp.973-982.

[11] Scaraggi, M., Putignano, C. and Carbone, G., 2013. Elastic contact of rough surfaces: A simple criterion to make 2D isotropic roughness equivalent to 1D one. Wear, **297**(1), pp.811-817.

Appendix A

Kelvin's Fundamental Solutions

In this appendix, the Kelvin's solution of a half-space with the boundary $z = 0$ is given in detail. The normal vector of $z = 0$ and the normal derivative $\partial\rho/\partial n$ are

$$n = [0, 0, -1], \quad \frac{\partial \rho}{\partial n} = \eta/\rho. \tag{A.1}$$

Thus, all the fundamental solutions of Eqs. (3.3) and (3.4) used in Eq. (3.11) are simplified and listed below:

$$\begin{aligned}
u^*_{13} &= \frac{1}{16\pi(1-\nu)G}(\xi - x)\eta\rho^{-3}, \\
u^*_{23} &= \frac{1}{16\pi(1-\nu)G}(\zeta - y)\eta\rho^{-3}, \\
u^*_{33} &= \frac{1}{16\pi(1-\nu)G}\left[(3-4\nu)\rho^{-1} + \eta^2\rho^{-3}\right], \\
p^*_{11} &= \frac{-1}{8\pi(1-\nu)}\left[(1-2\nu)\eta\rho^{-3} + 3\eta\rho^{-5}(\xi - x)^2\right], \\
p^*_{22} &= \frac{-1}{8\pi(1-\nu)}\left[(1-2\nu)\eta\rho^{-3} + 3\eta\rho^{-5}(\zeta - y)^2\right], \\
p^*_{33} &= \frac{-1}{8\pi(1-\nu)}\left[(1-2\nu)\eta\rho^{-3} + 3\eta^3\rho^{-5}\right], \\
p^*_{12} = p^*_{21} &= \frac{-3}{8\pi(1-\nu)}\eta\rho^{-5}(\xi - x)(\zeta - y), \\
p^*_{13} &= \frac{-1}{8\pi(1-\nu)}\left[3\eta^2\rho^{-5}(\xi - x) - (1-2\nu)\rho^{-3}(\xi - x)\right], \\
p^*_{31} &= \frac{-1}{8\pi(1-\nu)}\left[3\eta^2\rho^{-5}(\xi - x) + (1-2\nu)\rho^{-3}(\xi - x)\right], \\
p^*_{23} &= \frac{-1}{8\pi(1-\nu)}\left[3\eta^2\rho^{-5}(\zeta - y) - (1-2\nu)\rho^{-3}(\zeta - y)\right], \\
p^*_{32} &= \frac{-1}{8\pi(1-\nu)}\left[3\eta^2\rho^{-5}(\zeta - y) + (1-2\nu)\rho^{-3}(\zeta - y)\right].
\end{aligned} \tag{A.2}$$

For the convenience of the later derivation, the Fourier transform of the above fundamental solutions about $\xi' = \xi - x$ and $\zeta' = \zeta - y$ are also tabulated below:

$$\begin{aligned}
\mathcal{F}\left[u_{13}^*\right] &= \frac{-ik_x\eta}{8(1-\nu)Gk}e^{-2\pi k\eta}, \\
\mathcal{F}\left[u_{23}^*\right] &= \frac{-ik_y\eta}{8(1-\nu)Gk}e^{-2\pi k\eta}, \\
\mathcal{F}\left[u_{33}^*\right] &= \frac{1}{16\pi(1-\nu)G}\left[(3-4\nu)/k + 2\pi\eta\right]e^{-2\pi k\eta}, \\
\mathcal{F}\left[p_{11}^*\right] &= \left[-\frac{1}{2} + \frac{\pi}{2(1-\nu)}\frac{k_x^2}{k}\eta\right]e^{-2\pi k\eta}, \\
\mathcal{F}\left[p_{22}^*\right] &= \left[-\frac{1}{2} + \frac{\pi}{2(1-\nu)}\frac{k_y^2}{k}\eta\right]e^{-2\pi k\eta}, \\
\mathcal{F}\left[p_{33}^*\right] &= \left[-\frac{1}{2} - \frac{\pi}{2(1-\nu)}k\eta\right]e^{-2\pi k\eta}, \\
\mathcal{F}\left[p_{12}^*\right] = \mathcal{F}\left[p_{21}^*\right] &= \frac{\pi}{2(1-\nu)}\frac{k_xk_y}{k}\eta e^{-2\pi k\eta}, \\
\mathcal{F}\left[p_{13}^*\right] &= \left[\frac{\pi i}{2(1-\nu)}k_x\eta - \frac{i(1-2\nu)}{4(1-\nu)}\frac{k_x}{k}\right]e^{-2\pi k\eta}, \\
\mathcal{F}\left[p_{31}^*\right] &= \left[\frac{\pi i}{2(1-\nu)}k_x\eta + \frac{i(1-2\nu)}{4(1-\nu)}\frac{k_x}{k}\right]e^{-2\pi k\eta}, \\
\mathcal{F}\left[p_{23}^*\right] &= \left[\frac{\pi i}{2(1-\nu)}k_y\eta - \frac{i(1-2\nu)}{4(1-\nu)}\frac{k_y}{k}\right]e^{-2\pi k\eta}, \\
\mathcal{F}\left[p_{32}^*\right] &= \left[\frac{\pi i}{2(1-\nu)}k_y\eta + \frac{i(1-2\nu)}{4(1-\nu)}\frac{k_y}{k}\right]e^{-2\pi k\eta}.
\end{aligned} \tag{A.3}$$

The evaluation of the Kelvin's solutions in the frequency domain is based on the analogy between the 2D Fourier transform and the Hankel transform. More detail can be found in the appendix in [1].

References

[1] Sneddon, I.N., 1964. The use of transform methods in elasticity. Air Force Office of Scientific Research, United States Air Force.

Appendix B

Periodic Point Load Kernel

In this appendix, a half-space ($z \geq 0$) is subjected to a λ_x- and λ_y- periodic, unit, normal, point load acting on the boundary, $z = 0$. If one repeatable lies at (x, y), then the corresponding normal traction, $p(\xi, \zeta)$, can be expressed by

$$p(x, y) = \delta(\xi - x, \zeta - y), \tag{B.1}$$

where $\delta(x, y)$ is a two dimensional periodic Dirac function and can be expressed using an infinite double Fourier series [1]:

$$\begin{aligned} \delta(x, y) = a_{00} + &\sum_{m=1}^{\infty}\sum_{n=1}^{\infty} a_{mn} \cos\left(\frac{2\pi m}{\lambda_x}x\right)\cos\left(\frac{2\pi n}{\lambda_y}y\right) + \\ &\sum_{m=1}^{\infty}\sum_{n=1}^{\infty} b_{mn} \sin\left(\frac{2\pi m}{\lambda_x}x\right)\sin\left(\frac{2\pi n}{\lambda_y}y\right). \end{aligned} \tag{B.2}$$

Referring to the above expression, it is obvious that $\delta(x, y)$, as well as the applied traction, $p(x, y)$, are indeed δ_x- and δ_y- periodic.

According to the following identities:

$$a_{00} = \frac{1}{\lambda_x\lambda_y}\int_0^{\lambda_x}\int_0^{\lambda_y} \delta(x, y)dxdy, \tag{B.3}$$

$$a_{mn} = \frac{4}{\lambda_x\lambda_y}\int_0^{\lambda_x}\int_0^{\lambda_y} \delta(x, y)\cos\left(\frac{2\pi m}{\lambda_x}x\right)\cos\left(\frac{2\pi n}{\lambda_y}y\right)dxdy, \tag{B.4}$$

$$b_{mn} = \frac{4}{\lambda_x\lambda_y}\int_0^{\lambda_x}\int_0^{\lambda_y} \delta(x, y)\sin\left(\frac{2\pi m}{\lambda_x}x\right)\sin\left(\frac{2\pi n}{\lambda_y}y\right)dxdy, \tag{B.5}$$

$$1 = \int_0^{\lambda_x}\int_0^{\lambda_y} p(x, y)dxdy, \tag{B.6}$$

then

$$a_{00} = \frac{1}{\lambda_x\lambda_y}, \quad a_{mn} = \frac{4}{\lambda_x\lambda_y}, \quad b_{mn} = 0, \tag{B.7}$$

and the applied normal traction in Eq. (B.1), is rewritten as:

$$p(x,y) = \frac{1}{\lambda_x\lambda_y}\left\{1 + 4\sum_{m=1}^{\infty}\sum_{n=1}^{\infty}\cos\left[\frac{2\pi m}{\lambda_x}(x-\xi)\right]\cos\left[\frac{2\pi n}{\lambda_y}(y-\zeta)\right]\right\}. \tag{B.8}$$

From the Westergaard's solution, Johnson et al. [2] found that if the half-space is subjected to a bi-sinusoidal normal traction on $z = 0$, i.e.,

$$p(x,y) = p^{*}\cos\left(\frac{2\pi m}{\lambda_x}x\right)\cos\left(\frac{2\pi n}{\lambda_y}y\right), \tag{B.9}$$

then the corresponding normal displacement of $z = 0$ is

$$\bar{w}(x,y) = \frac{p^{*}}{\pi E^{*}\sqrt{m^2/\lambda_x^2 + l^2/\lambda_y^2}}\cos\left(\frac{2\pi m}{\lambda_x}x\right)\cos\left(\frac{2\pi n}{\lambda_y}y\right). \tag{B.10}$$

Applying the above correspondence and neglecting the rigid body displacement caused by the mean normal traction, the resultant normal displacement, $w(x,y)$, due to the periodic point load on $z = 0$ in Eq. (B.1) can be expressed $w(\xi,\zeta) = K(\xi - x, \zeta - y)\delta(x,y)$ where $K(\xi - x, \zeta - y)$ is

$$K(x,y) = \frac{4}{\lambda_x\lambda_y}\sum_{m=1}^{\infty}\sum_{n=1}^{\infty}\frac{1}{\sqrt{m^2/\lambda_x^2 + n^2/\lambda_y^2}}\cos\left[\frac{2\pi m}{\lambda_x}x\right]\cos\left[\frac{2\pi n}{\lambda_y}y\right]. \tag{B.11}$$

Unlike the non-periodic influence function, the periodic version in an infinite double Fourier series.

References

[1] Strang, G., 1986. *Introduction to applied mathematics*. Wellesley-Cambridge Press.

[2] Johnson, K.L., Greenwood, J.A. and Higginson, J.G., 1985. The contact of elastic regular wavy surfaces. International Journal of Mechanical Sciences, **27**(6), pp.383-396.

Appendix C

Revisit Barber's Theorem

Considering a rigid punch with arbitrary shape in contact with a half-space on $z = 0$ boundary under the external load P, Barber [1] gave proofs to a series of important theorems. Some theorems are listed below:

Theorem C.1. *The maximum normal surface displacement occurs in the regions where the contact pressures are compressive.*

This is established based on the analogy between the potential theory and contact mechanics.

Theorem C.2. *The contact area, A_r, and the contact pressure at each point within it monotonically increase with the increase of the load P.*

Barber [1] claimed that the above theorem should not be restricted to the case where the contact area is a simply connected region. Thus, the above theorem can be adapted for the contact between an infinite rigid flat and a half-space with nominally flat rough boundary:

Theorem C.3. *The contact ratio, A^*, and the contact pressure at each point within it monotonically increase with the increase of the average contact pressure, $\bar{p}$.*

In this appendix, we would like to extend Theorem C.3 to cover the following statement:

Theorem C.4. *The average interfacial gap, $\bar{g}$, is monotonically decreased with the increase of $\bar{p}$.*

Proof. A corollary of Theorem C.1 states that a contacting point would never be out-of-contact as long as $\bar{p}$ is monotonically increased.Assuming $\bar{p}$ is increased by $\delta\bar{p}$, the contact region Γ_c is enlarged into Γ_c' where $\Gamma_c \subset \Gamma_c'$. According to Theorem C.1, the differential pressure, δp, within Γ_c' is compressive everywhere. According to Eq. (3.21), the differential normal displacement $\delta\bar{w}$ is positive everywhere within the boundary Γ. On one hand, Theorem C.1 implies that $\delta\bar{w}$ inside Γ_c are the same, i.e., $\delta\bar{w}|_{\Gamma_c} = \delta$. On the other hand, Theorem C.3 requires $\delta\bar{w}$ outside Γ_c should be less than δ, i.e.,

$$\langle\delta\bar{w}\rangle < \delta.$$

According to Eq. (3.36), the change of the average interfacial gap is

$$\begin{aligned}\delta\bar{g} &= \langle h - \bar{w} - \delta\bar{w}\rangle|_{\Gamma_c'} - \langle h - \bar{w} - \delta\bar{w}\rangle - \langle h - \bar{w}\rangle|_{\Gamma_c'} + \langle h - \bar{w}\rangle \\ &= -\delta + \langle\delta\bar{w}\rangle \\ &< 0 \qquad \text{(C.1)}\end{aligned}$$

□

References

[1] Barber, J.R., 1974. Determining the contact area in elastic-indentation problems. The Journal of Strain Analysis for Engineering Design, **9**(4), pp.230-232.

Appendix D

Sneddon's Solutions for the Pressurized Penny-Shaped Crack

Consider a penny-shaped crack embedded inside an infinite body. The cylindrical coordinates, $r\theta z$, are chosen with the origins located at the center of the crack. The crack surfaces are parallel to the $z = 0$ plane. The boundaries at the infinity are stress-free. The radius of the crack is a and the crack surfaces are subjected to the axisymmetric normal traction, $p(r)$. The state of stress and the displacement components are solved analytically by Sneddon [1]. The normal stress, $\sigma_{zz}(r \geq a)$, in front of the crack tip and the crack surface normal displacements, $u_z(r \leq a)$, have the following forms [2, 3]:

$$\sigma_{zz}(r) = \frac{2}{\pi}\left[\frac{g(a)}{\sqrt{r^2 - a^2}} - \int_0^a \frac{g'(t)dt}{\sqrt{r^2 - t^2}}\right], \tag{D.1}$$

$$u_z(r) = \frac{4}{\pi E^*}\int_r^a \frac{g(t)dt}{\sqrt{t^2 - r^2}}. \tag{D.2}$$

where

$$g(t) = \int_0^t \frac{sp(s)}{\sqrt{t^2 - s^2}}, \tag{D.3}$$

$$g'(t) = p(0) + t\int_0^t \frac{p'(s)ds}{\sqrt{t^2 - s^2}}. \tag{D.4}$$

The corresponding stress intensity factor[1] (SIF), K_I, is

$$K_I = \frac{2}{\sqrt{\pi a}}\int_0^a \frac{rp(r)dr}{\sqrt{a^2 - r^2}}. \tag{D.5}$$

The above elementary solutions are applied to solve the following pressurized crack problems.

Case I: Parabolic Normal Traction Consider $p(r)$ of the following form:

$$p(r) = p_0 - \frac{\kappa}{2}r^2.$$

---

[1] The stress intensity factor is defined as follows: $K_I = \lim_{r\to a^+} \sigma_{zz}(r)\sqrt{2\pi(r-a)}$

Then, $\sigma_{zz}(r)$, $u_z(r)$ and K_I are

$$\sigma_{zz}(r) =\frac{2}{\pi}\left[\frac{(p_0 a - \frac{1}{3}\kappa a^3)}{\sqrt{r^2-a^2}} - (p_0 - \frac{\kappa}{2}r^2)\tan^{-1}\left(\frac{a}{\sqrt{r^2-a^2}}\right) - \frac{a\kappa}{2}\sqrt{r^2-a^2}\right], \tag{D.6}$$

$$u_z(r) =\frac{4}{\pi E^*}\sqrt{a^2-r^2}\left[p_0 - \frac{1}{9}\kappa(2r^2+a^2)\right], \tag{D.7}$$

$$K_I =2\sqrt{\frac{a}{\pi}}(p_0 - \frac{\kappa}{3}a^2). \tag{D.8}$$

Case II: Constant Normal Traction near the Crack Tip Consider $p(r)$ of the following form:

$$p(r) = \begin{cases} p_0 & c < r \leq a, \\ 0 & r \leq c. \end{cases}$$

The responses of $\sigma_{zz}(r)$, $u_z(r)$ and K_I are[2]:

$$\sigma_{zz}(r) =\frac{2}{\pi}\frac{p_0\sqrt{a^2-c^2}}{\sqrt{r^2-a^2}} - \frac{1}{2}p_0 + \frac{p_0}{\pi}\tan^{-1}\left(\frac{r^2-2a^2+c^2}{2\sqrt{a^2-c^2}\sqrt{r^2-a^2}}\right), \tag{D.9}$$

$$u_z(r) =\frac{4}{\pi E^*}\int_{\max(r,c)}^{a}\frac{p_0\sqrt{t^2-c^2}dt}{\sqrt{t^2-r^2}}, \tag{D.10}$$

$$K_I =\frac{2}{\sqrt{\pi a}}p_0\sqrt{a^2-c^2}. \tag{D.11}$$

For $r < c$, the crack opening displacement is

$$u_z(r) = \frac{2K_I}{E^*\sqrt{\pi a}}\sqrt{a^2-r^2} + \frac{4p_0 c}{\pi E^*}\left[\mathbf{E}(\varphi_1, r/c) - \mathbf{E}(r/c)\right], \tag{D.12}$$

where $\varphi_1 = \sin^{-1}(c/a)$. $\mathbf{E}(\varphi, k)$ and $\mathbf{K}(k)$ are incomplete and complete elliptic integral of the second kind, respectively. For $r \geq c$, the crack opening displacement is

$$u_z(r) = \frac{2K_I}{\sqrt{\pi a}E^*}\sqrt{a^2-r^2}+\frac{4p_0 r}{\pi E^*}\left[\mathbf{E}(\varphi_2, c/r) - \mathbf{E}(c/r)\right]-\frac{4p_0}{\pi E^*}\frac{r^2-c^2}{r}\left[\mathbf{F}(\varphi_2, c/r) - \mathbf{K}(c/r)\right], \tag{D.13}$$

where $\varphi_2 = \sin^{-1}(c/r)$. $\mathbf{F}(\varphi, k)$ and $\mathbf{K}(k)$ are incomplete and complete elliptic integral of the first kind, respectively.

Case III: Constant Normal Traction This case is a special case of case II where $c = 0$ and the response of $\sigma_{zz}(r)$, $u_z(r)$ and K_I can be obtained from the elementary solutions [3]:

$$\sigma_{zz}(r) =\frac{2p_0}{\pi}\left[\frac{a}{\sqrt{r^2-a^2}} - \sin^{-1}\left(\frac{a}{r}\right)\right] \tag{D.14}$$

$$u_z(r) =\frac{4}{\pi E^*}p_0\sqrt{a^2-r^2}, \tag{D.15}$$

$$K_I =2\sqrt{\frac{a}{\pi}}\sigma_0. \tag{D.16}$$

---

[2] Similar results can be found in pp. 178-179 in [3] but with typos in Eq. (3.128).

References

[1] Sneddon, I.N., 1946, The distribution of stress in the neighbourhood of a crack in an elastic solid. Proceedings of the Royal Society of London A: Mathematical, Physical and Engineering Sciences, **187**(1009), pp.229-260.

[2] Sneddon, I.N. and Lowengrub, M., 1969. *Crack problems in the classical theory of elasticity*, John Wiley & Sons Inc.

[3] Maugis, D., 2000. *Contact, adhesion and rupture of elastic solids*. Springer.

Appendix E

The Persson Model of Average Interfacial Gap

Persson [2] studied the average interfacial gap, $\bar{g}$, between an elastic half-space and a rough rigid surface and he gave the following form of the average pressure, $\bar{p}$, in the function of $\bar{g}$:

$$\bar{p} = -\frac{1}{A_n}\frac{\partial U_{el}}{\partial \bar{g}}, \tag{E.1}$$

where U_{el} is the elastic energy under $\bar{p}$ (the contribution from the rigid body motion is neglected). In order to use the consistent variables throughout the whole study, we gave a brief derivation using the new variables.

Following the contact theory of Persson [1,2], U_{el} can be approximated over the frequency domain[1]:

$$U_{el} = E^*\pi^2 A_n\gamma \int_{k_l}^{k_s} k^2 S[h](k) A^*(\bar{p},k)dk, \tag{E.2}$$

where γ is an empirical parameter. $S[h](k)$ is the axisymmetric PSD shown in Eq. (2.18). $A^*(\bar{p},k)$ is contact ratio under $\bar{p}$ where the upper cut-off frequency of PSD in Eq. (2.18) is $k \leq k_s$. A simple form of $A^*(\bar{p},k)$ is available from Eq. (5.59) [3]:

$$A^*(\bar{p},k) = \frac{2}{\sqrt{2\pi m_0^p(k)}}\int_0^{\bar{p}} \text{exp}\left[-\frac{(p-\bar{p})^2}{2m_0^p(k)}\right]dp, \tag{E.3}$$

where $m_0^p(k)$ is the spectral moment, m_0^p, where upper cut-off frequency is k. Substituting Eq. (2.18) (with $k_l = k_r$) into Eq. (2.56) results in the closed-form solution:

$$m_0^p(k) = (E^*)^2\frac{1}{8}\frac{(2\pi)^3 C}{1-H}\left[k^{-2(H-1)} - k_l^{-2(H-1)}\right]. \tag{E.4}$$

Substitute Eq. (E.2) into Eq. (E.1), we can have:

$$\bar{p} = -\frac{1}{A_n}\frac{\partial U_{el}}{\partial \bar{p}}\frac{\partial \bar{p}}{\partial \bar{g}}. \tag{E.5}$$

---

[1] The constant in front of the integral is different from the original formulation due to the different form of Fourier transform pair.

Rearranging the above equation, we can have the following concise form of $\bar{g}$:

$$\bar{g} = \int_{\infty}^{\bar{p}} -\frac{1}{\bar{p}} \frac{\partial U_{el}}{\partial \bar{p}'} \frac{d\bar{p}'}{\bar{p}'}. \tag{E.6}$$

Substituting Eq. (E.2) and (E.3) into the above equation, we can have the final form of $\bar{g}^* = \bar{g}/\sqrt{m_0^h}$

$$\bar{g}^* = \frac{E^* \pi^2 \gamma}{\sqrt{m_0^h}} \int_{k_s}^{k_l} k^2 S[h](k) \frac{2}{\sqrt{2\pi m_0^p(k)}} dk \int_{\bar{p}}^{\infty} \frac{1}{\bar{p}'} \exp\left[-(\bar{p}')^2 / \left(2m_0^p(k)\right)\right] d\bar{p}'. \tag{E.7}$$

The usage of empirical parameter, γ, implies that the elastic energy store in the contact region is, generally, less than the average elastic energy at complete contact. At nearly complete contact, however, these two energies should be close and $\gamma \approx 1$ [2]. A careful analysis of Eq. (E.7) we should be able to identify that the relation of $\bar{g}^*$ to $\bar{p}^*$ only relies on H, k_s and k_l.

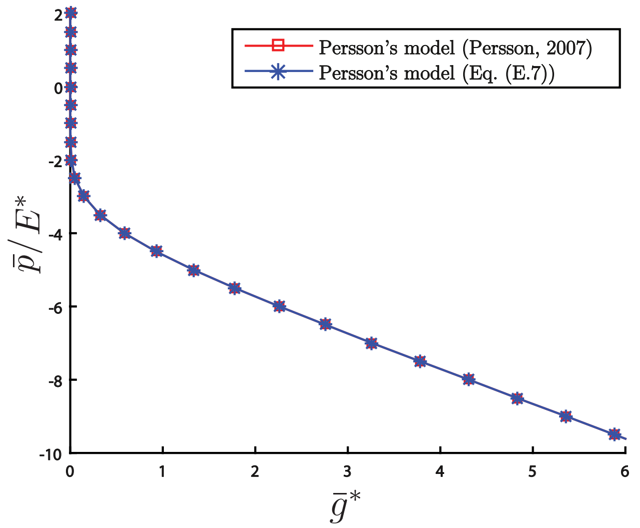

Figure E.1: Recreation of the relation of the dimensionless average interfacial gap, $\bar{g}/\sqrt{m_0^h}$, to the dimensionless contact pressure, $\bar{p}/E^*$, in a log-log plot in [2]. The lower and upper cut-off frequencies are: $2\pi k_l = 1 \times 10^4 [m^{-1}]$ and $2\pi k_s = 7.8 \times 10^9 [m^{-1}]$. Hurst dimension is $H = 0.8$. Surface root mean square roughness is $\sqrt{m_0^h} = 6[\mu m]$. $\gamma = 1$. Reprinted from Tribology International, Xu, Y., and Jackson, R.L., Statistical model of nearly complete elastic rough surface contact - comparison with numerical solutions, **105**, pp. 290, 2017, with permission from Elsevier.

References

[1] Persson, B.N., 2001. Theory of rubber friction and contact mechanics. The Journal of Chemical Physics, **115**(8), pp.3840-3861.

[2] Persson, B.N.J., 2007. Wet adhesion with application to tree frog adhesive toe pads and tires. Journal of Physics: Condensed Matter, **19**(37), pp.376110.

[3] Manners, W. and Greenwood, J.A., 2006. Some observations on Persson's diffusion theory of elastic contact. Wear, **261**(5), pp.600-610.